UNIVERSITY OF SOUTHAMPTON

FACULTY OF ENGINEERING AND APPLIED SCIENCE

AERODYNAMIC SOUND PRODUCTION IN LOW SPEED FLOW DUCTS

by

P.A. Nelson, B.Sc.(Eng.)

Thesis submitted for the degree of
Doctor of Philosophy
in the
Institute of Sound and Vibration Research

August 1980

TO JENNY

UNIVERSITY OF SOUTHAMPTON

ABSTRACT

FACULTY OF ENGINEERING AND APPLIED SCIENCE

INSTITUTE OF SOUND AND VIBRATION RESEARCH

Doctor of Philosophy

AERODYNAMIC SOUND PRODUCTION IN LOW SPEED FLOW DUCTS

by Philip Arthur Nelson

The work presented consists of three main parts. The first two parts consider specific engineering problems directly related to the production of aerodynamic sound in flow ducts, whilst the third part is concerned with an in-depth experimental study of the fluid dynamics of a flow excited acoustic resonance.

The first engineering problem dealt with is that of the prediction of the sound generated when an arbitrary obstruction is placed in a given flow duct. The problem is idealised by considering flat plate flow spoilers placed perpendicular to an oncoming low Mach number flow. Measurements of the sound power radiated by a series of spoilers are in excellent agreement with theoretical predictions based on an analysis which models the source of sound as an equivalent dipole distribution. A technique is thus produced which enables the accurate estimation of the noise generated by low speed flow in the wake of bluff bodies in ducts.

The second engineering problem considered is that of the noise generated by flow over the perforated facings of acoustically absorbent duct linings. Measurements of spectra of the noise generated by flow over practical perforated facings are found to be in good agreement with the predictions of an idealised model. A technique is evolved which enables the estimation of the level and spectral distribution of sound generated by flow over perforated duct liners.

The third part of the work describes detailed observations of the vortex shedding in the neck of a Helmholtz resonator excited to peak amplitude by a mean grazing flow. Results of flow visualisation are presented, together with measurements of the static pressure fluctuations in the resonator neck and measurements of the mean and fluctuating parts of the velocity field. The velocity measurements were undertaken using a two component Laser Doppler Velocimeter. Many of the features of the experimental results are explained using a simple model of the interference of periodic vortex shedding with a transverse reciprocating potential flow. An interpretation of these observations is presented in terms of the local momentum and energy balances occurring in the resonator neck. This analysis suggests that the vortex shedding is controlled by the reciprocating potential flow principally through the action of the Coriolis acceleration. The Coriolis acceleration is also responsible for the production of a source of 'generalised acoustic intensity' near the downstream edge of the resonator neck. This source produces energy which is a few times greater than the acoustic energy radiated to the far field.

ACKNOWLEDGEMENTS

The author wishes to express his grateful appreciation to Sound Attenuators Ltd. for the financial support which made this work possible. In particular, thanks are due to Mr. A.T. Fry for his encouragement and for the provision of the experimental facilities used during the work described in Chapter 2.

The author also wishes to express his gratitude to his supervisor, Professor P.E. Doak, for his continuing enthusiasm and support, and his constant willingness to assist in the progress of this work. Thanks are also due to Dr. C.L. Morfey for many helpful discussions and his particular assistance at crucial stages of the development of the theory presented in Chapter 2.

Dr. N.A. Halliwell also deserves special thanks for his enthusiastic collaboration in the work described in Chapter 4, especially for his skillful alignment and operation of the Laser Doppler Velocimeter.

Sincere thanks are also due to Mrs. B.E. Fahy for her excellent typing of the manuscript. Finally, the author wishes to express his gratitude to all those staff, both at I.S.V.R. and Sound Attenuators Ltd., whose practical assistance so often made this work such a pleasurable task.

CONTENTS

(Each Chapter of this thesis is presented as a self-contained piece of work. References, Figures and Appendices relevant to a particular Chapter appear at the end of that Chapter. The sub-section titles and equations in each Chapter have not been preceded with the number of the Chapter.)

		Page
CHAPTER 1:	INTRODUCTION	
1.	THE THEORY OF AERODYNAMIC SOUND	1.1
2.	THE APPLICATION OF THE ACOUSTIC ANALOGY	1.4
3.	THE PRODUCTION OF ACOUSTIC ENERGY FROM VORTEX SHEDDING	1.6
	REFERENCES	
CHAPTER 2:	AERODYNAMIC SOUND PRODUCTION IN LOW SPEED FLOW DUCTS	
1.	INTRODUCTION	2.1
2.	THEORY	2.3
2.1	The Solution for a Dipole Source Distribution in an Infinite Hard-Walled Duct	2.3
2.2	An Expression for the Acoustic Power Radiated by the Flow in the Wake of a Flat Plate Spoiler	2.6
2.3	Expressions for the Sound Power Radiated by Spoiler Flows at Frequencies above and below Cut-On	2.8
3.	EXPERIMENTAL PROCEDURE	2.12
3.1	Design of the Experimental Rig	2.12
3.2	Airflow Measurements	2.12
3.3	Acoustic Measurements	2.13
3.4	The Spoilers used in the Experiment	2.15
4.	ANALYSIS AND DISCUSSION OF RESULTS	2.15
4.1	The Basis for Normalisation of the Experimental Results	2.15
4.2	The Relationship between Fluctuating and Steady State Drag Forces	2.16
4.3	Scaling Laws for the Normalisation of the Experimental Results	2.17
4.4	Results for the Sound Power Radiated by Flat Plate Flow Spoilers	2.19
4.5	Comparison with Previous Work	2.21
5.	CONCLUSIONS	2.23
	REFERENCES	2.25
	APPENDIX 1: LIST OF SYMBOLS	2.27
	APPENDIX 2: THE DERIVATION OF THE EXPRESSION FOR THE MEAN ACOUSTIC POWER TRANSMITTED DOWN THE DUCT	2.30

Page

APPENDIX 3: EVALUATION OF THE SOURCE VOLUME INTEGRALS FOR FLAT PLATE FLOW SPOILERS 2.32

APPENDIX 4: AN EXPRESSION FOR THE SPECTRAL DENSITY OF THE SOURCE VOLUME INTEGRALS 2.33

FIGURES

CHAPTER 3: NOISE GENERATED BY FLOW OVER PERFORATED SURFACES

1. INTRODUCTION 3.1

2. THEORY 3.3

2.1 The Basis for the Equivalent Source Model 3.3

2.2 The Acoustical Properties of Perforated Screens 3.5

2.3 The Strength of the Equivalent Source 3.8

2.4 Scaling Laws for the Radiated Sound Field 3.12

3. EXPERIMENTAL PROCEDURE 3.15

3.1 The Design of the Experimental Rig and the Perforates Tested 3.15

3.2 Aerodynamic Measurements 3.16

3.3 Acoustic Measurements 3.18

4. ANALYSIS AND DISCUSSION OF RESULTS 3.18

4.1 Results for Unbacked Perforate Screens 3.18

4.2 Sound Generated by Perforated Facings on Dissipative Duct Lining Materials 3.21

4.3 Sound Generated by Perforated Facings on a Honeycomb Backing 3.23

5. CONCLUSIONS 3.24

REFERENCES 3.26

APPENDIX 1: LIST OF SYMBOLS 3.28

FIGURES

CHAPTER 4: THE FLUID DYNAMICS OF A FLOW EXCITED RESONANCE (I) THE EXPERIMENT

1. INTRODUCTION 4.1

2. THE ACOUSTICAL CHARACTERISTICS OF THE RESONATOR 4.5

2.1 The Design and Construction of the Resonator 4.5

2.2 The Response of the Resonator under Acoustic Excitation 4.6

2.3 Aerodynamic Excitation of the Resonator 4.8

2.4 The Sound Power Radiated at Peak Aerodynamic Excitation 4.9

3. FLOW VISUALISATION 4.10

3.1 Experimental Procedure 4.10

3.2 Discussion of Results 4.12

		Page
4.	THE MEASUREMENT OF THE VELOCITY FIELD IN THE RESONATOR NECK	4.14
	4.1 The Principles of Laser Doppler Velocimetry	4.14
	4.2 The Two Component Velocimeter	4.15
	4.3 Experimental Arrangement	4.16
	4.4 Velocimeter Operation	4.18
	4.5 Measurement Procedure	4.19
	4.6 Discussion of Results	4.22
5.	THE MEASUREMENT OF THE FLUCTUATING PRESSURE FIELD IN THE RESONATOR NECK	4.25
	5.1 The Measurement of Fluctuating Static Pressure	4.25
	5.2 Experimental Procedure	4.28
	5.3 Discussion of Results	4.31
6.	CONCLUSIONS	4.32
REFERENCES		4.34
APPENDIX 1:	LIST OF SYMBOLS	4.38
FIGURES		

CHAPTER 5: THE FLUID DYNAMICS OF A FLOW EXCITED RESONANCE (II) ANALYSIS AND DISCUSSION OF RESULTS

1.	INTRODUCTION	5.1
2.	THE VORTICAL FLOW FIELD	5.3
	2.1 The Specification of the Velocity Fields	5.3
	2.2 The Basis for Modelling the Vortex Shedding	5.6
	2.3 The Parameters Controlling the Behaviour of the Shed Vorticity	5.8
3.	A VORTEX SHEDDING MODEL	5.11
	3.1 A Model of Two Dimensional Periodic Vortex Shedding	5.11
	3.2 The Computation of the Vortically Induced Velocity Field	5.14
	3.3 The Deduction of the Vorticity Distribution from the Experimental Results	5.17
	3.4 The Influence of Viscosity on Shear Layer Development	5.20
4.	THE TOTAL FLUCTUATING VELOCITY FIELD	5.21
	4.1 A Model for the Reciprocating Potential Flow	5.21
	4.2 The Resultant Vertical Velocity Fluctuation	5.23
5.	THE FLUCTUATING PRESSURE FIELD	5.26
	5.1 The Pressure Fluctuations associated with the Passage of the Vortices	5.26

	Page
5.2 The Pressure Fluctuations associated with the Reciprocating Potential Flow	5.29
5.3 The Measured Pressure Fluctuation	5.31
6. CONCLUSIONS	5.33
REFERENCES	5.35
APPENDIX 1: LIST OF SYMBOLS	5.37
APPENDIX 2: LISTING OF PROGRAM YVCOEM.FTP	5.40
APPENDIX 3: LISTING OF PROGRAM YOCOEM.FTP	5.41
APPENDIX 4: LISTING OF PROGRAM YPCOEM.FTP	5.42
APPENDIX 5: LISTING OF PROGRAM XVTOTM.FTN	5.43
APPENDIX 6: LISTING OF PROGRAM XOTOTM.FTN	5.44
APPENDIX 7: LISTING OF PROGRAM XPTOTM.FTN	5.45
FIGURES	
CHAPTER 6: THE FLUID DYNAMICS OF A FLOW EXCITED RESONANCE (III) MOMENTUM AND ENERGY BALANCES	
1. INTRODUCTION	6.1
2. THE MOMENTUM BALANCE IN THE RESONATOR NECK	6.4
2.1 The Equation of Conservation of Momentum	6.4
2.2 The Vortical/Potential Flow Interaction	6.6
3. THE ENERGY BALANCE IN THE RESONATOR NECK	6.10
3.1 The Mean Energy Balance	6.10
3.2 The Production of Energy associated with Momentum Fluctuations	6.12
3.3 Evaluation of the Total Power Produced by the Energy Source	6.14
3.4 Energy Flow in the Resonator Neck	6.17
4. A CONCLUDING DISCUSSION OF THE MECHANICS OF THE FLOW EXCITED RESONANCE	6.19
4.1 The Mechanism of Self Excitation	6.19
4.2 A Discussion of the Likely Form of the Energy Balance	6.21
4.3 The Source of Far Field Acoustic Energy	6.23
4.4 The Energy Balance as a Limit to the Amplitude of Oscillation	6.24
4.5 The Physical Interpretation of the Vortex Shedding Model	6.26
5. CONCLUSIONS	6.27
REFERENCES	6.29
APPENDIX 1: LIST OF SYMBOLS	6.30
FIGURES	
CHAPTER 7: CONCLUSIONS	

CHAPTER 1

INTRODUCTION

1. THE THEORY OF AERODYNAMIC SOUND

Lighthill's (1) inspired rearrangement of the mass and momentum conservation equations of fluid motion led to the first formal theoretical framework for dealing with problems of aerodynamically generated sound. The true brilliance of Lighthill's contribution lies not in his relatively straightforward mathematics, but in his interpretation of the theoretical formulation produced. In fact, one is led to wonder how many other workers may previously have stumbled across that particular combination of the equations of fluid motion without realising its full significance. The concept of the "acoustic analogy" recognised by Lighthill is a very simple one. A fluctuating fluid flow surrounded by a "uniform acoustic medium at rest" is replaced by a distribution of "equivalent sources". The form of these equivalent sources is determined by the form of the turbulent fluctuations occurring in the real flow. The sound field in the surrounding medium is then calculated as acoustic waves are "forced" by the equivalent source distribution. Provided the equivalent sources are determined exactly from the characteristics of the real fluid motion, then the sound field produced by the equivalent sources exactly reproduces that generated by the real flow.

Such a simple formulation of what, to an observer of a turbulent flow, appears an immensely complicated problem, must necessarily have its drawbacks. The fundamental limitation, which the observer of turbulent flow may well find disappointing, is that the equivalent sources that replace the fluid motion in solving the acoustic problem do not necessarily bear any relationship to the sources generating the sound in the real flow. Lighthill, of course, fully realised that the sound generated by the real turbulence would be modified due to its "convection with the turbulent flow and propagation at a variable speed within it". In Lighthill's simple formulation "all these effects are replaced by equivalent forcing terms and incorporated in the hypothetical force field". That is, the equivalent sources actually contain the necessary information to account for any effects such as convection and refraction of sound within the flow.

Thus, although Lighthill's theory enables, at least in principle, the establishment of the relationship between the radiated sound and the characteristics of the turbulent flow, it does not allow explicit identification of the acoustic sources embedded in the flow. In

particular it is impossible to satisfactorily identify the specific form of the turbulent fluid motions that are ultimately responsible for the radiated sound. Lighthill's theory thus marked the beginning of a substantial research effort devoted towards a deeper understanding of the aerodynamic sound generation process.

The first significant extension to Lighthill's theory was devised by Curle (2) who provided a technique for dealing with aerodynamic sound problems involving the interaction of flow with solid surfaces. The strength of the equivalent sources replacing the flow in this case can be related directly to the fluctuating force induced by the flow on the solid body. Although providing an immensely powerful and useful technique for dealing with such problems, Curle's theory again allows no identification of the physical details of the sound generation process.

Further formulations of Lighthill's acoustic analogy were advanced by Ribner (3) and Powell (4). Both these theories attempted to compensate for the lack of physical insight provided by Lighthill's basic theory. Ribner's theory recast Lighthill's source term in the form of an "incompressible pressure" field induced by the flow. The fluid dilatations produced in the corresponding slightly compressible flow were then identified as the source of far field sound. Powell's theory adopted the physical notion that it was the acceleration of vorticity that was ultimately responsible for the sound radiated from turbulent fluid flow. The vorticity was identified as inducing the whole flow field, including the radiated sound field. Both the theories of Ribner and Powell however, were still in the form of Lighthill's acoustic analogy, despite their attempts at a plausible physical description of the sound generation process. The interaction of sound with the flow responsible for its generation could still not be dealt with.

The first attempt to produce a theory which accounted for the convection of the sound by the flow was that due to Phillips (5). An inhomogeneous convected wave equation was derived in which the effects of convection of the pressure disturbances is contained in the wave operator. The subsequent debate on the validity of this approach (see the review by Doak (6)) was centred on, as much as anything, the suitability of the wave operator for describing the propagation of small disturbances in a transversely sheared mean flow. Lilley (7) advocated the use of a third order partial differential equation to describe the propagation of pressure disturbances, although it transpired that this formulation also contained a description of the exponentially growing

waves of the developing mixing layer. These unstable solutions have to be suppressed in order to describe the pressure disturbances produced by sources embedded in a shear flow (Morfey and Tester (8)). The problem remains of dealing convincingly with flow models exhibiting unstable solutions representing the growth of hydrodynamic disturbances which themselves may be responsible for sound production (see, for example, the paper by Dowling, Ffowcs Williams and Goldstein (9)).

Further theoretical developments attempting to identify the particular class of fluid motions responsible for aerodynamic sound production are those of Doak (10) and Howe (11). Doak's momentum potential description of fluid motion provides a basis for unambiguous identification of "acoustic", "vortical" and "thermal" motions of unsteady fluid flow. Doak advances an inhomogeneous convected wave equation (of which the Lilley equation is a special case) describing the propagation of the acoustic part of the scalar momentum potential. The inhomogeneity representing the source of these acoustic disturbances is dependent upon only vortical and thermal quantities, thus giving a clear identification of cause and effect. Howe's formulation of the aerodynamic sound problem is based on a wave operator which governs the propagation of small amplitude disturbances in an irrotational isentropic mean flow. The "natural" propagation variable emerging from Howe's analysis is the stagnation enthalpy. Fluctuations in stagnation enthalpy (which become directly related to acoustic pressure fluctuations in a medium at rest) are driven by sources associated solely with regions of the flow where the vorticity vector and entropy gradient vector are non-vanishing.

Although Doak's theory has yet to be exploited, Howe has used his formulation to solve a wide range of model problems. Howe's work essentially confirms Powell's theory of vortex sound, although the production of sound by entropy inhomogeneities is also accounted for. The ability of Howe's theory to localise sound production to regions of the flow containing vorticity enables a further degree of physical insight to be gained into the sound production process. In particular, Howe demonstrates (11) that the Powell dipole source term, the strength of which is determined by the local Coriolis acceleration, is acoustically equivalent to Lighthill's quadrupole source term when dealing with free space radiation problems. When vorticity is accelerated in the region of a solid body, the more powerful dipole radiation is produced.

However, it is not the purpose here to provide an exhaustive review of these and many other experimental and theoretical developments.

A thorough treatment of the "conceptual adequacy and physical scope" of many of the theories of aerodynamic sound subsequent to that of Lighthill can be found in the paper by Doak (12), or in the more recent review by Ffowcs Williams (13). Rather, it is necessary to broadly outline these developments in order that the work described here is placed in its proper context. The work undertaken in this thesis contributes on two distinct levels. The first is the application of the now well established techniques of the acoustic analogy to two specific problems of engineering importance. As such, this work can be thought of as "applied research". The second contribution is directed towards the experimental investigation of the mechanics underlying the production of sound by the acceleration of vorticity. This falls very much in the category of "pure research". The two engineering problems dealt with will be described in Chapters 2 and 3, whilst the second contribution, involving the experimental investigation of the periodic vortex shedding coupled to an acoustic resonance, is presented in Chapters 4, 5 and 6. A further outline of this work, and its place in the general framework of the theory of aerodynamic sound, is presented in the two sections below.

2. THE APPLICATION OF THE ACOUSTIC ANALOGY

The first engineering problem dealt with is that of the sound generated by flow past an obstruction in a duct. The work presented is entirely contained in Chapter 2 which is entitled "Aerodynamic Sound Production in Low Speed Flow Ducts", from which this thesis also takes its title. The problem considered is one of wide ranging engineering importance. The initial investigation is, however, confined to duct flows at low Mach number. This enables Curle's (2) result to be used without any prior knowledge of the precise details of the unsteady wake flow responsible for the production of acoustic energy. The sound radiated can be thought of as emanating from a distribution of dipole type equivalent sources, the strength of these sources being exactly determined by the unsteady forces exerted by the flow on the duct obstruction.

Previous work on the generation of aerodynamic sound in flow ducts, notably that of Gordon (14,15) Heller and Widnall (16), and Davies and Ffowcs Williams (17), has emphasised the need for careful consideration of the effect of enclosure on the sound power output of equivalent source distributions. A theory is thus developed which is based on Doak's (18) solution for the acoustic pressure in an infinite hard walled duct containing an arbitrary source distribution. The effects of the mean flow in the duct are neglected in the low Mach number case considered. The

use of certain statistical assumptions about the nature of the dipole equivalent source distribution enables the relationship to be established between the sound power radiated and the total fluctuating drag force acting on the flow duct obstruction. Expressions are produced which are valid for plane wave propagation and for multi-modal propagation in the duct.

A series of experiments is described which enables the determination of the sound power radiated by various flat plate flow spoilers immersed in a low speed flow duct. The results produced completely confirm the validity of the assumptions used in the development of the theory. A further step is taken in the analysis of the results. It is assumed that the fluctuating drag force acting on the flow spoilers is in direct proportion to the steady state drag force acting, the two being related by a single Strouhal number dependent constant. This assumption was first used by Gordon (15) and later given some experimental verification by Heller and Widnall (16). The use of this relationship produces a surprisingly good collapse of experimental results. This opens up the possibility of techniques for the accurate prediction of the level and spectral distribution of the sound power radiated by arbitrary flow duct obstructions from a knowledge of straightforward engineering parameters. It remains to be seen whether such a scheme is applicable to other types of flow duct obstructions and discontinuities.

The second engineering problem considered is that of the additional sound generated by flow over the perforated surface of an acoustically absorbent flow duct lining. This work is presented in Chapter 3 entitled "Noise Generated by Flow over Perforated Surfaces". The objective in this instance is to provide a means of predicting the level of aerodynamic noise generated when a given perforate is used as a facing material over either a dissipative duct lining or a honeycomb type liner used in aircraft engine ducts.

The starting point for this study is the analysis of Ffowcs Williams (19) who determines the form of the radiated field when turbulence interacts with an infinite perforated screen. The important result deduced from this analysis is that the equivalent sources thought of as generating the sound can be represented by a pair of monopole type sources situated at each aperture location. The monopoles are of equal and opposite strength, one located immediately above the screen and one immediately below. When the screen is transparent to sound, the lower

monopole combines with the upper monopole to give a net dipole type radiated field. The strength of the monopoles is determined exactly by the rate of mass flow driven through the aperture by the hydrodynamic field.

Ffowcs Williams' analysis does, however, contain certain restrictive assumptions. The particular perforate screen geometry considered is not necessarily used in practice. A series of experiments is thus conducted in order to measure the sound field radiated when turbulence impinges on a variety of practical perforated screens. It is found that the experimental results are in good agreement with theoretical predictions based on the equivalent source representation suggested by Ffowcs Williams. In particular, the equivalent source representation makes explicit the dependence of the radiated sound on the Strouhal number based on perforation diameter.

These findings enable the level and spectral distribution of the sound power radiated to be predicted for arbitrary perforate geometries used as duct liner facings. Solution of the problem of a continuous absorption and generation of sound in a duct enables the predictions to be compared with measurements of the noise generated by flow over a dissipative duct lining. The predictions are in encouraging agreement with the results measured in practice.

The equivalent source representation of the sound generation process is again shown to be an immensely useful technique for dealing with such problems. However, a hint of the mechanism by which acoustic energy is extracted from the flow becomes evident from this work. It is found that the most efficient radiation of sound occurs when the eddies shed in the perforations are of a scale comparable to the size of the perforations. This suggests the importance of the interaction of the shed vorticity with the surrounding solid surface. One is thus led logically to the detailed investigation of these effects that is undertaken in the remainder of the thesis.

3. THE PRODUCTION OF ACOUSTIC ENERGY FROM VORTEX SHEDDING

Chapters 4, 5 and 6 of this thesis are directed towards the detailed investigation of a specific source of aerodynamic sound. The source chosen for study is that in the neck of a flow excited Helmholtz resonator. The principal intention of this work is to provide a deeper understanding of the means by which the shedding of vorticity is responsible for the production of aerodynamic sound. Despite the theoretical

developments outlined above, there is still a conspicuous gap in the understanding of the behaviour of real sound producing flows. The particular flow chosen is ideally suited to close experimental observation. Grazing flow over the neck of a Helmholtz resonator forms an initially unstable shear layer leaving the upstream lip of the neck. This layer rolls up to form vortices which then convect downstream and subsequently interact with the downstream lip of the neck. At the appropriate speed of the mean grazing flow, this entire process occurs periodically and is phase locked to the oscillations of the resonant cavity. This series of events is accompanied by the radiation of acoustic power which constitutes a significant fraction (of the order of one per cent) of the mean rate of energy flow of the impinging airstream. This mechanism constitutes one of the most efficient means of extracting acoustic energy from unsteady flow.

This investigation of "The Fluid Dynamics of a Flow Excited Resonance" is undertaken in three parts. Part I, "The Experiment", presented in Chapter 4, describes various observations of the behaviour of the two dimensional vortex shedding in the neck of a specifically designed Helmholtz resonator. All the measurements are undertaken at the condition of peak amplitude of excitation of the resonance. Firstly, the flow is visualised using a stroboscope triggered by a signal derived from the cavity pressure fluctuations. The introduction of a phase shift into the trigger circuit enables the flow to be "frozen" at various points during the periodic cycle. Although the results of flow visualisation have to be interpreted carefully, a number of interesting features are revealed. The most important observation is that the vortices formed undergo a rapid increase in convection speed on reaching the downstream lip of the resonator neck.

More quantitative details of the vortex shedding process are established by the use of a Laser Doppler Velocimeter. This relatively new experimental technique enables the simultaneous point measurement of two components of the velocity field. Both mean and fluctuating parts of the "streamwise" and "vertical" velocity components in the resonator neck are measured. Some striking features of the flow field are revealed which would have been difficult to deduce by any other means. The most significant observation is the rapidity with which the unstable shear layer begins to roll up into stable discrete vortices.

The use of a small microphone probe tube enables the accurate measurement of the static pressure fluctuations in the resonator neck to

be made. These measurements reveal a remarkable pressure interference pattern. In a region near the downstream edge of the resonator neck, the amplitude of the pressure fluctuations is driven to a surprisingly low value whilst the relative phase of the fluctuations changes extremely rapidly in the streamwise direction.

An attempt to further understand these experimental results is presented in Chapter 5 in Part II of the investigation. This initial analysis and discussion of results uses a simple model of periodic vortex shedding to aid in the interpretation of the experimental observations. For reasons which will be outlined in full in Chapter 5, it is shown that a reasonably simple representation of the flow is more profitable than a detailed analysis of the stability characteristics of the separating shear layer. It is demonstrated that many of the features of the measured velocity field can be described by a model of the periodic streamwise convection of discrete vortices which interfere with a transverse uniform reciprocating potential flow. It is also shown that the vortically induced velocity field appears to cancel the reciprocating potential flow at the upstream edge of the neck. This tends to confirm that the Kutta condition is satisfied, this also being apparent from the flow visualisation which shows the shear layer leaving the upstream edge tangentially at all times during the motion.

The model vortices used are characterised by two parameters: the vortex strength and the effective core radius. It is shown that the vortex strength is determined by the mean flow boundary conditions. The effective core radius of the vortices shed in the real case can be determined by the measured mean and fluctuating values of the streamwise velocity component. A knowledge of the vortex strength and core radius enables an estimate to be made of the static pressure fluctuations induced by the periodic passage of the vortices. It is then demonstrated that the measured pressure interference pattern can be explained by the interference of the vortex induced pressure fluctuations with those associated with the reciprocating potential flow.

This apparent superposition of pressure fields leads to an analysis of the local momentum balances occurring in the flow. This is undertaken in Chapter 6 which constitutes Part III of the investigation. It emerges from a reordering of the linearised momentum equation that there is one term which does not explicitly appear to be balanced by a pressure gradient. This is the Coriolis acceleration produced when the reciprocating potential flow deflects the shed vorticity. The suggestion

is then made that the reciprocating potential flow driven by the cavity pressure fluctuations controls the vortex shedding process principally through the action of the Coriolis acceleration. This hypothesis is partly confirmed by the observed streamwise acceleration of the vortices reaching the downstream edge. The increase in convection speed is in good agreement with the velocity change expected to occur as a result of the Coriolis acceleration.

Further insight into the part played by the Coriolis acceleration is given by an analysis of the energy interchanges occurring in the resonator neck. This is carried out within the framework of the energy balance equations derived by Doak (20). In an inviscid, non heat conducting fluid, the work done by the fluctuating Coriolis acceleration provides the only mechanism of achieving a transfer of energy from the mean energy flux associated with mean momentum to the mean energy flux associated with fluctuating momentum. Doak's definition of mean energy flux associated with fluctuating momentum has the property of continuity over a wide range of conditions. In an ideal fluid, the mean energy flux associated with the fluctuating motion can only be produced (or absorbed) in the presence of vorticity. The definition adopted also reduces to that of mean acoustic intensity in a medium at rest.

There is no generally accepted definition of "acoustic intensity" in the region of an unsteady non-uniform flow containing vorticity. This naturally prevents any explicit identification of the source of far field energy generated by such a flow. An approach suggested by Morfey (21) is to define an intensity which is "continuous" over the widest possible range of conditions and which also reduces to the usual definition of acoustic intensity in a medium at rest. It may then be possible to identify the source of this "generalised acoustic intensity".

It emerges that Doak's definition of the mean energy flux associated with fluctuating momentum is eminently suitable as a definition of "generalised acoustic intensity". The region of the resonator neck near the downstream edge is clearly identified as a source of this generalised intensity. The rate of production of energy from this source is a few times greater than the acoustic power radiated to the far field. It also transpires that the region of vortex formation near the upstream edge of the resonator neck constitutes a sink of energy associated with momentum fluctuations. The measurements of the mean and fluctuating parts of the two components of the velocity field and the fluctuating pressure field

also enables the flow of energy in the resonator neck to be established. This shows a recirculating flow of energy, a "feedback" of energy being evident along the lower half of the mean shear layer from the source region to the sink region.

The establishment of this information is followed by a concluding discussion of the mechanics of operation of the flow excited resonance. A reasonably coherent picture can be painted of the mechanism of operation of the oscillating system. The rôle of the Kutta condition is discussed in the context of determining the relationship between the reciprocating potential flow amplitude and the rate of accumulation of the shed vorticity into vortices. A discussion of the possible energy balance in the flow leads to the suggestion that the mean energy balance actually determines the maximum amplitude to which the system oscillations will grow.

The close examination of this particular source of aerodynamic sound thus reveals several interesting features of the fluid motions leading to acoustic energy production which would not be uncovered by an "equivalent source" representation of the process. The mechanism by which acoustic energy can be extracted from the energy of the mean flow is made clear. Although the location of the source of energy obviously depends on the particular definition of generalised acoustic intensity adopted, it is demonstrated that Doak's energy balance equations provide a conceptually useful framework for dealing with problems of aerodynamic sound generation.

REFERENCES

1. M.J. LIGHTHILL 1952 Proceedings of the Royal Society Series A 211, 564-587. On sound generated aerodynamically. I. General theory.

2. N. CURLE 1955 Proceedings of the Royal Society Series A 231, 505-514. The influence of solid boundaries upon aerodynamic sound.

3. H.S. RIBNER 1962 UTIAS Report No. 86, University of Toronto. Aerodynamic noise from fluid dilatations, a theory of the sound from jets and other flows.

4. A. POWELL 1964 Journal of the Acoustical Society of America 36, 177-195. Theory of vortex sound.

5. O.M. PHILLIPS 1960 Journal of Fluid Mechanics 9, 1-28. On the generation of sound by supersonic turbulent shear layers.

6. P.E. DOAK 1973 Journal of Sound and Vibration 28, 527-561. Fundamentals of aerodynamic sound theory and flow duct acoustics.

7. G.M. LILLEY 1972 in United States Air Force Technical Report AFAPL-TR-72-53-Volume IV. Theory of turbulence generated jet noise: generation of sound in a mixing region.

8. C.L. MORFEY and B.J. TESTER 1976 Journal of Sound and Vibration 46 79-103. Developments in jet noise modelling.

9. A.P. DOWLING, J.E. FFOWCS WILLIAMS and M.E. GOLDSTEIN 1978 Philosophical Transactions of the Royal Society of London 288, 321-349. Sound production in a moving stream.

10. P.E. DOAK 1973 Journal of Sound and Vibration 26, 91-120. Analysis of internally generated sound in continuous materials: 3. The momentum potential field description of fluctuating fluid motion as a basis for a unified theory of internally generated sound.

11. M.S. HOWE 1975 Journal of Fluid Mechanics 71, 625-673. Contributions to the theory of aerodynamic sound with application to excess jet noise and the theory of the flute.

12. P.E. DOAK 1972 Journal of Sound and Vibration 25, 263-335. Analysis of internally generated sound in continuous materials: 2. A critical review of the conceptual adequacy and physical scope of existing theories of aerodynamic noise, with special reference to supersonic jet noise.

13. J.E. FFOWCS WILLIAMS 1977 Annual Review of Fluid Mechanics 9, 447-468. Aeroacoustics.

14. C.G. GORDON 1968 Journal of the Acoustical Society of America 43, 1041-1048. Spoiler-generated flow noise. I. The Experiment.

15. C.G. GORDON 1969 Journal of the Acoustical Society of America 45, 214-223. Spoiler generated flow noise. II. Results.

16. H.H. HELLER and S.E. WIDNALL 1970 Journal of the Acoustical Society of America 47, 924-936. Sound radiation from rigid flow spoilers correlated with fluctuating forces.

17. H.G. DAVIES and J.E. FFOWCS WILLIAMS 1968 Journal of Fluid Mechanics 32, 765-778. Aerodynamics of sound generation in a pipe.

18. P.E. DOAK 1973 Journal of Sound and Vibration 31, 1-72. Excitation, transmission and radiation of sound from source distributions in hard walled ducts of finite length; (1) The effects of duct cross section geometry and source distribution space time pattern.

19. J.E. FFOWCS WILLIAMS 1972 Journal of Fluid Mechanics 51, 737-749. The acoustics of turbulence near sound absorbent liners.

20. P.E. DOAK 1974 Eighth International Congress on Acoustics. Contributed Papers Volume II, page 532. Acoustic, thermal and turbulent energy density and linear momentum density relationships and fluxes in fluctuating fluid flows. (A complete report on this work is being prepared for publication.)

21. C.L. MORFEY 1971 Journal of Sound and Vibration 14, 159-170. Acoustic energy in non-uniform flows.

CHAPTER 2

AERODYNAMIC SOUND PRODUCTION IN LOW SPEED FLOW DUCTS

1. INTRODUCTION

Noise generation by unsteady flow in the wake of an obstruction in a flow duct is a problem of considerable engineering importance. There are many instances where it is desirable to predict accurately the additional noise generated by the insertion of an obstruction in a ducted flow. The specific problem that motivates this study is that of the additional noise produced when sound absorbing splitters are placed in a flow duct. Splitter attenuators are commonly used in ducts for absorbing the noise produced by fluid handling equipment, such as ventilation system fans and ground based gas turbine installations. Such splitters generate noise as well as absorbing it. This "self noise" results mainly from unsteady flow and turbulence in the splitter wakes. Knowledge of the level of self noise is clearly of importance in the optimum design of attenuators.

The ultimate objective of the present investigation is the ability to predict the level and spectral distribution of the additional acoustic energy produced by any given obstruction in any given ducted flow. Initially, however, attention has been confined to the geometrically simple case of a flat plate placed perpendicular to the flow, and the flow Mach number has been assumed small. Noise production by flow spoilers in a duct was first given detailed attention by Gordon (1,2), who was partly successful in producing scaling laws to collapse his measured sound power data onto a "generalised spectrum". The essence of Gordon's approach has been used here. That is, an attempt has been made to establish scaling laws which relate the sound power radiated to the geometrical and flow parameters involved.

Subsequent work by Heller and Widnall (3) clarified the acoustical significance of the duct enclosing the noise source. Gordon had derived his scaling laws from a free-field radiation model in which the noise was produced by a point fluctuating force and the presence of the duct was neglected. A rigorous development of the theory for in-duct spoiler noise has been pursued here, in order to retain any factors that may influence the net sound power output. Curle's (4) extension of Lighthill's (5) original acoustic analogy has been used to model the equivalent aerodynamic noise source in terms of the fluctuating drag force acting on the spoiler. The problem has thus been reduced to one of a dipole source distribution in an infinite duct.

Extension of Doak's (6) analysis of the latter problem allows the sound power radiated by the source distribution to be derived from the solution of the inhomogeneous wave equation in an infinite hard-walled duct. The expression for the sound power radiated can then be considerably simplified by making fairly realistic statistical assumptions about the nature of the fluctuating force distribution acting on the spoiler. Under these conditions, the sound power radiated can be related to the total fluctuating drag force acting on the spoiler. At frequencies below the cut-on frequency of the first transverse duct mode, the presence of the infinite duct drastically modifies the radiation: the drag dipole behaves like a free-field monopole, with a consequent U^4 velocity dependence of the sound power radiated. At frequencies above the cut-on frequency of the first transverse duct mode, the contributions from all the propagating modes may be summed to produce an approximate expression for the sound power radiated. As the number of propagating modes increases, this expression approaches that for the power radiated by a dipole in a free field, with a resulting U^6 velocity dependence.

These theoretical conclusions have been verified experimentally by measuring the sound power radiated by a series of flat plate spoilers mounted in a duct with flow. The predicted velocity dependence of the sound power radiated has been confirmed. It is found that in practice the transition from a U^4 to a U^6 velocity dependence occurs very rapidly as the frequency is increased above the cut-on frequency of the first transverse duct mode.

In analysing the experimental results, it has further been assumed that the fluctuating drag force acting on the test spoilers is in direct proportion to the steady state drag force acting. This assumption was also used by Gordon (1,2) and is supported by the experiments of Heller and Widnall (3). Evaluation of the constant of proportionality between the fluctuating and steady state drag forces from the experimental results produces an excellent collapse of data onto a generalised spectrum.

Most of the experimental data obtained were at high Strouhal numbers and low Mach numbers (large dimensions and low velocities), whereas the data of Gordon and others were obtained at low Strouhal numbers and high Mach numbers (small dimensions and high velocities). Comparison of the data presented here with the data from previous workers has been made. Gordon's data at low speeds (maximum local velocities below 100 m/s) are in good agreement with the results presented here. At higher speeds,

Gordon's results give a strong indication that the equivalent source distribution dominating the radiation changes from a dipole type to a quadrupole type. The scaling laws derived from the dipole source model are thus limited to maximum local flow Mach numbers below 0.3.

Initial data from measurements of the noise produced by attenuator exit flows have also been found to collapse on the same basis as the spoiler noise data. The indication is that the approach taken here could well form the basis of a useful engineering prediction technique for arbitrary obstructions in low speed flow ducts.

2. THEORY

2.1 The Solution for a Dipole Source Distribution in an Infinite Hard-Walled Duct

When a solid body is immersed in a fluid flow, sound is radiated by the unsteady flow produced in the region of the body. Curle (4) showed that, for a non-vibrating body, the resulting sound field could be expressed as that due to a distribution of dipole sources over the surface of the body and a distribution of quadrupoles in the surrounding fluid. For flows at low Mach numbers, and other things being equal, the dipole sources dominate the radiation. The local strength of the surface dipole distribution is given by the fluctuating normal stress exerted by the body surface on the fluid. Thus, at low Mach numbers, the problem of sound produced by a flow spoiler in a duct can be treated by replacing the spoiler and the turbulence by a distribution of dipole sources radiating into a duct filled with fluid at rest. The strengths of these equivalent dipole sources are determined by the fluid forces acting on the spoiler in the real flow.

The equation to be solved, when the problem is formulated in this way, is that for the propagation in a duct of sound produced by an equivalent dipole source distribution located in the duct, with given boundary conditions:

$$\left(\nabla^2 - \frac{1}{c_o^2}\,\frac{\partial^2}{\partial t^2}\right) p(x_k,t) = \rho_o \frac{\partial}{\partial x_i}\left[f_i(x_k,t)\right]. \qquad (1)$$

Here the surface dipole distribution is expressed as a volume distribution within the context of Lighthill's acoustic analogy, $f_i(x_k,t)$, which is the total equivalent force field per unit mass of fluid acting over a finite region V within the duct. The speed of sound c_o is taken to be large compared with both mean and fluctuating velocity components in the duct. (A list of symbols is given in Appendix 1.)

The solution to the inhomogeneous wave equation in a hard-walled duct of infinite length has been found by Doak (6), for sound radiation by an arbitrary source distribution located within a finite region of the duct. The solution is evaluated in the frequency domain, and leads to an expression for the Fourier spectrum of the pressure, defined as

$$p(x_k,\omega) = \lim_{T\to\infty} \frac{1}{2\pi} \int_{-T}^{T} p(x_k,t)\, e^{-i\omega t} dt. \qquad (2)$$

This has been given in terms of the Fourier spectrum of the arbitrary source distribution. In the case considered here, the solution can be expressed in terms of the Fourier spectrum of the fluctuating force distribution $f_i(x_k,\omega)$ where

$$f_i(x_k,\omega) = \lim_{T\to\infty} \frac{1}{2\pi} \int_{-T}^{T} f_i(x_k,t)\, e^{-i\omega t} dt. \qquad (3)$$

It is a simple matter to deduce the solution for $p(x_k,\omega)$ by direct substitution into equation (42) of Reference (6). The solution quoted here is valid for observation points x_k outside the source region V on the $+x_3$ side. A sketch of the co-ordinate system used is shown in Figure 1. The solution is given in terms of tne normalised characteristic functions $\psi_{mn}(x_1,x_2)$ of the duct cross-section:

$$p(x_k,\omega) = \sum_{m,n} \frac{1}{2A} \rho_o c_{mn} \psi_{mn}(x_1,x_2)\, e^{-ik_{mn}x_3}\, Q_{mn}(\omega) \qquad (4)$$

where $Q_{mn}(\omega)$ is an integral over the source volume given by

$$Q_{mn}(\omega) = -\frac{1}{i\omega} \iiint_V \frac{\partial f_i(x_k',\omega)}{\partial x_1'} \psi_{mn}^*(x_1',x_2')\, e^{ik_{mn}x_3'}\, dV. \qquad (5)$$

A complete description of the construction of this solution for arbitrary source distributions can be found in Reference (6). An exactly similar solution has been used by Davies and Ffowcs Williams (7) in their treatment of sound generated by turbulence in an infinite duct. The equivalent source distribution in that case was Lighthill's quadrupole source distribution, rather than the above dipole distribution. A detailed description of the behaviour of this solution for various forms of source distribution can also be found in Reference (6). The major features of equation (4), however, are worth brief discussion here.

Firstly, it can be seen that the solution for the spectral components of the pressure is a series of modal contributions. The terms $\psi_{mn}(x_1,x_2)e^{-ik_{mn}x_3}$ can be thought of as denoting wave propagation in the x_3 direction with a wavenumber k_{mn}. The propagating waves have an amplitude distribution $\psi_{mn}(x_1,x_2)$ over the duct cross-section. The values of the characteristic functions $\psi_{mn}(x_1,x_2)$, for a rectangular duct of side a in the x_1 direction and side b in the x_2 direction, are given by

$$\psi_{mn}(x_1,x_2) = \sqrt{(2-\delta_{om})(2-\delta_{on})}\cos\frac{m\pi x_1}{a}\cos\frac{n\pi x_2}{b}, \qquad (6)$$

where the normalising factor $\sqrt{(2-\delta_{om})(2-\delta_{on})}$ ensures that $|\psi_{mn}(x_1,x_2)|^2$ has an average value of unity over the duct cross-section, $\delta_{\mu\nu}$ being the Kronecker delta function which is zero for $\mu \neq \nu$ and unity for $\mu = \nu$. Thus the modal contributions $\psi_{mn}(x_1,x_2)e^{-ik_{mn}x_3}$ can be thought of as propagating interference patterns. The wavenumbers k_{mn} of the propagation are determined by the following relation which follows from the wave equation:

$$k_{mn}^2 = k^2 - \left[\left(\frac{m\pi}{a}\right)^2 + \left(\frac{n\pi}{b}\right)^2\right]. \qquad (7)$$

By defining the "cut-on" frequency of the m,n-th mode as

$$\omega_{mn} = c_o\sqrt{\left(\frac{m\pi}{a}\right)^2 + \left(\frac{n\pi}{b}\right)^2}, \qquad (8)$$

the value of k_{mn} for the m,n-th mode can be expressed as

$$k_{mn} = \pm\sqrt{\omega^2 - \omega_{mn}^2}/c_o. \qquad (9)$$

For frequencies ω below the cut-on frequency ω_{mn}, the wavenumber k_{mn} is imaginary and the amplitude of the mode will decay exponentially as a function of x_3. The pressure $p(x_k,\omega)$ thus consists of a sum of contributions from propagating modes (where $\omega > \omega_{mn}$) and non-propagating modes (where $\omega < \omega_{mn}$). The latter make a negligible contribution to the net field beyond a certain distance from the source region.

It can also be seen from equation (4) that other factors also influence the contribution of a given mode to the total pressure field. The term $\rho_o c_{mn}$ represents the characteristic impedance of the m,n-th mode. The mode speed $c_{mn} = \omega/k_{mn}$ is given by

$$c_{mn} = c_o / \sqrt{1 - \omega_{mn}^2/\omega^2} \quad . \tag{10}$$

It can be seen that below cut-on ($\omega < \omega_{mn}$) this is imaginary. Hence, since the characteristic impedance $\rho_o c_{mn}$ then is also imaginary, no energy is carried away by the exponentially decaying modes. At cut-on ($\omega = \omega_{mn}$), c_{mn} becomes infinite. Hence in an ideal "loss free" environment, a mode can potentially be excited to infinite amplitude. Well above cut-on ($\omega >> \omega_{mn}$) the characteristic impedance of the mode tends to $\rho_o c_o$, the characteristic impedance of the medium.

Lastly, the amplitude of a given mode will be substantially affected by the magnitude of the source volume integral $Q_{mn}(\omega)$. Essentially, this term quantifies the degree to which the space-time pattern of the source distribution matches the mode structure of the duct. This aspect has also been given detailed attention in reference (6).

2.2 An Expression for the Acoustic Power Radiated by the Flow in the Wake of a Flat Plate Spoiler

The above solution for the acoustic pressure in the duct can thus be influenced by a large number of factors. At first sight, any attempt to produce usable engineering results from this solution appears to be formidably complicated. Nevertheless, it is important to work from these first principles in order to retain all the factors influencing the scaling laws governing the radiation of sound from the flow in the wake of a bluff body in the duct.

An initial simplifying step can be taken by recognising that it is the acoustic power radiated by the equivalent source distribution that is of ultimate engineering interest. It is a relatively straightforward matter to deduce the spectral density of the acoustic power radiated in one direction down an infinite duct. This can be derived directly from the above solution for the Fourier spectrum of the acoustic pressure. A full description of the derivation of this expression is given in Appendix 2. The spectral density $W(\omega)$ of the radiated power is directly related to the spectral density $S_{mn}(\omega)$ of the source volume integral $Q_{mn}(\omega)$ such that

$$W(\omega) = \sum_{m,n}^{N} \frac{1}{4A} \rho_o c_{mn} S_{mn}(\omega) \, , \tag{11}$$

where N represents the upper limit of the summation which includes propagating modes only. The spectral density $S_{mn}(\omega)$ is given by

$$S_{mn}(\omega) = \lim_{T\to\infty} \frac{\pi}{T} |Q_{mn}(\omega)|^2. \qquad (12)$$

Thus, provided the source volume integral $Q_{mn}(\omega)$ given by equation (5) can be evaluated for the particular source distribution in question, the resulting acoustic power radiated can be found by summing the contributions made by the propagating modes. However, it is obvious that the precise value of $Q_{mn}(\omega)$, or more specifically that of $S_{mn}(\omega)$, is not readily deduced in simple terms for any arbitrary dipole distribution.

The approach taken here is thus to produce a good approximation to the likely form taken by $S_{mn}(\omega)$ for the particular case of the equivalent dipole distribution representing the source of sound generated by the flow in the wake of a flat plate flow spoiler. For a thin flat plate perpendicular to an oncoming flow, it is legitimate to assume that only drag forces act on the plate. For a thin plate nearly parallel to a flow, the lift force will dominate, but the former case is more representative of a body which produces a large wake of separated flow. Thus forces on the plate are considered to act in the axial (x_3) direction only. Under these circumstances, it is shown in Appendix 3 that the expression for $Q_{mn}(\omega)$ can be considerably simplified. An equation results which relates $Q_{mn}(\omega)$ to the force $f_3(x_1',x_2')$ per unit density acting per unit area over the cross section $x_3' = x_3''$ occupied by the plate:

$$Q_{mn}(\omega) = \frac{1}{c_{mn}} \iint_S f_3(x_1',x_2')\,\psi^*_{mn}(x_1',x_2')\,e^{ik_{mn}x_3''}\,dx_1'dx_2'. \qquad (13)$$

The expression for $Q_{mn}(\omega)$ has now become more physically meaningful. The value of $Q_{mn}(\omega)$ given by expression (13) will depend on the way the axial force distribution in the plane (x_1',x_2') matches the mode shape function $\psi^*_{mn}(x_1',x_2')$. The physical origin of $f_3(x_1',x_2',\omega)$ is, of course, the difference in fluctuating pressure acting on both sides of the thin flat plate. These fluctuations in pressure are caused mainly by the formation and convection of eddies as the oncoming flow separates at the edge of the plate. Further simplification of the expression for $Q_{mn}(\omega)$ can be made by considering the way in which the surface pressure fluctuations are correlated over the plate. This will govern the extent to which $f_3(x_1',x_2')$ matches the "chess-board" pattern of $\psi^*_{mn}(x_1',x_2')$.

It is now necessary to deduce the value of $S_{mn}(\omega)$ from equation (13). In Appendix 4 an analysis is presented which enables $S_{mn}(\omega)$ to be related to the spectral density $S_F(\omega)$ of the <u>total</u> fluctuating drag force acting on the plate. In order to derive this relationship, it

is necessary to make certain fairly realistic assumptions about the correlation of the fluctuating surface pressures acting on the plate. Full details of these assumptions are presented in Appendix 4. The resulting expression for the spectral density $S_{mn}(\omega)$ is

$$S_{mn}(\omega) = \frac{1}{\rho_o^2 |c_{mn}|^2} S_F(\omega) \frac{1}{A_s} \iint_{A_s} |\psi_{mn}(x_k')|^2 dS(x_k'). \qquad (14)$$

Substitution of this expression into equation (11) gives an expression for the spectral density of the acoustic power radiated in one direction down an infinite duct from the assumed form of source distribution. Thus

$$W(\omega) = \frac{1}{4A\rho_o} S_F(\omega) \sum_{m,n}^{N} \frac{1}{|c_{mn}|} \frac{1}{A_s} \iint |\psi_{mn}(x_k')|^2 dS(x_k'). \qquad (15)$$

This is valid for an axial force distribution acting only over the area of duct occupied by a flat plate spoiler perpendicular to a low Mach number flow. The force fluctuations at a given frequency have a correlation length small compared to the acoustic wavelength at that frequency. The expression will be valid for uniform force distributions having a correlation length large compared to spoiler dimensions. For correlation lengths that are small compared to spoiler dimensions, the expression will be valid provided the force distribution has a uniform product of amplitude and correlation area at a given frequency. The validity of the expression decreases as the value of the correlation length approaches either dimension of the spoiler.

2.3 Expressions for the Sound Power Radiated by Spoiler Flows at Frequencies above and below Cut-on

Equation (15) for the spectral density of the radiated sound power can be further simplified for the limits of low-frequency and high-frequency sound propagation in the duct. These limits are defined by the relationship of the acoustic wavelength at a given frequency to the dimensions of the duct under consideration. Thus, for a rectangular duct, when $\lambda >> a,b$ only plane waves can propagate in the duct, whereas when $\lambda << a,b$ many modes can propagate in the duct.

In the first instance, equation (15) reduces to a very simple expression for plane wave propagation, defined by $m,n = 0$. The expression produced is valid for all frequencies below the cut-on frequency of the first transverse duct mode:

$$W(\omega) = \frac{1}{4A\rho_o c_o} S_F(\omega), \qquad \text{(plane waves)} \tag{16}$$

This is the expression derived by Morfey (8) for the sound power travelling in one direction down an infinite hard walled duct, when plane waves are driven by the application of a fluctuating axial force.

In the case of multi-modal sound propagation in the duct, one has to consider the nature of the term in equation (15) involving the summation over all propagating modes. Firstly, the effect on the integration over the spoiler area of the duct characteristic functions can be examined. For a given m and n the integration can be performed for a rectangular spoiler having sides d and h parallel respectively to the sides of a rectangular duct of sides a and b. If the co-ordinates of the spoiler centre are $(\bar{a},\bar{b})$ it can be shown that

$$\frac{1}{A_s} \iint_{A_s} |\psi_{mn}(x_k')|^2 dS(x_k')$$

$$= \left[1 + \frac{a}{m\pi d} \sin\frac{m\pi d}{a} \cos\frac{2m\pi\bar{a}}{a}\right]\left[1 + \frac{b}{n\pi h} \sin\frac{n\pi h}{b} \cos\frac{2n\pi\bar{b}}{b}\right]. \tag{17}$$

It is easy to see that the most probable value of this product is unity for all modes. The probability of the value being unity is enhanced as the values of m and n are increased, and also as the spoiler dimensions d and h become larger compared to the duct sides a and b. The integral becomes exactly 1, by definition, when the spoiler fills the duct section. One may thus make the assumption that the integral evaluated in expression (17) always has a value of unity. This assumption has decreasing validity for lower order modes and relatively small spoilers.

One is then left in equation (15) with the summation of $(1/|c_{mn}|)$ for all the propagating modes. First it can be noticed that the ratio (c_o/c_{mn}) for a given mode can be expressed in terms of the integers m and n. By combining equations (8) and (10) one obtains

$$(c_o/c_{mn}) = \sqrt{\left[1 - \left(\frac{m\pi}{ka}\right)^2 - \left(\frac{n\pi}{kb}\right)^2\right]}. \tag{18}$$

If m and n are now thought of as continuous variables, the ratio (c_o/c_{mn}) can be thought of as another continuous variable, which is a function of m and n: i.e.,

$$(c_o/c_{mn}) \simeq f(m,n). \tag{19}$$

The summation of the terms $(1/c_{mn})$ for all propagating modes can now be considered as a double integration of $f(m,n)$ over the range of the variables m and n for which modes are propagating. Thus we estimate

$$\sum_{m,n}^{N} \frac{1}{c_{mn}} = \frac{1}{c_o} \sum_{m,n}^{N} \frac{c_o}{c_{mn}} \simeq \frac{1}{c_o} \int_0^{kb/\pi} \int_0^{ka/\pi} f(m,n)\, dm dn, \qquad (20)$$

where (ka/π) and (kb/π) are the maximum values of the continuous variables m and n for which modes propagate at the frequency in question.

This approach can be better understood with reference to Figure 2. Each mode is represented by a discrete point in the (m,n) plane. The value of (c_o/c_{mn}) for a given mode is represented by a point at a height (c_o/c_{mn}) vertically above the relevant point in the (m,n) plane. As the number of modes in the (m,n) plane becomes large, one can think of a continuous distribution of modes rather than a series of discrete points. The distribution of (c_o/c_{mn}) is then represented by the height of a surface f(m,n) above the (m,n) plane. The surface f(m,n) is, in fact, the surface of an ellipsoid. This can be seen from equation (18) which is the equation of the surface of an ellipsoid having semi-axes of length 1, (ka/π) and (kb/π). Note $f(m,n) = 1$ defines the phase speed of the plane wave mode, represented by the corner of the (m,n) plane at $m,n = 0$.

Also, $f(m,n) > 0$ defines the phase speeds of all propagating modes contained in the elliptical "cut-on boundary" in the (m,n) plane.

The double integration expressed in equation (20) evaluates the volume enclosed by the surface f(m,n) for all propagating modes. This is simply given by the volume of the ellipsoidal segment illustrated in Figure 2. Notice that taking this volume, only gives half the proper weight to the contribution from the "edge modes" lying along the m and n axes. A better estimate of the summation is thus achieved by adding the volume of two "slices" at the edges of the ellipsoidal segment. Each "slice" has a width of (1/2) and an elliptical cross-section. Remembering the volume of an ellipsoid having semi-axes S_1, S_2 and S_3 is given by $(4/3)\pi S_1 S_2 S_3$ and the area of an ellipse of semi-axes S_1 and S_2 is given by $\pi S_1 S_2$, the total volume representing the summation of (c_o/c_{mn}) can be written as

$$\sum_{m,n}^{N} (c_o/c_{mn}) \simeq \frac{1}{8} \cdot \frac{4}{3} \cdot \pi \left(\frac{ka}{\pi} \cdot \frac{kb}{\pi}\right) + \frac{1}{4} \cdot \frac{1}{2} \cdot \pi \left(\frac{ka}{\pi}\right) + \frac{1}{4} \cdot \frac{1}{2} \cdot \pi \left(\frac{kb}{\pi}\right)$$

$$\simeq \frac{k^2 ab}{6\pi} + \frac{k}{8}(a + b). \qquad (21)$$

Re-writing k as ω/c_o one has for the summation of $(1/c_{mn})$ for all propagating modes

$$\sum_{m,n}^{N} \frac{1}{c_{mn}} = \frac{1}{c_o} \sum_{m,n}^{N} \left(\frac{c_o}{c_{mn}}\right) \simeq \frac{\omega^2 A}{6c_o^3\pi}\left[1 + \frac{3\pi c_o}{4\omega}\frac{(a+b)}{A}\right]. \qquad (22)$$

Substitution of this approximation for the summation in equation (15) then gives a simple expression for the spectral density of the sound power radiated in either direction along the duct:

$$W(\omega) \simeq \frac{\omega^2}{24\pi\rho_o c_o^3} S_F(\omega)\left[1 + \frac{3\pi c_o}{4\omega}\frac{(a+b)}{A}\right], \quad \text{(multimode)} \qquad (23)$$

Note that the spectral density of the sound power radiated by a point dipole in a free field is given by

$$W(\omega) = \frac{\omega^2}{12\pi\rho_o c_o^3} S_F(\omega). \qquad (24)$$

Thus, for frequencies when higher order modes can propagate in the duct, the source exhibits a free field type of behaviour. In fact, if the total power radiated down the duct (in both directions) is considered, then for $(\omega/c_o) >> (a + b)/A$ equation (23) tends exactly to equation (24). This confirms the intuitively obvious result that in a duct having dimensions very much larger than the acoustic wavelength, a source will radiate the same power as it does in a free field.

The approximation for the summation term appearing in equation (15) thus produces a sensible result having useful simplicity. The range of validity of this approximation needs to be tested experimentally. For example, one must establish the validity of assuming a value of unity for all modes for the surface integral expressed in equation (17). It is worth noting that this integral could also be expressed as a continuous function of m and n, g(m,n) say. The summation over all modes of the product $(1/c_{mn})$ and the surface integrals could then be expressed as a double integration of f(m,n) g(m,n):

$$\frac{1}{c_o}\sum_{m,n}^{N}\left(\frac{c_o}{c_{mn}}\right)\frac{1}{A_s}\iint_{A_s}|\psi_{mn}(x_k')|^2 dS(x_k') \simeq \frac{1}{c_o}\int_0^{kb/\pi}\int_0^{ka/\pi} f(m,n)\,g(m,n)\,dmdn. \qquad (25)$$

Although possible in principle, this integration has not been evaluated, since the final result would probably do little to enhance the accuracy of equation (23) whilst complicating it considerably.

Thus two very simple results have been derived for the sound power radiated by an assumed form of source distribution, under the conditions of plane wave and multi-modal sound propagation in an infinite duct. In the following sections a series of experiments is described which allow the validity of these approximate results to be tested.

3. EXPERIMENTAL PROCEDURE

3.1 Design of the Experimental Rig

An outline drawing of the test rig used for the determination of the sound power generated by flow past flat plate spoilers is shown in Figure 3. Air flow was provided by two 1.22 m diameter axial flow fans, one having pneumatically controlled blade pitch angle. The fans were heavily attenuated on the downstream side by a large splitter attenuator and the air fed into an acoustically lined plenum. This arrangement minimised the amount of upstream fan noise passing into the test duct. Further steps were taken to reduce the upstream noise by lining each side of the first 5.5 m of the 0.3 m square test duct with 150 mm thickness of absorbing material. An inlet cone was provided at the entrance to the test duct, together with a 150 mm section of "egg-crate" flow straightener having a 50 mm mesh size. A quiet, fully developed turbulent pipe flow was thus provided at the test section 9.2 m from the duct entrance. The total length of the duct was 14.5 m. The test duct was passed into a reverberation chamber, which was provided with a lined outlet duct allowing air to escape without allowing noise from outside to penetrate. The system was designed such that the maximum airflow velocity in the test section was always substantially larger than the velocity in any other part of the system. The application of this principle proved successful in ensuring that the level of sound to be measured was always well above the noise level from other sources in the system.

3.2 Airflow Measurements

A thorough investigation of the velocity profile in the empty test duct was carried out by using the procedure established in Reference (9). A pitot tube was used to sample the velocity pressure at specified points in the duct cross-section at the position shown in Figure 4. This enabled the calculation of the mean duct velocity at five duct velocities over the working range to be accomplished. Plots of the duct velocity profile at several test velocities are shown in Figure 4. The mean velocity calculated for each of the five velocities was found to have a

linear relationship with the velocity measured at a fixed position near the centre of the duct (shown in Figure 4). This relationship held in each case to within 2%. Subsequent measurements of the mean duct velocity were thus made by using only this single "calibrated" position of the pitot tube.

The static pressure drop across the various spoilers tested was measured by using two piezometric rings located at the positions shown in Figure 3. Each ring consisted of four static pressure tappings, one in each duct face. The downstream ring was far enough away from the test section to ensure that full static pressure recovery could take place in the wake of the flow obstructions under test.

The precision manometers used during the tests could be read to an accuracy of 2%. The variable fan blade pitch control system was checked for drift by monitoring the duct velocity over a four minute period. The velocity changed only by 0.5% during this time. The fan controls could thus be relied upon to provide a steady mean flow for the duration of each test. The total error involved in the measurement of both mean duct velocity and static pressure drop was thus within 4%

3.3 Acoustic Measurements

The reverberation chamber used for the determination of the sound power radiated from the duct exit had a volume of 200 m^3. The reverberation time was measured by the usual procedure of recording the decay rate of sound in the room. This was performed for 1/3 octave centre frequencies between 63 Hz and 10 kHz. An approximately 10% bandwidth warble tone was generated by using a Bruel & Kjaer Sine Random Generator, Type 1024. This was amplified and fed to a loudspeaker in the room. The level of decay when the signal was switched off was monitored by a 12 mm B & K condenser microphone. Eight different positions of the microphone were used for the frequencies between 63 Hz and 800 Hz, and three positions were used for frequencies between 1 kHz and 10 kHz. The average reverberation time measured at each frequency is shown in Figure 5. The sound power level radiated from the duct exit was then calculated from

$$SWL = SPL + 10 \log_{10} V_R - 10 \log_{10} T_R - 14, \qquad (26)$$

where V_R is the room volume (m^3), T_R the reverberation time(s), and SPL the space averaged sound pressure level in the room.

The average sound pressure level was determined by feeding the signals from six 12 mm B & K microphones suspended in the room into a General Radio amplifier/power supply/microphone switching device, Type GR 1566. This enabled automatic selection of each microphone signal to be made in turn before processing by a Multi-Channel RMS Detector, Type GR 1926, and a 1/3 octave Multifilter, Type GR 1925. Each microphone signal was processed by using a four second integration time. A digital readout of the average of the six microphone signals in each 1/3 octave band was obtained. These readings were each found to be repeatable to within 0.5 dB for a given flow obstruction at a given test velocity. The time averaging used on each microphone signal was thus adequate. Daily calibration of the microphone was performed by using a pistonphone.

The largest error in the measurement of the sound power radiated from the duct was in the spatial averaging of the sound field produced in the reverberation chamber. An estimate of this error was made by sampling the sound pressure level at 50 randomly selected microphone positions for a given obstruction in the duct at a given flow velocity. Each microphone position was at least 1 m from the room walls and the duct exit. The standard deviation S_D of the variation in sound pressure level was then calculated for each 1/3 octave band. Assuming that the measured value of S_D is the true standard deviation of a normal distribution of sound pressure levels, one finds that the 95% confidence limits for the mean of the distribution estimated from n_s samples are then given by $\pm 1.96\ S_D/\sqrt{n_s}$. The 95% confidence limits for a mean level estimated from six microphone positions are shown in Figure 6 for each 1/3 octave band. The low modal density in the room at low frequencies clearly results in large errors (±3 dB). A diffuse field is established in the middle of the frequency range so that reliable results (±0.5 dB) can be obtained. At high frequencies the accuracy decreases again as the absorption in the room increases and the direct field of the duct exit encroaches on the reverberant field.

The "background" noise due to the flow in the duct with no spoilers inserted was monitored at five test velocities. The ambient background noise level was also measured after each test. Levels were recorded only if they were at least 10 dB above both the ambient level and the background flow noise level at the given test velocity in the duct. Background interference was found to be a problem only at low frequencies and low test velocities.

3.4 The Spoilers used in the Experiment

The flat plate flow spoilers used in the experiment were selected in order to test the validity of the theory developed in section 2. The spoilers represent the type of flow duct obstruction upon which the theory was based. The spoiler plates selected were made from 3 mm thick mild steel plate. These plates were bolted between the flanges of two adjoining sections of the test duct and the gap sealed with a compressed foam rubber seal. The spoilers provided a perfectly rigid obstruction to the flow in the duct and could not vibrate in the airstream. Seven different spoiler geometries were tested, each geometry being tested with at least four duct flow velocities. Four of the spoilers were vertical strips of plate placed centrally in the airstream. Their height was that of the test duct and their widths were 0.0125 m, 0.1 m, 0.15 m and 0.2 m, respectively. The other three geometries consisted of plates protruding symmetrically from both sides of the duct, leaving a central vertical strip of the duct open. The plates again had the same height as the duct and the width of the two side plates were equal. The total width of plate in the duct in the three configurations was 0.1 m, 0.15 m and 0.2 m.

4. ANALYSIS AND DISCUSSION OF RESULTS

4.1 The Basis for Normalisation of the Experimental Results

The results measured for the sound power radiated from the end of the duct can be normalised with the help of expressions (16) and (23) derived in section 2. However, the theory has been developed for an infinite duct. The duct used in the experiment was of finite length with a considerable length of absorbent lining upstream of the test section. The test duct can be assumed to be semi-infinite. Thus, in order to measure the sound power that would be radiated by the spoiler flows down one direction of an infinite duct, the experimental results had to be corrected for the sound power reflected at the duct outlet.

It is also assumed here that the actual "source strength" of the spoiler flow is not affected by its acoustic environment. This is a safe assumption provided there is no feedback from duct resonances, which could affect the flow and, hence, the forces on the spoiler. No evidence of this type of interaction was found and so the results were corrected for duct termination reflection according to the amount given in Reference (9).

Note also that the spoilers were always located at distance of 15 duct widths upstream of the duct outlet. The noise source could always be treated as an "in-duct" source, without considering end effects due to the proximity of the outlet, as shown by Heller and Widnall (3). Since all tests were conducted at duct flow Mach numbers below 0.1, the effect of flow on sound propagation and reflection in the duct could be assumed negligible, as shown in Reference (10).

4.2 The Relationship between Fluctuating and Steady State Drag Forces

Before the theoretical predictions embodied in equations (16) and (23) can be used for the normalisation of the experimental results, one has to assume that the r.m.s. fluctuating drag force acting on the spoiler is directly proportional to the steady state drag force $\overline{F}_3$. This was, in fact, used by Gordon (1) with some success, and later experimentally confirmed by Heller and Widnall (3). Consider the proportional frequency band defined by the limits $(f_c/\alpha, f_c\alpha)$ where f_c is the centre frequency. Within this band, the ratio of the mean square force $\overline{F_3^2}$ to the square of the steady state force $(\overline{F}_3)^2$ is expected to depend only on the Strouhal number. This can be expressed as

$$(F_3)_{rms} = K(St)\overline{F_3}\,, \qquad (\text{band } f_c/\alpha \text{ to } f_c\alpha) \tag{27}$$

where the numerical factor K(St) depends on the choice of α. The Strouhal number is given by $St = f_c d/U_c$ where U_c is the flow velocity in the constriction provided by the spoiler and d a characteristic dimension. In general, the value of d chosen will depend on the particular spoiler geometry. For the spoilers used in the experiment, the height remained constant and was equal to the duct dimension, whilst the width was always smaller than the height. The obvious choice for the dimension d was thus the width of the spoiler. The velocity in the restriction U_c is defined by the volume flow rate q and the area of the duct constriction A_c, such that $U_c = q/A_c$. This velocity will at least be representative of the convection speed of eddies shed in the spoiler wake, although the shedding process in reality will depend on the details of the velocity profile in the constriction.

The mean drag force $\overline{F_3}$ acting on a spoiler will be balanced by an equal and opposite mean force acting on the fluid. The force on the fluid (which acts in the upstream direction) is given by the product of

the static pressure drop across the spoiler and the area of the test duct. The static pressure difference Δp_s across the spoiler must be measured between a location upstream of the spoiler, and a location sufficiently far downstream to allow full static pressure recovery in the fluid after the flow constriction. The steady state force on the spoiler can thus be written as

$$\overline{F_3} = A\Delta p_s. \tag{28}$$

This is a low Mach number approximation, valid since the duct flow Mach number is always less than 0.1. The drag force on a bluff body can also be written in terms of a drag coefficient C_D. For a spoiler of area A_s perpendicular to an oncoming flow of free stream velocity U_∞, it is usual to write the mean drag force as

$$\overline{F_3} = C_D(\tfrac{1}{2}\rho U_\infty^2)A_s. \tag{29}$$

If U_∞ is considered to be the duct velocity q/A this force can be written in terms of constriction velocity U_c and open area ratio $\sigma = A_c/A$, such that

$$\overline{F_3} = C_D(\tfrac{1}{2}\rho U_c^2)\sigma^2(1-\sigma)A. \tag{30}$$

4.3 Scaling Laws for the Normalisation of the Experimental Results

With the use of the relation (27) between the steady state and fluctuating drag forces, expressions (27) and (30) can be substituted into equations (16) and (23) for the sound power radiated for plane wave and multi-modal sound propagation in the duct. Firstly note that the sound power $W_{\Delta f}$ radiated in a given bandwidth can be written as follows for frequencies above and below the cut-on frequency f_o of the transverse duct mode:

$$(f_c < f_o)\ W_{\Delta f} = \int_{\omega_1}^{\omega_2} \frac{1}{4A\rho_o c_o} S_F(\omega)\, d\omega, \tag{31}$$

$$(f_c > f_o)\ W_{\Delta f} \simeq \int_{\omega_1}^{\omega_2} \frac{\omega^2}{24\pi\rho_o c_o^3} S_F(\omega) \left[1 + \frac{3\pi c_o}{4\omega}\frac{(a+b)}{A}\right] d\omega, \tag{32}$$

where ω_1 and ω_2 represent the frequency limits of the band in question.

Since the mean square value of the fluctuating force in a given band is given by

$$\overline{(F_3^2)}_{\Delta f} = \int_{\omega_1}^{\omega_2} S_F(\omega)\, d\omega, \tag{33}$$

then equations (31) and (32) can be written

$$(f_c < f_o)\ W_{\Delta f} = \frac{1}{4A\rho_o c_o}\ \overline{(F_3^2)}_{\Delta f}, \tag{34}$$

$$(f_c > f_o)\ W_{\Delta f} \simeq \frac{\omega_c^2}{24\pi\rho_o c_o^3}\ \overline{(F_3^2)}_{\Delta f}\left[1 + \frac{3\pi c_o}{4\omega_c}\ \frac{(a+b)}{A}\right]. \tag{35}$$

This of course assumes that the measurement band Δf can be considered sufficiently narrow that the frequency ω in equation (32) can be replaced by the centre frequency ω_c of the band.

With the use of equations (27) and (30), the sound power radiated in a given measurement bandwidth can be written in terms of drag coefficient. After some algebraic manipulation it can be shown that

$$(f_c < f_o)\ W_{\Delta f} = (\rho_o/16c_o)\, A\, K^2(St)\left[\sigma^2(1-\sigma)\right]^2 C_D^2\, U_c^4, \tag{36}$$

$$(f_c > f_o)\ W_{\Delta f} = (\rho_o \pi/24c_o^3)\left[1 + \frac{3\pi c_o}{4\omega_c}\left(\frac{a+b}{A}\right)\right]$$

$$\times\ \left(\frac{A}{d}\right)^2 (St)^2 K^2(St)\left[\sigma^2(1-\sigma)\right]^2 C_D^2\, U_c^6. \tag{37}$$

These scaling laws can thus be expressed in terms of easily measurable engineering parameters, together with the single Strouhal number dependent constant $K(St)$. The inherent differences between the two laws are self-evident. Equation (37) for multi-modal sound propagation exhibits a free field dipole dependence of the type $W \propto (U_c^6/c_o^3)$, whereas equation (36) for plane wave propagation exhibits a dependence of the type $W \propto (U_c^4/c_o)$, which is usually associated with a free field monopole source. The effect of enclosure in the duct clearly has a profound influence on the radiation properties of the source, illustrating the need for considerable care in the analysis of aerodynamic noise sources in engineering situations.

Since the sound power measurements were made in proportional frequency bands, the above scaling laws could be used directly for the normalisation of the experimental results. The cut-on frequency f_o of the first

transverse mode in the test duct had a value of 564 Hz. All experimental results measured in 1/3 octave bands having a centre frequency f_c below this value were normalised on the basis of equation (36). All results in bands having f_c above this value were normalised on the basis of equation (37). With the correction made for the reflection of sound at the duct termination, the measured infinite duct values of radiated sound power level SWL_D in 1/3 octaves were thus normalised by evaluating

$$(f_c < f_o) \quad 20 \log_{10} K(St) = SWL_D - 10 \log_{10} \left[\frac{\rho_o A [\sigma^2 (1-\sigma)]^2 C_D^2 U_c^4}{16 c_o} \right], \tag{38}$$

$$(f_c > f_o) \quad 20 \log_{10} K(St) = SWL_D - 10 \log_{10} \left[\frac{\rho_o \pi A^2 (St)^2 [\sigma^2 (1-\sigma)]^2 C_D^2 U_c^6}{24 c_o^3 d^2} (1 + \frac{860}{f_c}) \right]. \tag{39}$$

The Strouhal number St was determined by $St = f_c d/U_c$. The value of U_c used for both spoilers and splitters was determined from $U_c = (q/A_c)$ where the volume flow rate q was measured by using the calibrated pitot tube. The value of d used was always the spoiler width. In the case of spoilers protruding from the duct side, twice the width of the protrusion (hence, the total spoiler width) was taken. This is justified since the flow in the wake of the protrusion and its "image" in the duct walls is analogous to the flow around a single spoiler having twice the width of the protrusion. All the results normalised were in 1/3 octave bands having centre frequencies between 160 Hz and 6 kHz.

The drag coefficient C_D which quantifies the steady state force acting on the fluid was evaluated depending on the particular geometry dealt with. The evaluation of C_D for the spoilers tested, and the resulting collapse of normalised results, will be described in the next section.

4.4 Results for the Sound Power Radiated by Flat Plate Flow Spoilers

The drag coefficient C_D used in the normalisation of the results for the spoilers was evaluated from the measurements of the static pressure drop across the spoilers. The two expressions (28) and (30) for the steady state drag force acting on the spoiler can be equated to give

$$C_D = \Delta p_s / [\tfrac{1}{2}\rho_o U_c^2 \sigma^2 (1 - \sigma)]. \qquad (40)$$

The value of C_D for each spoiler was found by averaging the values calculated from the measurements of Δp_s and U_c at each test velocity. For most of the spoilers tested, the value of C_D calculated did not vary by more than 2% over the range of test velocities used. For the spoilers having a width of 0.1 m, the pressure drop measured was corrected for the pressure drop due to the duct alone. For the smallest spoiler having a width of 0.0125 m, the pressure drop could not be measured and the value of C_D was assumed to be 2.0. This is the value of drag coefficient for an infinitely long flat plate in a free stream (11).

The results normalised on the basis of equations (38) and (39) and with the measured values of C_D used are shown in Figures 7 to 13. In view of the vastly different forms of the scaling laws for frequencies above and below the cut-on frequency f_o of the first transverse duct mode, the collapse of the experimental data is remarkably good. The results for each individual spoiler configuration all confirm the change at f_o from U_c^4 to U_c^6 velocity dependence. Figure 14 illustrates this change more dramatically. Sound power spectra have been plotted against Strouhal number for a given spoiler at several test velocities. The "infinite duct" sound power level SWL_D has been plotted against velocity for two values of Strouhal number, 1.5 and 3.0. The respective dependence on U_c^4 and U_c^6 at these two Strouhal numbers is clearly shown. For this particular configuration and this range of test velocities, the maximum number of modes that can propagate at a Strouhal number of 3.0 is only 4. The results show that in practice, the change from U_c^4 to U_c^6 velocity dependence occurs fairly rapidly after the cut-on of the first transverse duct mode.

Strictly speaking, a change to U_c^6 velocity dependence does not occur as soon as transverse modes can propagate, since the "edge mode" term $[1 + (3\pi c_o(a + b))/(4\omega_c A)]$ is frequency dependent and thus velocity dependent at a constant Strouhal number. It is worth noting that this term, which becomes $(1 + 860/f_c)$ in equation (39), is important in producing a good collapse of experimental data at frequencies just above f_o. For the first 1/3 octave band above the cut-on frequency, the term produces a factor of about 2.5, which corresponds to roughly 4 dB. Without this factor, the collapse of data at frequencies just above cut-on is not nearly so good. The "edge mode" contribution to the modal summation at lower frequencies cannot be neglected. This is exactly

analogous to the accuracy of low frequency mode counts used in room acoustics (see, e.g., Reference (12)).

Figure 15 shows a comparison of the values of 20 $\log_{10}K(St)$ for all the spoilers tested. The overall collapse of the data is excellent in view of the widely differing drag coefficients associated with the various spoilers. In general, there is a decay of the value of 20 $\log_{10}K(St)$ at about 20 dB per decade as the Strouhal number is increased. There also appears to be a systematic deviation from this trend at the high frequency end of the spectra associated with the individual spoilers. In order to get a better idea of the possible usefulness of this constant, one needs to compare these results with those of previous workers.

4.5 Comparison with Previous Work

Previous experimental investigations of spoiler noise by Gordon (2) and Szewczyk (13) have both been carried out at higher flow Mach numbers ($M > 0.3$). Both investigations were carried out with a jet pipe radiating into an anechoic chamber. Szewczyk reported that the velocity dependence of the power radiated from the duct exit changed from U^6 to U^8 at the cut-on frequency of the first duct mode. Gordon showed that his results could be normalised on a U^6 basis for all frequencies below the cut-on frequency of the first duct mode; above this frequency an additional frequency squared term was used to produce a collapse of results.

Before these results can be compared with the results reported here, the effect of flow on the reflection of sound power at the duct exit must be considered. Several studies (10,14,15) have shown that as the flow velocity at the exit of a jet pipe is increased, the reflection coefficient of the duct exit is substantially reduced. However, Bechert, Michel and Pfizenmaier (15) have shown that even if the sound from an in-duct source is not "reflected" as such, it does not reach the far field but is "absorbed" by the flow. The level of this "absorption" is very similar in magnitude and frequency dependence to the "reflection" normally produced under no-flow conditions. Howe's (16) theoretical study of this phenomenon indicates that the fraction of sound power absorbed is dependent on both frequency and jet exit Mach number.

Further work by Munt (17) has shown that the net result of these effects is to produce an overall reduction in sound power transmission to the far field. This reduction is very close to that produced due to

end reflection only under no-flow conditions. It is thus reasonable to assume that the no-flow end reflection corrections can be used in the presence of a flow to calculate the difference in in-duct sound power levels and those radiated to the far field.

In order to compare the order of magnitude of Gordon's results with those measured here, some of Gordon's results taken at the lower end of his speed range have been collapsed according to the dipole type scaling laws derived in section 2. The results for a 25 mm wide flat strip spoiler located centrally in a 47 mm diameter pipe have been taken for values of the velocity U_c in the constriction of around 60 m/s and 80 m/s. Results at low frequencies have been corrected for end reflection with flow assumed to have no effect. The pipe exit Mach number in this case is less than about 0.1. A bandwidth correction has also been made to enable comparison of Gordon's octave band data with the 1/3 octave data measured here. The results for 20 $\log_{10}K(St)$ thus derived are shown in Figure 16. Despite the considerably different geometry of Gordon's experiment his results at low speeds are in excellent agreement with those reported here. The curve of 20 $\log_{10}K(St)$ derived from Gordon's data again shows a decay of 20 dB per decade with increasing Strouhal number for values of St above about 0.2.

At low values of constriction velocity (< 100 m/s), Gordon's results are thus in good agreement with those presented here. However as the velocity in the constriction is increased above about 100 m/s, Gordon's results do not appear to collapse according to the dipole type scaling laws. Even at low frequencies, the in-duct sound power increases with a higher power of velocity than U^4. Heller and Widnall (3) have attempted to explain the observed U^6 dependence of the power radiated from the duct exit on the modifying effect of end reflection on the U^4 dependence of an in-duct dipole. This does not appear to be an entirely satisfactory explanation, in view of the observations above.

Thus, Gordon's observation of a U^6 dependence for the sound radiated from a semi-infinite duct at low frequencies does not necessarily imply a dipole type U^4 scaling for the source in an infinite duct. Certainly, his observation of a U^8 dependence at high frequencies (where there is not expected to be any substantial difference between the incident and transmitted power at the pipe outlet) implies a quadrupole type source distribution in the duct. A change in velocity scaling from U^6 to U^8 at the pipe cut-on frequency would be consistent

with the analysis by Davies and Ffowcs Williams (7) of the sound power radiated by a quadrupole source distribution in an infinite duct. On the basis of the evidence available at present, results of both Gordon and Szewczyk thus imply that the dominant equivalent source distribution associated with in-duct spoiler flows is of a quadrupole type at higher Mach numbers. At low Mach numbers, however, it thus seems that there may be some justification for regarding K(St) as being at least widely, if not universally, applicable as the constant of proportionality between the steady state and fluctuating drag force acting for a variety of bluff body flows. Further reliable experimental data may well show this to be the case.

Finally, it is worth noting that the growing spread of the different curves of 20 $\log_{10}K(St)$ as the Strouhal number increases may be due to the choice of the spoiler width in the duct to determine the scale of the unsteady wake flow. As the spoiler width d is increased it seems logical that it will be the size of the "gap" rather than the size of blockage that begins to determine the scale of the unsteady flow. An argument of this kind could possibly be used to improve the collapse of the measured data from the individual spoilers.

5. CONCLUSIONS

A theory has been developed for the radiation of sound from a flat plate placed normal to a low Mach number flow in a duct, at Reynolds numbers where the downstream flow is turbulent. The equivalent acoustic source distribution was assumed to be of a dipole type, consisting of a distribution of axial force fluctuations acting perpendicular to a plane of the duct cross section. The force fluctuations were assumed to be statistically uniform over the area of the duct cross section occupied by the spoiler plate, and were assumed to have a correlation length either much smaller or larger than the dimensions of the plate. The formal solution to the inhomogeneous wave equation governing the propagation of sound in an infinite hard walled duct has been used to relate the radiated sound power to the total fluctuating drag force acting on the spoiler. Approximate expressions are obtained for the sound power radiated at frequencies above and below the cut-on frequency of the transverse duct mode. The low frequency expression (plane wave propagation only) has been shown to be in agreement with Morfey's (8) previous result. The expression for sound power radiated in the high frequency limit was found to be in agreement with the expression for the sound power radiated by a point dipole in a free field.

The assumption that the r.m.s. fluctuating drag force in a given frequency band acting on the spoiler is in direct proportion to the steady state drag force has been used to derive scaling laws governing sound power radiation in an infinite duct. These laws predict that sound power radiated has a velocity dependence of U^4 at frequencies below the cut-on frequency of the first transverse duct mode and U^6 at frequencies well above this frequency.

Measurements were made of the sound power radiated by a series of spoilers in a low Mach number ducted flow. The results gave an excellent collapse when normalised on the basis of the derived scaling laws. The experimental results firmly establish the validity of the theory. The measurements are also in good agreement with results of Gordon (2) at low speeds. Gordon's results indicate that at constricted flow Mach numbers above about 0.3, the dipole model will no longer be applicable and the equivalent source distribution dominating the radiation will be of a quadrupole type. The experimental results indicate that there may be a universally applicable constant of proportionality between the steady state and fluctuating force acting on the fluid due to spoiler flow. This constant of proportionality can be used as the basis of a technique for further predictions of spoiler generated noise.

Measurements of the sound power generated by splitter attenuator exit flows have been found to obey the same scaling laws as the spoiler noise measurements. These are reported in full in Reference (18). The steady state force acting on the fluid at an attenuator exit can be derived from the rate of change of momentum of the fluid due to the expansion in the duct cross sectional area. The constant of proportionality between this steady state force and the fluctuating force associated with noise generation is almost identical to the constant of proportionality derived from the measurements of spoiler noise. This constant can also be used for further predictions of attenuator self-noise.

A technique has thus been developed which permits the prediction of noise generated by spoiler flows and which requires the knowledge of only simple engineering parameters. It remains to be seen if this technique can also be applied to a wider range of low-speed flow duct obstructions, discontinuities and changes in cross section. The present investigation certainly indicates that this may be possible.

REFERENCES

(1) C.G. GORDON 1968 Journal of the Acoustical Society of America 43, 1041-1048. Spoiler-generated flow noise. I: The experiment.

(2) C.G. GORDON 1969 Journal of the Acoustical Society of America 45, 214-223. Spoiler-generated flow noise. II: Results.

(3) H.H. HELLER and S.E. WIDNALL 1970 Journal of the Acoustical Society of America 47, 924-936. Sound radiation from rigid flow spoilers correlated with fluctuating forces.

(4) N. CURLE 1955 Proceedings of the Royal Society, Series A 231, 505-514. The influence of solid boundaries upon aerodynamic sound.

(5) M.J. LIGHTHILL 1952 Proceedings of the Royal Society, Series A 211, 564-587. On sound generated aerodynamically. I: General theory.

(6) P.E. DOAK 1973 Journal of Sound and Vibration 31, 1-72. Excitation, transmission and radiation of sound from source distributions in hard walled ducts of finite length. (1) The effects of duct cross-section geometry and source distribution space time pattern.

(7) H.G. DAVIES and J.E. FFOWCS WILLIAMS 1968 Journal of Fluid Mechanics 32, 765-778. Aerodynamics of sound generation in a pipe.

(8) C.L. MORFEY 1964 Journal of Sound and Vibration 1, 60-87. Rotating pressure patterns in ducts; their generation and transmission.

(9) BRITISH STANDARD 848 1966 British Standards Institution. Methods of testing fans for general purposes. Part 2: Fan noise testing.

(10) R.H. SCHLINKER 1977 AIAA Paper No. 77-22. Transmission of acoustic plane-waves at a jet exhaust.

(11) B.S. MASSEY 1970 Mechanics of Fluids (2nd Edition). Van Nostrand.

(12) P.M. MORSE and K.U. INGARD 1968 Theoretical Acoustics, Chapter 9, p. 576, Room Acoustics. McGraw-Hill.

(13) V.M. SZEWCZYK 1974 M.Sc. Thesis, University of Southampton. An investigation into tailpipe noise in jets.

(14) F. MECHEL, W. SHILZE and J. DIETZ 1965 Acustica 15, 199-206. The acoustic impedance of orifices with flow (in German).

(15) D. BECHERT, U. MICHEL and E. PFIZENMAIER 1977 AIAA Paper 77-1278. Experiments on the transmission of sound through jets.

(16) M.S. HOWE 1978 Bolt, Beranek and Newman Inc. Report No. 3762. Attenuation of sound in a low Mach number nozzle flow.

(17) R.M. MUNT 1980 Private communication.

(18) P.A. NELSON 1978 Sound Attenuators Ltd. Report No. TRC102. Rectangular attenuator self noise.

(19) M.K. BULL, J.F. WILBY and D.R. BLACKMAN 1963 University of Southampton, A.A.S.U. Report No. 243. Wall pressure fluctuations in boundary layer flow and response of simple structures to random pressure fields.

APPENDIX 1. LIST OF SYMBOLS

a,b	duct cross-section dimensions
A	area of duct cross-section
A_s	face area of flat plate spoiler
A_c	area of cross section of duct constriction
c_o	ambient speed of sound
c_{mn}	mode axial phase speed
C_D	drag coefficient
d	width of rectangular spoiler
f_o	cut-on frequency of first transverse duct mode
f_i	force per unit mass
f_c	centre frequency of measurement band
F_i	total force
$f(m,n)$, $g(m,n)$	continuous functions of m,n
h	height of rectangular spoiler
i	square root of minus one, except where used as a subscript
i,k	subscripts used as Cartesian indices
I_i	acoustic intensity vector
k	acoustic wave number, except where used as a subscript
k_{mn}	mode axial wave number
ℓ_c	correlation length
m,n	summation indices used as subscripts
M	Mach number
N	summation index limit
n_s	number of samples of sound pressure level
p	acoustic pressure
q	volume flow rate
Q_{mn}	modal source volume integral

S_D	standard deviation
St	Strouhal number
S_{ff}	cross spectral density of force fluctuations
S_F	spectral density of total force fluctuation
S_{mn}	spectral density of source volume integral
SPL	space averaged sound pressure level
SWL	sound power level emerging from duct exit
SWL_D	in-duct sound power level
t	time
T	averaging time
T_R	reverberation time
u_i	acoustic particle velocity vector
U	velocity
U_c	velocity in duct constriction
U_∞	free stream velocity
V	volume containing source region
V_R	reverberation room volume
W	total acoustic power
$W(\omega)$	spectral density of acoustic power
$x_i, x_k, x_k', y_k, y_k'$	Cartesian position vectors
α	factor determining proportional frequency band limits
$\delta_{\mu\nu}$	Kronecker delta
Δf	measurement frequency band
ΔP_s	static pressure drop
λ	acoustic wavelength
Λ_m, Λ_n	mode cross-section wavelengths
μ, ν	subscripts used as summation indices
ω	radian frequency

ω_c	centre radian frequency of measurement band
ω_{mn}	mode cut-on radian frequency
ρ_o	ambient density
σ	duct cross section open area ratio
ψ_{mn}	normalised mode cross-section function

APPENDIX 2. THE DERIVATION OF THE EXPRESSION FOR THE MEAN ACOUSTIC POWER TRANSMITTED DOWN THE DUCT

The mean acoustic intensity of the disturbances propagating down the duct can be written

$$I_i(x_k) = \lim_{T\to\infty} \frac{1}{2T} \int_{-T}^{T} p(x_k,t)\, u_i(x_k,t)\, dt. \qquad (A2.1)$$

If this time averaging operation is assumed to be of infinite duration, by Parseval's Theorem, the integral with respect to time can be written

$$\int_{-\infty}^{\infty} p(x_k,t)\, u_i(x_k,t)\, dt = 2\pi \int_{-\infty}^{\infty} p(x_k,\omega)\, u_i^*(x_k,\omega)\, d\omega, \qquad (A2.2)$$

where $u_i(x_k,\omega)$ is the Fourier spectrum of the acoustic particle velocity $u_i(x_k,t)$ given by

$$u_i(x_k,\omega) = \lim_{T\to\infty} \frac{1}{2\pi} \int_{-T}^{T} u_i(x_k,t)\, e^{-i\omega t} dt. \qquad (A2.3)$$

The expression for the mean acoustic intensity can be written as

$$I_i(x_k) = \int_{-\infty}^{\infty} \lim_{T\to\infty} \frac{\pi}{T}\, p(x_k,\omega)\, u_i^*(x_k,\omega)\, d\omega, \qquad (A2.4)$$

where the quantity under the integral is thus the cross spectral density of the pressure and velocity fluctuations.

The acoustic particle velocity $u_i(x_k,t)$ is related to the acoustic pressure by the linearised equation of conservation of momentum which, neglecting mean flow effects, can be written as

$$\rho_o \frac{\partial u_i(x_k,t)}{\partial t} = - \frac{\partial p(x_k,t)}{\partial x_i}. \qquad (A2.5)$$

It thus follows that $u_i(x_k,\omega)$ is given by

$$u_i(x_k,\omega) = - \frac{1}{i\omega\rho_o} \frac{\partial p(x_k,\omega)}{\partial x_i}. \qquad (A2.6)$$

The total mean acoustic power transmitted down the duct in the positive x_3 direction is given by

$$W = \iint_S I_3(x_1,x_2)\, dS. \qquad (A2.7)$$

Thus the total mean acoustic power can be deduced from the solution of the pressure $p(x_k,\omega)$ given by equation (4) of the main text. The relation (A2.6) can first be used to deduce $u_3^*(x_1,x_2,\omega)$ which can be written as

$$u_3^*(x_1,x_2,\omega) = \sum_{\mu\nu} \frac{1}{2A} \psi_{\mu\nu}^*(x_1,x_2) e^{ik_{mn}^* x_3} Q_{\mu\nu}^*(\omega). \tag{A2.8}$$

The acoustic power W is thus given by

$$W = \iint_S \int_{-\infty}^{\infty} \lim_{T\to\infty} \frac{\pi}{T} \{ \Big[\sum_{m,n} \frac{1}{2A} \rho_o c_{mn} \psi_{mn}(x_1,x_2) e^{-ik_{mn} x_3} Q_{mn}(\omega) \Big]$$

$$x \Big[\sum_{\mu,\nu} \frac{1}{2A} \psi_{\mu\nu}^*(x_1,x_2) e^{ik_{\mu\nu}^* x_3} Q_{\mu\nu}^*(\omega) \Big] \} d\omega dS. \tag{A2.9}$$

Since the characteristic functions are orthonormal, i.e.

$$\frac{1}{A} \iint_S \psi_{mn}(x_1,x_2) \psi_{\mu\nu}^*(x_1,x_2) dS = \begin{cases} 0 & \mu,\nu \neq m,n \\ 1 & \mu,\nu = m,n \end{cases}, \tag{A2.10}$$

then the expression for the acoustic power reduces simply to

$$W = \int_{-\infty}^{\infty} \{ \sum_{m,n} \frac{1}{4A} \rho_o c_{mn} \lim_{T\to\infty} \frac{\pi}{T} |Q_{mn}(\omega)|^2 \} d\omega. \tag{A2.11}$$

Defining the spectral density of the source volume integral as $S_{mn}(\omega)$ where

$$S_{mn}(\omega) = \lim_{T\to\infty} \frac{\pi}{T} |Q_{mn}(\omega)|^2, \tag{A2.12}$$

and defining $W(\omega)$ as the spectral density of the radiated power where

$$W = \int_{-\infty}^{\infty} W(\omega) d\omega, \tag{A2.13}$$

enables equation (A2.11) to be written more simply as

$$W(\omega) = \sum_{m,n}^{N} \frac{1}{4A} \rho_o c_{mn} S_{mn}(\omega). \tag{A2.14}$$

Note that in this expression the summation of the modal contributions has been confined to propagating modes only, where N represents the upper limit of the summation. This has been specified since only modes having a real mode speed c_{mn} can carry energy. Thus any non-propagating modes having imaginary c_{mn} give an imaginary contribution to the spectral density of the radiated power which must be excluded on physical grounds. This point has also been discussed by Doak (6).

APPENDIX 3. EVALUATION OF THE SOURCE VOLUME INTEGRALS FOR FLAT PLATE FLOW SPOILERS

Firstly, the expression for the integrals $Q_{mn}(\omega)$ will be conveniently rearranged. Using the properties of the derivative of the product of two functions, the expression (5) of the main text for $Q_{mn}(\omega)$ can be re-written as

$$Q_{mn}(\omega) = \frac{1}{i\omega} \iiint_V f_i(x_k') \frac{\partial}{\partial x_i'} \left[\psi_{mn}^*(x_1', x_2') e^{ik_{mn}x_3'}\right] - \frac{\partial}{\partial x_i'} \left[f_i(x_k') \psi_{mn}^*(x_1', x_2') e^{ik_{mn}x_3'}\right] dV. \quad \text{(A3.1)}$$

The second term in the volume integral will make zero net contribution to the value of $Q_{mn}(\omega)$. This can be seen from the application of the divergence theorem. The volume integral of the divergence of the product $f_i(x_k')\psi_{mn}^*(x_1', x_2') e^{ik_{mn}x_3'}$ can be re-written as the integral of this product over a surface surrounding the volume containing the force $f_i(x_k')$. Since $f_i(x_k')$ vanishes on this surface, then the volume integral vanishes. The expression for $Q_{mn}(\omega)$ can thus be written simply as

$$Q_{mn}(\omega) = \frac{1}{i\omega} \iiint_V f_i(x_k') \frac{\partial}{\partial x_i'} \left[\psi_{mn}^*(x_1', x_2') e^{ik_{mn}x_3'}\right] dV. \quad \text{(A3.2)}$$

One can now make the assumption that the dominant component of force produced on the body by the flow is the fluctuating drag force. Thus forces on the flat plate are considered to act in the x_3 direction only. If they are assumed to act only in the plane (x_1', x_2') of the plate in the duct cross-section at x_3'', the expression for $Q_{mn}(\omega)$ can then be written as

$$Q_{mn}(\omega) = \frac{1}{i\omega} \iiint_V f_3(x_1', x_2') \delta(x_3' - x_3'') \frac{\partial}{\partial x_3'} \left[\psi_{mn}^*(x_1', x_2') e^{ik_{mn}x_3'}\right] dx_3' dx_2' dx_1'. \quad \text{(A3.3)}$$

Note that $f_3(x_1', x_2')$ now denotes the force per unit density acting per unit of cross-sectional area. Performing the differentiation with respect to x_3' and then integrating with respect to x_3' gives

$$Q_{mn}(\omega) = \frac{1}{c_{mn}} \iint_S f_3(x_1', x_2') \psi_{mn}^*(x_1', x_2') e^{ik_{mn}x_3''} dx_1' dx_2'. \quad \text{(A3.4)}$$

APPENDIX 4. AN EXPRESSION FOR THE SPECTRAL DENSITY OF THE SOURCE VOLUME INTEGRALS

Since it is the spectral density of the acoustic power radiated by the flow that is ultimately of interest, the value of the spectral density $S_{mn}(\omega)$ has to be deduced. For the given assumption of an axial force distribution in a plane, it follows from equation (13) of the main text that

$$S_{mn}(\omega) = \lim_{T\to\infty} \frac{\pi}{T} |Q_{mn}(\omega)|^2$$

$$= \lim_{T\to\infty} \frac{\pi}{T} \frac{1}{|c_{mn}|^2} \iiiint_S f_3(x_k',\omega) f_3^*(y_k',\omega) \psi_{mn}(x_k') \psi_{mn}^*(y_k')$$

$$dS(x_k')\, dS(y_k'), \quad \text{(A4.1)}$$

where y_k' are additional position coordinates, the subscript henceforth taking the values 1 and 2 only. Defining the cross power spectral density of the force fluctuations acting on the plate as

$$S_{ff}(x_k',y_k',\omega) = \lim_{T\to\infty} \frac{\pi}{T} f_3(x_k',\omega) f_3^*(y_k',\omega), \quad \text{(A4.2)}$$

enables equation (A4.1) to be written as

$$S_{mn}(\omega) = \frac{1}{|c_{mn}|^2} \iiiint_S S_{ff}(x_k',y_k',\omega) \psi_{mn}(x_k') \psi_{mn}^*(y_k')\, dS(x_k')\, dS(y_k'). \quad \text{(A4.3)}$$

The cross power spectral density $S_{ff}(x_k',y_k',\omega)$ is determined by the degree to which the forces at x_k' and y_k' are correlated. The value of this is determined by the correlation of the fluctuating surface pressures. For the given flow, the value of $S_{ff}(x_k',y_k',\omega)$ will decay as the separation $(x_k' - y_k')$ is increased. This decay can be characterised by a correlation area, expressed here as the square of a correlation length ℓ_c, such that

$$\iint_S S_{ff}(x_k',y_k',\omega)\, dS = \ell_c^2\, S_f(x_k',\omega), \quad \text{(A4.4)}$$

where $S_f(x_k',\omega)$ is the spectral density of the force fluctuations at a given position (x_1',x_2') in the plane of the duct cross section.

To the author's knowledge, no data is available for the value of ℓ_c to be expected for the surface pressure fluctuations arising from this type

of flow. However, data is available for surface pressure fluctuations due to other similar types of flow. For example, Bull (19) has measured the narrow band space time correlation of the wall pressure field in a wind tunnel, due to a turbulent boundary layer flow. Examination of his data for "lateral" (i.e. in a direction perpendicular to the direction of the flow) correlation lengths indicates that $\ell_c \simeq \lambda M$, where λ is the acoustic wavelength at the frequency of the fluctuations examined and M is the Mach number of the flow. Thus, for small Mach numbers, the correlation length was found to be considerably less than the acoustic wavelength. It is very likely that this will also be the case for the type of flow under consideration.

Now consider the spatial behaviour of $\psi_{mn}(y_k')$. Reference to equation (6) of the text shows that the chessboard pattern of $\psi_{mn}(y_k')$ across the duct cross-section has "wavelengths" given by $\Lambda_m = 2a/m$ and $\Lambda_n = 2b/n$. The condition for a given mode to propagate is given from equation (8) of the text by $\omega > \omega_{mn}$ or

$$\omega > c_o \sqrt{\left(\frac{m\pi}{a}\right)^2 + \left(\frac{n\pi}{b}\right)^2} \quad . \tag{A4.5}$$

This can be written in terms of the acoustic wavelength λ at the frequency ω and the wavelengths Λ_m and Λ_n as

$$\frac{1}{\lambda^2} > \frac{1}{\Lambda_m^2} + \frac{1}{\Lambda_n^2} \quad . \tag{A4.6}$$

Thus for any propagating mode the wavelengths of the spatial pattern of $\psi_{mn}(y_k')$ are always greater than the acoustic wavelength.

Since it has been shown that $\ell_c << \lambda$ at low Mach numbers and that $\lambda < \Lambda_m, \Lambda_n$ for any propagating mode, then under these conditions one has $\ell_c << \Lambda_m, \Lambda_n$. The consequence of this is that the integral in equation (A4.3) can be simplified. At a given x_k', $S_{ff}(x_k', y_k', \omega)$ decays rapidly with $(x_k' - y_k')$, whereas $\psi_{mn}(y_k')$ changes only slowly. A contribution will be made by the inner surface integral in equation (A4.3) only over small values of $|x_k' - y_k'|$, i.e. when $\psi_{mn}(y_k') = \psi_{mn}(x_k')$. If the force is assumed to act only over the area A_s of the duct cross-section occupied by the spoiler, equation (A4.3) can be written as

$$S_{mn}(\omega) = \frac{1}{|c_{mn}|^2} \iint_{A_s} |\psi_{mn}(x_k')|^2 \{ \iint_{A_s} S_{ff}(x_k', y_k', \omega)\, dS(y_k') \}\, dS(x_k') \, . \tag{A4.7}$$

The bracketed integral in the above equation will now be assumed to be independent of the position x_k' on the surface of the spoiler. This will be a valid assumption under certain conditions. Firstly, for correlation lengths ℓ_c much larger than spoiler dimensions, the bracketed integral will be independent of x_k' provided the spectral density $S_f(x_k',\omega)$ of the force fluctuations is uniform over the spoiler area. Secondly, for correlation lengths much smaller than spoiler dimensions, the assumption will be valid provided the product $\ell_c^2 S_f(x_k',\omega)$ is uniform over the spoiler area. For correlation lengths close to spoiler dimensions, however, the result of the evaluation of the inner integral is likely to be dependent on x_k' when x_k' is close to the limits of integration, i.e. at the edges of the spoiler. Equation (A4.7) can thus be re-written in a form which will have decreasing validity as the correlation length ℓ_c approaches either dimension of the spoiler and is increasingly valid for force distributions having a uniform amplitude;

$$S_{mn}(\omega) \simeq \frac{1}{|c_{mn}|^2} \{\iint_{A_s} S_{ff}(x_k',y_k',\omega)\, dS(y_k')\} \iint_{A_s} |\psi_{mn}(x_k')|^2 dS(x_k'). \tag{A4.8}$$

This expression can be written in terms of the spectral density $S_F(\omega)$ of the total fluctuating force acting on the spoiler. The Fourier spectrum $F_3(\omega)$ of the total fluctuating force acting is related to the Fourier spectrum $f_3(x_k',\omega)$ of the force per unit density acting per unit area of the spoiler by

$$F_3(\omega) = \rho_o \iint_{A_s} f_3(x_k',\omega)\, dS(x_k'). \tag{A4.9}$$

It thus follows that

$$\lim_{T\to\infty} \frac{\pi}{T} |F_3(\omega)|^2 = \rho_o^2 \iint_{A_s} \{\iint_{A_s} \lim_{T\to\infty} \frac{\pi}{T} f_3(x_k',\omega) f_3^*(y_k',\omega)\, dS(y_k')\} dS(x_k'), \tag{A4.10}$$

and thus the spectral density of the total fluctuating force can be written as

$$S_F(\omega) = \rho_o^2 \iint_{A_s} \{\iint_{A_s} S_{ff}(x_k',y_k',\omega)\, dS(y_k')\} dS(x_k'). \tag{A4.11}$$

Under exactly the same conditions that allow equation (A4.7) to be written as equation (A4.8), the bracketed integral in equation (A4.11) can be assumed independent of x_k' and the spectral density of the total fluctuating force becomes

$$S_F(\omega) \simeq \rho_o^2 A_s \{ \iint_{A_s} S_{ff}(x_k', y_k', \omega)\, dS(y_k') \}. \qquad (A4.12)$$

This expression can be substituted into equation (A4.8) to yield the final expression for the spectral density of the source volume integral for the assumed form of the source distribution. This gives

$$S_{mn}(\omega) \simeq \frac{1}{\rho_o^2 |c_{mn}|^2} S_F(\omega) \frac{1}{A_s} \iint_{A_s} |\psi_{mn}(x_k')|^2 dS(x_k'). \qquad (A4.13)$$

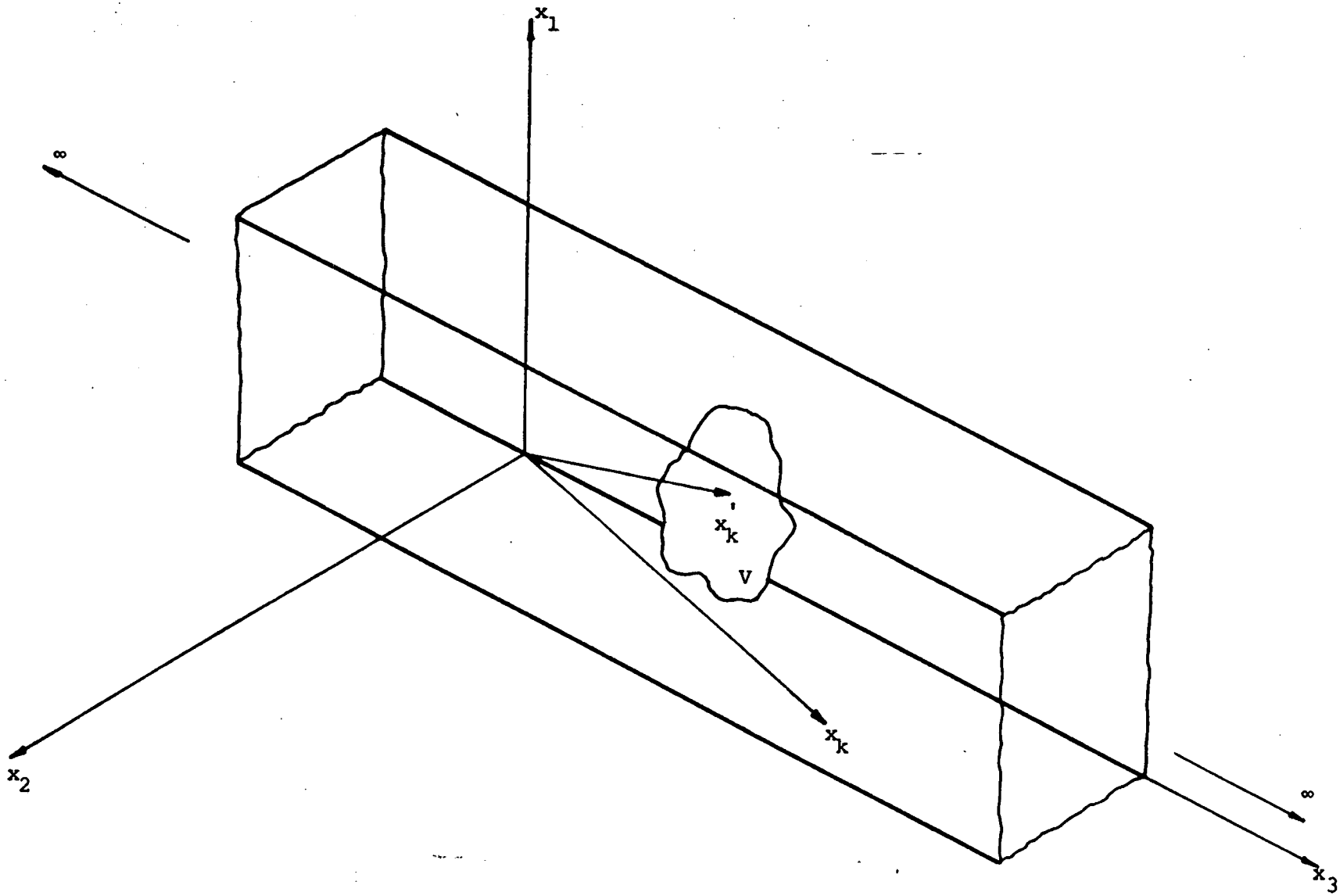

FIGURE 1 The Co-ordinate System for the Infinite Duct Model

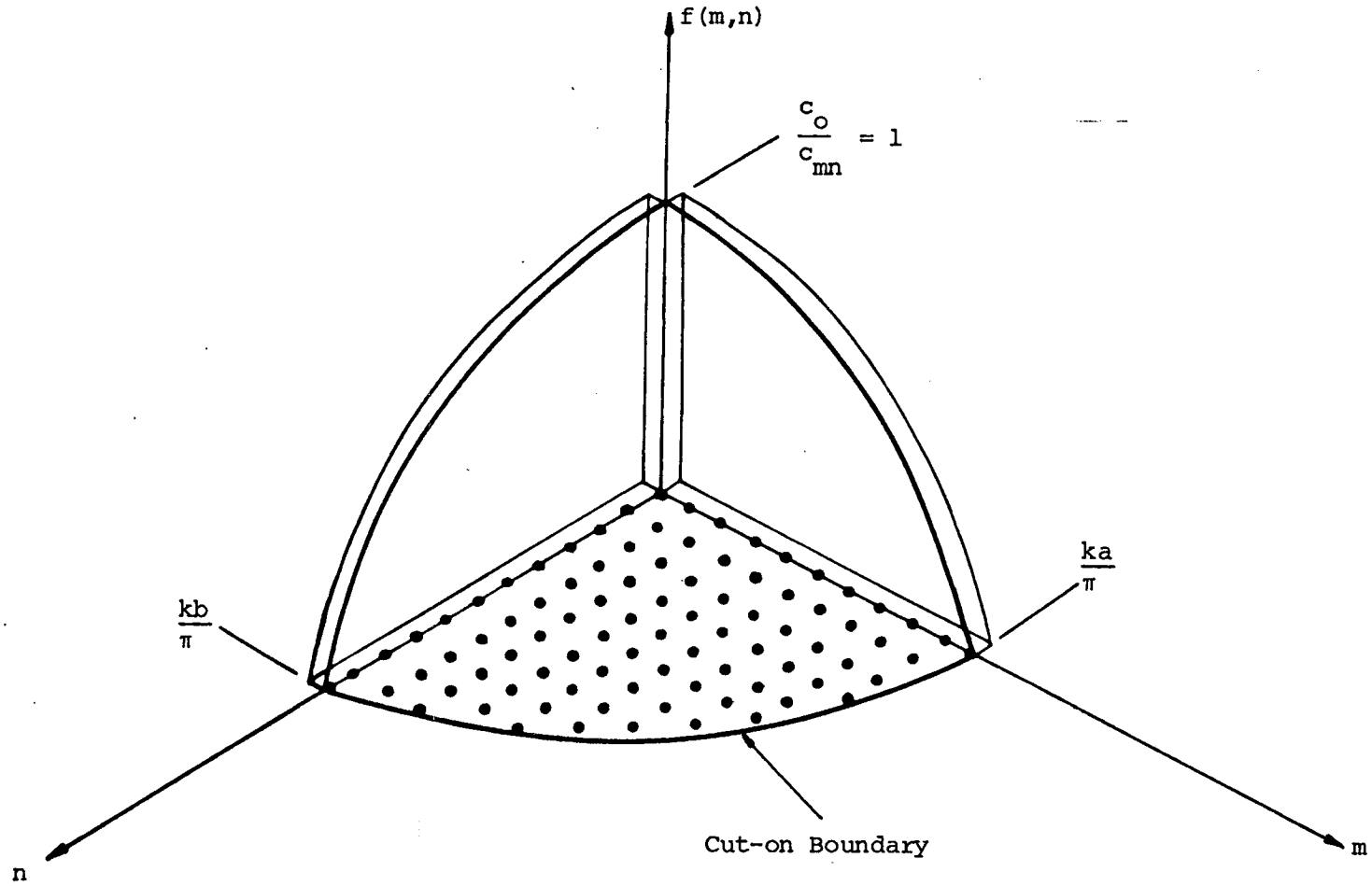

FIGURE 2 A Representation of the Mode Inverse Phase Speed as a Continuous Function

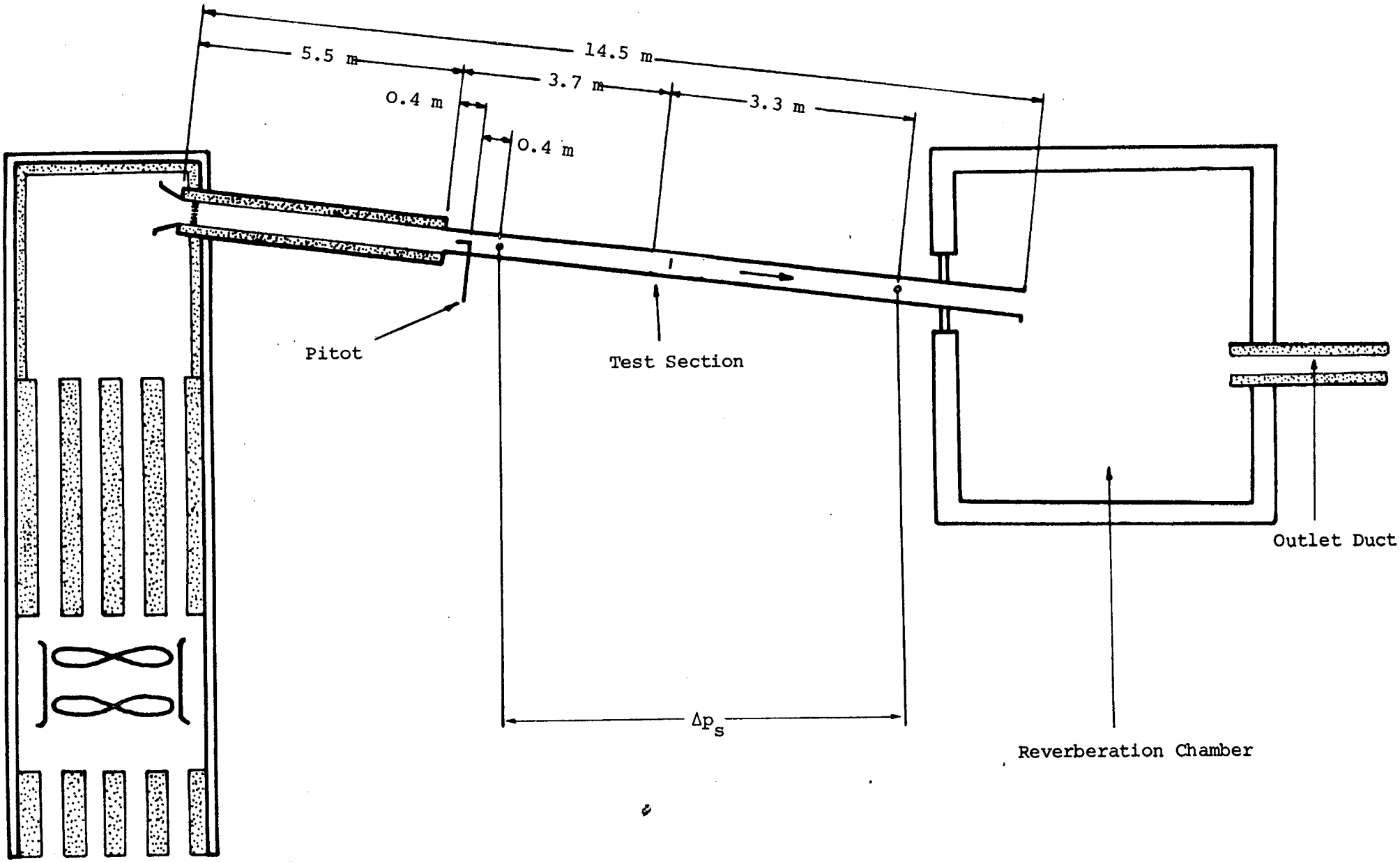

FIGURE 3 A Schematic Diagram of the Test Rig

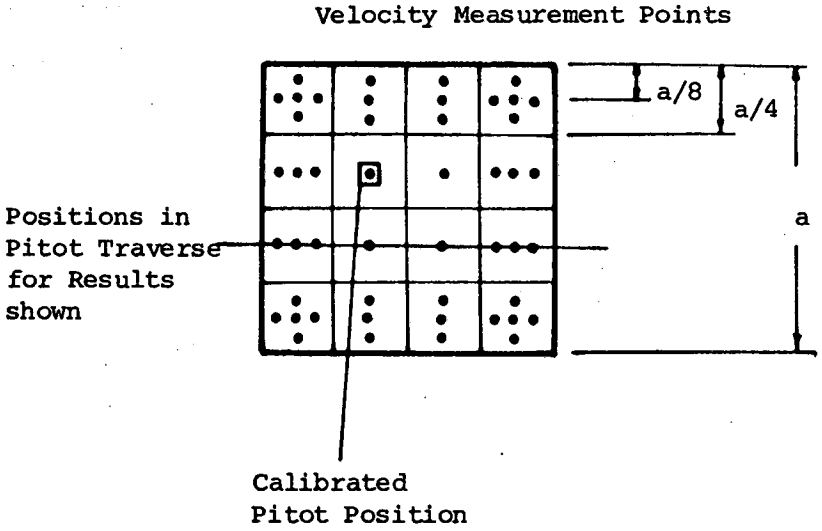

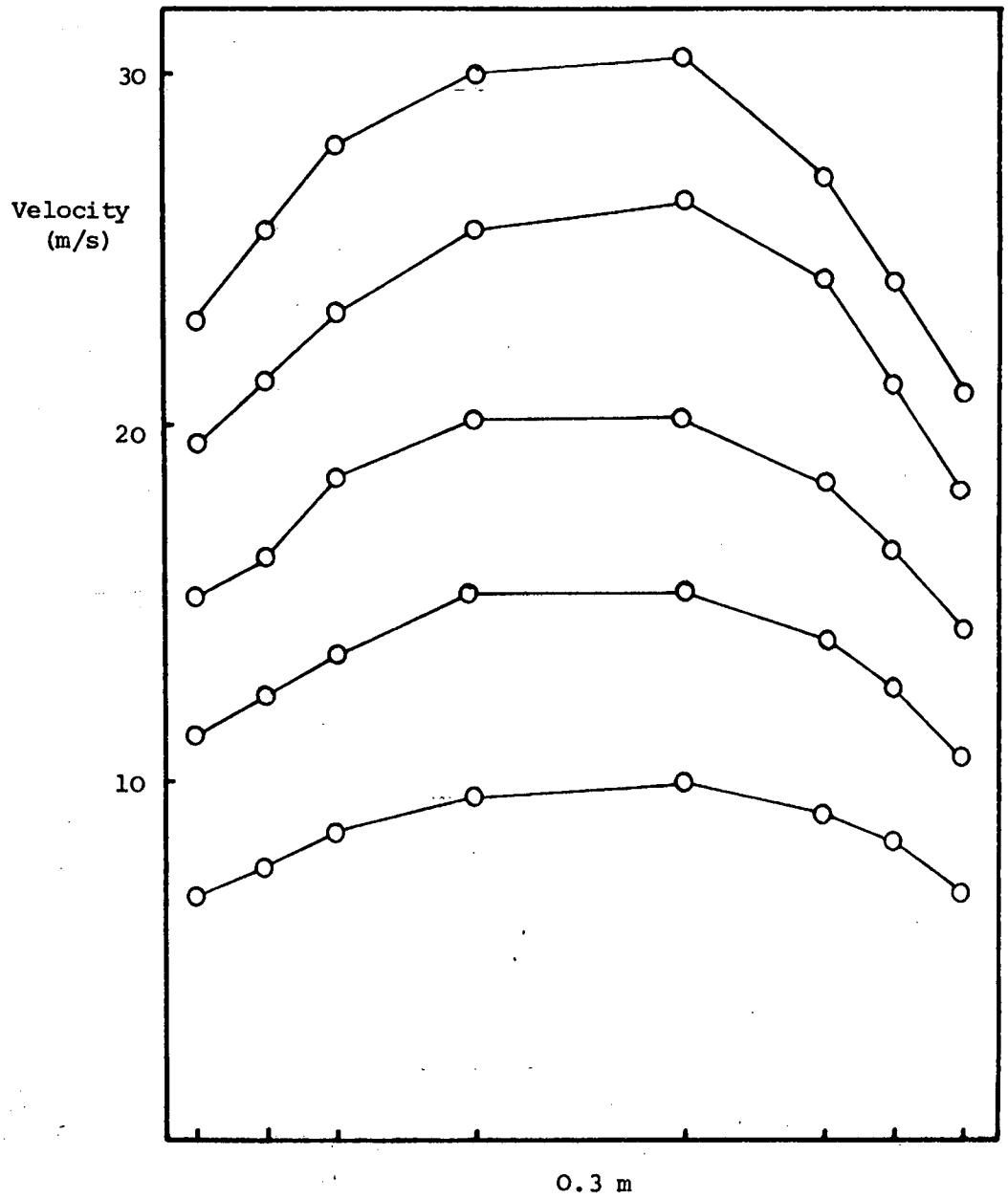

FIGURE 4 Test Duct Velocity Profiles

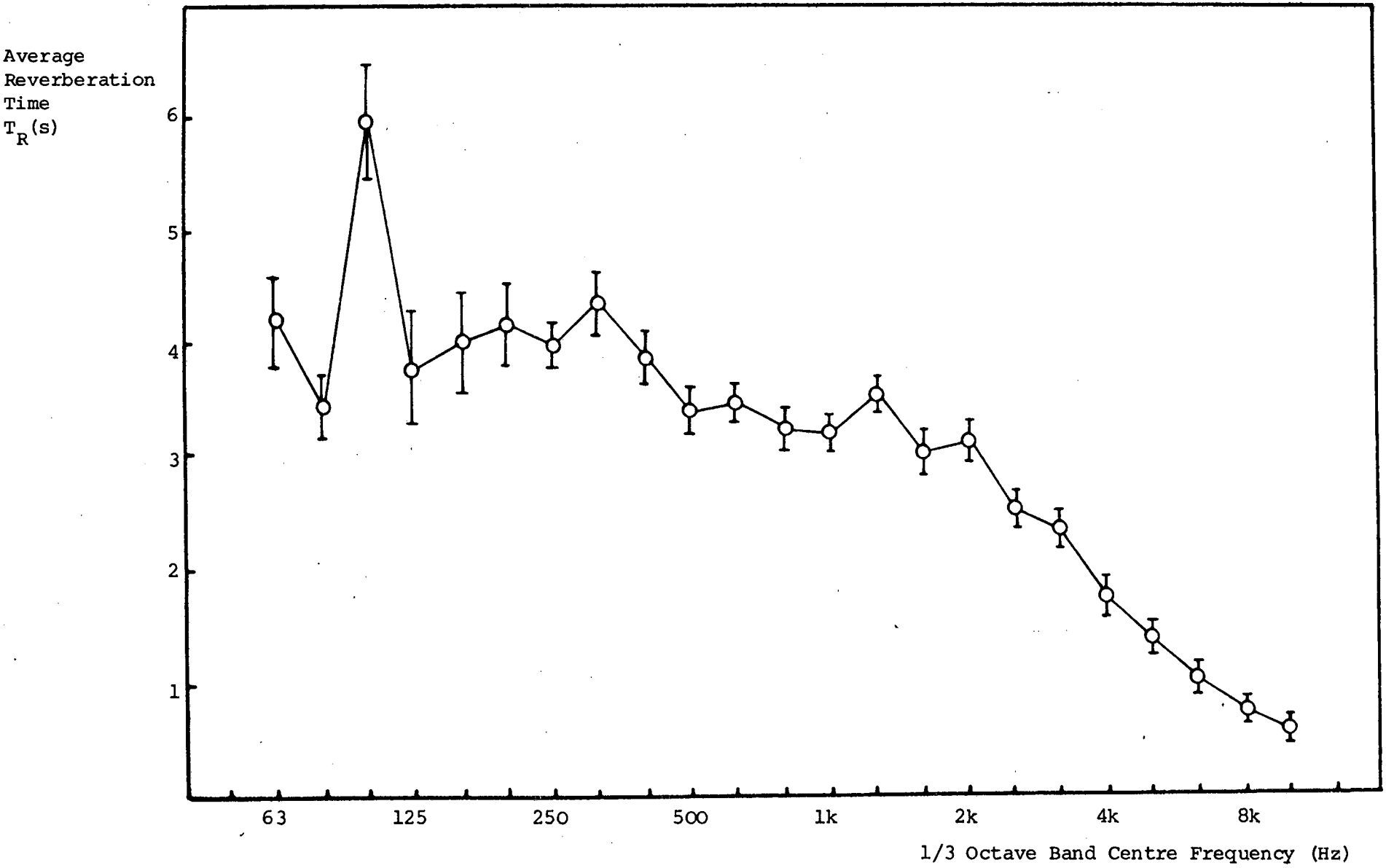

FIGURE 5 Average Reverberation Times for the Test Chamber
Eight microphone positions were used for 63 Hz - 800 Hz and three microphone positions for 1 kHz - 10 kHz. Error bars denote the spread of results.

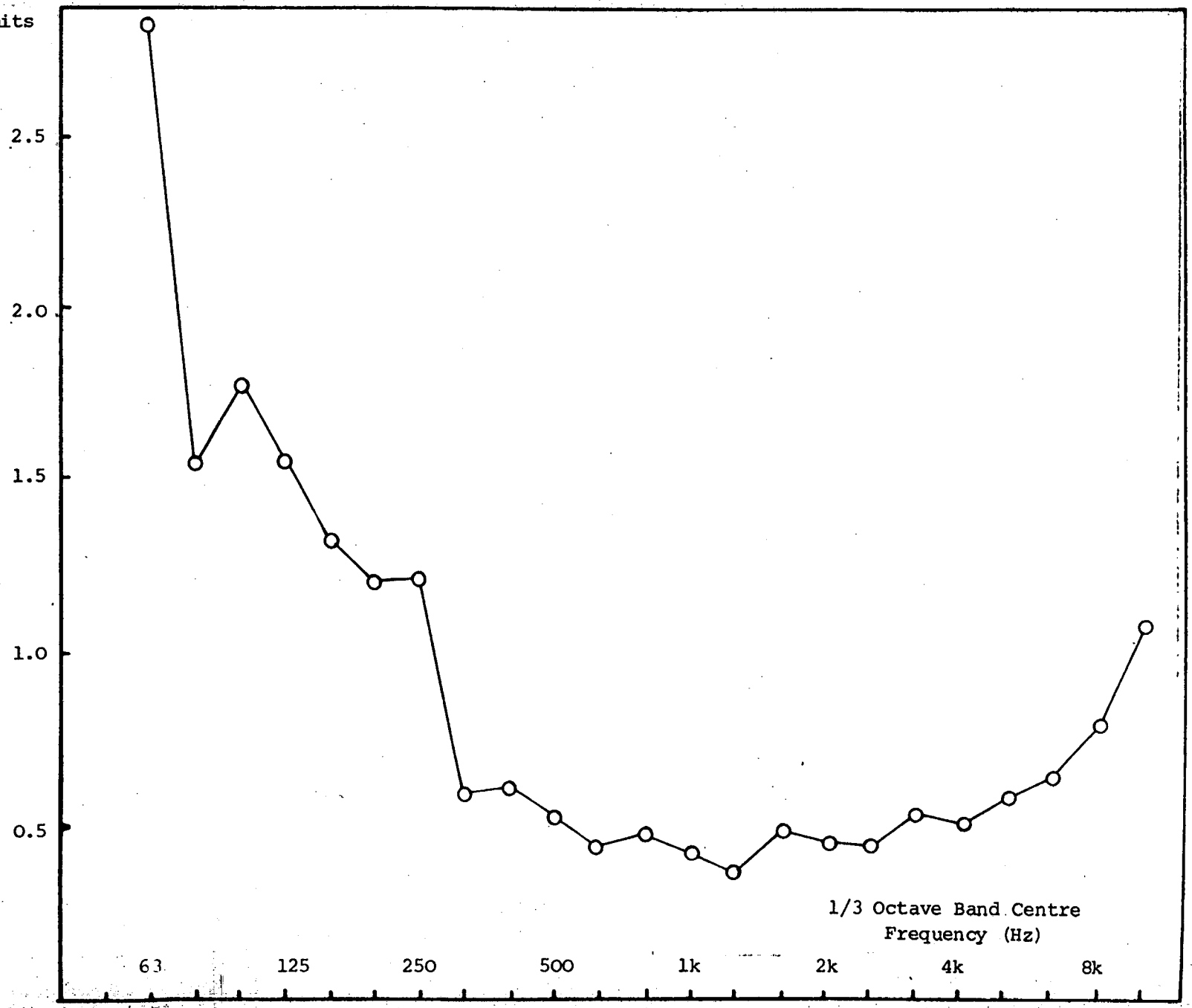

FIGURE 6 95% Confidence Limits for an Estimate of Mean SPL in the Test Chamber from Six Microphone Positions

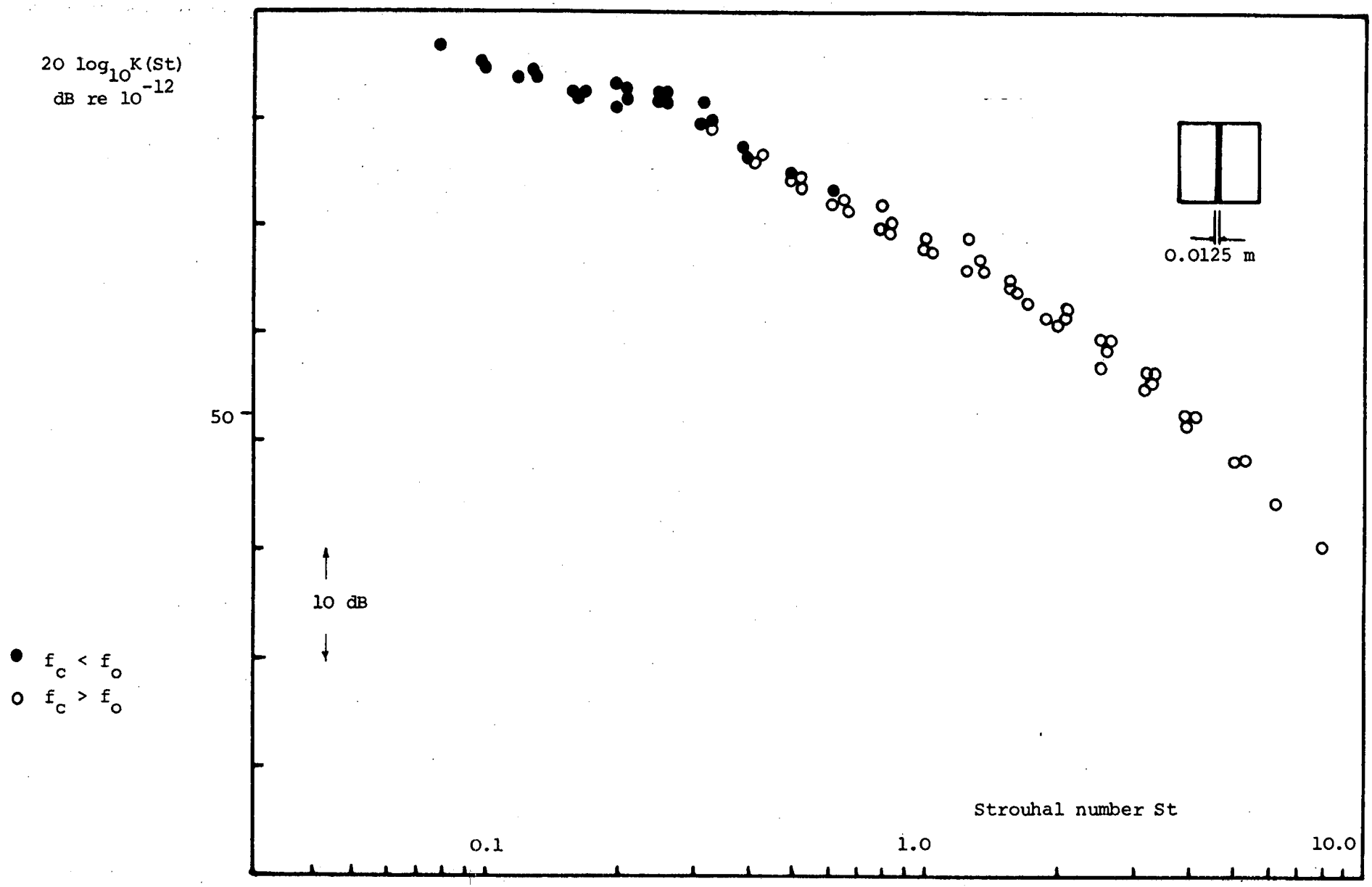

FIGURE 7 Normalised 1/3 Octave Band Results for 0.0125 m Centre Strip Spoiler
Assumed C_D = 2.0. U_c in range 10 → 40 m/s

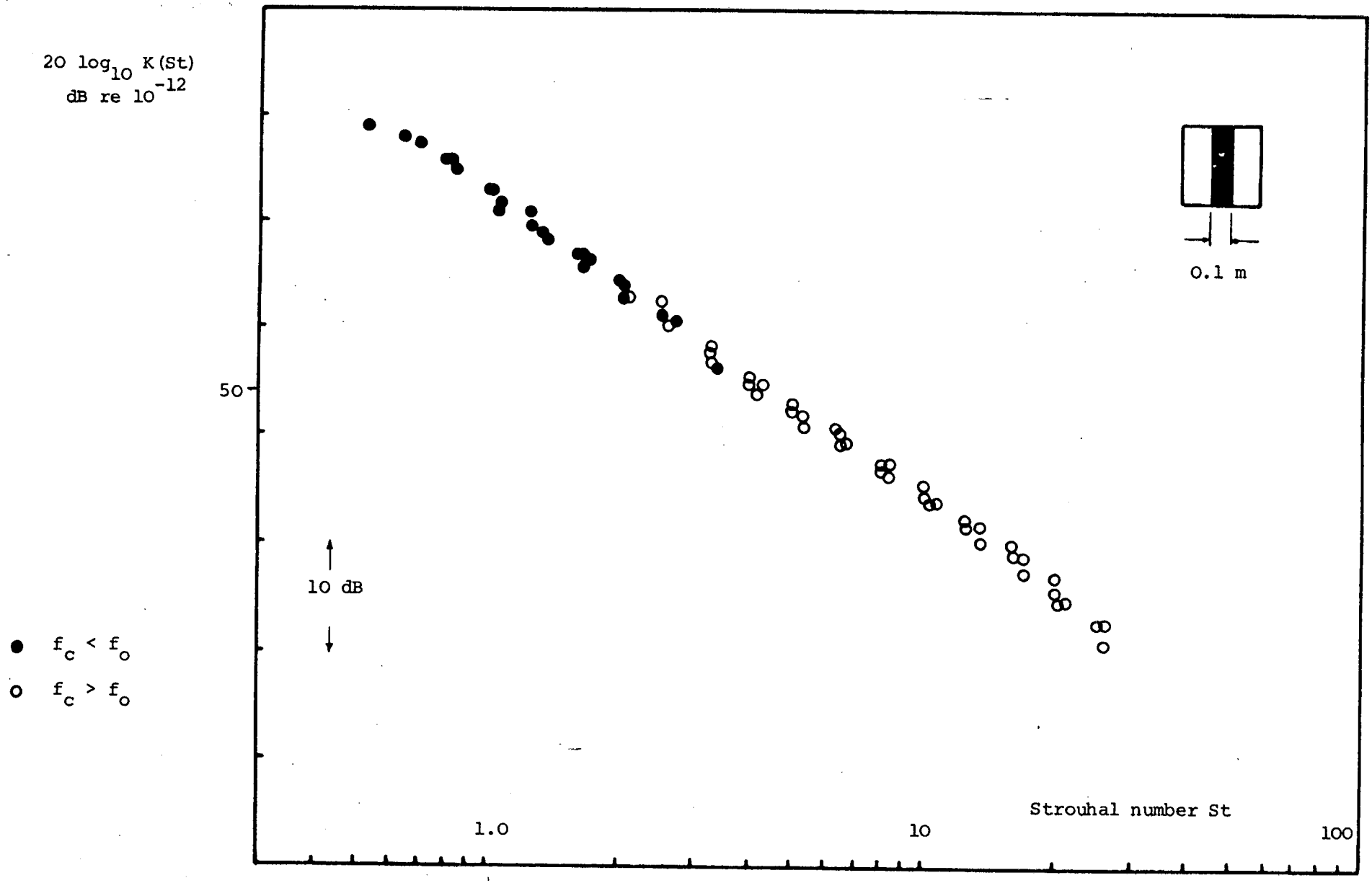

FIGURE 8 Normalised 1/3 Octave Band Results for 0.1 m Centre Strip Spoiler
C_D = 2.3. U_c in range 10→40 m/s

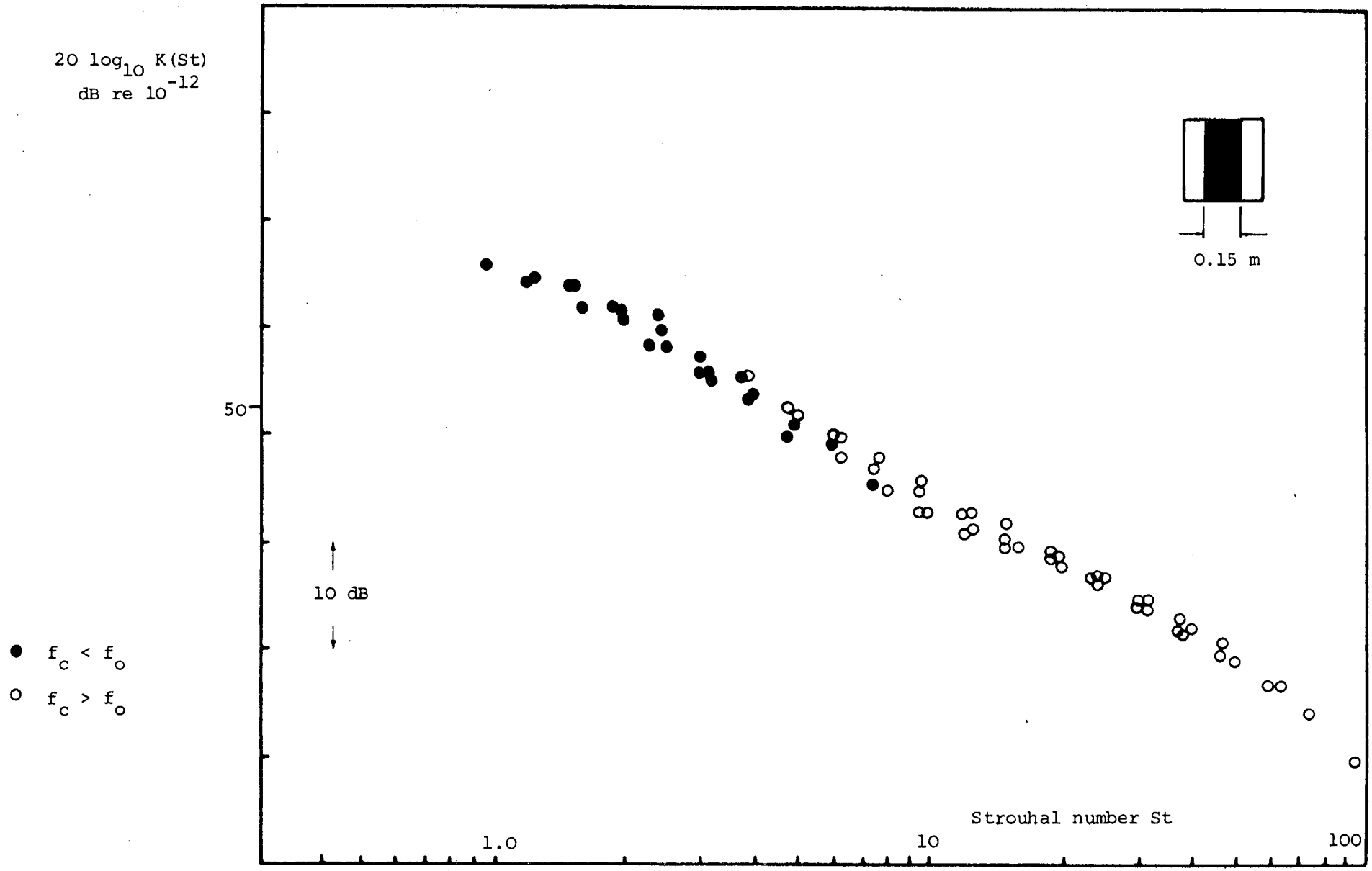

FIGURE 9 Normalised 1/3 Octave Band Results for 0.15 m Centre Strip Spoiler
C_D = 15.5 . U_c in range 10→40 m/s

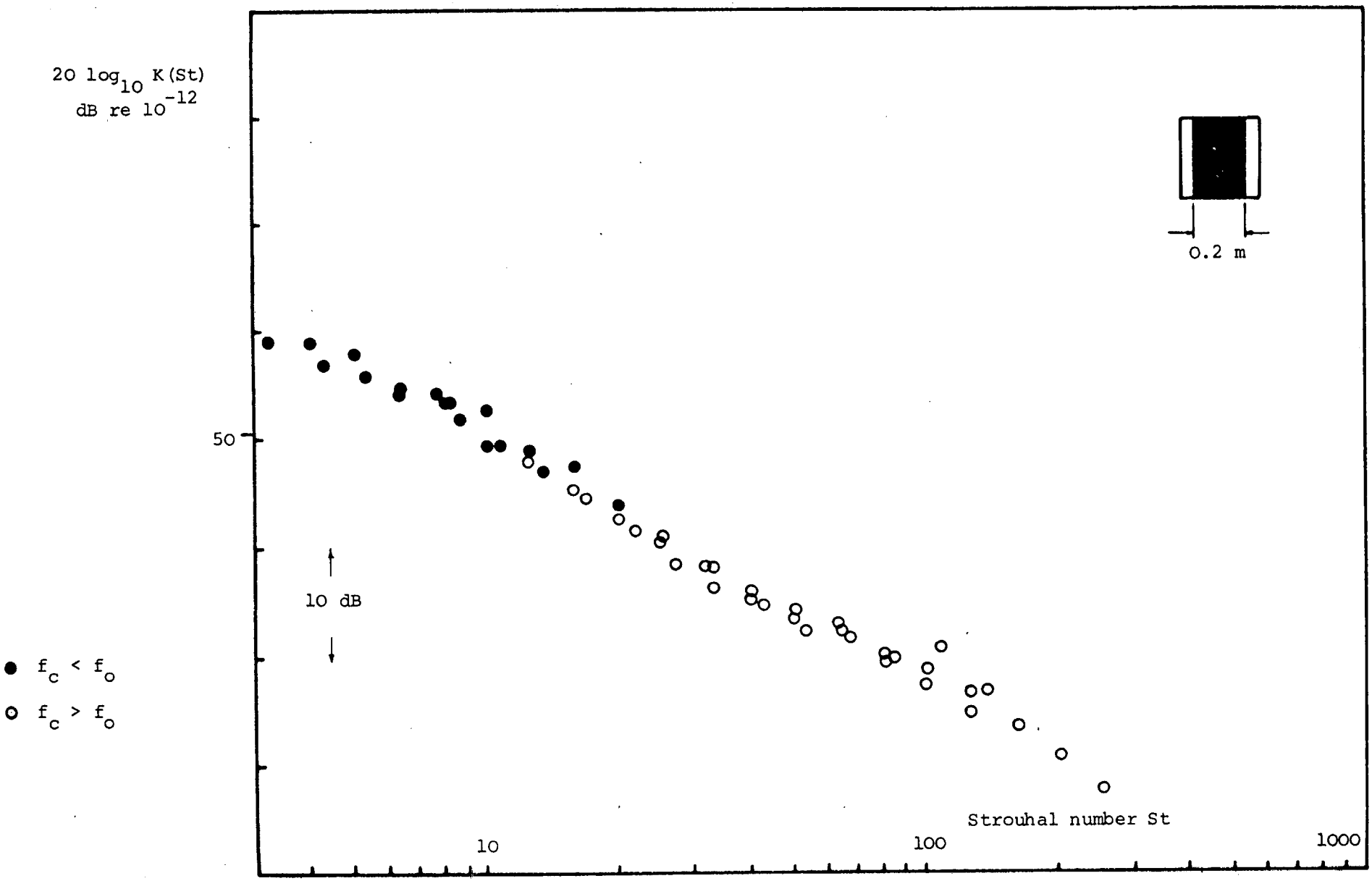

FIGURE 10 Normalised 1/3 Octave Band Results for 0.2 m Centre Strip Spoiler
C_D = 190.0 U_c in range 10→40 m/s

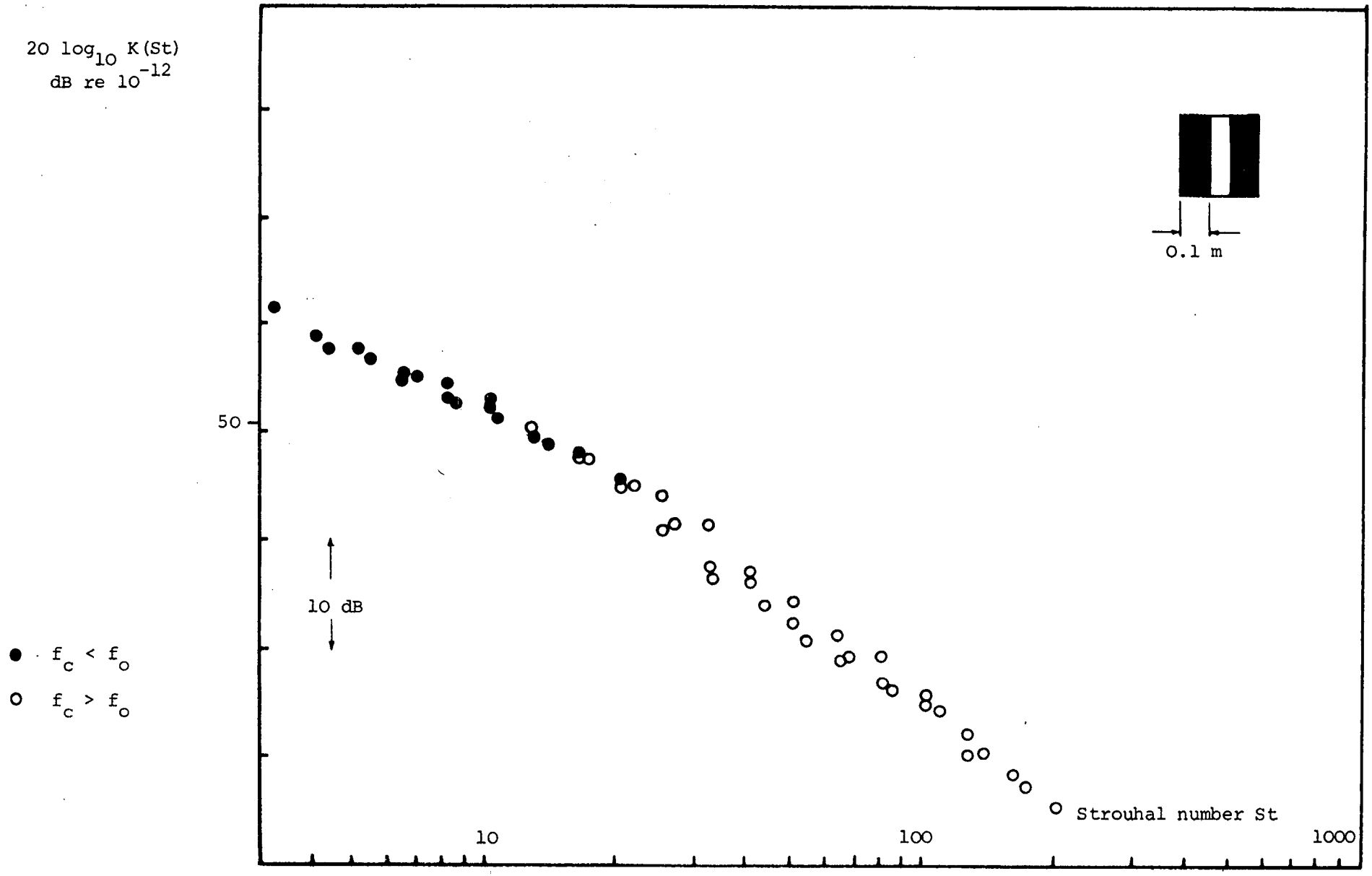

FIGURE 11 Normalised 1/3 Octave Band Results for 0.2 m Side Strip Spoiler
C_D = 162.0 U_c in range 10 → 40 m/s

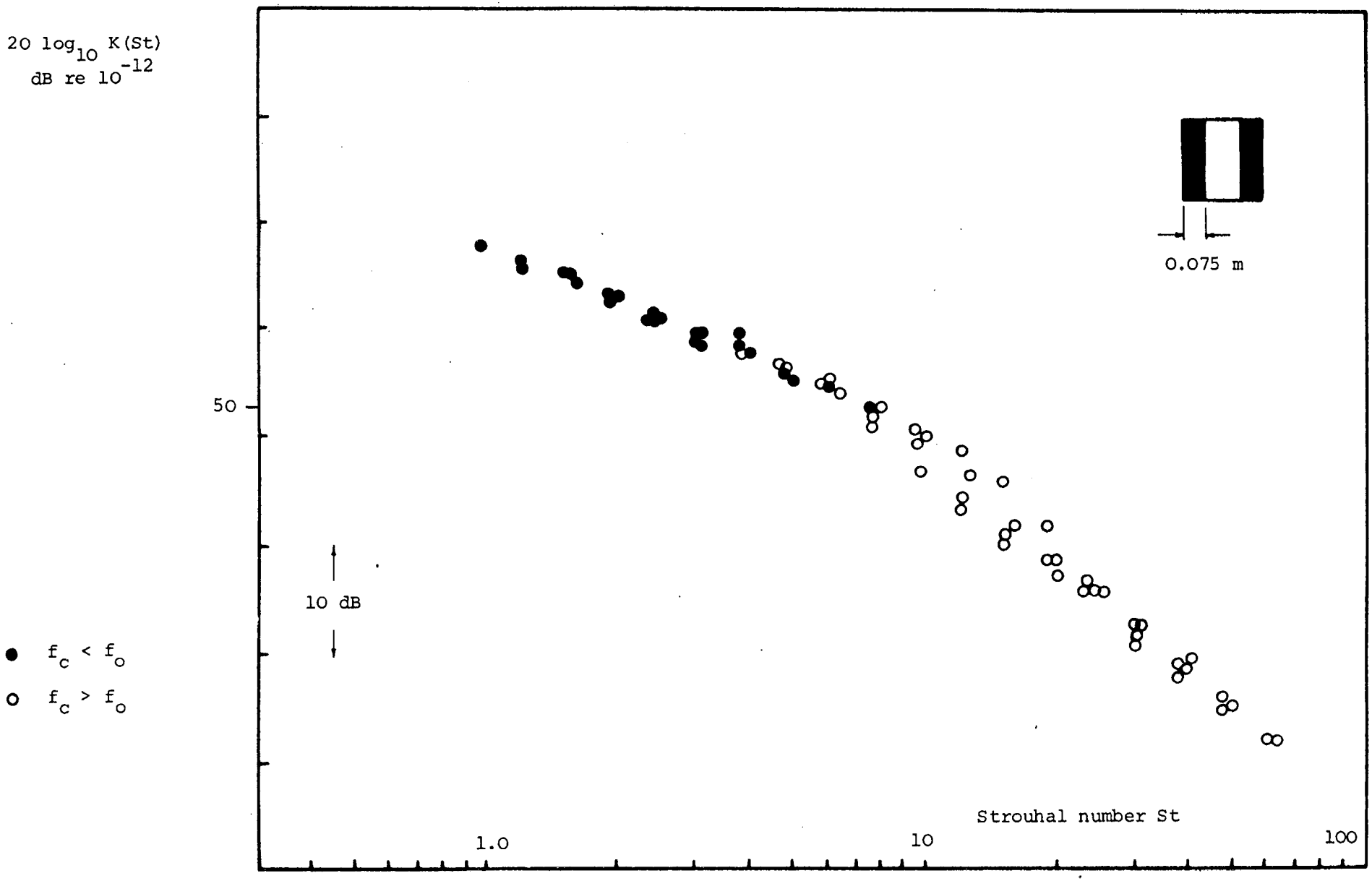

FIGURE 12 Normalised 1/3 Octave-Band Results for 0.15 m Side Strip Spoiler
C_D = 12.5 u_c in range 10 → 40 m/s

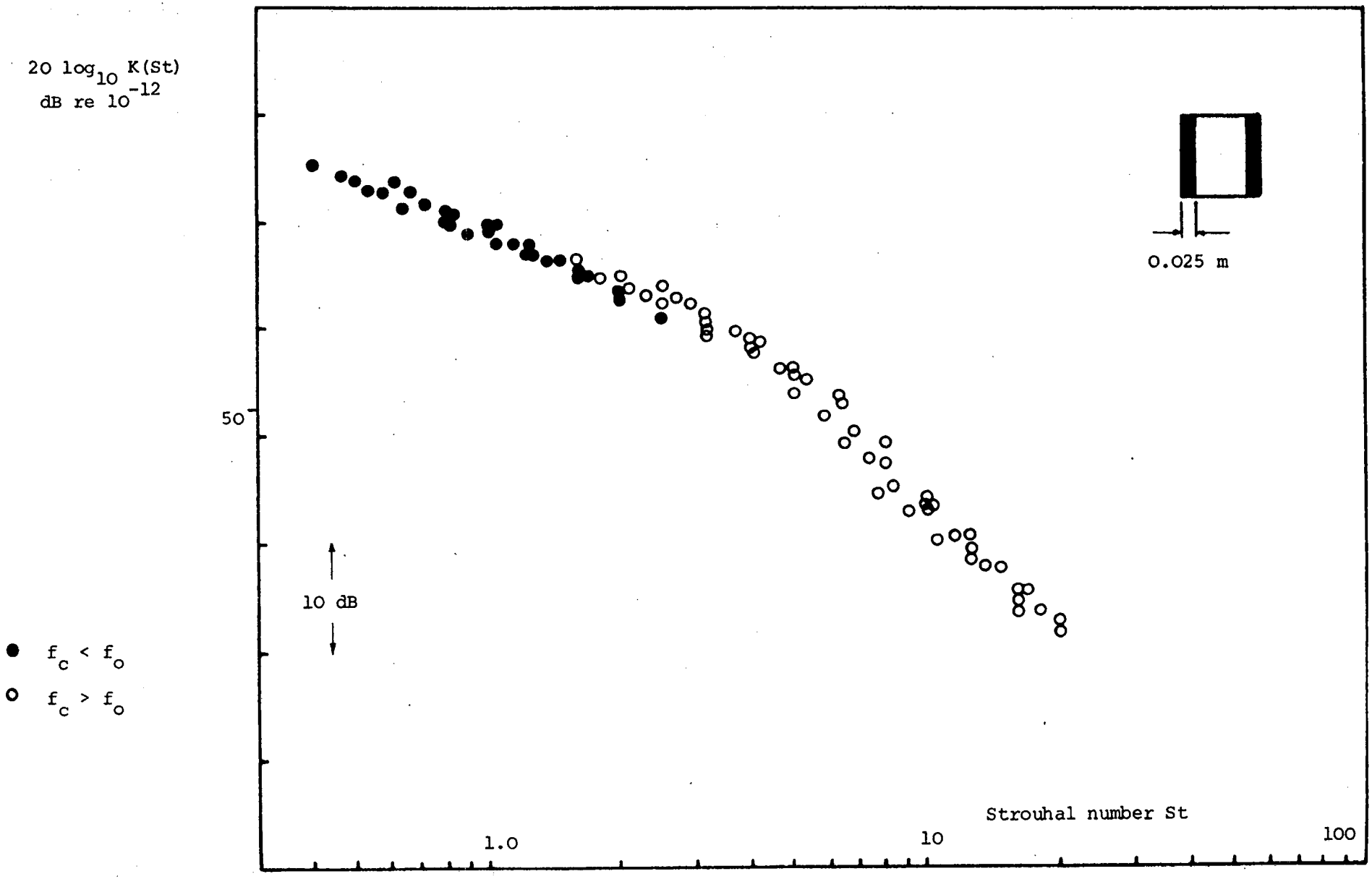

FIGURE 13 Normalised 1/3 Octave Band Results for 0.05 m Side Strip Spoiler
$C_D = 1.3$ U_c in range 10→40 m/s

FIGURE 14 Velocity Scaling of the In-Duct Sound Power Level Radiated by the 0.05 m Side Strip Spoiler

The results are for constriction velocity U_c = 20, 25, 30, 35, 40 m/s.

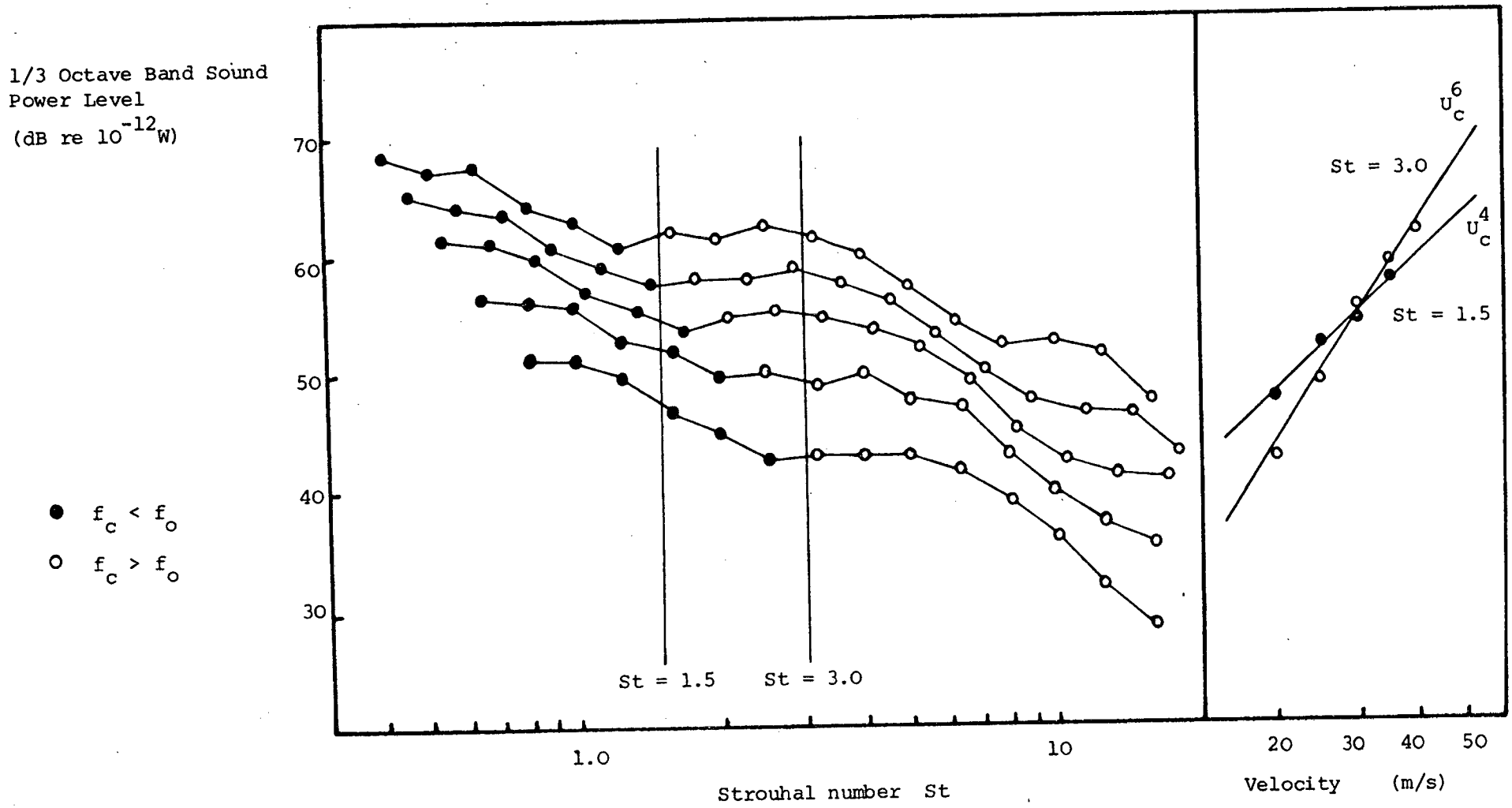

FIGURE 15 The Overall Collapse of Normalised Data for all Test Spoilers

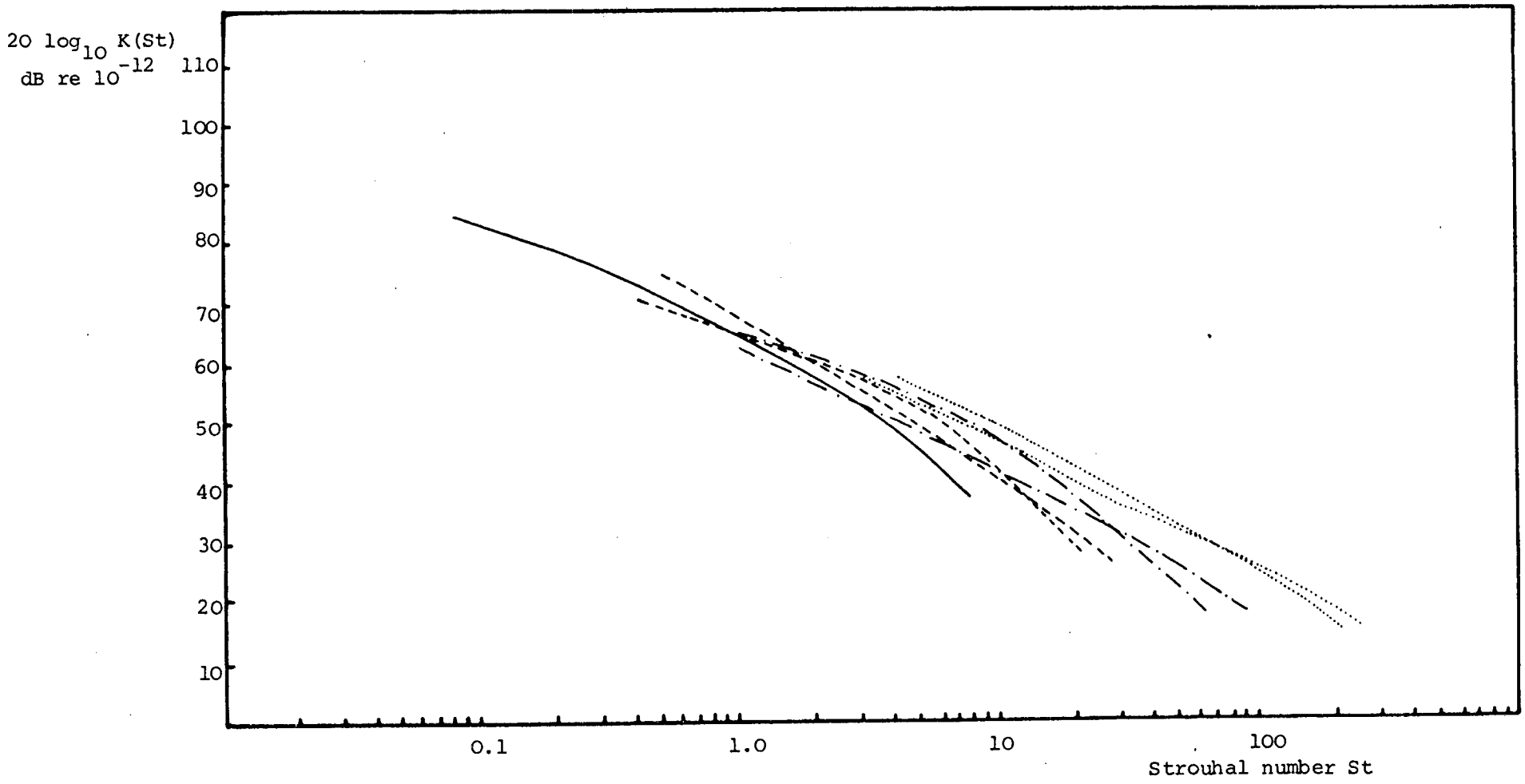

FIGURE 16 Comparison of the Normalised 1/3 Octave Band Test Spoiler Results with Gordon's (2) Data for a 0.075 m Centre Strip Spoiler in a 0.047 m diameter Pipe.

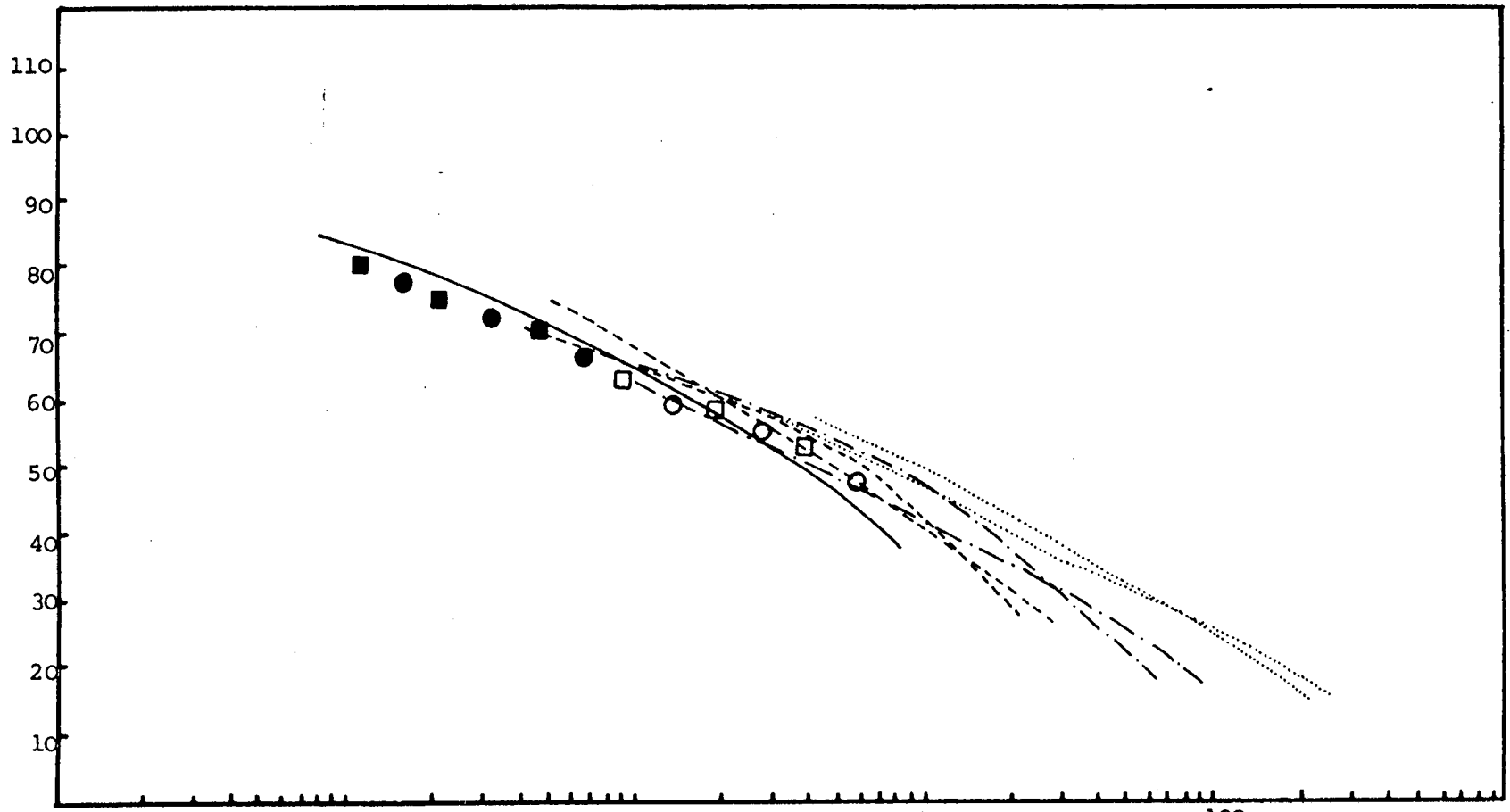

CHAPTER 3

NOISE GENERATED BY FLOW OVER PERFORATED SURFACES

1. INTRODUCTION

Flow over perforated metal facings of acoustically absorbent duct linings can generate a significant amount of noise. This has been well known for some time (1) and the problem has already received some attention. Recent work of Tsui and Flandro (2) and Bauer and Chapkis (3) has concentrated on the "singing" phenomenon produced by flow over resonant cavity duct liners used in aero-engine applications. Vortex shedding in the perforations in the liner surface can excite either cavity resonances or duct modes near their resonant (cut-on) frequency, the shedding becoming coupled to the resonance with the consequent production of very high sound pressures in the duct. Discrete frequency noise generated by flow through the perforated walls of transonic wind tunnels has also been studied by various authors (4,5,6). The mechanism of noise generation in this instance is again attributed to either a locking-in of the vortex shedding with an acoustic resonance, or an edge-tone type mechanism where the acoustic feedback is provided by the interaction of eddies with the downstream edge of the perforation in which the eddies are shed.

When a strong feedback mechanism is not present, flow over perforated liner facings can still generate a substantial amount of broad band noise. This is generally the case when the perforate facing is used over a fibrous backing material as a lining in attenuator sections in low speed flow ducts. It is obviously important in the optimisation of attenuator performance to be able to predict and, if necessary, reduce this source of attenuator self-noise. The objective of this work is to provide a method of predicting the broad band noise which is generated when a given type of perforate facing is used in any particular engineering application. The work reported in this Chapter was not aimed at accounting for the production of discrete frequency noise, but only towards quantifying the "base level" of broad band noise to be expected from the installation of various liner configurations.

The only detailed theoretical treatment of this problem is that undertaken by Ffowcs Williams (7). He treated the model problem of sound generation by a body of turbulence near an infinite, rigid, thin screen with circular perforations. Unfortunately, the analysis he has presented contains certain restrictive assumptions. Firstly, it is assumed that the size of the perforations is much smaller than the distance between them. This is not the case for many facing materials

used in practice. Secondly, variations in pressure within individual apertures are neglected. Experiments indicate that most sound is produced by flow over perforated surfaces when the eddies shed in the perforations are of a smaller scale than the size of the perforations. Pressure fluctuations will not then be uniform over the holes.

Nevertheless, Ffowcs Williams' analysis for this somewhat restricted case provides an important fundamental result: that the sound scattered from the perforated screen can be directly related to the mass flow driven through the apertures by the hydrodynamic field. This result has been used in the present work as a basis for modelling the sound generation process associated with flow over practical perforated screens. The flow driven through a given aperture results in a fluctuating volume flow through the upper surface of the screen. This is thought of as constituting an equivalent monopole source. The strength of this monopole is directly related to the real volume flow through the aperture. Since a volume inflow through the upper surface results in a simultaneous outflow through the lower surface, there is an equal and opposite equivalent monopole below the perforate screen. The net field radiated from the given aperture is the combination of the fields due to the two equivalent monopoles. The form of the net field is thus dependent on the acoustical properties of the screen. For acoustically opaque screens, the lower monopole cannot radiate into the region above the screen and only the field from the upper monopole is observed. For transparent screens, the lower monopole radiates into the region above the screen and has a cancelling effect on the field of the upper monopole. The net radiated field then exhibits dipole characteristics.

This equivalent source model has been found to give an excellent description of the sound produced by perforate facing materials used in practice, even though the Ffowcs Williams' analysis is not strictly applicable. The model is developed by assuming a fairly realistic form for the driving hydrodynamic velocity that determines the strength of the equivalent monopoles. This makes clear the inherent dependence of the radiated noise on the turbulence intensity above the liner surface and the Strouhal number based on the diameter of the perforate apertures.

A series of experiments has been conducted in order to test the predictions of the equivalent source model. The noise radiated by flow over the perforated screens tested was found to exhibit both the magnitude and spectral distribution predicted by the theory. The sound power

generated per unit area by a liner facing of given geometry under given flow conditions has thus been firmly established.

In practical applications, the noise generated by a given liner facing will also be absorbed by the liner. In order to estimate the net sound power generated by a given liner facing, the problem of continuous absorption and generation of sound down the duct length has been examined. The treatment follows a simple analysis by Ingard (8). This analysis has been used, together with the knowledge of the sound power generated per unit area of liner facing, in order to predict the net power radiated from a given length of lined duct. It has been found that a good estimate of the liner self-noise can be made from a knowledge of the liner geometry, mean flow speed, the turbulence intensity above the liner surface and the rate of attenuation down the duct.

The application of Ffowcs Williams' theoretical result will first be described in the next section. In sections 3 and 4 the measurement of noise from liner facings is described and the experimental results are discussed, whilst the main conclusions of the work are outlined in Section 5.

2. THEORY

2.1 The Basis for the Equivalent Source Model

As has already been mentioned, the theoretical foundation for this work stems from Ffowcs Williams' analysis of the acoustic properties of turbulence near perforated screens. A brief description of that analysis will be given here, but for full details of the work and the assumptions used, the reader is referred to the original paper (7). Essentially, Ffowcs Williams solves the inhomogeneous wave equation for a region with boundary conditions imposed by the presence of an infinite perforated screen. The screen is rigid and thin and has a uniform distribution of N identical circular perforations per unit area. (A list of symbols is given in Appendix 1) Each aperture has a radius a that is much smaller than the typical distance $(\pi N)^{-\frac{1}{2}}$ between adjacent apertures. The analysis is carried out at a single frequency ω corresponding to an acoustic wavelength λ that is much larger than both the hole radius and the typical distance between holes. There are thus many holes per acoustic wavelength and the screen behaves as a continuous homogeneous boundary towards incoming acoustic waves.

The screen is situated at $x_2 = 0$ (see Figure (1)). The fluid in a region just above the screen in $x_2 > 0$ is turbulent. Elsewhere,

including the entire region $x_2 < 0$, the fluid is an ideal acoustic medium at rest. The typical length scale of the turbulent fluctuations at the frequency ω is roughly $M\lambda$ where M is the Mach number of the flow. M is chosen to be small such that the scale of the turbulence is much smaller than the scale of the sound field. The turbulence above the screen gives rise to a quadrupole type inhomogeneity in the wave equation representing the generation of acoustic radiation by sources in the turbulent boundary layer above a liner surface. Scattering of the incident quadrupole sound field leads to a scattered field which is the dominant contributor to the far field radiation at low Mach numbers.

By solving an integral equation for the normal pressure gradient over the surface of the apertures in the screen, Ffowcs Williams derives an exact expression (for the model problem) for the acoustic radiation into the far field of the region $x_2 > 0$. The solution is valid for the given screen geometry and as the distance $|x_k - y_k|$ tends asymptotically to infinity. The field at x_k consists of three contributions. The first is the sound that arrives directly from the quadrupole sources in the turbulent boundary layer. The second is the component of the quadrupole generated wave that travels to x_k after reflection from the screen surface, which behaves as a homogeneous boundary having a reflection coefficient R. In principle, the first two contributions to the net radiated field are known. The third part of the radiated field consists of the waves generated from the scattering of the turbulent pressure fluctuations by the individual screen apertures. This is the component of the radiated noise that is of interest here, since it is much larger than the other two at low Mach numbers.

Ffowcs Williams shows that this contribution can be expressed in terms of the purely hydrodynamic pressure fluctuations that drive a mass flow through the apertures. Pressure is assumed to be uniform over each aperture, but the hydrodynamic pressure fluctuations are distinguished from the acoustic pressure fluctuations by their much smaller length scale. The sound field thus produced in an individual aperture can be interpreted as the net field radiated by two equal and opposite monopole sources situated on either side of the screen. The monopole strength of these sources is given exactly as the fluctuations in mass flow driven through the aperture by the turbulent field. As far as the radiation from the monopoles above and below the screen is concerned, the screen again behaves as a homogeneous transparent boundary.

This forms the basis of the equivalent source model that has been used in this work. Ffowcs Williams' result is "exact" for his given perforate geometry (and an inviscid fluid), but the basic model suggested by his result has been applied to arbitrary perforate geometries and has then been tested experimentally. A more precise description of the model will be given in the next section.

2.2 The Acoustic Properties of Perforated Screens

As pointed out by Ffowcs Williams, the acoustic properties of a perforated screen having many holes per acoustic wavelength can be deduced from the acoustic properties of a single aperture in an infinite baffle. Consider the problem illustrated in Figure (2). Plane waves of a single frequency ω are incident on an infinite perforated screen at a polar angle θ. The incident wave pressure having amplitude p_i can be thought of as being produced by a simple source at x_k where $|x_k - y_k| \to \infty$. We wish to deduce the transmitted pressure amplitude p_t and the reflected pressure amplitude p_r. The difference in pressure across the screen drives a volume flow through each aperture. For wavelengths much larger than hole size, the volume flow q driven by the pressure difference $(p_i + p_r - p_t)$ applied uniformly across an aperture face can be expressed in terms of the conductivity C of the aperture, (Morfey (9)):

$$q = (p_i + p_r - p_t) \frac{iC}{\omega \rho_o} . \qquad (1)$$

The conductivity of a circular opening in a thin infinite baffle has been shown by Rayleigh (10) to be equal to twice the aperture radius. Thus,

$$q = (p_i + p_r - p_t) \frac{i2a}{\omega \rho_o} . \qquad (2)$$

From this the net volume flow through a unit area of screen can be determined by adding the volume flows driven through the individual apertures. This net volume flow per unit area of screen can be interpreted as an equivalent velocity u that is driven across the homogeneous boundary representing the screen. Thus, if there are N holes per unit area of screen, one can write

$$u = (p_i + p_r - p_t) i \frac{2aN}{\omega \rho_o} . \qquad (3)$$

This step will be valid for arbitrary hole spacings provided there is no interaction of the flow through adjacent apertures that can change the conductivity of the individual apertures. Ingard (11) and Nesterov (12) have investigated the effects of hole spacing on the conductivity of an array of apertures for normally incident plane waves, and empirical data on the magnitude of this effect are available. For the moment one can continue to assume here that there is no effect of aperture spacing on aperture conductivity.

Continuity across the homogeneous boundary also ensures that the velocity u across the boundary is related to the particle velocities in the incident, reflected and transmitted waves by

$$u = u_t = u_i + u_r. \tag{4}$$

Since these particle velocities are related to the pressure in the waves by $u_i = p_i\cos\theta/\rho_o c_o$, $u_r = -p_r\cos\theta/\rho_o c_o$ and $u_t = p_t\cos\theta/\rho_o c_o$, one has

$$u = \frac{p_t\cos\theta}{\rho_o c_o} = \frac{p_i\cos\theta}{\rho_o c_o} - \frac{p_r\cos\theta}{\rho_o c_o}. \tag{5}$$

Equations (3) and (5) can be used to express the transmitted and reflected pressures in terms of the incident wave pressure. By straightforward algebraic manipulation, it can be shown that:

$$p_r = Rp_i \tag{6}$$

$$p_t = (1 - R)p_i \tag{7}$$

where

$$R = \frac{1}{1 + \frac{4aiN}{k\cos\theta}}. \tag{8}$$

This result for the reflection coefficient R is that obtained by both Ffowcs Williams (7) and Leppington and Levine (13) for low frequencies and aperture spacings that are large compared to aperture size. This brief analysis indicates that the result will also be true for arbitrary aperture spacings, provided there are many apertures per acoustic wavelength and there is no interaction between them.

The impedance of the surface having this reflection coefficient is given by

$$Z = \frac{\rho_o c_o}{\cos\theta}\left(\frac{1+R}{1-R}\right) = \frac{\rho_o c_o}{\cos\theta} - i\rho_o c_o \frac{k}{2aN} . \qquad (9)$$

The resistive part of the impedance is simply the radiation resistance provided by the waves transmitted through the screen. The reactive part is due to the apparent surface mass per unit area $\rho_o/2aN$ provided by the flow through the screen apertures.

The next step is to derive the field radiated by a monopole source situated just above the screen surface at y_k' and also the field radiated by a monopole just below the surface at y_k''. These are easily deduced from the above analysis by using the principle of reciprocity. The field at y_k' due to the source at x_k (where $|x_k' - y_k'| \to \infty$) is the sum of the incident pressure p_i and the reflected pressure p_r. From (6) this is simply $p_i(1 + R)$. Thus, for a single frequency source having a source strength amplitude $Q(x_k)$

$$p_i(y_k') = \frac{Q(x_k)\, e^{ik|y_k'-x_k|}}{4\pi|y_k' - x_k|} \qquad \text{for } |y_k' - x_k| \to \infty, \qquad (10)$$

then the total field $p(y_k')$ at the point y_k' due to the source at x_k' is simply

$$p(y_k') = \frac{(1+R)Q(x_k)\, e^{ik|y_k'-x_k|}}{4\pi|y_k' - x_k|} \qquad \text{for } |y_k' - x_k| \to \infty. \qquad (11)$$

Since the system is passive and linear, the field at x_k due to a source at y_k' will be identical to the field at y_k' produced by a source at x_k. Thus

$$p(x_k) = \frac{(1+R)Q(y_k')\, e^{ik|x_k-y_k'|}}{4\pi|x_k - y_k'|} \qquad \text{for } |x_k - y_k'| \to \infty. \qquad (12)$$

Similarly, since the pressure at y_k'' due to a source at x_k is the transmitted pressure p_t (which from (7) is $(1 - R)p_i$), then the field at x_k due to a source at y_k'' is

$$p(x_k) = \frac{(1-R)Q(y_k'')\, e^{ik|x_k-y_k''|}}{4\pi|x_k - y_k''|} \qquad \text{for } |x_k - y_k''| \to \infty. \qquad (13)$$

It is now assumed that the field radiated by turbulence interacting with a given aperture can be expressed in terms of the field of two monopole type equivalent sources above and below the aperture. The upper monopole at y_k' has a strength $-Q_h(y_k')$ which is determined exactly

by the rate of mass addition driven through the aperture by the hydrodynamic field into the upper half space $x_2 > 0$. The lower monopole at y_k'' has a strength $+Q_h(y_k'')$ which is determined by the rate of mass addition into the lower half space $x_2 < 0$. Since the distance $|y_k'' - y_k'|$ is very much smaller than a wavelength, one can write the net field $p(x_k)$ due to an individual aperture by combining expressions (12) and (13) to give

$$p(x_k) = \frac{-2RQ_h(y_k)\, e^{ik|x_k - y_k|}}{4\pi|x_k - y_k|} \qquad \text{for } |x_k - y_k| \to \infty. \tag{14}$$

It is worth noting that although this solution is valid asymptotically as the observation point at x_k tends to infinity, in practice it may prove valid for distances of a few wavelengths from the source. Equation (14) has certainly been found (14) to describe accurately the field of a point source above an absorbing boundary for distances from the source of this order of magnitude.

It should also be noted that any effect of the mean flow on the acoustic properties of the screen or on the radiation field of the equivalent monopole has been neglected. This will be valid at the low Mach numbers considered. The effect of the screen on the mean flow is assumed to be accounted for by the model. Thus, if a given screen allows a high level of turbulence to persist near its surface, then the high mass flow through the apertures will result in a large equivalent source strength.

2.3 The Strength of the Equivalent Source

Having conducted the above analysis for equivalent sources radiating at a single frequency, it is now necessary to generalise the above result for source strengths having an arbitrary time dependence. Thus defining the Fourier spectrum of the source strength $Q_h(y_k,\omega)$ as

$$Q_h(y_k,\omega) = \lim_{T\to\infty} \frac{1}{2\pi} \int_{-T}^{T} Q_h(y_k,t)\, e^{-i\omega t} dt, \tag{15}$$

where $Q_h(y_k,t)$ is the corresponding time domain variable, then the Fourier spectrum of the radiated pressure is given by

$$p(x_k,\omega) = \frac{-2R\, Q_h(y_k,\omega)\, e^{ik|x_k - y_k|}}{4\pi|x_k - y_k|} \,. \tag{16}$$

Defining the spectral density of the radiated pressure fluctuations as

$$S_p(x_k,\omega) = \lim_{T\to\infty} \frac{\pi}{T} |p(x_k,\omega)|^2, \tag{17}$$

and the spectral density of the source strength as

$$S_Q(y_k,\omega) = \lim_{T\to\infty} \frac{\pi}{T} |Q_h(y_k,\omega)|^2, \tag{18}$$

gives the relationship

$$S_p(x_k,\omega) = \frac{4|R|^2}{16\pi^2 r^2} S_Q(y_k,\omega), \tag{19}$$

where $r^2 = |x_k - y_k|^2$ is the square of the distance from x_k to the centre of the aperture considered.

The source strength $Q_h(y_k,t)$ resulting from the volume flow driven through the aperture can be written in terms of the normal velocity $v_2(y_1,y_3,t)$ over the aperture surface S such that

$$Q_h(y_k,t) = -\rho_o \iint_S \frac{\partial}{\partial t} v_2(y_1,y_3,t)\, dS, \tag{20}$$

or in terms of the Fourier spectrum $v_2(y_1,y_3,\omega)$ of the normal velocity fluctuations as

$$Q_h(y_k,\omega) = -i\,\omega\,\rho_o \iint_S v_2(y_1,y_3,\omega)\, dS. \tag{21}$$

This enables the source strength spectral density $S_Q(y_k,\omega)$ to be written in terms of the cross spectral density of the normal velocity fluctuations over the aperture such that

$$S_Q(y_k,\omega) = \rho_o^2 \omega^2 \iiiint_S S_{vv}(y_k,z_k,\omega)\, dS(y_k)\, dS(z_k), \tag{22}$$

where the cross spectral density of the normal velocity fluctuations is defined by

$$S_{vv}(y_k,z_k,\omega) = \lim_{T\to\infty} \frac{\pi}{T} v_2(y_1,y_3,\omega)\, v_2^*(z_1,z_3,\omega), \tag{23}$$

where the asterisk indicates the complex conjugate and z_k are additional position coordinates.

The source strength, and thus the radiated field, is determined by the form of the cross spectral density of the hydrodynamic velocity fluctuations over the hole. The phase relationships at a given frequency between the velocity fluctuations at different points on the aperture surface would be determined by the length scale and convection speed of the turbulent eddies that pass over the hole. If the flow is in the y_1 direction, then eddies travelling in the y_1 direction will result in a distinct phase relationship between velocity fluctuations at points along the paths taken by the eddies. The loss of correlation between points along lines in the y_1 direction will be determined by the decay of the eddy structures as they are convected. The degree of correlation between points along lines in the y_3 direction will decay faster than in the y_1 direction and will be determined by the lateral length scale of the eddies. The following form is assumed for the cross spectral density of the velocity fluctuations

$$S_{vv}(y_k, z_k, \omega) = S_v(y_k, \omega)\, e^{iK(y_1 - z_1)}\, F(y_3 - z_3), \tag{24}$$

where $S_v(y_k, \omega)$ is the spectral density of the normal velocity fluctuations given by

$$S_v(y_k, \omega) = \lim_{T \to \infty} \frac{\pi}{T} \left| v_2(y_1, y_3, \omega) \right|^2. \tag{25}$$

This is similar to the expression used by Corcos (15) for the cross spectral density of boundary layer pressure fluctuations. Here, however, it has been assumed that there is no decay of the eddy structures in the y_1 direction. The correlation in the y_1 direction is determined solely by the 'phase' term $e^{iK(y_1 - z_1)}$, where K is a 'hydrodynamic' wave number given by $K = \omega/U_c$, U_c being the convection speed of the eddies. This will be a valid assumption provided the eddies do not decay as they travel over distances of the order of an aperture diameter. Examination of Bull's (16) data for the longitudinal correlation between boundary layer pressure fluctuations indicates that this will be a fair assumption for Strouhal numbers based on hole diameters that are less than about 1.0. The correlation between velocity fluctuations along lines in the y_3 direction is determined by the function $F(y_3 - z_3)$. This function is assumed to be unity for zero separation distance $(y_3 - z_3)$ and to decay very rapidly for increasing separation such that the lateral correlation lengths are very much less than hole diameter. Bull's data for the

lateral correlation of boundary layer pressure fluctuation indicates that this will be a fair assumption for Strouhal numbers based on hole diameters that are greater than about 0.1. Further assuming that $S_v(y_k,\omega)$ is uniform over the surface of the aperture, one can write

$$S_Q(y_k,\omega) = \rho_o^2\omega^2 S_v(y_k,\omega) \int_{y_3}\int_{y_1}\int_{z_1}\int_{z_3} e^{iK(y_1-z_1)} F(y_3 - z_3)\, dz_3 dz_1 dy_1 dy_3. \tag{26}$$

Since the function $F(y_3 - z_3)$ decays rapidly, the result of the integration of the function with respect to z_3 can be considered independent of the limits of integration provided by the boundaries of the hole. Thus, defining a lateral correlation length ℓ as

$$\ell = \int_{z_3} F(y_3 - z_3)\, dz_3 , \tag{27}$$

then one has

$$S_Q(y_k,\omega) = \rho_o^2\omega^2 S_v(y_k,\omega)\, \ell \int_{y_3}\int_{y_1}\int_{z_1} e^{iK(y_1-z_1)}\, dz_1 dy_1 dy_3 . \tag{28}$$

For the integrations with respect to both y_1 and z_1, the limits of integration are from $-a\cos\alpha$ to $a\cos\alpha$ where a is the hole radius and α is as shown in Figure 3. Performing these two integrations yields

$$S_Q(y_k,\omega) = \rho_o^2\omega^2 S_v(y_k,\omega)\, \ell (4/K^2) \int_{y_3} \sin^2(Ka\cos\alpha)\, dy_3. \tag{29}$$

Putting $y_3 = a\sin\alpha$ and using the relation $2\sin^2 B = 1-\cos 2B$ enables the expression to be written as

$$S_Q(y_k,\omega) = \rho_o^2\omega^2 S_v(y_k,\omega)\, \ell a (4/K^2) \left[2 \int_0^{\pi/2} \tfrac{1}{2}\cos\alpha\, d\alpha - 2 \int_0^{\pi/2} \tfrac{1}{2}\cos\alpha\cos(2Ka\cos\alpha)\, d\alpha \right]. \tag{30}$$

The first integral has a value of unity. The second can be shown (17) to be equal to $(1-(\pi/2)H_1(2Ka))$ where H_1 is a Struve function of the first kind. Thus

$$S_Q(y_k,\omega) = \rho_o^2\omega^2 S_v(y_k,\omega)\, \ell a (2\pi/K^2) H_1(2Ka) . \tag{31}$$

Note that Ka can be written in terms of Strouhal number St based on hole diameter. Assuming the convection velocity U_c to be half the mean flow speed U_∞ at the outer edge of the boundary layer, one has $Ka = 2\pi(fd/U_\infty) = 2\pi(St)$. The function $H_1(2Ka)$ has been plotted against Strouhal number in Figure 4. Thus, the fairly realistic flow model used illustrates an inherent dependence of the source strength on the Strouhal number based on hole diameter.

2.4 Scaling Laws for the Radiated Sound Field

The scaling laws governing the sound produced by a given perforate screen can be deduced from the equivalent source model and the reflection coefficient of the screen. From equation (8) one has

$$|R|^2 = \left[1 + (4aN/k\cos\theta)^2\right]^{-1}. \qquad (32)$$

Figure 5 shows a plot of $|R|^2$ against the ratio $(4aN/k\cos\theta)$. From this it can be seen that, approximately,

$$|R|^2 \simeq (k\cos\theta/4aN)^2 \quad \text{for} \quad (4aN/k\cos\theta) > 2. \qquad (33)$$

The inequality can be written as $ka\cos\theta < (2\sigma/\pi)$, where $\sigma = N\pi a^2$ is the open area ratio of the screen. This approximation for $|R|^2$ will be valid for screens of high porosity at low frequencies and grazing incidence angles. This is the most likely form for perforate screens used in practice. For a 40% open area screen having 2 mm diameter holes, equation (33) will give a good approximation to the reflection coefficient for frequencies up to 14 kHz at normal incidence. For screens of this type the expression (33) can be used in equation (19) to give the spectral density of the sound field radiated by a single aperture:

$$S_p(x_k,\omega) = \frac{4}{(4\pi r)^2}\left[\frac{k\cos\theta}{4aN}\right]^2 S_Q(y_k,\omega). \qquad (34)$$

Now consider an area A of screen containing $\sigma A/\pi a^2$ holes. If one assumes that the quantities $S_Q(y_k,\omega)$ are all equal to each other for each aperture (i.e., $S_v(y_k,\omega)$ is uniform over the surface of each aperture) and that each aperture radiates sound independently, then the total mean square pressure will be given by adding the mean square pressures from each aperture. The fields from neighbouring holes will be uncorrelated unless the eddy scales are large compared to the distance between holes. This will be unlikely except at very low

tance to x_k from the centre of the scattering area is r_o, where r_o is much larger than the dimensions of the area, then the total mean square pressure can be written as

$$S_p(x_k,\omega) = \frac{Ak^2\cos^2\theta S_Q(y_k,\omega)}{64\sigma\pi r_o^2} . \qquad (35)$$

Equation (31) for $S_Q(y_k,\omega)$ can be substituted into this expression and the terms re-arranged to give

$$S_p(x_k,\omega) = \left[\frac{A}{64\sigma}\right]\left[\frac{\pi\rho_o\cos\theta}{c_o r_o}\right]^2\left[\frac{f\ell}{U_\infty}\right] S_v(y_k,\omega)\, U_\infty^4\, St\, H_1(4\pi St) . \qquad (36)$$

It has again been assumed that the eddy convection velocity U_c is always $(U_\infty/2)$ and $St = fd/U_\infty$. Now the radiated mean square pressure in a given bandwidth is given by

$$\overline{(p^2(x_k,t))}_{\Delta f} = \int_{\omega_1}^{\omega_2} S_p(x_k,\omega)\, d\omega . \qquad (37)$$

Also, the turbulence intensity $I_{\Delta f}$ in a given bandwidth can be defined as the ratio of the rms velocity fluctuation in a given bandwidth to the free stream velocity U_∞ at the outer edge of the boundary layer, such that

$$(I^2)_{\Delta f} = (1/U_\infty^2) \int_{\omega_1}^{\omega_2} S_v(y_k,\omega)\, d\omega . \qquad (38)$$

Provided the frequency dependent terms in equation (36) can be considered constant over the narrow bandwidth Δf considered, then the equation can be written as

$$\overline{(p^2(x_k,t))}_{\Delta f} = \left[\frac{A}{64\sigma}\right]\left[\frac{\pi\rho_o\cos\theta}{c_o r_o}\right]^2\left[\frac{f_c\ell}{U_\infty}\right] (I^2)_{\Delta f} U_\infty^6 St.H_1(4\pi St) . \qquad (39)$$

Here f_c is the centre frequency of the given band and the Strouhal number based on hole diameter is now defined as $St = f_c d/U_\infty$. The sound radiated by an area of perforated screen clearly follows a dipole-like dependence. The equivalent monopole source below the screen combines with the monopole above the screen to produce a sound field having a U_∞^6 velocity dependence and a directional peak normal to the screen surface. The dependence on the level of turbulence over the screen surface is self-evident. One of the most important consequences of the flow modelling used is the predicted Strouhal number dependence of the

scattered sound. The form of the function $H_1(4\pi St)$ indicates that the most efficient sound production occurs for Strouhal numbers based on hole diameter that are larger than about 0.25. This corresponds to "hydrodynamic wavelengths" that are less than twice the hole diameter. It thus transpires from the equivalent source model presented here that perforate screens used in practice will scatter a dipole type field, predominantly at frequencies produced by eddies of a smaller size than the screen apertures.

Now one can consider the sound produced by a perforated screen of low porosity. From Figure 5 it can be seen that approximately:

$$|R|^2 \simeq 1 \quad \text{for} \quad (4aN/k\cos\theta) < 1/2. \tag{40}$$

In terms of open area ratio, this inequality can be written $ka\cos\theta > (8\sigma/\pi)$. Screens of low porosity behave as perfectly reflecting surfaces at high frequencies and normal incidence angles. Notice, however, that the theory that has been used may not adequately describe the properties of low porosity screens. Since many holes are then required per acoustic wavelength, it is necessary that $k(\pi N)^{-\frac{1}{2}} << 1$ where $(\pi N)^{-\frac{1}{2}}$ is the typical distance between apertures. Since $\sigma = N\pi a^2$ in terms of open area ratio, one must have $ka << \sigma^{\frac{1}{2}}$. It is thus necessary to satisfy both $ka << \sigma^{\frac{1}{2}}$ and $ka\cos\theta > (8\sigma/\pi)$. This requires that $\sigma << (\pi^2/64)$ and may be possible for values of open area ratio that are of the order of one per cent. $[O(10^{-2})]$, depending on the strictness of the requirement that $ka << \sigma^{\frac{1}{2}}$. Assuming for the moment one can make the approximation $|R|^2 = 1$, one can deduce the mean square pressure radiated by a given area of low porosity screen by making the same assumptions that were used in the derivation of equation (39). The resulting expression is

$$\overline{(p^2(x_k,t))}_{\Delta f} = (\sigma A)\left[\frac{\rho_o}{2\pi r_o}\right]^2\left[\frac{f\ell}{U_\infty}\right](I^2)_{\Delta f}U_\infty^4\left[\frac{H_1(4\pi St)}{St}\right]. \tag{41}$$

This predicts a remarkably efficient production of sound by turbulence. The radiated field clearly follows a monopole type dependence. Only the equivalent monopole source above the screen surface contributes to the net radiation. It is unusual for screens having $\sigma = O(10^{-2})$ to be used in practice and this form of radiation is not likely to be encountered.

The dipole type radiation predicted in equation (39) thus seems the most relevant to practical applications. The scaling laws and

Strouhal number dependence predicted can be tested experimentally and an estimate of the unknown factors in the equation made. Essentially, one must test both the basic equivalent source model and the assumed form for the equivalent source strength. An experimental technique for determining the sound produced by liner facings will be described in the next section.

3. EXPERIMENTAL PROCEDURE

3.1 The Design of the Experimental Rig and the Perforates Tested

The theory developed in the preceding section is based on the analysis of the problem of an infinite perforated screen exposed to turbulence. In order to test the scaling laws and Strouhal number dependence predicted by the theory, an experimental method had to be chosen that would as far as possible simulate the ideal conditions upon which the model was based. A good test of the model would be the measurement of the sound radiated when an air jet impinges on a perforated screen having dimensions much larger than the wavelength of interest. However, it was also important to have a uniform mean flow over the part of the screen exposed to turbulence in order that the Strouhal numbers based on hole diameter would all be equal to each other for each of the scattering apertures. The test rig used provided a compromise between these two requirements. A flat nozzle jet exit was used to deliver air from a high pressure supply such that the velocity profile of the jet was uniform over a large fraction of the width of the nozzle. An outline drawing of the test rig used is shown in Figure 6. The jet pipe consisted of a constant area duct, which transformed from dimensions of 65 x 65 mm to 128 x 33 mm in a length of 745 mm.

The outlet of the jet was directed onto a baffle board measuring 1.22 x 1.58 m. A slot measuring 70 x 250 mm was cut in the board at the jet outlet. This enabled specimens of either perforated metal screen or honeycomb duct liner to be placed in the slot such that the surface of a given specimen was flush with the baffle board surface. The size of the slot was chosen such that the mean flow velocity (measured at the edge of the boundary layer over the specimen surface) was as far as possible uniform over the entire area of the specimen. Thus, strictly speaking, the "infinite" perforated screen was only simulated for acoustic wavelengths much less than the specimen size. This corresponds to

frequencies much greater than about 2 kHz. Since most of the sound scattered by the specimens tested was at frequencies above 2 kHz and the tests were performed in a room that was anechoic at these frequencies, the experimental rig used gave a fair simulation of the model conditions. It also provided a convenient and practical means of measuring the noise generated by different forms of liner facings.

The perforate screens tested were intended to be representative of those used for duct liner facings in practice. The three screens used were each made from 1 mm thick mild steel sheet containing a uniform distribution of circular perforations. The diameters of the holes in the screens were 1.75 mm, 3.5 mm and 4.8 mm. The corresponding open area ratios of the screens were 0.24, 0.43 and 0.39, respectively. When one of the screens was tested it was supported by its ends in the slot such that the space beneath the screen remained open.

Three honeycomb liner specimens were also tested. All three consisted of 1 mm thick aluminium sheet with a uniform distribution of circular perforations over a honeycomb cell backing. Two of the liner specimens had a honeycomb backing with 21 mm depth and a cell volume of 4.3 cm^3. These had facings with perforations of 1.0 mm and 2.4 mm diameter and open area ratios of 0.07 and 0.09, respectively. The third liner specimen had a 35 mm honeycomb backing depth with a cell volume of 10.3 cm^3. The facing on this specimen had perforations of 1.6 mm diameter with an open area ratio of 0.23. The honeycomb liner specimens were supported in the slot by metal brackets below the baffle board. A full specification of all these test specimens is given in Figure 7.

3.2 Aerodynamic Measurements

A pitot tube placed in the centre of a section of the upstream ductwork was used to give a reference value of the mean flow velocity for all the measurements undertaken. The boundary layer over the surface of the baffle board at the jet exit was first investigated. A section of flat board was placed in the baffle board slot so that the jet impinged on a continuous flat surface. Vertical traverses were made with a pitot tube at positions along the jet centre-line at distances of 50 mm, 150 mm and 250 mm from the jet exit. The results of these traverses for a mean velocity of 28 m/s at the upstream pitot are shown in Figure 8. The boundary layer has an approximate thickness of between 20 mm and 10 mm as the jet expands in the downstream direction.

The mean velocity profile over the board surface was also investigated. Mean velocities were measured with a pitot tube at a distance of 20 mm above the board surface. Measurements were made at intervals of 20 mm across the width of the jet along traverses at distances 0, 50, 100, 150, 200 and 250 mm from the jet exit. This series of measurements was repeated at three mean velocities of 20, 28 and 40 m/s measured at the upstream pitot. The mean velocity profile at 40 m/s upstream velocity is shown in Figure 9. The mean velocity was found to be uniform to within 10% over the entire test specimen area at each test velocity. It was also found that the mean velocity at the upstream pitot gave a good estimate of the average velocity over the specimen surface. For subsequent experiments, the mean velocity at the upstream pitot was assumed to give the average mean velocity over the specimen surface to within 5%.

The turbulence intensity in the boundary layer over the test specimens was measured by using an I.S.V.R. constant temperature hot wire anemometer. The frequency response of the instrument was flat up to 20 kHz. The output of the lineariser was calibrated against a pitot tube. Further details of the instrument can be found in reference (18). The signal from the anemometer was processed using a B & K 6% Bandwidth Analyser, type 2107. A comparison was first made between the overall turbulence levels in the flow above the flat board surface and the perforated screen having a 4.8 mm hole diameter. Figure 10 shows the overall rms velocity fluctuation normalised on the upstream mean flow speed for these two cases. These measurements were taken with the hot wire held perpendicular to the mean flow direction such that contributions from "streamwise" and "vertical" velocity components were sensed. The turbulence levels with the perforate screen in place are higher than those above the flat board surface, since the perforate screen allowed a degree of inflow through the apertures with the consequent persistence of turbulence near the surface.

The spectral distribution of the turbulence near the surface of the screen having 4.8 mm diameter apertures was also measured. The hot wire was held across the diameter of a hole in the centre of the specimen at a distance of 1 mm above the specimen surface. The wire was again perpendicular to the direction of flow. The 6% bandwidth analysis of the velocity signal at mean flow speeds of 15, 20, 30, 40 and 50 m/s is shown in Figure 11. This experiment was repeated using the perforated screen with 1.75 mm diameter apertures. The spectra of the turbulent velocity fluctuations above the surface of the two screens were found

to be identical. The turbulence was thus unaffected by the screen hole diameter, presumably because the screens were of a relatively high porosity.

3.3 Acoustic Measurements

Each of the six specimens was tested over a range of velocities between 20 and 50 m/s. The far field radiation was measured by using a 12 mm condenser microphone (B & K Type 4132). This was positioned vertically above the test specimens at a distance of 0.3 m. (See Figure 6). This distance was as close as possible to the specimens without entering the near field of the source. This enabled the difference between the radiated sound and the background noise to be maximised. Background noise was a problem. It was generated both by the air jet itself and in the air supply system in the laboratory. Thus, for each test on a perforate or liner specimen in the background noise was measured by replacing the given specimen by a flat wooden board and repeating the test under otherwise identical conditions.

The microphone signal was processed by using a B & K 6% Bandwidth Analyser, type 2107. Some typical measured spectra from perforate screen and honeycomb liner specimens are shown in Figures 12 and 13, respectively. The background noise spectra for both cases are also shown in the figures. The sound radiated from the perforate surface was usually sufficiently far above the background noise for a simple correction to be made to take account of any background noise contribution. The error involved in the measurement of the far field sound pressure level was thus within 1 dB.

The directivity of the radiation from the perforated screen having 4.8 mm hole diameter was measured at a velocity of 30 m/s. Measurements of sound pressure level were made on a hemispherical arc about the jet axis at a radius of 0.3 m. Sound pressure levels were measured in the 1/3 octave bands having centre frequencies of 4 kHz, 8 kHz and 16 kHz. The measurements were corrected for background noise contributions. The results are shown in Figure 14.

4. ANALYSIS AND DISCUSSION OF RESULTS

4.1 Results for Unbacked Perforated Screens

The scaling laws predicted from theory show that the mean square sound pressure in a given bandwidth radiated by a particular screen will be dependent on the intensity of the turbulence that impinges on the

apertures of the screen. In order to test the predicted scaling laws, a generalised spectrum of the measured turbulence incident on a given aperture was first evaluated. The 6% bandwidth velocity spectra measured as described above were normalised on the mean flow velocity U_∞ and plotted against $(f_c\delta/U_\infty)$. The boundary layer thickness δ was assumed to be 10 mm. It was also assumed that the turbulence intensity in the "streamwise" and "vertical" component directions were equal and 3 dB was subtracted from the measured levels to give the intensity of only the vertical component of the turbulence. The resulting collapse of data is shown in Figure 15. The turbulence intensity $(I(St))_{6\%}$ at a given Strouhal number based on hole diameter could then be found from the value of $(I(f_c\delta/U_\infty))_{6\%}$ at a value of Strouhal number based on boundary layer thickness given by $(f_c\delta/U_\infty) = (St)(\delta/d)$.

The measured 6% bandwidth sound pressure levels for each test specimen under each test condition were then normalised on the basis of the predicted scaling laws. Since the specimens tested were all of relatively high porosity (see Figure 7), then the scaling laws predicted by equation (39) were used for the collapse of experimental data. A function L(St) was evaluated for comparison with the predicted Strouhal number dependence. This function is given by

$$10\log_{10}L(St) = SPL_{6\%} + 10\log_{10}\sigma - 20\log_{10}(I(St))_{6\%} - 60\log_{10}U_\infty - 10\log_{10}(St) - 10\log_{10}\left[\frac{A}{64}\right]\left[\frac{\pi\rho_o\cos\theta}{c_o r_o p_{ref}}\right]^2 . \quad (42)$$

The area A of the test specimens was 0.0175 m^2, the distance r_o from the field microphone to the specimen centre was 0.3 m, and the polar angle θ was zero. Note that the non-dimensional lateral correlation length $(f_c\ell/U_\infty)$ is unknown, and has been omitted from the normalisation. For any given Strouhal number it will be a constant depending on the boundary layer flow under consideration, but not on the hole size or flow speed. Hence the results for different hole sizes and flow speeds should collapse.

The plots of L(St) for the three specimens tested are shown in Figures 16, 17 and 18. The Strouhal number dependence of the radiated noise is almost exactly as predicted by the theory. Most of the noise radiated occurs at frequencies corresponding to Strouhal numbers greater than 0.1. At frequencies lower than this, any radiated noise was indistinguishable from the background levels. A peak in the spectra

occurs around St ≈ 0.25 for all the specimens tested and further "bumps" in the spectra occur at progressively higher Strouhal numbers. Spectral peaks predicted by the theory at St ≈ 0.75, 1.25, etc., are not convincingly reproduced by the experimental results. This is probably due to non-uniformity of the convection velocity of the eddies shed in the holes. This is likely to have a dependence on frequency and will not be perfectly uniform for all the specimen apertures. Nevertheless, the simplified assumption that U_c is always $U_\infty/2$ produces an excellent description of the radiated noise spectra.

A comparison of all the measured data is shown in Figure 19 and a comparison with the theoretically predicted Strouhal number dependence is shown in Figure 20. It can be seen that the overall collapse of data is excellent. There are some significant differences between the theory and the results for the specimens with larger hole sizes at low Strouhal numbers. The larger the hole, the less sound is scattered. This is due to the hole size becoming comparable with the boundary layer thickness, which determines the scale of the largest eddies. At low Strouhal numbers based on a value of hole size that is roughly equal to boundary layer thickness, there will be fewer large scale eddies present to produce sound at these frequencies. The specimen having the smallest hole size (where $d \ll \delta$) thus shows the best agreement with theory.

The theoretical curve of $H_1(4\pi St)$ in Figure 21 has been drawn on the assumption of a value of the non-dimensional lateral correlation length of 10^{-2}. Thus, the results indicate that

$$L(St) \simeq \left[\frac{f_c \ell}{U_\infty}\right] H_1(4\pi St) = 10^{-2} H_1(4\pi St). \qquad (43)$$

This value of $(f_c \ell/U_\infty)$ is perhaps a little low. Boundary layer pressure measurements (16) indicate a value of $O(10^{-1})$. Nevertheless, the result here is not unreasonable considering the simplified nature of the flow model used.

The collapse of the experimental data gives a convincing justification of the scaling laws predicted by the equivalent source model. The dipole nature of the radiated sound is well established, although the directivity patterns measured (see Figure 14) did not show a convincing dipole behaviour at all frequencies. This is due to the presence of the baffle board. At the higher frequencies (8 kHz, 16 kHz) a dipole directivity pattern began to be observed, since the wavelength of the radiated sound was becoming sufficiently small compared to the size of

the slot in which the specimens were supported. Certainly, when the baffle board was removed and a perforate specimen held in the jet flow, a distinct dipole directivity could be detected.

4.2 Sound Generated by Perforated Facings on Dissipative Duct Lining Materials

Having established the magnitude and spectral distribution of noise scattered by flow over perforated screens, one can attempt to estimate the net sound scattered by a perforated facing used in a length of lined duct. Obviously, a perforated screen on a fibrous backing material constitutes a rather different situation to that dealt with so far. Firstly, the presence of the backing material may decrease the fluctuating mass flow driven through the screen apertures. This will depend on the degree of contact between the backing material and the screen and how far the material protrudes into the apertures. An estimate of the magnitude of this effect can be made by estimating the reduction in the turbulence intensity over the holes that is produced. Secondly, the backing material will alter the acoustic properties of the screen surface. In general, at the high frequencies of interest there will be an increase in the resistive impedance of the screen. However, this may not significantly alter the radiation mechanism of the noise source, provided the backing material is fairly porous.

An effect that may be substantial is the absorption of the generated sound as it travels down the duct. An attempt can be made to estimate this effect by considering a continuous absorption and generation of sound down a duct. This has been treated by Ingard (8). Firstly, it can be assumed that the surface radiates sound as it does in a free field. This will be valid provided there is a high density of duct modes at the frequency considered. From equation (42) one can write the far field mean square pressure in a given bandwidth in terms of the measured function L(St):

$$\overline{(p^2(x_k,t))}_{\Delta f} = \left[\frac{A}{64\sigma}\right]\left[\frac{\pi\rho_o\cos^2\theta}{r_o c_o}\right]^2 (I^2(St))_{\Delta f} U_\infty^6 \, St \, L(St). \qquad (44)$$

The sound power radiated per unit area of screen in a given bandwidth can thus be found by integrating $\overline{(p^2(x_k,t))}_{\Delta f}/\rho_o c_o A$ over a hemisphere of radius r_o. Since the integral of $\cos^2\theta$ over the hemisphere is given by $(2/3)\pi r_o^2$, the sound power radiated per unit area becomes

$$(W_A)_{\Delta f} = \left[\frac{\rho_o \pi^3}{96\sigma c_o^3}\right] (I^2(St))_{\Delta f} U_\infty^6 \, St \, L(St). \qquad (45)$$

Now consider an element of liner facing of width dy_1 and height h. The sound power generated in a given bandwidth by this element will be $(W_A)_{\Delta f} h dy_1$. With any effects of flow on the propagation of sound in the duct neglected, half the power from the element will be radiated upstream and half downstream. As the sound propagates down the duct it will be attenuated by the lining. If β is the energy absorption coefficient per unit length of the duct, the power generated by the element that emerges from the end of a lined duct section of length b will be

$$\delta W_{\Delta f} = (\tfrac{1}{2})(W_A)_{\Delta f} h dy_1 e^{-\beta(b-y_1)}. \qquad (46)$$

If the lining starts at $y_1 = 0$, the total power emerging from the lined section will be the sum of all the elemental powers:

$$(W)_{\Delta f} = \int_0^b \tfrac{1}{2}(W_A)_{\Delta f} h e^{-\beta(b-y_1)} dy_1 = \left[\frac{(W_A)_{\Delta f} h}{2\beta}\right](1 - e^{-\beta b}). \qquad (47)$$

Thus, in terms of the measured function L(St), the net sound power generated by one facing of height h and length b of a lined duct having an attenuation coefficient β is

$$(W)_{\Delta f} = \frac{h}{\beta}(1 - e^{-\beta b})\left[\frac{\rho_o \pi^3}{192\sigma c_o^3}\right](I^2(St))_{\Delta f} U_\infty^6 (St) L(St). \qquad (48)$$

Note that for large values of β this result is independent of the length of the lining. Equation (48) has been used to estimate the net sound power radiated in 1/3 octaves by a 1.2 m splitter attenuator section. The linings consisted of glass fibre faced with perforated screens of 43% open area ratio and 3.5 mm hole diameter. The spectrum of the turbulence intensity impinging on the liner facing was assumed to be exactly the same as measured in the free jet test rig. A comparison of the self-noise levels predicted on this basis with the levels measured as described in Reference (19) is shown in Figure 21. The values of β used in the calculation were of the order of magnitude measured by Phelps (20) for this attenuator configuration. It can be seen that the predicted spectrum levels are in good agreement with those measured. It is also worth noting that the same attenuator section with a cloth facing had a considerably lower self-noise spectrum. Levels generated by perforate facings used in the I.S.V.R. anechoic wind tunnel were also successfully predicted by using the free jet test rig data (21). A cloth facing placed over the perforate facings in this case was effective

in producing a similar reduction of the noise generated.

Thus the results indicate that equation (48) can be effectively used to give good engineering estimates of the net noise produced by a length of lined duct faced with a perforated screen. Use of the free jet test rig data probably, if anything, will overestimate the noise produced, since the turbulence levels represent an upper limit to those that would be expected in a ducted situation.

4.3 Sound Generated by Perforated Facings on a Honeycomb Backing

The results for the honeycomb liner specimens tested are shown in Figures 22-24. These have been collapsed by evaluating ($SPL_{6\%} - 60 \log_{10} U_\infty$) and plotting the results against Strouhal number based on hole diameter. In general, the sound produced by the liner specimens was of the same order of magnitude as the sound produced by the open backed perforates, except for the presence of strong resonant peaks in the spectra. These peaks occurred at particular frequencies, which could be identified with various resonant frequencies of the honeycomb cavities. For example, the liner specimen with a 2.4 mm hole diameter (see Figure 22) showed spectral peaks at roughly 1.8 kHz, 8.5 kHz and 16 kHz. These frequencies can be identified with the cavity Helmholtz resonance and the first two longitudinal "open pipe" resonances of the cavity depth, respectively.

The peaks are produced by a flow excited resonance phenomenon. This only occurs at Strouhal numbers greater than about 0.1 and this implies that eddies of a size smaller than the diameter of the hole somehow interact with the motion produced in the perforate apertures by the cavity resonances. The flow becomes coupled to the resonance and a large amount of narrow band sound is radiated. This phenomenon has also been found to occur when the flow in the apertures becomes coupled to duct modes near their cut-on frequency. For a fuller discussion of this process, the reader is referred to References (2) and (3). The dependence of the amplitudes of level produced on parameters such as the damping ratio of the resonance involved has yet to be firmly established. However, it has been shown by Bolton (22) that peak amplitudes will tend to occur at Strouhal numbers ($f_r d/U_\infty$) of roughly 0.25, 0.75, 1.25, etc., where f_r is the resonant frequency considered. These values correspond to the "edgetone stages" found to occur (4), when discrete frequency noise is produced by flow over the perforated walls of transonic wind tunnels. It is worth noting that these values of Strouhal number

correspond to the maximum values of net mass flow produced by the passage of eddies across the perforate apertures.

Although the level of understanding of the phenomenon is, at this stage, still very elementary, it is unlikely that a flow excited resonance phenomenon will occur for Strouhal numbers less than about 0.1. Thus, where f_r is the frequency of any "strong" resonance present in the application considered, then no exceptionally large levels will be expected, provided

$$f_r < (0.1\ U_\infty)/d. \tag{49}$$

This inequality is likely to hold in general for high speeds, small holes and large duct widths. In such cases, a fairly reasonable order of magnitude estimate of the net sound generated can be made using equation (48). This will give an engineering estimate of the "base level" of noise scattered by honeycomb liners which, from the experimental results, is of a similar order of magnitude to the sound generated by the perforate screens with no backing.

5. CONCLUSIONS

The source of noise generated by flow over perforated screens used as duct liner facings has been modelled on a basis suggested by Ffowcs Williams' theoretical analysis of the problem for a particular screen geometry (7). The equivalent source of sound has been modelled as two equal and opposite monopole sources situated immediately above and below the screen at each aperture position. The strength of the monopole sources is determined exactly by the mass flow driven through the aperture by the hydrodynamic field. The radiation properties of the monopoles are determined by the acoustic properties of the screen. A fairly realistic flow model has been used to express the strength of the monopole sources in terms of the turbulent flow over the aperture.

Measurement of the sound generated by perforated facings used in practice has confirmed the predictions of the equivalent source model, even though the Ffowcs Williams' analysis is not applicable to the perforate geometries studied, according to the assumptions inherent in his model. The measured values are consistent in both magnitude and spectral distribution with the noise levels predicted. The dipole type scaling laws governing the sound scattered from high porosity screens are firmly established. The two equivalent monopoles when situated

above and below a relatively transparent screen combine to give a net dipole field. A dipole type equivalent source distribution could have been used to model the sound generated by porous screens. After all, the fluctuating momentum of the mass flow driven through the apertures must be balanced by an equivalent fluctuating force on the solid surfaces of a screen. However, the equivalent source formulation used has produced a very useful description of the sound field generated.

The inherent dependence of the sound generated on Strouhal number based on hole diameter has been made clear by both the equivalent source model and the experimental results. From an engineering standpoint, this is one of the most important results of the analysis. Liners used in high speed applications (such as aero engines) will tend to be operating at low Strouhal numbers. Thus, little sound will be generated at the frequencies of interest. Liners in lower speed applications (such as ventilation systems) will tend to operate at high Strouhal numbers and more sound will be generated at frequencies of interest. The Strouhal number dependence predicted also indicates that most sound is generated by eddies of a scale smaller than the aperture size. This indicates that the fundamental mechanism of the sound generation process may be related to the interaction of vorticity shed in the apertures with the surrounding aperture edges, even though on an equivalent source basis the source can be successfully modelled in terms of the net mass flow through the aperture.

By considering the absorption of facing generated noise by the liner, it has been found that the experimentally measured values of the sound generated can be used to give good estimates of the net sound produced by flow over a lined duct facing. The application of a cloth facing over a perforate facing has been found to give useful reductions in the level of noise generated. The cloth acts to prevent the shedding of eddies in the screen apertures.

The level of noise generated by honeycomb liners indicates that the noise is of the same order of magnitude and spectral distribution of the noise generated by unbacked perforates, but with spectral peaks associated with flow excited resonance phenomena. Coupling of vortex shedding in a perforate aperture with a particular acoustic resonance of frequency f_r is unlikely to occur, provided $f_r < (0.1\ U_\infty/d)$. In such cases, it is probable that a good estimate of the noise generated will be made by treating the situation as a perforate facing with a dissipative backing.

REFERENCES

(1) F. MECHEL 1960 Acustica 10, 133-148. Schalldampfung und Schallverstarking in Luftströmungen durch Absorbierend Ausgekuidete Kanäle.

(2) C.Y. TSUI and G.A. FLANDRO 1977 Journal of Sound and Vibration 50, 315-331. Self induced sound generation by flow over perforated duct liners.

(3) A.B. BAUER and R.L. CHAPKIS 1977 Journal of Aircraft 14, 157-160. Noise generated by boundary layer interaction with perforated acoustic liners.

(4) G.F. McCANLESS and J.R. BOONE 1974 Journal of the Acoustical Society of America 56, 1501-1510. Noise reduction in transonic wind tunnels.

(5) M.O. VARNER 1975 AIAA Journal 13, 1417-1418. Noise generation in transonic tunnels.

(6) N.S. DOUGHERTY, C.F. ANDERSON and R.L. PARKER 1976 AIAA Paper No. 76-50. An experimental study on suppression of edgetones from perforated wind tunnel walls.

(7) J.E. FFOWCS WILLIAMS 1972 Journal of Fluid Mechanics 51, 737-749. The acoustics of turbulence near sound absorbent liners.

(8) U. INGARD 1959 Journal of the Acoustical Society of America 31, 1202-1212. Attenuation and regeneration of sound in ducts and jet diffusers.

(9) C.L. MORFEY 1969 Journal of Sound and Vibration 9, 357-366. Acoustic properties of openings at low frequencies.

(10) LORD RAYLEIGH 1878 The Theory of Sound (Vol. II). New York: Dover Publications, Second Edition, 1945 re-issue.

(11) U. INGARD 1953 Journal of the Acoustical Society of America 25, 1037-1062. On the theory and design of acoustic resonators.

(12) V.S. NESTEROV 1959 Soviet Physics Acoustics 5, 451-455 (translation). Conductivity of a group of holes.

(13) F.G. LEPPINGTON and H. LEVINE 1973 Journal of Fluid Mechanics 61, 109-127. Reflection and transmission at a plane screen with periodically arranged circular perforation.

(14) M.E. DELANEY and E.N. BASLEY 1970 Journal of Sound and Vibration 13, 269-279. Monopole radiation in the presence of an absorbing plane.

(15) G.M. CORCOS 1963 Journal of the Acoustical Society of America 35, 192-199. Resolution of pressure in turbulence.

(16) M.K. BULL, J.F. WILBY and D.R. BLACKMAN 1963 University of Southampton A.A.S.U. Report No. 243. Wall pressure fluctuations in boundary layer flow and response of simple structures to random pressure fields.

(17) N.W. McCLACHLAN 1955 Bessel Functions for Engineers, 2nd Edition, Ch. 4, p. 77. Clarendon Press: Oxford, England.

(18) P.O.A.L. DAVIES and J. MASON 1974 I.S.V.R. Technical Report No. 66. The I.S.V.R. constant temperature hot wire anemometer.

(19) P.A. NELSON 1978 Sound Attenuators Ltd. Report No. TRC102. Rectangular attenuator self noise.

(20) G.B. PHELPS 1978 M.Sc. Thesis, University of Bath. A practical measurement of sound attenuation in lined ducts.

(21) B.L. PRITCHARD 1979 Ph.D. Thesis, University of Southampton. Noise sources in an airflow.

(22) J.S. BOLTON 1976 M.Sc. Thesis, University of Southampton. The excitation of an acoustic resonator by pipe flow.

APPENDIX 1. LIST OF SYMBOLS

a	aperture radius
A	area of perforated screen
b	length of dissipative lining on duct wall
c_o	ambient speed of sound
C	aperture conductivity
d	aperture diameter
f	frequency
f_r	resonant frequency
f_c	centre frequency of a measurement band
F	function defining degree of lateral correlation (in a direction perpendicular to the flow) of aperture normal velocity fluctuations
h	height of dissipative lining on duct wall
H_1	Struve function of the first kind
i	square root of minus one
I	turbulence intensity
k	acoustic wavenumber
ℓ	lateral correlation length (in a direction perpendicular to the flow) of aperture normal velocity fluctuations
L	measured function of Strouhal number
M	Mach number
N	number of perforations per unit area of screen
p	acoustic pressure
p_{ref}	reference pressure
q	acoustic volume flow
Q	acoustic source strength (rate of change of mass addition)
Q_h	equivalent acoustic source strength produced by hydrodynamic velocity fluctuations
r	distance of observation point from the centre of an aperture
r_o	distance of observation point from the centre of the radiating area of perforated screen

R	screen reflection coefficient
S_p	spectral density of radiated pressure
S_Q	source strength spectral density
S_v	spectral density of normal velocity fluctuations over an aperture
S_{vv}	cross spectral density of normal velocity fluctuations over an aperture
St	Strouhal number based on aperture diameter
SPL	sound pressure level
T	averaging time
u	acoustic particle velocity fluctuations
U_c	eddy convection velocity
U_∞	mean flow velocity at outer edge of boundary layer
v	hydrodynamic velocity fluctuations
W	acoustic power
x_k, y_k, z_k	cartesian coordinates, where the subscript k can take the value 1, 2 or 3
Z	acoustic impedance
α	angular coordinate position on aperture surface
β	energy absorption coefficient per unit length of dissipative duct wall lining
θ	polar angle measured relative to normal to the perforated screen surface
λ	acoustic wavelength
ρ_o	ambient air density
σ	open area ratio of perforated screen
ω	radian frequency

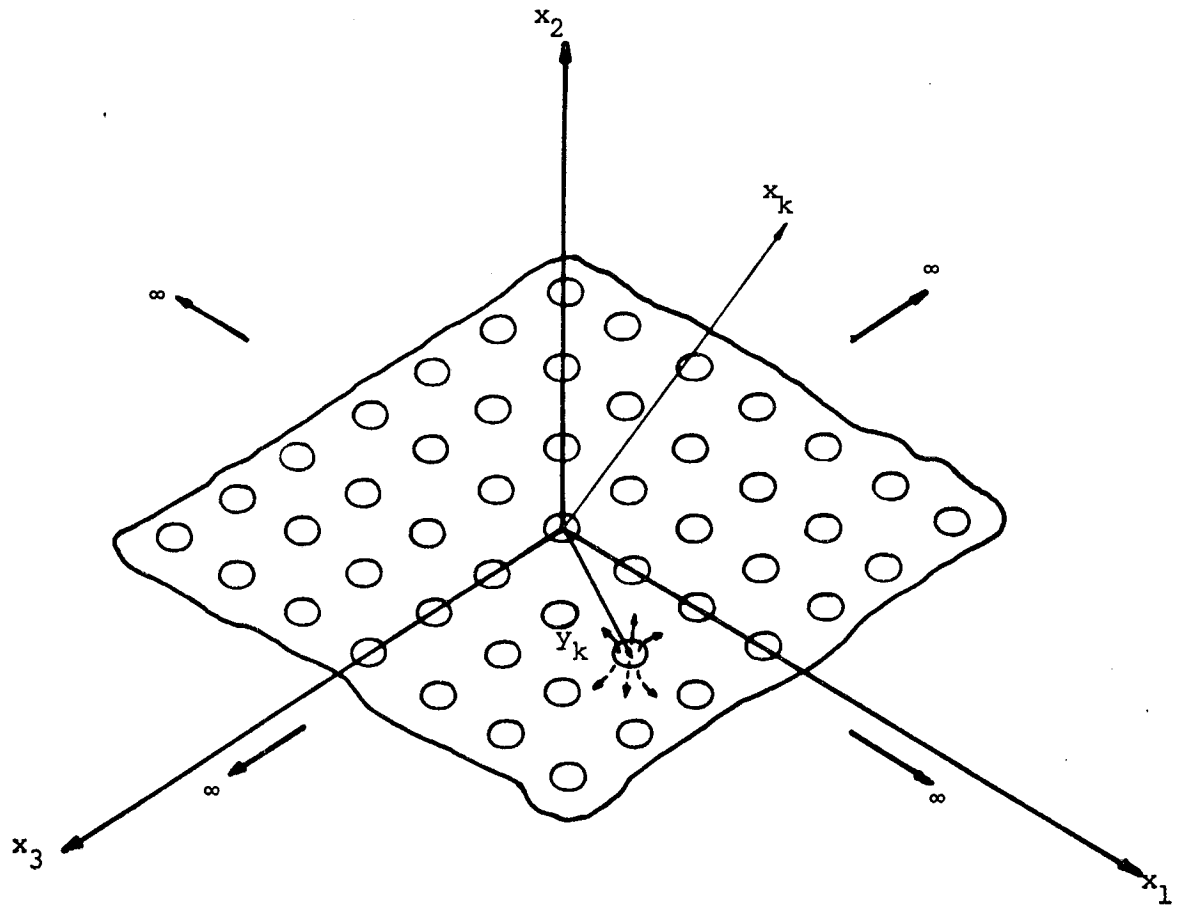

FIGURE 1. The coordinate system for the infinite perforated screen model

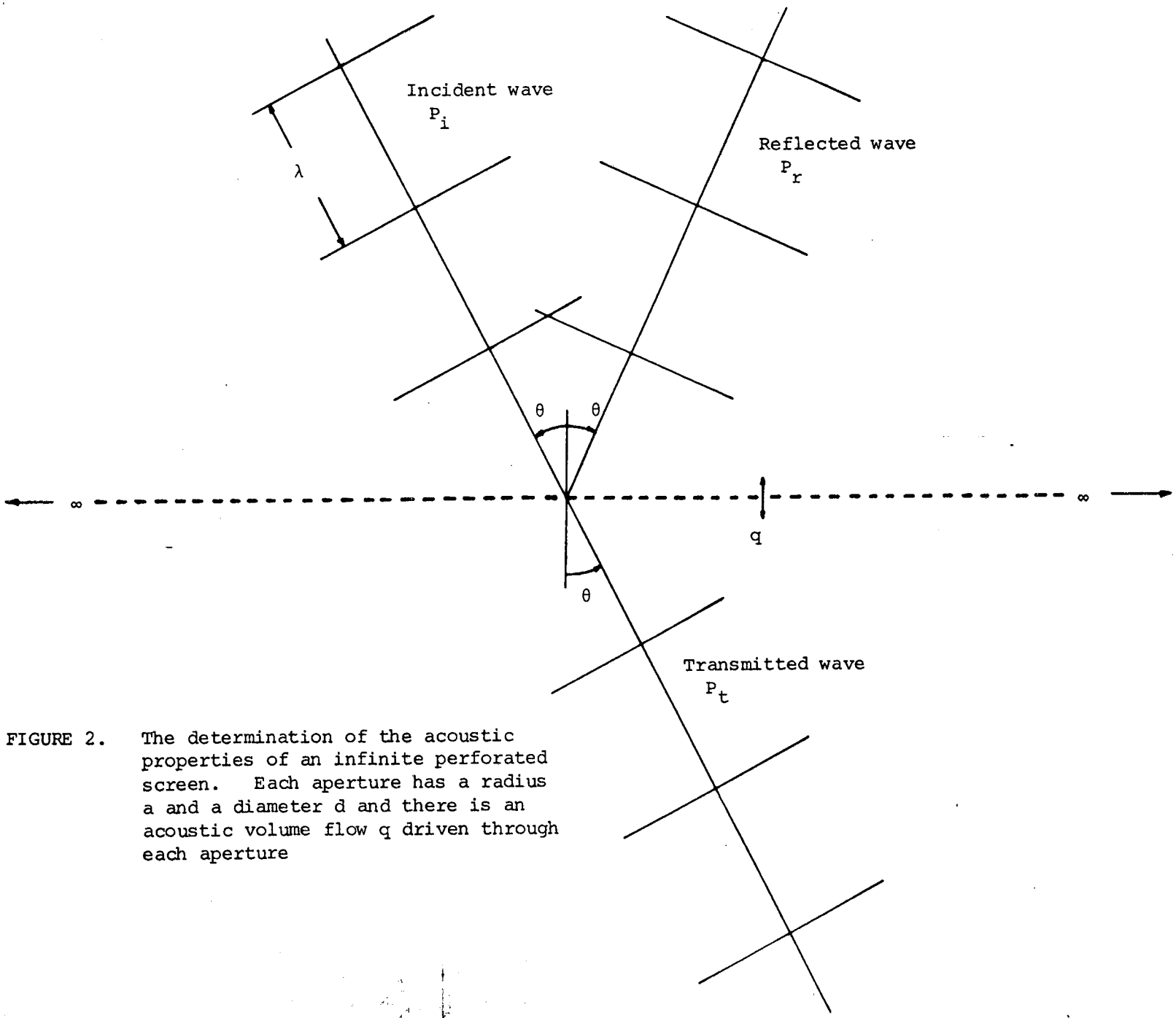

FIGURE 2. The determination of the acoustic properties of an infinite perforated screen. Each aperture has a radius a and a diameter d and there is an acoustic volume flow q driven through each aperture

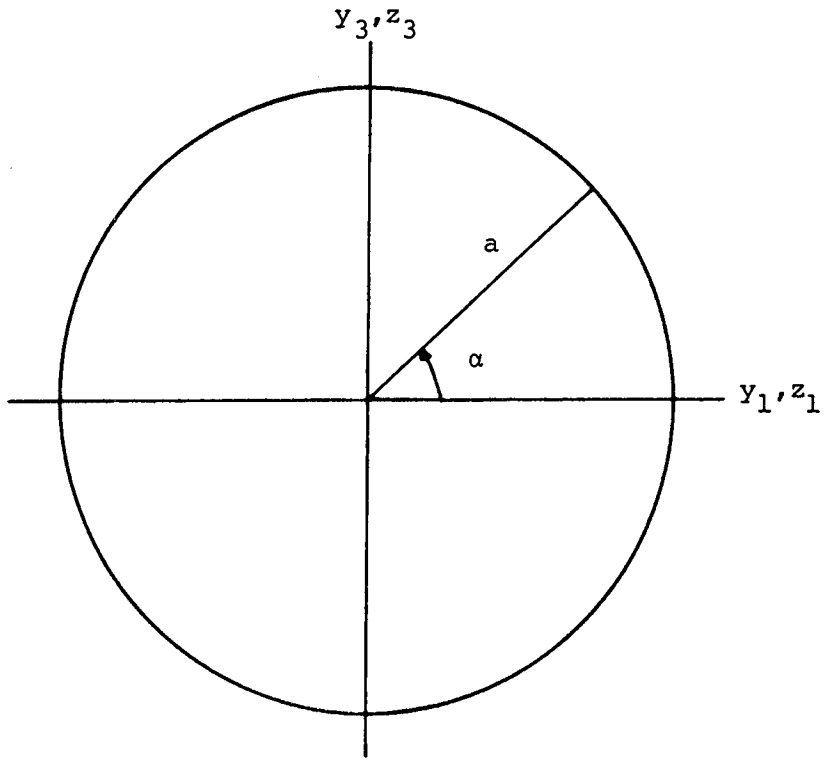

FIGURE 3. The coordinate system for the evaluation of $S_Q(y_k, \omega)$ for a given aperture

FIGURE 4. A plot of the function $H_1(2Ka)$ against Strouhal number based on hole diameter

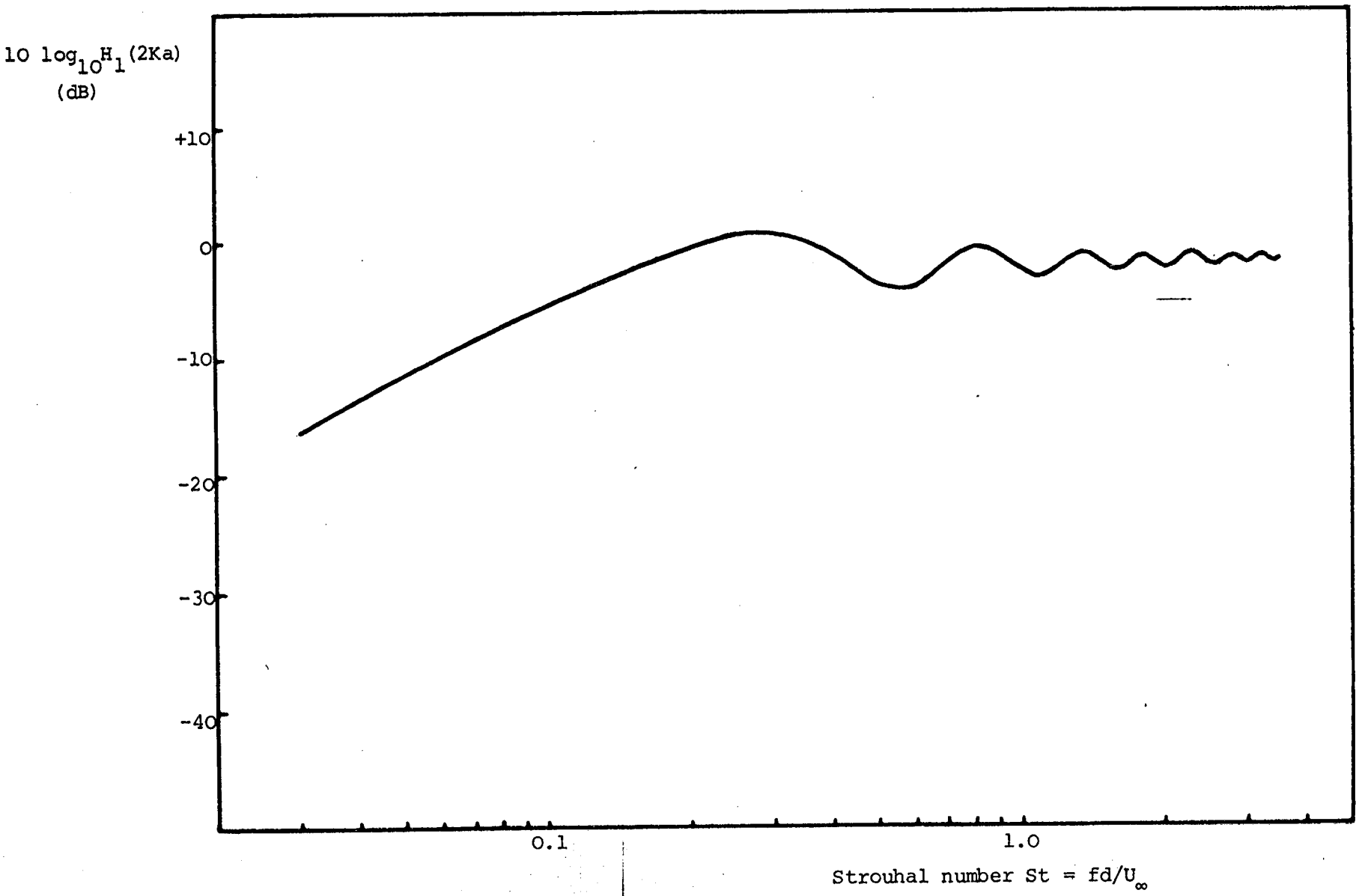

FIGURE 5. The screen reflection coefficient as a function of the ratio $(4aN/k\cos\theta)$

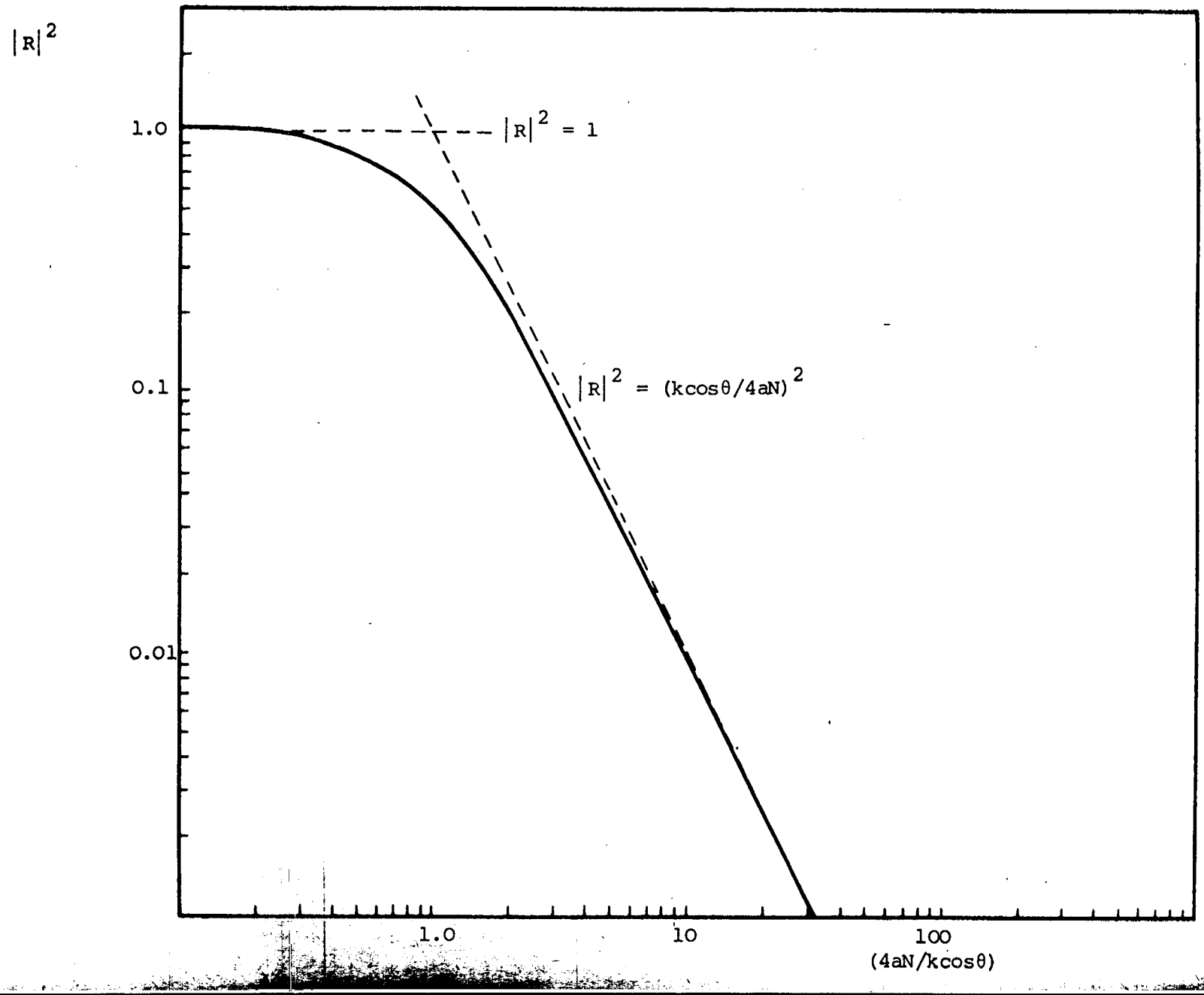

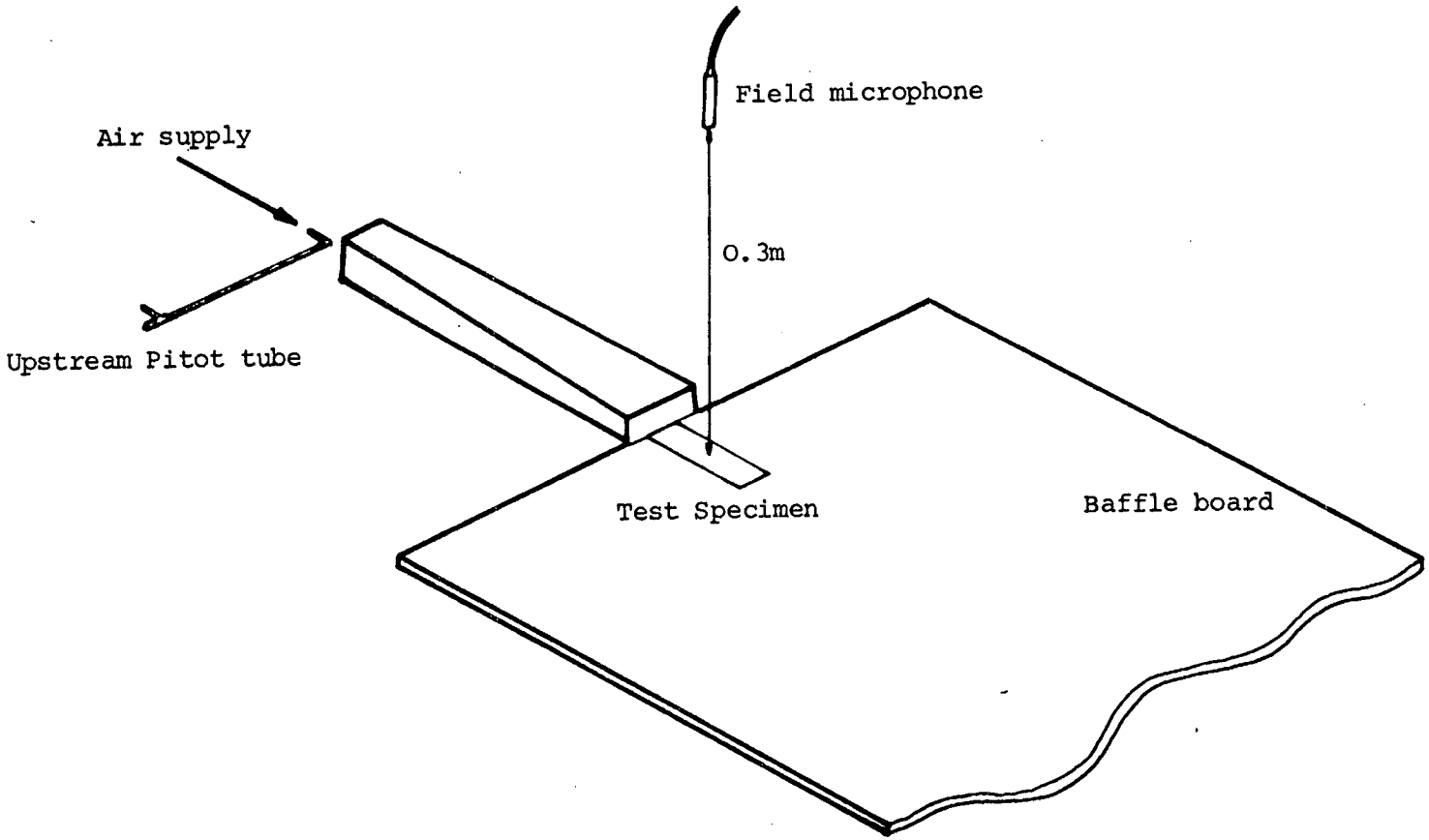

FIGURE 6. A schematic drawing of the perforate noise test rig

(a) Perforate Screens

Hole diameter d (mm)	Number of holes/unit area N (per m^2)	Open area ratio
4.5	2,170	0.39
3.5	4,470	0.43
1.75	10,060	0.24

(b) Honeycomb Liners

Hole diameter d (mm)	Number of holes/unit area N (per m^2)	Open area ratio	Cavity depth (mm)	Cavity volume (mm^3)
2.4	18,800	0.09	21	4,305
1.6	115,650	0.23	35	10,300
1.0	82,500	0.07	21	4,305

FIGURE 7. The specification of the perforate screen and honeycomb liner test specimens

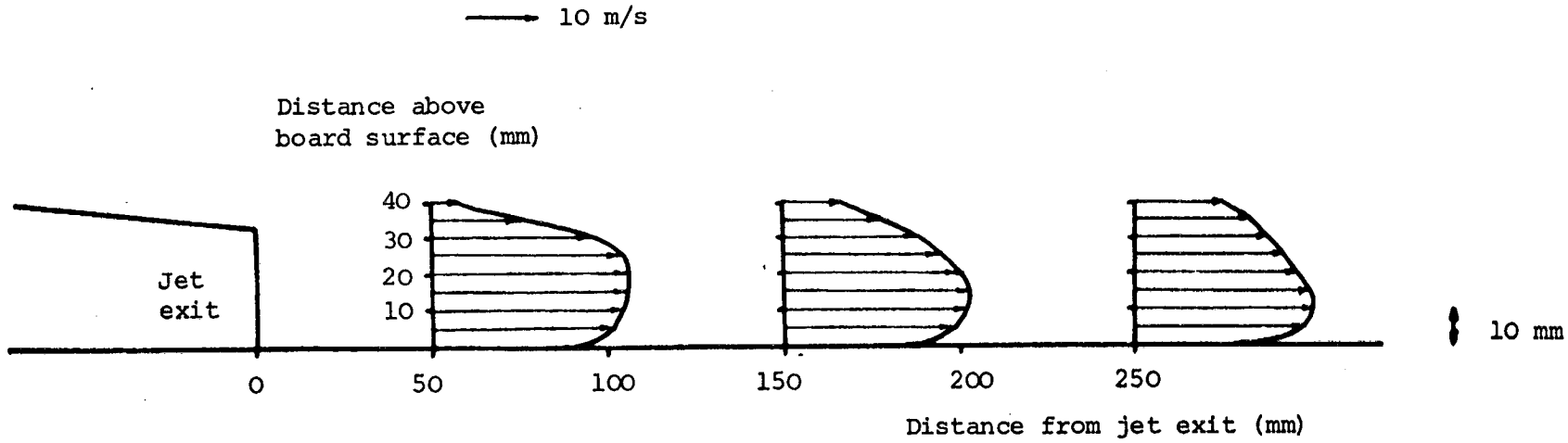

FIGURE 8. The boundary layer velocity profile above the flat board surface (upstream pitot reading 28 m/s)

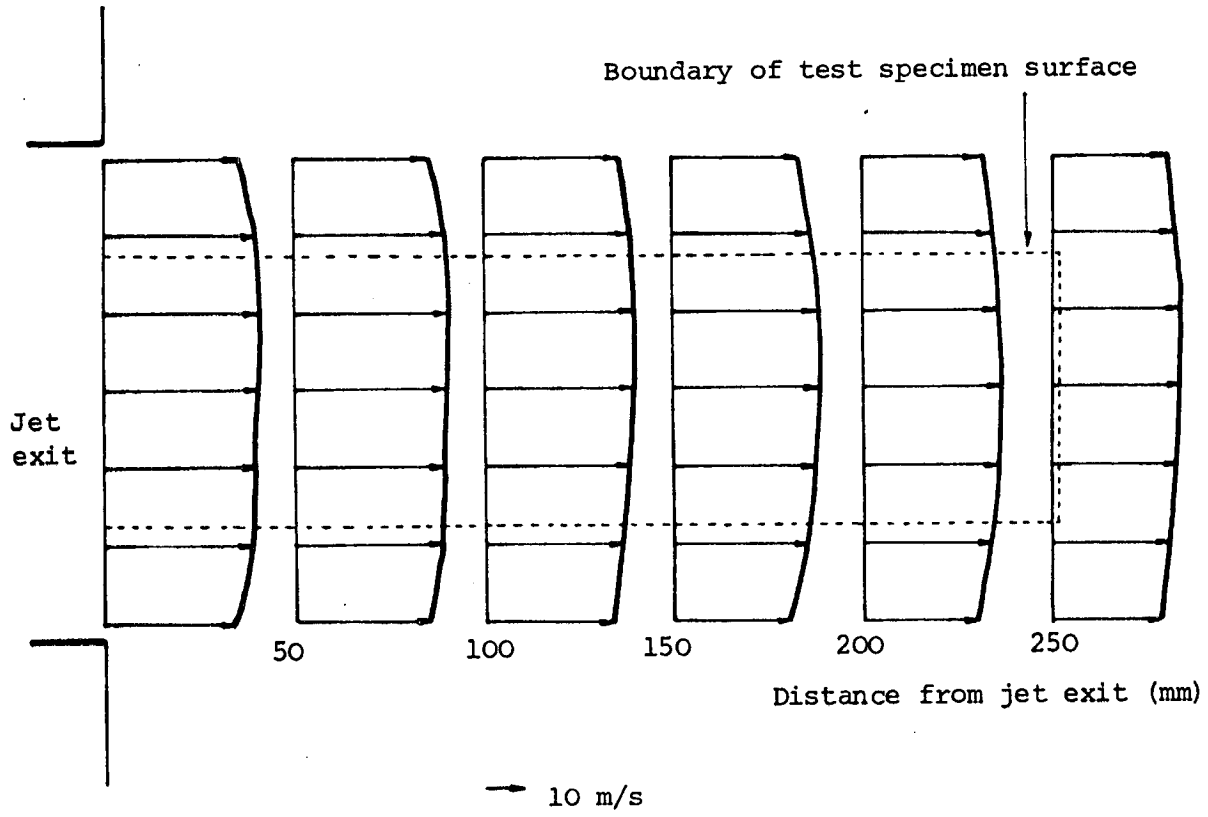

FIGURE 9. Mean flow velocity profiles at 20 mm above the flat board surface (upstream pitot reading 40 m/s)

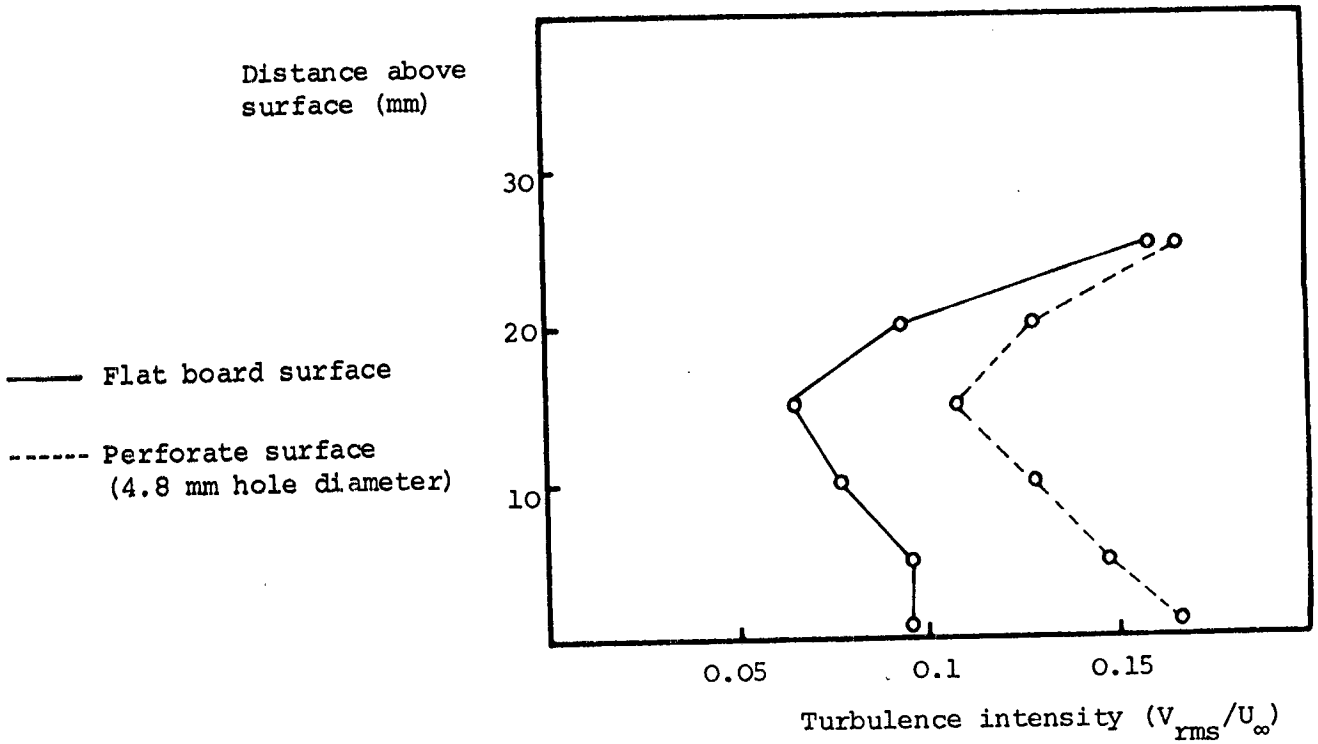

FIGURE 10. The turbulence intensity in the boundary layer, given by the ratio of the total rms velocity signal to the free stream velocity. (Note the total measured rms velocity signal includes contributions from both "vertical" and "streamwise" fluctuating velocity components)

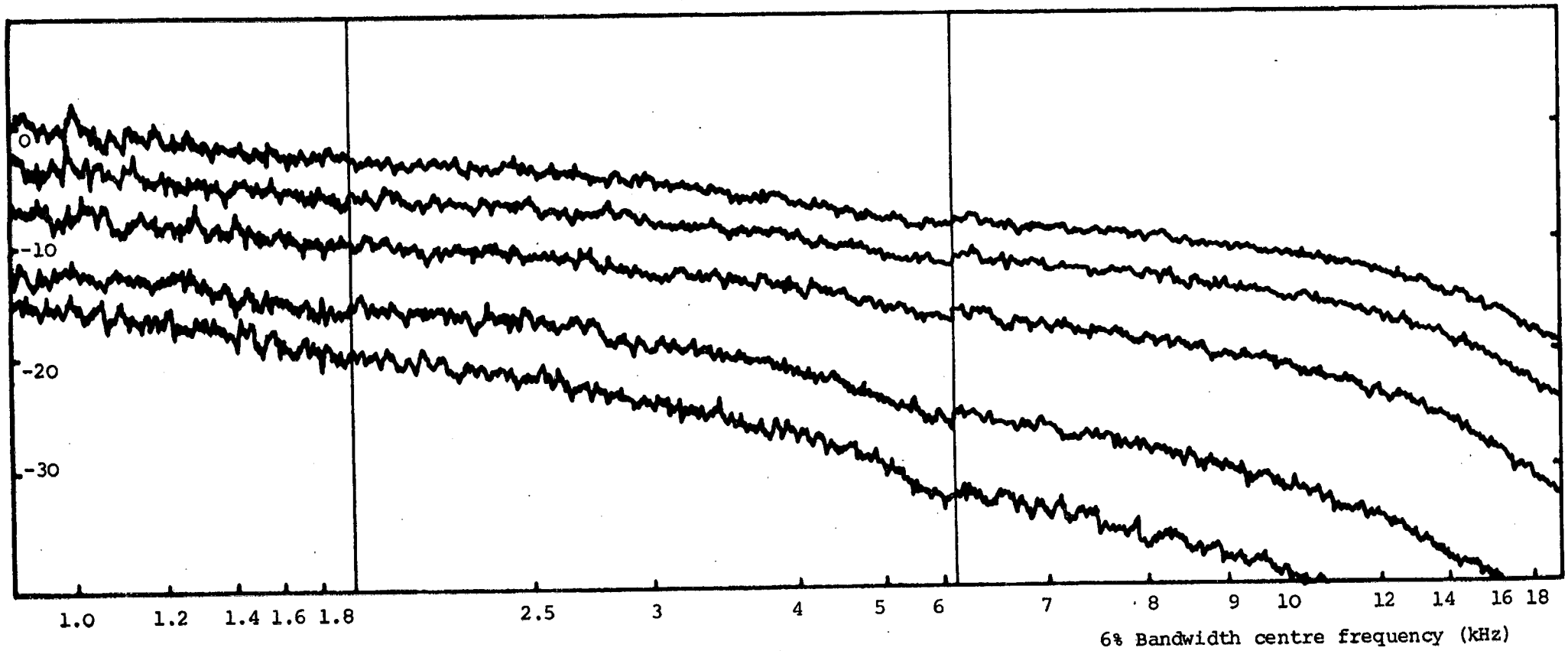

FIGURE 11. A 6% bandwidth analysis of the turbulent velocity fluctuations measured 1 mm above an open backed perforate screen test specimen (d = 4.8, σ = 0.39) at mean velocities U_∞ = 15, 20, 30, 40, 50 m/s

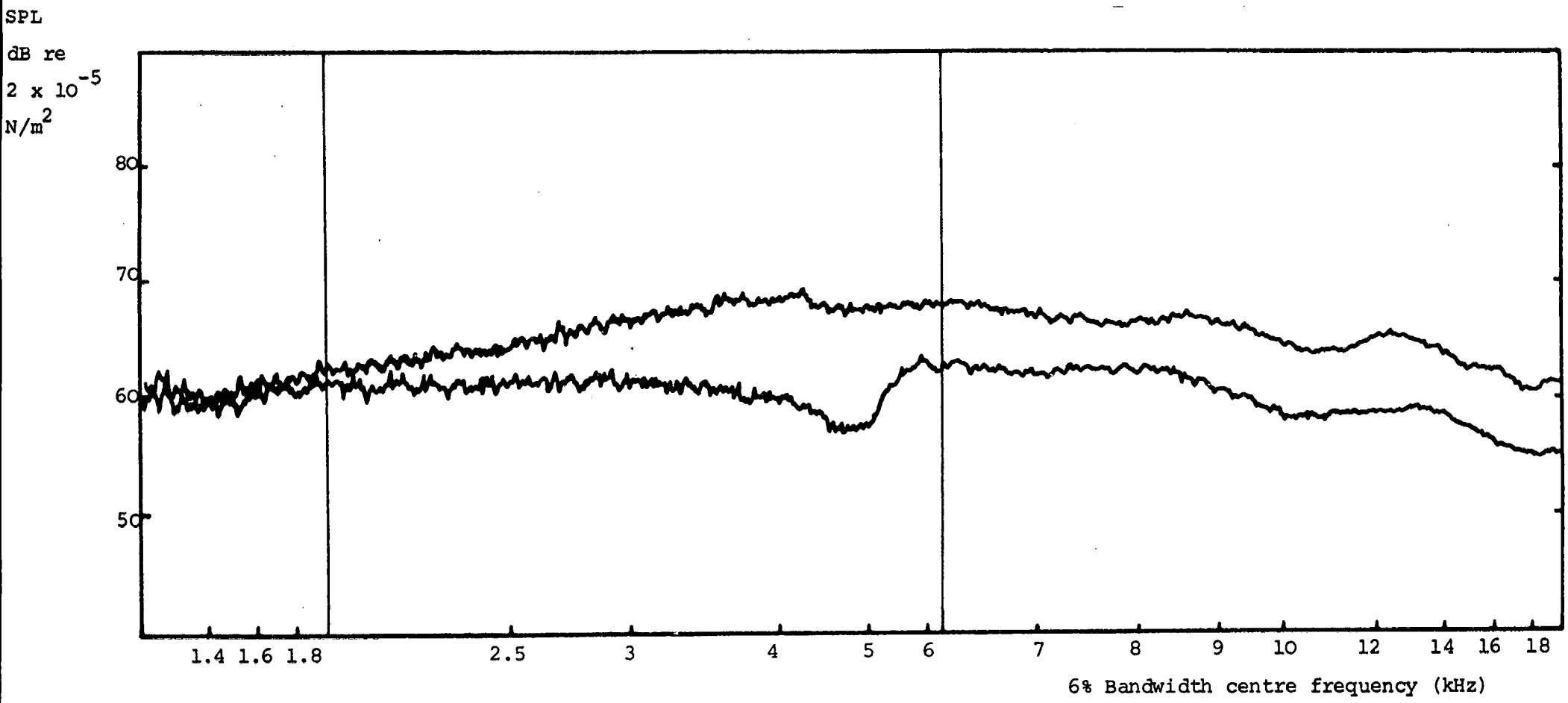

FIGURE 12. A typical 6% bandwidth analysis of the SPL measured 0.3 m above an open backed perforate screen test specimen with d = 4.8 mm, σ = 0.39, U_∞ = 50 m/s. (The lower trace shows the background noise)

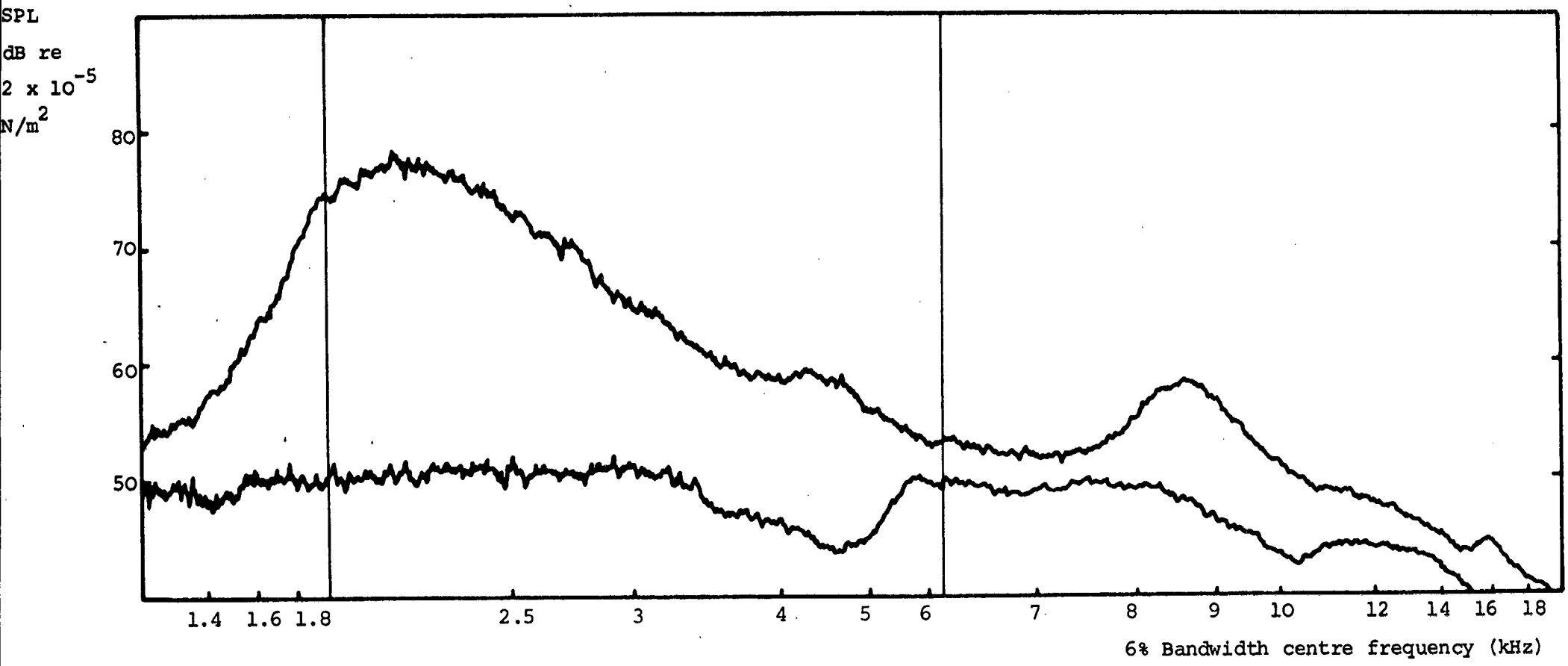

FIGURE 13. A typical 6% bandwidth analysis of the SPL measured 0.3 m above a honeycomb liner test specimen with $d = 2.4$ mm, $\sigma = 0.09$, $U_\infty = 30$ m/s. (The lower trace shows the background noise)

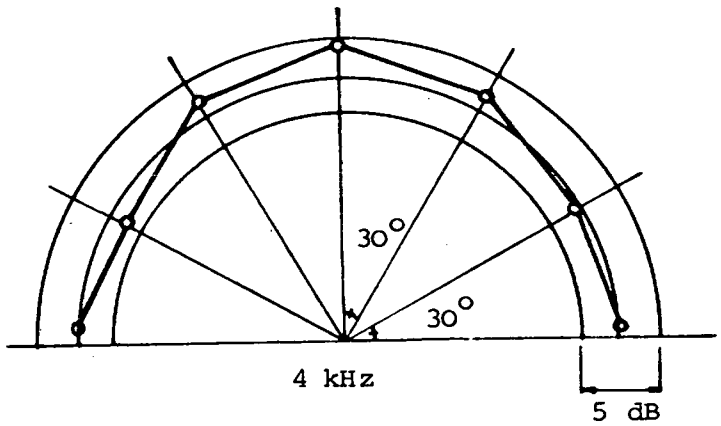

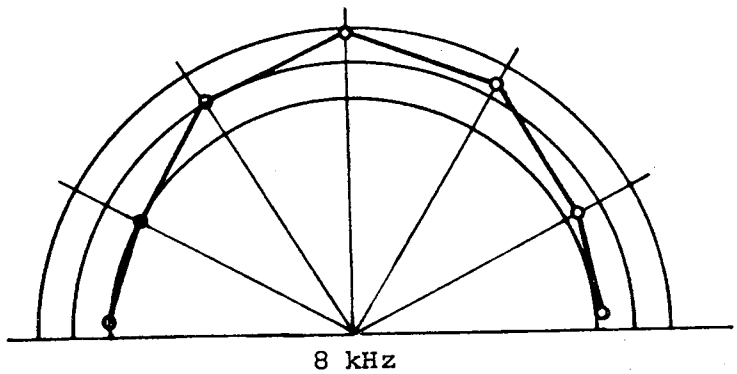

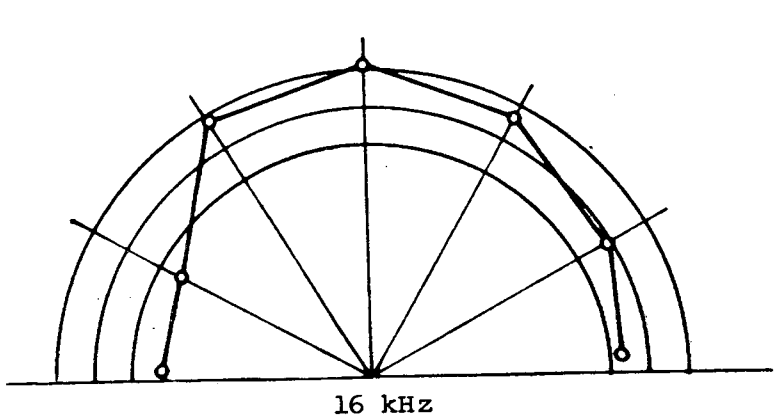

FIGURE 14. Measured Directivity Patterns

A microphone traverse was taken in an arc about the jet axis. Levels were measured in 1/3 octave bands.

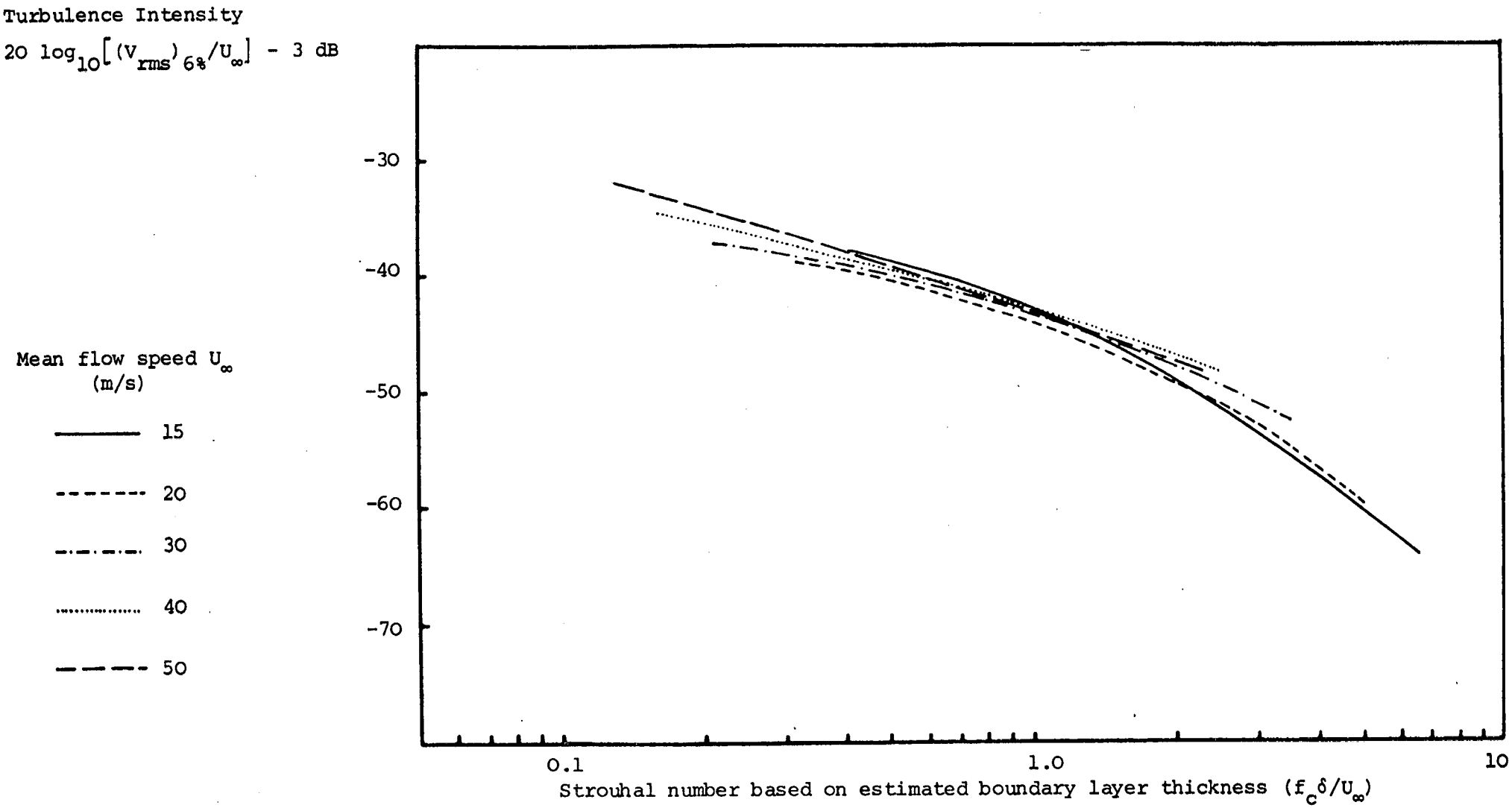

FIGURE 15. The generalised 6% bandwidth turbulence intensity spectrum measured 1 mm above 4.8 mm hole diameter perforate surface.

FIGURE 16. Normalised 6% bandwidth results for the perforate specimen with hole diameter d = 4.8 mm and open area ratio σ = 0.39

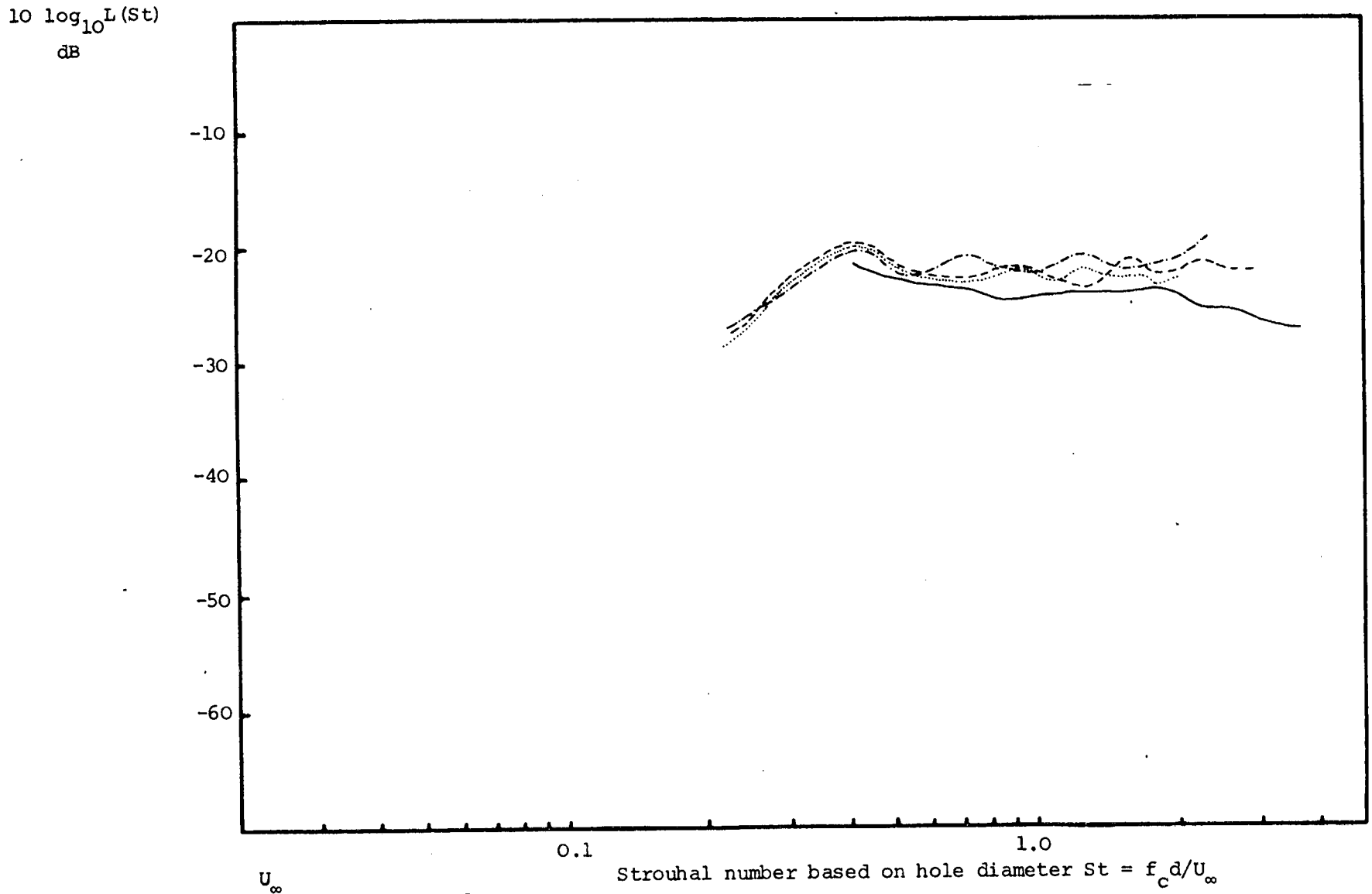

FIGURE 17. Normalised 6% bandwidth results for the perforate specimen with hole diameter d = 3.5 mm and open area ratio σ = 0.43

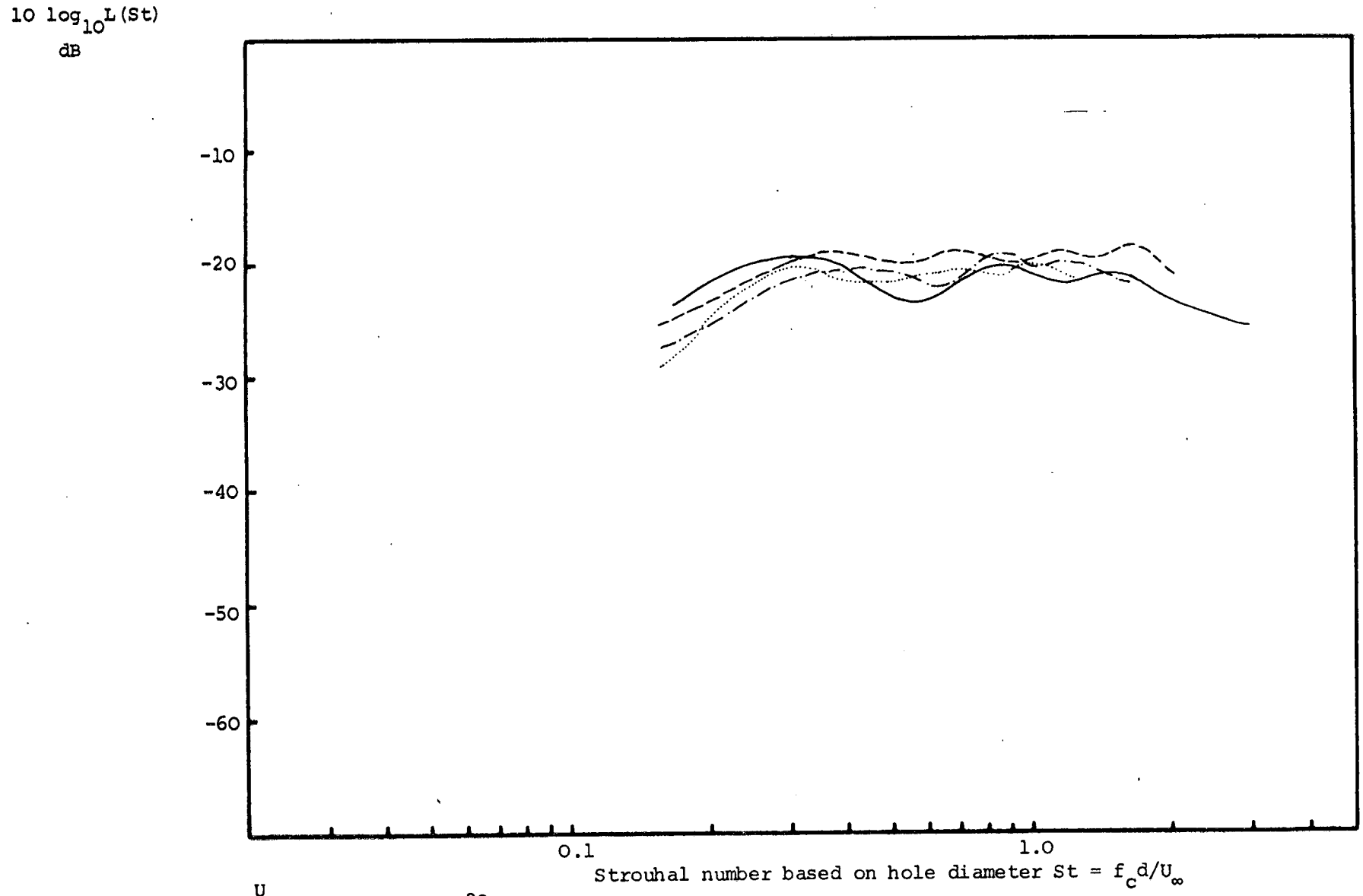

FIGURE 18. Normalised 6% bandwidth results for the perforate specimen with hole diameter d = 1.75 mm and open area ratio σ = 0.24

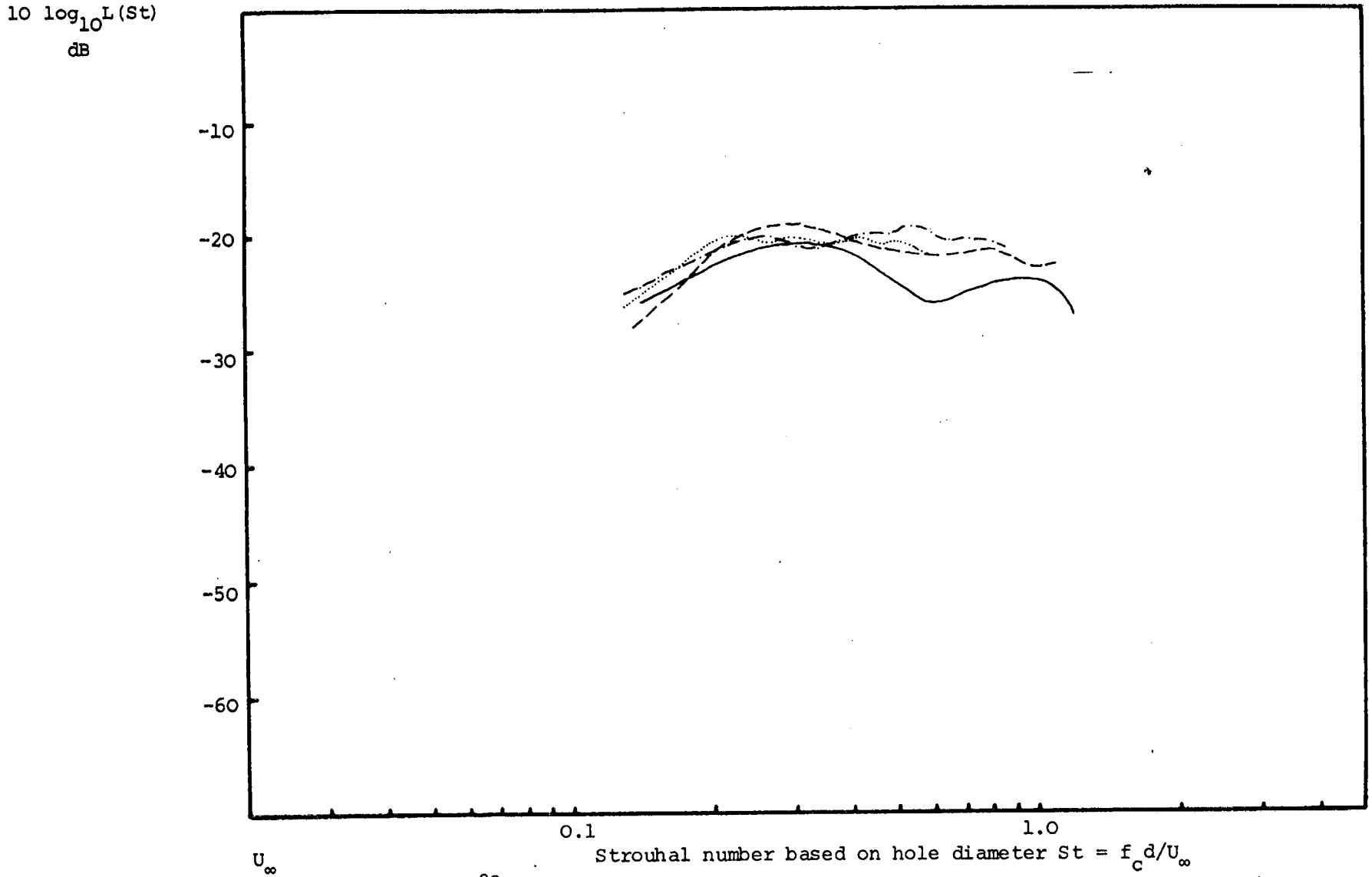

FIGURE 19. The overall collapse of normalised 6% bandwidth results for all the perforate specimens tested

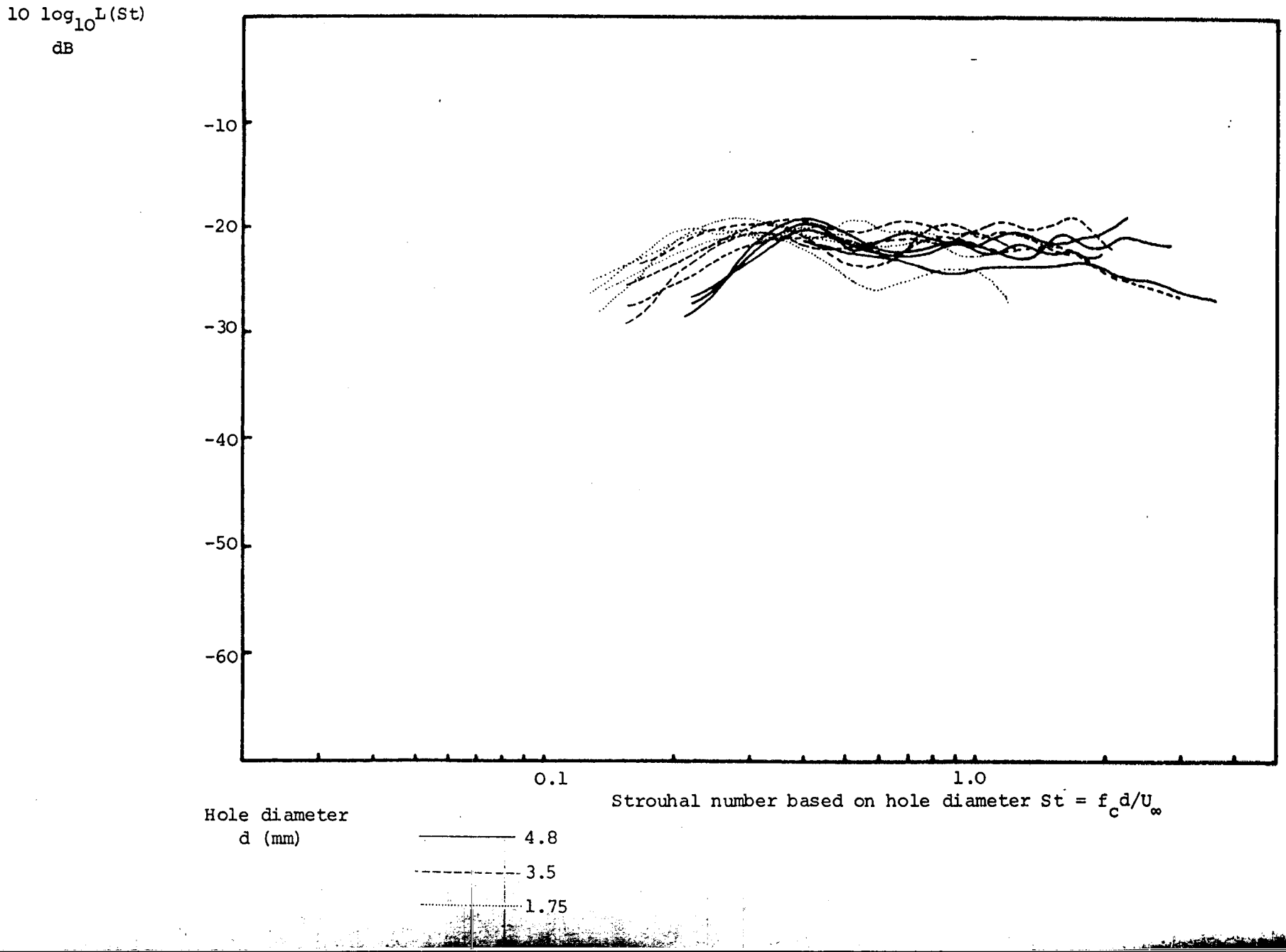

FIGURE 20. Comparison of normalised 6% bandwidth results for all perforate specimens with predicted Strouhal number dependence

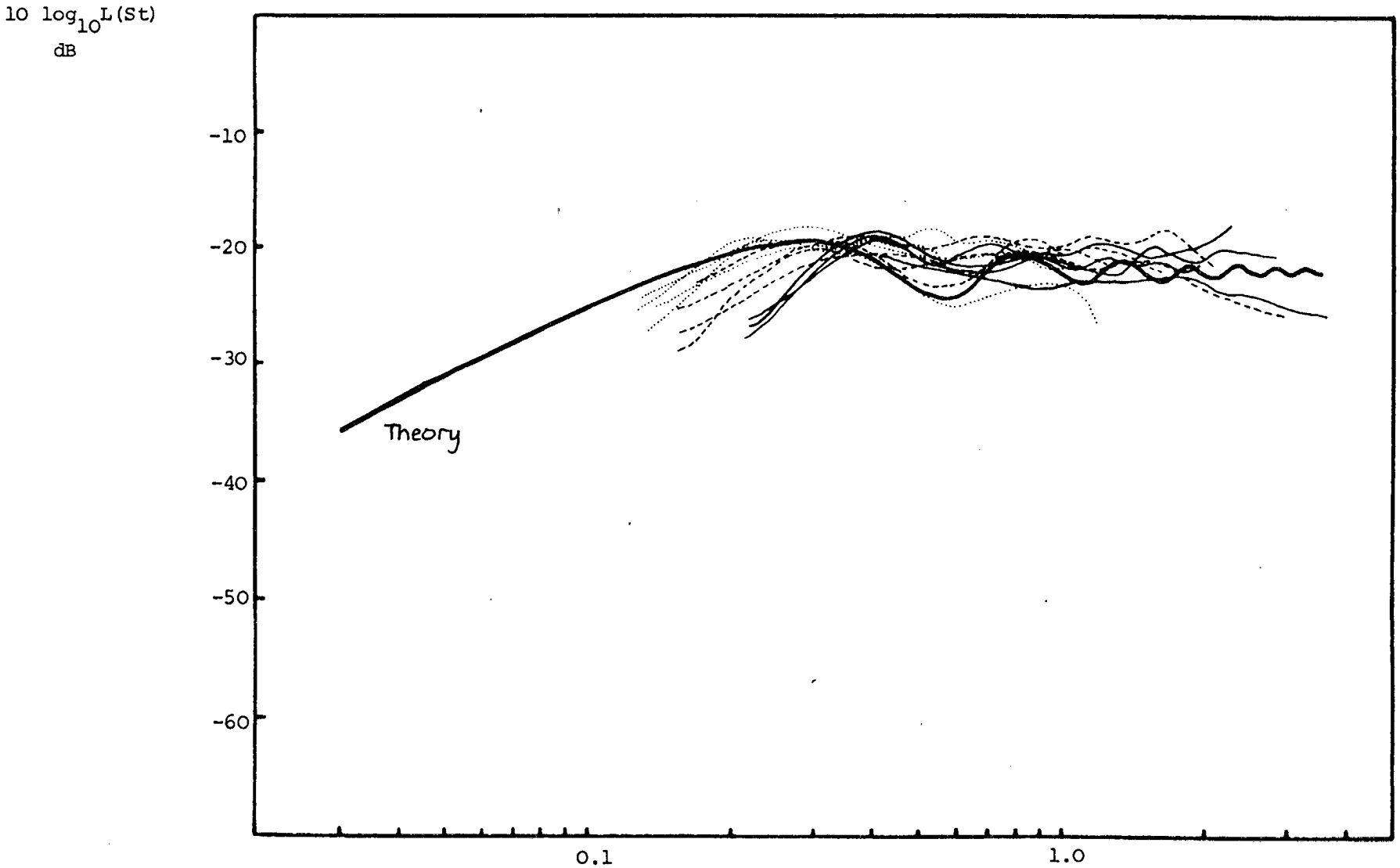

FIGURE 21. A comparison of measured and predicted 1/3 octave band sound power levels generated by flow over a dissipative liner perforate facing

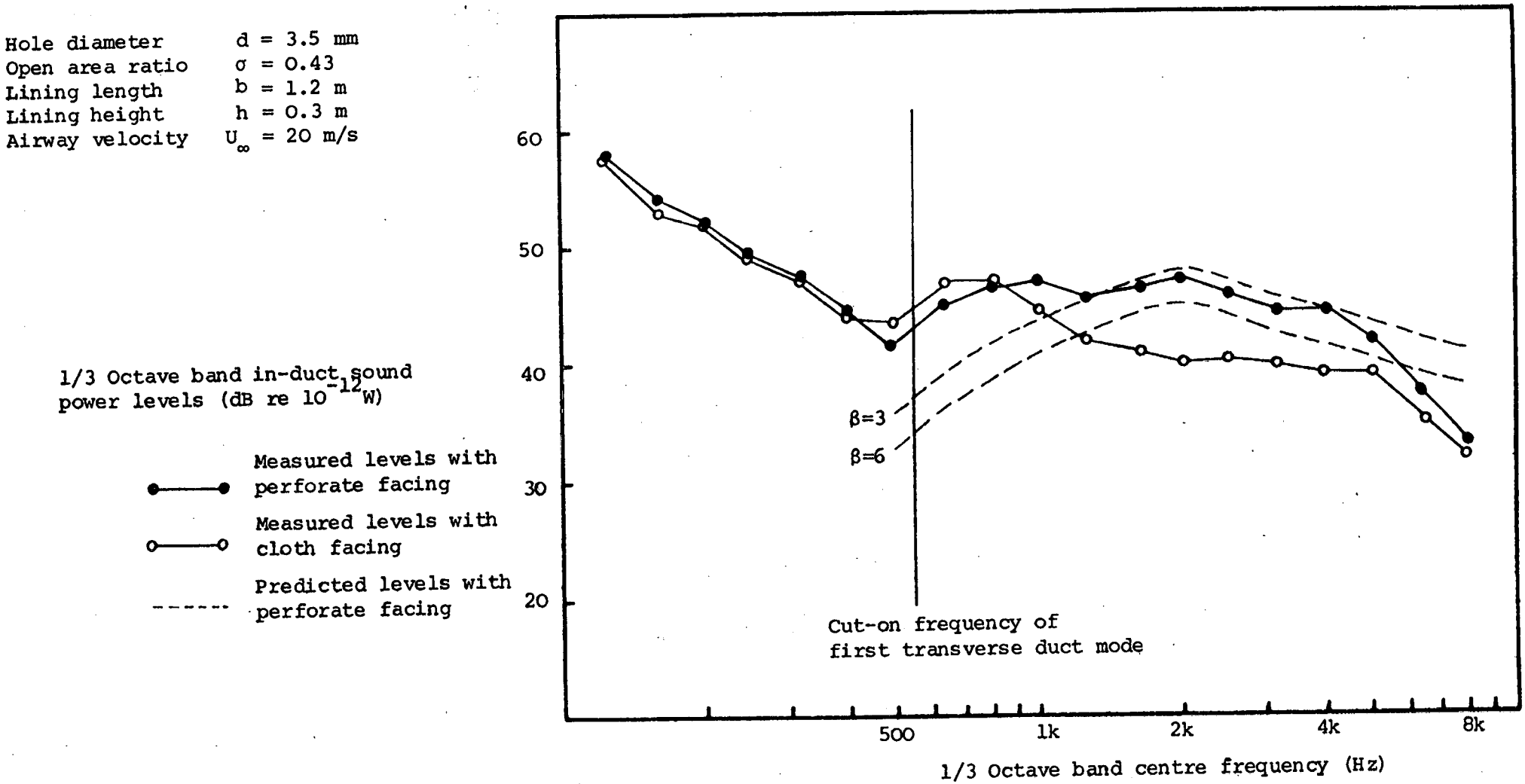

FIGURE 22. Normalised 6% bandwidth results for the honeycomb liner specimen with hole diameter d = 2.4 mm, open area ratio σ = 0.09

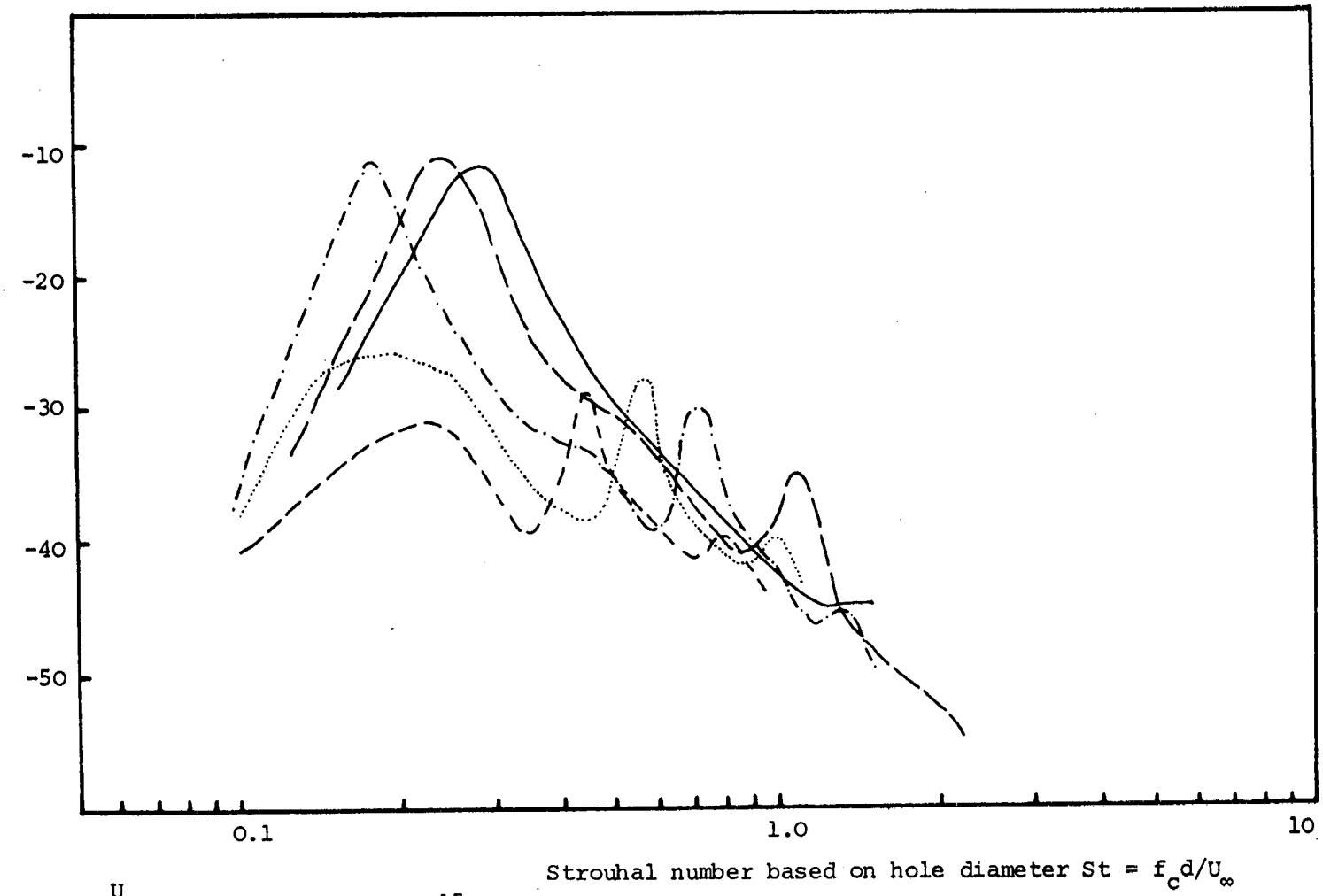

FIGURE 23. Normalised 6% bandwidth results for the honeycomb liner specimen with hole diameter d = 1.6 mm, open area ratio σ = 0.23

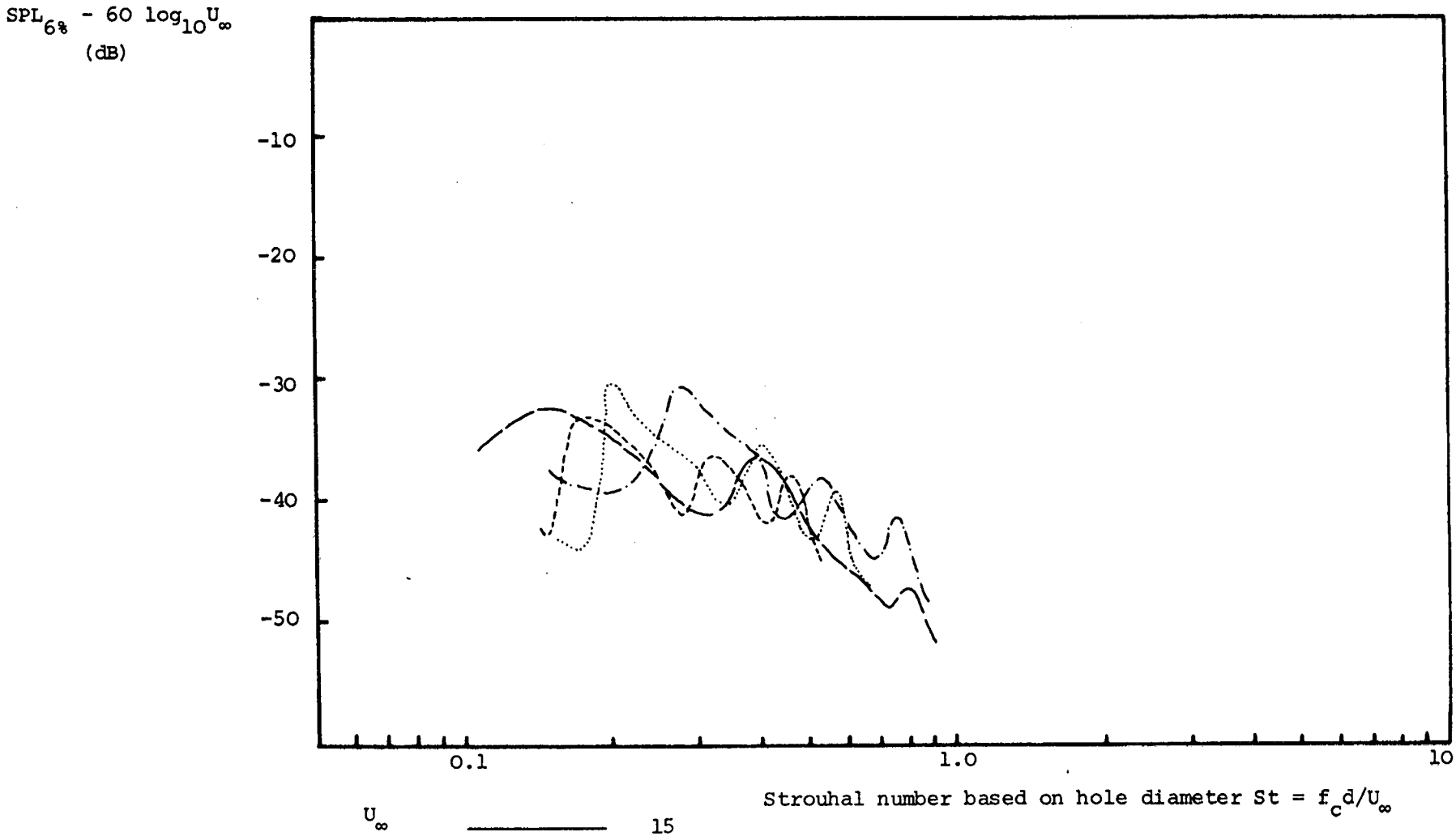

FIGURE 24. Normalised 6% bandwidth results for honeycomb liner specimen with hole diameter d = 1.0 mm, open area ratio σ = 0.07

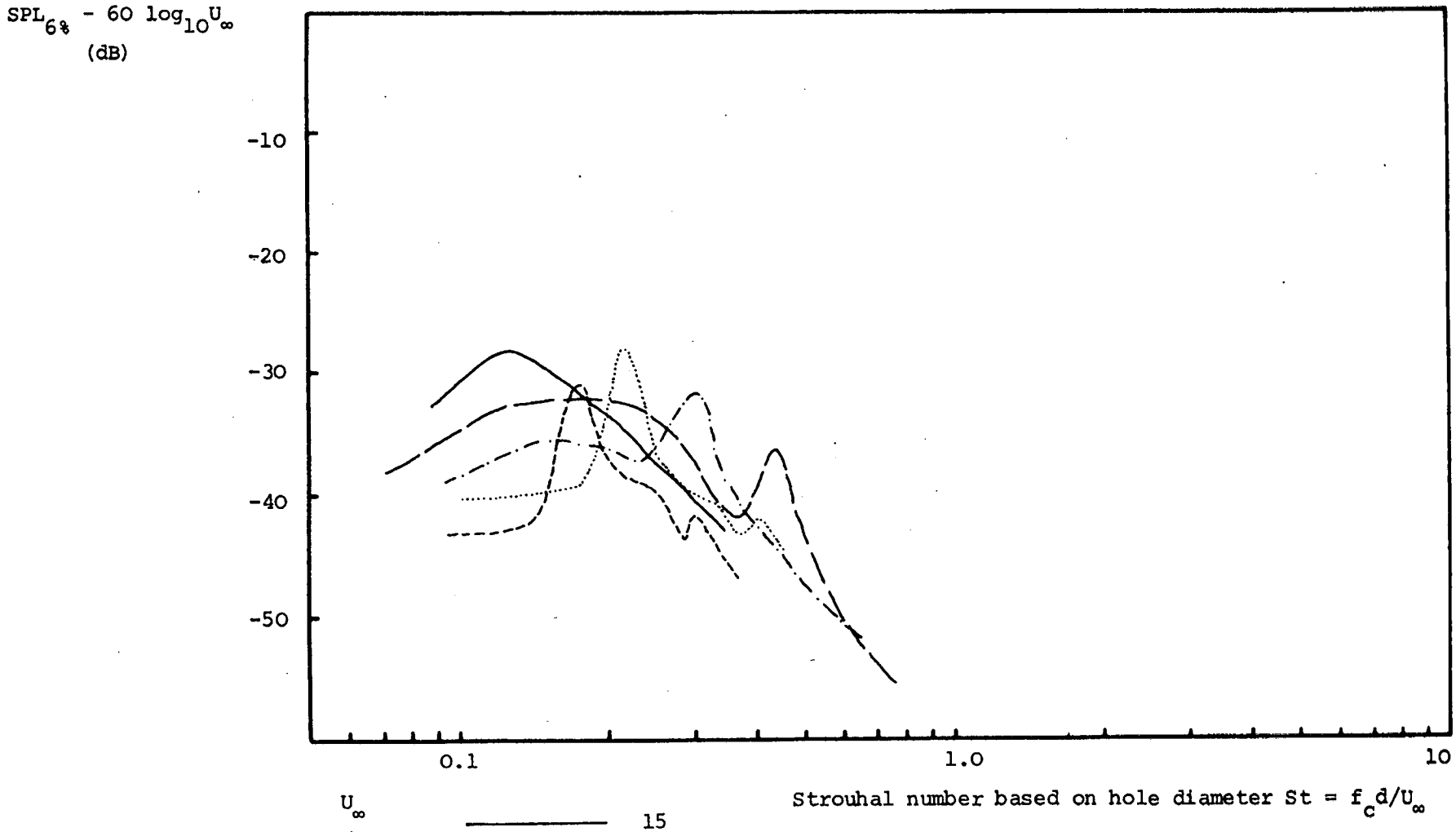

CHAPTER 4

THE FLUID DYNAMICS OF A FLOW EXCITED RESONANCE (I) THE EXPERIMENT

1. INTRODUCTION

In the context of aerodynamic noise generation, the phenomenon of flow excited acoustic resonance is both of engineering importance and of fundamental interest. The self-excitation of an acoustic resonance occurs in a wide variety of engineering applications involving fluid movement. Large amplitude oscillation of various types of resonant acoustic system has been found in compressor stages (1), tubebank heat exchangers (2), transonic wind tunnels (3) and lined ducts (4). In general, the production of high sound levels is a consequence of the coupling of the acoustic resonance to some form of periodic flow disturbance resulting from instability of the fluid motion. Energy is in some way extracted from the flow in order to sustain the acoustic oscillation. It is the fluid dynamics of the interaction between the unsteady flow and the acoustic resonance that is the subject of this study.

A considerable understanding of this type of sound source has been gained through previous work on specific instances of flow excited resonance and other related phenomena. The mechanism of sound production in organ pipes has been studied in some detail. The work of Cremer and Ising (5) forms the foundation for many subsequent refinements of organ pipe theory (6), although the underlying principles of their work have largely remained unchanged. Cremer and Ising were successful in modelling an organ pipe and the jet oscillating in its mouth as a feedback control system. The jet issuing into the pipe is unstable and supports the propagation of wave-like disturbances, which travel towards the downstream lip of the mouth, the amplification and propagation of the waves being well described by Rayleigh's (7) theory. As a result, the jet crosses the downstream lip of the mouth such that it is alternately directed into and out of the pipe. This oscillatory volume flow into the pipe acts as the source which excites the pipe resonance. The resonance of the pipe then produces an "acoustic" volume flow in the pipe mouth, which, in turn, controls the growth of the waves on the jet, hence closing the feedback loop. By deriving the details of the complex locii of the controlled system (organ pipe) and the controller (jet), Cremer and Ising were successful in predicting the frequency and amplitude of self-excitation using the criterion that the loop gain should be unity.

This approach was initially applied in the study of edgetones. The production of discrete frequency sound by a jet impinging on an edge was first given detailed attention by Brown (8) and later by Curle (9),

although the most comprehensive explanation of the process has been offered by Powell (10). The description again relies on the development of waves on the unstable jet which impinge on the edge downstream of the jet exit. The oscillations of the jet about the lip of the edge give rise to a net fluctuating force on the edge. Powell showed that the radiated sound field could be described exactly by an equivalent dipole source at the edge, the strength of which was determined by the fluctuating force. The near field of this dipole source provides the feedback which controls the growth of the jet instability waves. The contribution of edge-tone effects to organ pipe oscillation has generally been found to be negligible (11), the pipe resonance being the dominant source of feedback to modulate the jet. However, the exact relationship between edgetones and "pipetones" is still a matter of debate (12,13).

The high amplitude single frequency acoustic radiation produced by flow over rectangular cavities and cut-outs can also be described in terms of a feedback mechanism. Rossitter (14) succeeded in deriving a semi-empirical equation relating the frequencies of tonal production to the mean flow speed over the cavity and the length of the cavity in the streamwise direction. In Rossitter's study, the unstable shear layer over the cavity formed discrete vortices, which convected downstream and interacted with the downstream edge of the cavity to produce "acoustic pulses" which were fed back upstream to trigger the formation of subsequent vortices. This basic view of the phenomenon has changed little, although the feedback process has been found to vary depending on the type of cavity considered and the Mach number of the flow. The feedback controlling the behaviour of the shear layer can be dominated by the various acoustic resonances of the cavity. This process has been reviewed by Rockwell and Naudascher (15). At high subsonic and supersonic Mach numbers the feedback is largely dominated by direct radiation from the downstream edge of the cavity. Bilanin and Covert (16) have modelled this latter process by applying linear stability theory to describe the oscillatory motion of the shear layer as waves travel in the downstream direction. The consequent fluctuations in mass flow produced at the downstream edge of the cavity were considered as determining the strength of an equivalent monopole acoustic source. This model has recently been successfully refined by Tam and Block (17), who take into account finite shear layer thickness, distributed excitation of the shear layer and reflections by the cavity surfaces of the acoustic waves from the downstream monopole.

A further type of flow excited resonance that has been given considerable attention is the excitation of flow duct resonances by wake shedding from plates parallel to the airstream. Extensive studies by Parker (18,19) led to a more detailed treatment of the process by Cumpsty and Whitehead (20). The Parker β resonance was excited in a wind tunnel by the periodic shedding of vortices in the wake of a flat plate in the centre of a wind tunnel cross section. Cumpsty and Whitehead succeeded in describing the excitation of the resonance using Ribner's (21) formulation of the acoustic analogy. The unsteady "incompressible" pressure field associated with the wake was considered to be the source of acoustic excitation. The study of the feedback loop in this instance was later completed by Archibald (22), who measured the influence of an externally applied sound field on the vortex shedding in the wake of the plate. A criterion of a loop gain of unity was again used to illustrate the conditions necessary for self-excitation of the resonance.

As this brief review indicates, there is already a wealth of knowledge of the characteristics of the behaviour of the various instances of flow excited resonance and other mechanisms of discrete frequency sound production. Despite this, however, the understanding of the fluid dynamics involved in any of these processes is still of a superficial nature. As most of the foregoing examples illustrate, the analysis of these problems is often confined to the use of stability theory to describe the growth of waves on a jet or shear layer and an equivalent source to describe the radiation of sound providing the feedback. The exact mechanics of either the generation of sound by the shear layer or the stimulation of shear layer disturbances by the sound is poorly understood. The work that will be described in this and the next two chapters is directed towards increasing the level of understanding of these interactions. A rather different approach has thus been taken in this work. A specific instance of flow excited resonance has been chosen for study and the details of the flow have been measured in one resonant condition. Effort has been directed toward analysing the properties of the fluid motion in terms of the momentum and energy exchanges occurring inside the fluid. Little attempt has been made to describe the gross properties of the flow or the resonance as a function of the parameters necessary to determine the behaviour of the feedback system.

The phenomenon that has been chosen for this study is that of the flow excited Helmholtz resonator. This choice was largely determined

by experimental convenience. Previous work on this type of flow excited resonance by Bolton (23) and Elder (24) has again been directed towards describing experimental observations in terms of a feedback model. Bolton treated the process as Bilanin and Covert (16) had described cavity resonance, although the monopole at the downstream edge was believed to excite the resonator which dominated the feedback controlling the shear layer. Elder has undertaken a comprehensive analysis of the mechanism, which he has described in terms of organ pipe theory. The excitation of the resonance is by the net fluctuating mass flow into the cavity produced by the shear layer oscillations. Both these descriptions of the mechanism of the flow/resonance interaction give good predictions of the onset of self-excitation, and Elder's more thorough treatment is also successful in predicting amplitudes of self-excitation. Neither of these works deal with the details of the fluid dynamical interactions involved, although Elder describes measurements of the wave-like behaviour of the shear layer.

The work described in this Chapter covers the measurement of the mean and fluctuating parts of the velocity field and the fluctuating parts of the pressure field in the neck of a Helmholtz resonator excited to peak amplitude by a grazing flow. There are several obvious advantages in conducting this study. Firstly, the flow is two dimensional. A complete description of the velocity field has been accomplished using a two component Laser Doppler Velocimeter (LDV) capable of simultaneous point measurement of the mean and fluctuating parts of the velocity vector in two orthogonal component directions. The second major experimental advantage is the periodic nature of the flow field. The fluctuating motion produced repeats itself during each cycle of the oscillation. Thirdly, once the resonator is "singing" at its peak amplitude, the flow field becomes phase locked to the acoustic motion in the resonant cavity and is not easily disturbed. This enables accurate fluctuating pressure measurements to be taken inside the flow using a small probe tube that does not influence the flow being measured.

The measurements that have been taken reveal some very interesting details of the flow field. Essentially, the flow consists of discrete vortices formed periodically from the unstable shear layer leaving the upstream lip of the resonator mouth. These interact with a reciprocating flow through the resonator neck associated with the pressure fluctuations in the resonant cavity. This leads to a particularly interesting net

fluctuating pressure field. The dynamics of the interaction of the vortices with the reciprocating flow will be examined in Chapter 5 in an attempt to explain the details of the experimental results. In Chapter 6, particular attention will be paid to the momentum balances involved and the energy interchanges produced within the flow.

In this Chapter the measurement of the velocity field using the LDV will be described and the initial implications of the experimental data discussed. The measurement of the fluctuating pressure field will also be described. Firstly, however, the design and acoustical characteristics of the resonator used in the study will be presented. Additionally, results of flow visualisation will be shown in an initial qualitative investigation of the flow in the resonator neck.

2. THE ACOUSTICAL CHARACTERISTICS OF THE RESONATOR

2.1 The Design and Construction of the Resonator

Figure 1 shows a drawing of the resonator used for the series of experiments that will be described in this Chapter. The basic design was largely determined by the requirements of the LDV used to make the velocity measurements. This will be further discussed in section 4. However, in order to allow access for the interfering laser beams, the neck of the resonator was made by cutting a slot of 100 mm length across the top of the rectangular box forming the body of the resonator. The slot was 10 mm wide in the direction of the flow across the top of the resonator. This length was chosen in order that the resonator would "sing" at a flow speed that could be easily maintained by the available air supply and at a frequency which would be convenient for far field acoustic measurements.

This frequency f_n and flow speed U_∞ are related to the length L of the neck in the flow direction by the relationship

$$\frac{f_n L}{U_\infty} \simeq 0.25. \qquad (1)$$

(A list of symbols is given in Appendix 1.) This Strouhal number has been found to describe the peak singing frequencies of the Helmholtz resonators excited by pipe flow in Bolton's (23) experiments. f_n is the natural frequency of the resonator and U_∞ (in this case) is the velocity at the edge of the boundary layer over the resonator. This equation was used in the initial design of the resonator in order to determine the volume of the cavity.

The body of the resonator was constructed from 12.5 mm thick aluminium in order to provide perfectly rigid cavity walls. The slot forming the neck of the resonator was cut in the top surface of the cavity, which was constructed from 0.6 mm thick aluminium. Two "windows" were constructed in the sides of the resonator at each end of the slot in the top surface. These were made from 0.5 mm thick glass sheets measuring 27 mm x 39 mm and allowed access for the laser beams used in the velocity measurement. The glass sheets could be removed for cleaning so that scattering of the laser light by matter collecting on the glass surface could be minimised. The top of the resonator was extended with a lip of 100 mm length in the flow direction so that the flow did not separate from the resonator surface until well downstream of the resonator neck.

2.2 The Response of the Resonator under Acoustic Excitation

A simple experiment was performed in order to measure the frequency response of the resonator when excited by an incident sound wave. The arrangement used is illustrated in Figure 2. A reference microphone was placed close to the upper surface of the resonator. The compressor circuit on the B & K sine random generator was used in order to maintain a constant pressure at the reference microphone as the sound produced by the loudspeaker was swept through the frequency range. The pressure in the cavity of the resonator was monitored using a 12.5 mm microphone mounted inside the cavity such that the microphone diaphragm was flush with the inner surface of the cavity. The level recorder output in Figure 3 shows the output of the cavity microphone and the reference microphone as the excitation was varied from 100 Hz to 10 kHz. The level of the excitation was maintained constant to within 0.5 dB up to 4 kHz. The Helmholtz resonance of the cavity is clearly shown at about 600 Hz, the next cavity depth mode resonance occurring around 2.2 kHz.

A more accurate determination of the Helmholtz resonance frequency of the cavity was undertaken by slowly changing the excitation frequency in the region of 600 Hz. The frequency of the cavity pressure signal was monitored on a digital frequency counter (accurate to within 1 Hz) and the frequency response curve was again plotted for constant excitation. This is shown in Figure 4. The peak response of the resonator is shown to be 605 Hz, although this could only be determined to within ±3 Hz, since the frequency response curve is not sufficiently sharply defined. The quality factor Q of the resonator was measured from the bandwidth of the response curve. This is 61 Hz (±3 Hz) giving a value of $Q = 10$ (±0.5).

From the measured values of resonant frequency and quality factor it is possible to determine the acoustic impedance of the resonator. The differential equation for the volume displacement ξ of the slug of air in the resonator neck can be written (Reference (25)) as

$$M \frac{d^2\xi}{dt^2} + R \frac{d\xi}{dt} + \frac{\xi}{C} = p, \qquad (2)$$

where p is the complex driving pressure, M the inertance of the mass of air in the resonator neck, C the compliance of the air in the cavity, and R is the resistance providing the damping of the motion. Defining the impedance z as the ratio of driving pressure to the volume velocity in the neck gives

$$z = R + i \{\omega M - \frac{1}{\omega C}\} . \qquad (3)$$

The compliance C results from the stiffness of the air in the cavity and is easily calculated from the volume of the cavity. The internal volume V of the cavity is $4.41 \times 10^{-4} m^3$. C is given by $V/\rho_o c_o^2$ where ρ_o is the ambient density of air and c_o the sound speed. Taking $\rho_o = 1.2$ Kg/m^3 and $c_o = 344$ m/s, the value of C becomes $3.1 \times 10^{-9} m^4 s^2 Kg^{-1}$.

At the natural frequency ω_n, the reactive part of the impedance $(\omega_n M - 1/\omega_n C)$ is equal to zero. Thus, taking 605 Hz as the resonant frequency of the system, we can calculate the inertance M from $M = 1/\omega_n^2 C$. This gives a value of M of 22 Kg m^{-2}. Defining ℓ as the effective length of the mass of air in the neck, the inertance is given by $M = \ell / S$, where S is the area of the neck. The inertance M thus corresponds to an effective length ℓ of 18 mm.

The resistive part of the resonator impedance can be calculated from the measured value of Q of the resonator. The resistance R and the inertance M are related to Q by $Q = \omega_n M/R$. Taking Q to be exactly 10 thus gives a value for R of 8.4×10^3 kg $m^{-4} s^{-1}$. It is interesting to compare this value with the radiation resistance of a piston in an infinite baffle. At low frequencies, where the wavelength is much larger than the dimensions of the radiating piston, the resistance R_r is given by $\rho_o c_o k^2/2\pi$ where k is the wavenumber of the radiated sound. For radiation at 605 Hz, this value is 8.0×10^3 kg $m^{-4} s^{-1}$. The dominant contribution to the resistive impedance of the cavity is thus due to radiation losses. An estimate of the contribution due to viscous losses can be made from the analysis of Morse and Ingard (26) of the viscous resistance of a slit of width L in a two dimensional duct. When L is much smaller than the duct width, the resistance due to viscous

action is given by

$$R_\mu = \frac{2\rho_o \omega d_\mu}{2\pi S} \ell n \frac{L}{2h} , \qquad (4)$$

where d_μ is the viscous boundary layer thickness given by $(2\mu/\rho_o\omega)^{\frac{1}{2}}$ and h is the thickness of the slit, in this case equal to 0.6 mm. The value of R_μ computed, again at 605 Hz, was approximately 0.2 x 10^3 kg m^{-4} s^{-1}. This confirms that the resistive part of the impedance is dominated by the radiation resistance with a small contribution (less than 5%) from viscous losses. This is in marked contrast to the resonator examined by Howe (27), in which the viscous losses were found to dominate. This is probably because the present resonator has a relatively large neck area and a small neck length compared to that examined by Howe.

Note also that no account has been taken of any nonlinear contribution to the mouth resistance. The sound pressure levels in the cavity during the frequency response test were always below 100 dB and nonlinear losses associated with high particle velocities in the resonator neck would not be expected. Particle velocities were of the order of 0.01 m/s, which is well below the onset of nonlinearity found by Ingard and Ising (28). Under aerodynamic excitation, however, levels in the cavity were considerably larger and in the region where nonlinear losses may make some contribution.

2.3 Aerodynamic Excitation of the Resonator

All the experiments that will be described that involve the aerodynamic excitation of the resonator were performed using the free jet nozzle illustrated in Figure 1. It is the same nozzle used for the experimental determination of noise generated by flow over perforates described in Chapter 3. The velocity profile was thus uniform over the span of the slot forming the resonator neck. This can be seen from Figure 9 of Chapter 3. The turbulent boundary layer formed over the surface of the resonator has a velocity profile illustrated in Figure 8 of Chapter 3. The velocity U_∞ at the edge of the boundary layer occurs at a distance of about one half of the nozzle height above the resonator surface. The nozzle measures 34 mm in height and the velocity U_∞ was thus taken to be the velocity at a position 17 mm directly above the centre of the resonator neck. A pitot tube was used to measure U_∞ as the air supply was adjusted to give a range of velocities between 15 m/s and 30 m/s.

The amplitude and frequency of the cavity pressure fluctuations were

monitored using a B & K 12.5 mm microphone, again mounted with the diaphragm flush with the inner wall of the cavity. The microphone signal was amplified using a B & K frequency analyser, type 2107, although no filtering was applied to the signal. The frequency of the signal was again measured using a digital frequency counter. The results of the variation in amplitude and frequency of the cavity pressure are plotted as a function of the velocity U_∞ in Figure 5. The peak amplitude of excitation produced a level of 134 dB inside the cavity. The precise frequency of this peak excitation is again a little difficult to determine because of the large bandwidth of the response curve. However, it is certainly in the region of 605 Hz, the nominal natural frequency of the resonator, and occurs at a value of U_∞ of 22 m/s.

All the subsequent experiments on the aerodynamic excitation of the resonator were performed at this peak excitation condition. It was found that a measurement of the frequency of cavity oscillation provided an accurate means of monitoring the excitation. The frequency of the cavity pressure signal, rather than the flow velocity, was thus monitored and kept to within a range of 602 Hz to 608 Hz. This corresponds to a value of U_∞ of 22 m/s ± 0.25 m/s. A greater accuracy of control could not be achieved because of drift in the air supply.

2.4 The Sound Power Radiated at Peak Aerodynamic Excitation

An experiment was conducted in order to determine the total sound power radiated to the far field when the resonator was excited to its nominal peak amplitude. The experimental arrangement used is shown in Figure 6. The resonator was mounted as usual at the free jet nozzle exit. The jet nozzle itself was connected via flexible ducting to the air supply and was mounted in the centre of a semi-anechoic room. The area in which far field pressure measurements were made was surrounded by anechoic wedges, in order to give as near as possible truly anechoic conditions. The decay of sound pressure level away from the resonator was measured above and below the resonator along the x_2 axis (see Figure 7), and away from each side of the resonator along the x_3 axis. The resulting plots of sound pressure level against distance are shown in Figure 7. The values of SPL shown were measured in the 1/3 octave band centered on 630 Hz. It can be seen that the decay of SPL is at 6 dB/distance doubling out to about 0.8 m where small reflections from the anechoic wedges interfere with the sound radiated directly from the resonator.

Accurate measurements of the far field pressure could thus be made at a distance of 0.5 m from the centre of the resonator neck, this distance being about a wavelength at the frequency of interest. The SPL was measured at twenty positions 0.5 m from the resonator. Each measuring position corresponded to the centre of a face on the surface of an icosahedron surrounding the resonator. The measurements were made using a B & K 12.5 mm microphone and a B & K AF spectrometer, type 2111. All measurements were made in the 1/3 octave band centered on 630 Hz. The microphone was calibrated using a pistonphone.

Each set of twenty measurements was repeated three times. The measurements taken are tabulated in Figure 8. The arithmetic average SPL was found for each set of measurements and the sound power level of the source calculated. The results for the sound power level of the source were 97.2, 97.8 and 97.8 dB re 10^{-12} watts, respectively, for the three sets of measurements performed. These levels correspond to 5.2, 6.0 and 6.0 mW of sound power, respectively. The average rate of acoustic energy generation by the flow can thus be estimated to be 6 mW to within an accuracy of ±1 mW.

It can be seen from the measured results (Figure 8) that the radiation from the resonator is roughly omnidirectional, although SPL measurements over the hemisphere above the resonator were up to 5 dB higher than those over the hemisphere below the resonator. This form of directivity is observed for the radiation from a piston on a spherical baffle (see Reference 29), when the wavelength of the radiated sound approaches the circumferential dimension of the sphere.

The far field radiation was dominated by the fundamental frequency of the resonator. The second harmonic was detectable, although it produced a far field SPL in the 1250 Hz 1/3 octave band that was 25 dB lower than the fundamental measured in the 630 Hz 1/3 octave band. No third harmonic was detectable above the background noise and there was no evidence of any sub-harmonics.

3. FLOW VISUALISATION

3.1 Experimental Procedure

In order to first obtain a qualitative assessment of the nature of the flow in the neck of the resonator, an additional resonator was built to enable visualisation of the flow. This additional resonator was made with an identical internal cavity volume and with a neck of identical dimensions to the first. The only major difference in construction

was that the sides of the resonator were extended 18 mm above the top surface. This is illustrated in Figure 9. One of these sides was made from perspex to enable a clear view of the neck cross-section. The remainder of the resonator was painted with a matt black finish.

The additional resonator was attached to the free jet nozzle and excited aerodynamically in an identical fashion to the first. Oil mist was introduced into the flow using a T.E.M. Engineering smoke probe. This was inserted through the rear wall of the resonator and held against the underside of the upper surface of the resonator near to the upstream lip of the neck. The air supply was adjusted until the resonator was "singing" at 605 Hz and the flow was illuminated using an E.M.I. Type 6 stroboscope. The periodic shedding of vortices from the upstream lip of the resonator neck could be clearly observed. Figure 10 shows a photograph taken with the flow "frozen" at a particular point in the cycle. The shedding shown was observed by viewing the flow through the perspex side of the resonator. The oil mist was introduced at the mid point of the span of the resonator neck. By increasing the flow of oil mist, the shedding could be observed from above the resonator and was shown to be correlated along the entire span of the resonator neck. The flow observed at the mid point was thus taken to be representative of the two dimensional flow occurring in the neck.

A more detailed examination of the flow was undertaken by triggering the stroboscope using a signal from a microphone monitoring the cavity pressure oscillation. A phase shifting circuit was then introduced in order to change the point in the shedding cycle at which the flow was "frozen" by the stroboscopic illumination. A schematic diagram of the instrumentation used is shown in Figure 11. Since the oil mist could contaminate a microphone diaphragm, the cavity pressure oscillation was monitored using a B & K 12.5 mm microphone fitted with a 2 mm diameter probe tube. The phase shift introduced by the probe tube was measured using an identical technique to that used by Dean (30). The probe tube and a reference microphone are fixed in a small cavity above a horn loudspeaker driver unit. The frequency of the cavity pressure fluctuations produced by the driver unit is varied and the outputs of the probe and reference microphones compared using an AD-YU precision phase meter. At 605 Hz the probe microphone signal was found to have a phase lead of 156^{o} over the reference microphone signal.

The phase relationship between the trigger signal applied to the stroboscope and the flash produced was also measured. This was

accomplished using a photo-diode with a reverse bias voltage, which produced an increase in leakage current when light impinged on the surface. An oscilloscope trace was thus produced which consisted of a series of "spikes", each corresponding to a flash of the stroboscope. This trace was compared with the trace of the trigger signal input to the stroboscope. It was found that at a frequency of 605 Hz, the stroboscope flash occurred at a time before the peak value of the input trigger signal corresponding to a phase lead of 10 degrees.

Knowing the phase shifts of the various components in the trigger circuit illustrated in Figure 11, the point in the cycle at which the flow was frozen could be related to the pressure fluctuation occurring in the resonator cavity. The phase shifting circuit introduced was specifically designed to produce a change in phase of the trigger signal of up to 360 degrees at a frequency of approximately 600 Hz. The shift introduced was monitored using the AD-YU precision phase meter. A series of twelve photographs were taken using a phase shift that was changed in increments of 30 degrees. These photographs are shown in Figure 12. The point in the cycle at which the flow was frozen is shown for each of the photographs. The period T of the oscillation is 1653 μs. The fraction of a period after the minimum pressure occurs in the cavity is shown for each photograph. The photographs were taken using a Miranda R.E. Sensomat camera with a 1/15 sec. exposure time. Each photograph thus shows a superposition of the flow occurring in approximately 40 consecutive cycles of the motion. The clarity produced indicates that the flow is closely duplicated during each consecutive cycle.

3.2 Discussion of Results

The results of any flow visualisation study must be interpreted with caution. The photographs taken indicate the periodic formation of discrete vortices near the upstream lip of the resonator neck. These vortices appear to grow in size as they are convected towards the downstream lip of the neck. The vortices then appear to be "pushed out" of the resonator before being convected downstream over the upper surface of the resonator. It must be pointed out that these photographs of streaklines produced by the oil mist particles injected into the flow will not give a good representation of the streamlines of the flow. The work of Hama (31) has illustrated that an apparent "growth" in streakline oscillations can be produced by a neutrally stable shear layer disturbance. Hama also concluded that "one cannot positively identify the presence of discrete vortices merely based on the rolling

up of the streakline". Additionally, the number of individual cycles captured in each photograph will result in a space averaged picture of the flow field. More quantitative information is thus required before any firm conclusions can be reached regarding the formation and growth of the discrete vortices observed.

Nevertheless, certain useful information can be tentatively deduced from the photographs. Figure 13 shows a series of sketches of the flow in which the positions of the observed vortices has been approximately identified by tracing the photographs taken. The approximate path taken by a vortex during the course of two cycles of oscillation has thus been plotted. A discrete vortex appears to be formed during the first half cycle after the cavity pressure reaches its minimum value. During this period the cavity pressure is increasing and the air below the neck is being displaced into the cavity. The vortex reaches the mid point of the resonator neck on completion of the first half cycle. At this stage the cavity is at its maximum pressure and the air below the neck at its maximum downwards displacement. During the next half cycle, as the cavity pressure falls and the air below the neck is displaced upwards, the vortex convects towards the downstream lip. On completion of the cycle, the vortex appears to have been wrapped around the lip and has almost been ejected as the air below the neck reaches its maximum upwards displacement. During the second half cycle, between the photographs taken at 0.47 T and 0.97 T, the vortex has travelled a distance of approximately 5 mm, which implies a convection speed of about 6 m/s.

After ejection from the resonator neck, during the third half cycle illustrated in Figure 13, the vortex appears to travel a distance of the order of 10 mm, although the apparently "stretched" shape of the vortex makes it difficult to locate accurately. This implies an increased convection speed of about 12 m/s. This is confirmed during the fourth half cycle illustrated. The trailing end of the vortex again appears to travel a distance of about 10 mm between the photographs corresponding to 1.47 T and 1.97 T after the start of the first cycle. Further evidence of this increased convection speed is given by Figure 10. The vortices travelling downstream from the resonator neck appear to be a distance of two neck widths (20 mm) apart. Since one vortex is released every period, this again implies that the convection speed is of the order of 12 m/s.

Finally, a feature of the flow visualisation results that is worthy of note is the behaviour of the fluid at the upstream lip of the

resonator neck. The shear layer at the upstream lip of the neck always appears to be leaving in a direction tangential to the upper surface of the resonator. This implies that the Kutta condition is satisfied at the upstream lip of the neck. The consequences of this and the other results revealed by the flow visualisation will be discussed in more detail in the next Chapter. The remainder of this Chapter will be aimed at establishing more quantitative information about the vortex shedding process.

4. THE MEASUREMENT OF THE VELOCITY FIELD IN THE RESONATOR NECK

4.1 The Principles of Laser Doppler Velocimetry

The use of LDV for flow measurement is now well established and has been applied to a wide variety of problems since its use was first demonstrated by Yeh and Cummins (32) some 15 years ago. Relatively speaking, however, it is still a fairly new technique and so a brief outline of the principles involved will be given here. Attention will be confined to the particular LDV used for measuring the vortex shedding in the resonator neck. A more comprehensive survey of the underlying principles and alternative techniques available can be found in the text by Durst, Melling and Whitelaw (33).

Figure 14 shows the basic optical arrangement used in order to measure fluid velocity in one component direction. The laser beam is focussed onto a rotating translucent disc, which allows the beam to pass through at the same time as scattering laser light in the forward direction onto the mask M2. A small hole in this mask allows some of this scattered light through into the next lens. This lens focusses this light into the flow region in order to form a "reference beam" of scattered light. This low intensity reference beam intersects with the main beam of laser light to form a small "control volume" at the point O. This defines the measurement position in the flow. Particles in the flow travelling through this control volume scatter light from the high intensity main beam. The scattered light is allowed to pass through the mask M3 and heterodyne with the reference beam light, which is passed through the third lens and collected as a parallel beam by the photomultiplier. The photomultiplier detects the modulation of the light intensity at a Doppler frequency given by

$$f_d = (2nU/\lambda_\ell)\sin(\theta/2) + f_o, \qquad (5)$$

where n is the refractive index of the scattering medium, λ_ℓ the wavelength of the laser light, and θ is the "scattering angle" between the main beam and reference beam. U is the velocity of the scattering particles. The direction of the velocity component measured bisects the complement of the scattering angle between the two beams and lies in the plane of beams (Figure 14).

The frequency f_o is the Doppler shift already introduced into the reference beam light by the motion of the particles on the scattering disc. This frequency pre-shift removes the ambiguity in the sign of the velocity component U. A Doppler frequency f_d greater than f_o means the particles scattering light from the control volume are moving in the same direction as the particles on the scattering disc. A frequency f_d less than f_o means the fluid is moving in the opposite direction to the disc. The value of f_o is given by

$$f_o = \omega_d r \sin\phi \, (2n/\lambda_\ell) \sin(\theta/2), \qquad (6)$$

where r is the radial distance of the scattering point from the disc axis, ϕ is the azimuthal angle on the disc (see Figure 14) and ω_d is the angular velocity of the disc.

The amount of frequency pre-shift that is introduced into the reference beam light can thus be controlled by changing the position at which the main beam impinges on the disc. This has several advantages in the processing of the Doppler frequency generated. In particular the signal produced can be shifted into the frequency range most suitable for following the fluctuations in Doppler frequency produced by fluctuations in the flow. The fluctuations in Doppler frequency are followed using an autodyne frequency tracker. The photomultiplier signal is input to the tracker, which provides a means of producing a voltage output proportional to the Doppler frequency of the input signal. A voltage analogue of the velocity of the scattering particles in the flow is thus produced. A complete description of the principles of operation of the autodyne frequency tracker can be found in References (33) and (34).

4.2 The Two Component Velocimeter

The LDV used to perform simultaneous measurement of the vertical and streamwise velocity components in the resonator neck was that devised by Rizzo and Halliwell (35). A brief version of this description will be reproduced here. The two component instrument is a

straightforward development of the single component velocimeter described in the previous section. An additional lens is inserted to form separate measuring and frequency shifting modules, with parallel beams being transmitted between the two. Figure 15 shows the two module arrangement.

The measurement module consists of two lenses, L_1 and L_2, having a common focus at O which defines the position of the measurement control volume. The main laser beam and two reference beams, R_1 and R_2, enter L_2 normal to its plane ABCD. All three beams are focussed at O and pass out of L_1 normal to its plane EFGH. The main beam and reference beam R_1 combine to measure the streamwise velocity U_1, which lies in the inclined plane ABHG. The main beam and reference beam R_2 combine to measure the vertical component U_2 which lies in the inclined plane BCEH.

The reference beams R_1 and R_2 are produced in the frequency shifting module. This consists of two lenses, L_3 and L_4, which share a common focus at O' which is in the plane of the rotating scattering disc. The light scattered by the disc is collinated by L_3 to form a circular scattering pattern on the surface of the mask M_1. The small holes A' and C' allow this scattered light through to form the two reference beams. The three beams emerging from M_1 are thus suitably arranged for collection by lens L_2 when the measuring and frequency shifting modules are aligned on the same optical axis.

The two beams emerging from the measurement module through mask M_4 are each collected by a photomultiplier. The photomultiplier outputs are individually processed using frequency trackers to produce real time voltage analogues of the vertical and streamwise velocity components. A thorough description of the procedure necessary to give the correct optical alignment of the velocimeter is given in Reference (35).

4.3 Experimental Arrangement

Figure 16 shows the arrangement used. The two component velocimeter was aligned with the measurement control volume located in the plane perpendicular to the optical axis at the mid point of the span of the resonator neck. The beam from a 30 mW Scientifica Helium-Neon laser was passed through the holes in the alignment masks M_3 and M_2. The lens L_4 was a 114 mm diameter plano-convex lens having a focal length of approximately 190 mm. The lens L_3 collecting the light scattered by the rotating disc was a 44.5 mm diameter bi-convex lens having an approximate focal length of 127 mm.

The scattering disc placed at the focii of lenses L_3 and L_4 consisted of a 70 mm diameter perspex disc 1.5 mm thick with a 90 mm diameter Melinex disc only 0.1 mm thick cemented to its surface. The perspex served to keep the Melinex steady when rotated. Plasticine particles were rubbed onto the Melinex surface to give a good scattering medium. A synchronous motor provided a constant drive for the disc at 3000 r.p.m. The main laser beam impinged on the Melinex disc at a radial distance r of 85 mm and an azimuthal angle ϕ of approximately 30°. The scattering angle θ formed between the main beam and the two reference beams in the frequency shifting module was 8.98°. From equation (6) the frequency pre-shifts applied to the reference beams were thus of the order of 5.7 MHz and 3.3 MHz for the streamwise and vertical component measuring beams respectively.

The main beam and the pre-shifted reference beams were collected by lens L_2. This was a 44.5 mm diameter bi-convex lens having a focal length of 102 mm. From here the beams were focussed into the control volume in the neck of the resonator and collected by the 114 mm diameter plano-convex lens L_1 having a focal length of 190 mm. Mirrors were then used to deflect the two reference beams into the photomultipliers. The scattering angle used in the measurement module was 11.18°. Thus, from equation (5) a particle moving at 1 m/s in either component direction would produce a further Doppler shift of 0.308 MHz in the frequency of the reference beam.

The reference beam measuring the vertical velocity component was passed into the resonator neck through the glass window in the resonator side before reaching the measurement control volume. At the angle of incidence used the refraction of the beam produced by the thickness of the glass window resulted in an estimated lateral displacement of only 0.02 mm. Both the main beam and the streamwise component measuring beam were subject to similar displacements on passing through the window on the other side of the resonator after interfering in the measurement control volume.

The arrangement of the beams in the resonator is shown in Figure 17. The area of the resonator neck that could be examined is illustrated. This area was defined by the geometry used. It was limited by the extent to which the resonator could be moved relative to the beams without a solid surface intersecting one of the beams. The size of the control volume was determined from the size of the "waist" of the interfering beams when focussed by L_2 from their original size.

The main beam was 1.5 mm diameter and was focussed down to 0.07 mm diameter. The reference beams were each 3 mm diameter and were focussed down to 0.03 mm in diameter. The resulting control volume was thus 0.5 mm in length in the x_3 (spanwise) direction and less than 0.1 mm in diameter.

Errors in spatial resolution were, in fact, determined by the accuracy of positioning of the measurement point rather than the size of the control volume. It was obviously convenient to move the flow relative to the laser velocimeter. The jet nozzle and resonator were thus traversed in the streamwise and vertical directions using the arrangement shown in Figure 18. The relative position of the resonator was monitored using a travelling microscope. This located the centre of a cross scribed on a plate fixed to the side of the jet nozzle. The traversing mechanism could locate the position of the resonator to within an accuracy of 0.25 mm. The resonator was initially positioned relative to the control volume by first observing the magnified image of the reference beams produced by the lens L_1. A pointer was then inserted into the control volume such that the shadow produced by its tip could be observed at the centre of both beam images. The resonator was then traversed such that the top of the edge of the upstream lip of the neck was brought into contact with the pointer. At this position of the traverse, the control volume location in the resonator neck was thus known to within an accuracy of 0.1 mm.

4.4 Velocimeter Operation

The provision of adequate seeding for the flow was one of the most important aspects of the use of the laser velocimeter. The instrument itself proved relatively easy to assemble and align, but considerable care had to be taken to ensure that sufficient seeding was provided in the flow to give a continuous Doppler signal from the photomultiplier output. The seeding was provided by two oil mist generators. The first was the probe made by T.E.M. Engineering. This was inserted through the rear of the resonator and held under the upper surface of the resonator such that its outlet was near the upstream lip of the resonator neck. This provided adequate seeding for the region inside the resonator beneath the level of the neck. Regions above this level suffered from a periodic lack of seeding as air from the boundary layer above the resonator was entrained during the vortex shedding process. This is visible on the flow visualisation photographs. An additional supply of oil mist particles was thus provided in order to seed the air

travelling over the upper surface of the resonator. The smoke provided by an additional oil mist generator was injected into the jet nozzle just upstream of the jet exit.

The Doppler signal was monitored at all times during the taking of measurements to ensure continuous seeding of the flow in the control volume. The size of the particles injected was of the order of 1 μm and were thus suitable for following turbulent velocity fluctuations of up to 10 kHz (see Reference (33)).

The frequency trackers used to process the photomultiplier signals were those made by Communications and Electronics Ltd. from the design of Wilmshurst and Rizzo (34). All measurements were made using the highest possible slew rate in the phase locked loop of the trackers. The trackers thus had an amplitude and phase response that was flat for fluctuations in the flow of up to 10 kHz. The trackers were calibrated by adjusting the frequency input from an Airmec type 201A signal generator and monitoring the output voltage on a digital voltmeter. The streamwise and vertical component trackers produced an output of 0.330 and 0.336 V/MHz, respectively. Since the beam configuration used produced a velocity calibration of 0.308 MHz (m/s), the calibrations of the trackers were 9.83 (m/s)/v and 9.66 (m/s)/v for the streamwise and vertical components, respectively.

The frequency pre-shifts produced by the scattering disc were measured with no flow. The streamwise and vertical pre-shifts were found to be 5.1 MHz and 3.2 MHz, respectively. This is in good agreement with the values predicted from the approximate position of the intersection of the main beam with the scattering disc. The streamwise component tracker was thus operated over its frequency range between 4 and 10 MHz, whilst the vertical component tracker range used was between 1.5 and 5 MHz. The range of flow velocities that could be measured were thus approximately -3 to +15 m/s in the streamwise direction and -5 to +5 m/s in the vertical direction.

4.5 Measurement Procedure

Figure 19 shows the instrumentation used for the processing of the outputs of the frequency trackers. All the measurements were made with the resonator at peak aerodynamic excitation. A probe tube was used to monitor the cavity pressure and it was ensured that the frequency of pressure fluctuations was always in the range 602 to 608 Hz when taking measurements.

The time averaged values of the tracker outputs corresponding to the mean flow values in the resonator were measured using a Rockland Labs. Dual Hi-Lo Filter. Both channels were set for low pass filtering with a nominal cut-off frequency of 20 Hz. The steady voltage outputs reached after filtering were monitored on digital voltmeters. Mean flow values in the two component directions were recorded over a grid of points spaced 0.5 mm apart. The values measured were repeatable to within ±0.2 m/s. The accuracy of the measurements was limited by the positional accuracy of the traverse gear and the drift in the air supply, although the latter was kept within the limits defined by the allowable change in the frequency of the cavity pressure oscillation. The measured data as a function of position is shown in Figures 20 and 21.

The fluctuating velocity field in the resonator neck was first examined by measuring the power spectra of the velocity fluctuations in the two component directions. The I.S.V.R. PDP 11/45 digital computer was used to acquire both the streamwise and vertical tracker outputs directly and evaluate the power spectral density of the velocity signals. A sample length of 1.25 sec. was acquired from each signal at a rate of 10^4 samples/sec. Power spectra were produced having a resolution of 10 Hz, which were accurate to within ±3 dB with 95% confidence. The noise spectrum of the velocimeter was measured with no flow. This was dominated by the velocity fluctuations of the scattering disc and was predominantly at the rotational frequency of the disc and its harmonics.

Figure 22 shows typical power spectra of the velocity fluctuations in the flow in the two component directions. The measuring point was at a position x_1 = 5 mm, and x_2 = -3 mm, where the x_1 and x_2 co-ordinates are in the streamwise and vertical directions, respectively and the origin is at the corner of the upstream lip of the neck on the upper surface of the resonator. It can be seen that the background noise of the velocimeter is well below the level of the measured velocity spectra. In both directions, the velocity spectra are dominated by the fundamental frequency of the vortex shedding (605 Hz). Higher harmonics of the shedding are clearly visible on the spectra and up to four higher harmonics were detected on the spectra measured at various points in the flow. The fundamental frequency was always at least 5 dB higher in amplitude than the second harmonic on all the spectra sampled, although no systematic investigation of the harmonic content of the measured signals was carried out.

The variation of the amplitude and relative phase of the fundamental frequency of the two velocity components was, however, investigated thoroughly throughout the measurement plane. The amplitude of the velocity fluctuation in each component direction at the fundamental frequency was measured by filtering the tracker output signals with a B & K bandpass filter set, type 1612, using the 1/3 octave band centered on 630 Hz. The root mean square values of the filtered output voltages were then measured using a Hewlett Packard RMS voltmeter, type 3400A. The resulting values of rms velocity fluctuations are tabulated in Figures 23 and 24. The results were repeatable to within ±0.2 m/s, although in some cases, particularly for the vertical component near the centre of the neck, the results were only repeatable to within ±0.4 m/s. These errors were largely determined by positional accuracy. This was obviously more important in regions of large velocity gradient.

The phase of the velocity fluctuations at the fundamental frequency was measured relative to the phase of the cavity pressure fluctuations. The cavity pressure was monitored using a B & K 12.5 mm condenser microphone with a 1 mm diameter probe tube. The probe tube was calibrated using the method described in section 3.1. It was found to produce a phase lag of 164° with reference to the measured pressure signal at a frequency of 605 Hz. The signal from the probe microphone was amplified using a B & K A.F. spectrometer, type 2111. The signal was also filtered using the 1/3 octave centered on 630 Hz. The phase matching of the two 1/3 octave filters used for the velocity and cavity pressure signals was checked. The same single frequency input was applied to both filters and the phase difference of the output was measured using an AD-YU precision phase meter. At 605 Hz the output of the velocity signal filter lagged the output of the pressure signal filter by 7°. The relative phase between the filtered velocity and cavity pressure signals was then measured using a Hewlett Packard analogue correlator, type 3721A. Conventional phase meters were found unsuitable for the measurements required, since any unsteadiness in the input velocity signal produced wild fluctuations in the phase meter readings. The correlator was used to produce a time averaged reading of the relative phase of the input signals. The first negative going zero crossing of the sinusoidal correlelogram on the time delay axis was measured. This value was then corrected for the various phase shifts in the measuring system to yield the phase of the velocity signal relative to the cavity pressure. The results for the two components over the 0.5 mm grid in the measurement plane in the resonator neck are tabulated in Figures 25 and 26. The

results were repeatable to within $\pm 10^{o}$, this again being limited by positional accuracy. This error was considerably greater in the region of the flow just below the resonator neck where $-0.5 \text{ mm} > x_2 > -1.5 \text{ mm}$ for the streamwise component measurements. In this region, the phase of the streamwise component was very difficult to measure accurately.

Finally, the time histories of the frequency tracker outputs were recorded at a variety of positions over the measurement grid in the resonator neck. The unfiltered tracker outputs giving the voltage analogues of the streamwise and vertical velocity components were recorded using a storage oscilloscope. The oscilloscope traces were photographed using a polaroid camera. The results are shown in Figure 27.

4.6 Discussion of Results

The discussion presented in this section will be confined to an initial analysis of the principal features of the results obtained. A more detailed discussion of the implications of these velocity measurements will be undertaken in the next Chapter. The results for the mean flow have been plotted as a vector field in Figure 28. The dominance of the mean streamwise component is clearly shown, substantial vertical flow components only being evident at the lower levels of the shear layer and towards the upstream end of the neck. The results show the entrainment of air from within the cavity. This is the result of a large-scale slowly recirculating mean flow inside the cavity. This was visible during the flow visualisation and is driven by mean flow entering the cavity below the downstream lip. This travels around the inside of the cavity and is entrained into the underside of the shear layer towards the upstream lip.

The spreading of the shear layer is also indicated in Figure 28 where the contour corresponding approximately to a streamwise mean flow of 1 m/s is shown. The spread of the layer appears roughly linear with distance from the upstream edge. This is confirmed by the collapse of the streamwise mean flow data shown in Figure 29. A reasonable collapse of data has been produced by normalising the streamwise mean flow values by the velocity $\bar{u}_{1max}$ at the upper edge of the shear layer and plotting the results against (x_1/x_2). The value of $\bar{u}_{1max}$ was taken to be 12 m/s and the origin is again the point at the corner formed by the upstream lip and the upper surface of the resonator.

The results of the measurement of the fluctuating streamwise velocity component provide some of the most important information regarding the

vortex shedding process. Velocity fluctuations in the streamwise direction are unlikely to contain any contribution from the reciprocating flow through the resonator neck associated with the cavity pressure fluctuations and are thus representative of the behaviour of the shed vortices. The results for the amplitude and phase of the fluctuating streamwise component are illustrated by the contour plots in Figures 30 and 31. The contour plots were produced using a standard routine on the I.S.V.R. PDP 11/45 computer. The input results were smoothed within experimental error (±0.2 m/s and ±10°) and a 100 point curve fit applied to the data in the x_1 direction.

The presence of discrete vortices is clearly shown by the difference in relative phase between the streamwise velocity fluctuations in the upper and lower halves of the shear layer. The phase change occurring when the shear layer is traversed in the vertical (x_2) direction is of the order of 180°. This can be understood using the simple model illustrated in Figure 34. The streamwise velocity fluctuation induced above the path taken by a vortex convecting in the x_1 direction will experience a positive peak velocity whilst a point below the path experiences a negative peak velocity. The time histories recorded also illustrate this remarkably well. Figure 27 shows the change in form of the streamwise component time histories between the upper and lower halves of the shear layer. The form of time histories shown is in good agreement with those predicted qualitatively from the simple model of convecting vortices illustrated in Figure 34.

The position of the 180° phase change in the fluctuating streamwise velocity component defines the position of the path taken by the centre of the vortex cores. This path is given to within ±0.5 mm by the results in Figure 31. The amplitude of the fluctuating streamwise component is also at its least value in this region. The results are thus consistent with streamwise convected vortices having a solid body rotation in the core. The vortices will induce only small streamwise velocity fluctuations close to the path taken by the cores. This is further illustrated by the time histories in Figure 27. The fluctuations measured in the region of the path of the cores become small and irregular. The form of these fluctuations explains why the phase of the streamwise fluctuations was difficult to measure repeatably in the region of the path of the cores.

The value of the streamwise mean flow velocity along the path of the cores is 6 m/s (±1 m/s). This is the convection speed of the

vortices for the length of the path travelled before reaching the region of the downstream lip. The results in this area are not well enough defined to enable an accurate deduction of the path taken by the vortex cores.

The amplitude of the streamwise velocity fluctuations is greatest in the upper half of the shear layer near the upstream lip of the neck. As shown in Figure 30, the peak fluctuating streamwise velocities induced by the passage of the vortices become smaller in the downstream direction. This is again confirmed by the time histories in Figure 27. At the positions (x_1 = 2 mm, x_2 = 0 mm) and (x_1 = 3 mm, x_2 = 0 mm) for example, the peak positive velocity fluctuations are large and strongly defined. The fluctuations become weaker and more irregular in the downstream direction. The contour plot in Figure 30 also indicates a spreading of the vortices as they travel downstream. The area influenced by the streamwise velocity fluctuations induced appears to increase roughly in accordance with the spreading of the mean shear layer.

The amplitude and phase of the vertical velocity fluctuations is shown in Figures 32 and 33. The velocity fluctuations in the vertical direction are likely to contain any fluctuations resulting from the reciprocating flow driven through the resonator neck by the cavity pressure fluctuations. Any fluctuating flow of this kind will be combined with the vertical velocity fluctuations induced directly by the vortices. The order of magnitude of the velocity fluctuation in the neck produced by the cavity pressure fluctuation can be calculated from the compliance of the cavity deduced in Section 2. The SPL in the cavity at peak aerodynamic excitation was 134 dB re 2 x 10^{-5} N/m^2. This corresponds to an rms value of 100 N/m^2 for the cavity pressure fluctuations. This implies a volume flow into the cavity corresponding to an rms neck velocity of 1 m/s. This is certainly of the order of the velocity fluctuations induced by the vortex shedding.

The maximum values of the vertical velocity fluctuations were found to occur in the region of the flow between the centre of the shear layer and the downstream lip of the neck (Figure 32). This is again well illustrated by the time histories of the velocity fluctuations. Note also that the form of the vertical component time histories is well predicted by the convecting vortex model illustrated in Figure 34. The measured values of the phase of the vertical component fluctuations show that in the centre of the neck the vertical velocity fluctuations phase lag the cavity pressure by 90°. The reciprocating flow inside the cavity also lags the pressure by 90°. The relative phase of the

reciprocating flow in the neck will depend on the acoustic impedance presented to the cavity pressure fluctuations. However, it is possible that the maximum vertical velocity fluctuation found in the centre of the neck is due to a constructive interference between the vortex induced velocity and the reciprocating flow driven through the neck by the cavity pressure fluctuations. This will be discussed in more detail in the next Chapter.

Finally, there are substantial and well defined phase differences between the vertical and streamwise velocity components. Figure 35 shows the measured phase difference between the components as a function of x_1, at positions in the shear layer above and below the path taken by the vortex cores. These levels in the shear layer correspond to x_2 = 0.5 mm and x_2 = -1.5 mm, respectively. It can be seen that the phase difference between the components is greater than 90° above the path taken by the cores (x_2 = +0.5 mm) and less than 90° below the path taken by the cores (x_2 = -1.5 mm). The phase differences are larger and smaller than 90° at the upstream end of the shear layer and approach 90° towards the downstream end. Defining u_1' and u_2' as the fluctuations in the streamwise and vertical directions, the Reynolds shear stress $\rho_o \overline{u_1' u_2'}$ (the overbar denoting time average) is given by

$$\rho_o \overline{u_1' u_2'} = \rho_o u_{1rms} u_{2rms} \cos(\psi_1 - \psi_2), \qquad (7)$$

where ρ_o is the ambient density, u_{1rms} and u_{2rms} are the rms values of the measured velocity components, and ψ_1 and ψ_2 are the relative phases of the streamwise and vertical components, respectively.

The measured values of rms amplitudes and phases have been used to plot a contour map of the Reynolds shear stress in the shear layer in Figure 36. The map is accurate to within the error shown. There are clearly regions of negative and positive Reynolds shear stress above and below the path of the vortex cores. These stresses are concentrated at the upstream end of the shear layer. The precise nature of the shear stress pattern near the downstream end is difficult to determine within experimental error. The implications of these and the other deductions made will be discussed more fully in the next Chapter.

5. THE MEASUREMENT OF THE FLUCTUATING PRESSURE FIELD IN THE RESONATOR NECK

5.1 The Measurement of Fluctuating Static Pressure

The measurement of static pressure fluctuations in an airflow

necessarily involves the positioning of some form of probe in the air-stream. This introduces two specific problems. Firstly, one needs to know if the flow is the same as it was before the insertion of the probe. Secondly, the pressure sensed by the probe will not necessarily be the same as the pressure in the flow before the insertion of the probe. Fluid brought to rest at the sensing point of the probe will result in the corresponding stagnation pressures being registered in the pressure measurement.

The static pressure fluctuations in the neck of the resonator were measured using a 0.5 mm diameter microphone probe tube made by B & K for use with a 12.5 mm condenser microphone. The probe was held such that the tube pointed vertically downwards into the resonator neck. The open end of the probe tube was thus in the plane parallel to the upper surface of the resonator (the x_1, x_3 plane). The details of the experimental procedure will be discussed fully in the next section. However, the performance of the probe will first be considered in the light of the two questions posed above.

The nature of the flow being measured is such that it is very unlikely that the introduction of the probe tube in any way disturbed the fluctuating flow field at the frequency of interest. The vortex shedding is locked in by the reciprocating flow driven through the resonator neck by the cavity pressure fluctuations. In fact, the flow is remarkably difficult to disturb by introducing solid objects into the neck. For example, a 4 mm diameter probe tube held vertically into the resonator produced no change in the amplitude or frequency of the cavity pressure fluctuations when the resonator was excited at its peak amplitude. The locked-in flow is thus difficult to disturb, although the probe is likely to produce a local distortion of the flow in the region of the probe itself. The probe tube will produce a turbulent wake as flow sweeps past in the streamwise direction. However, the size of the wake is obviously approximately determined by the size of the probe. For the 0.5 mm diameter probe tube the wake flow will be considerably smaller than the scale of the vortices being measured. Also, assuming the peak shedding frequency in the wake is given by a Strouhal number of 0.2 based on probe diameter, the fluctuations of pressure in the wake will be at frequencies around 4 kHz, i.e., much higher than the fluctuations at the frequency of interest. Thus it can confidently be assumed that the basic structure of the fluctuating flow field in the resonator neck is left unchanged by the insertion of the 0.5 mm probe tube held in the vertical direction.

However, one also has to consider the magnitude of the error introduced by the measurement of stagnation pressures at the end of the probe, where flow in the vertical component direction will be brought to rest. As stated by Morse and Ingard (36), the detailed analysis of errors introduced is quite complex. For the sake of simplicity, one has to assume that the flow in the region of the tube is irrotational and that the stagnation pressure produced is simply $\frac{1}{2}\rho_o u_2^2$. Here, u_2 is the total velocity in the vertical component direction, which is normal to the plane of the open end of the probe tube. It will thus be assumed that the flow is irrotational even though there is clearly a rotational component in the flow being measured. Nevertheless, this is likely to give a correct order of magnitude of the error involved. Certainly, Morse and Ingard (36) arrive at this conclusion. Siddon (37) has undertaken careful experiments to assess the error in measuring the fluctuating static pressure using a conventional pitot tube arrangement. He concludes that the error is again of the order of the stagnation pressure of the velocity component normal to the sensing holes. This conclusion was also reached by Strasberg (38).

Thus, if p_t is defined as the true instantaneous static pressure in the flow before insertion of the probe and p_m as the measured static pressure, one can write

$$p_m - p_t \simeq \tfrac{1}{2}\rho_o u_2^2 . \tag{8}$$

Taking the mean and fluctuating parts of this equation gives

$$(\bar{p}_m + p_m') - (\bar{p}_t + p_t') \simeq \tfrac{1}{2}\rho_o(\bar{u}_2 + u_2')^2 . \tag{9}$$

The time average of this equation is

$$\bar{p}_m - \bar{p}_t \simeq \tfrac{1}{2}\rho_o \bar{u}_2^2 + \tfrac{1}{2}\rho_o \overline{u_2'^2} . \tag{10}$$

Subtracting this from equation (9) gives the required expression for the difference between the measured and true fluctuating pressures which can be written as

$$p_m' - p_t' \simeq \rho_o \bar{u}_2 u_2' + \tfrac{1}{2}\rho_o(u_2'^2 - \overline{u_2'^2}) . \tag{11}$$

For the flow considered, the measurements of the mean and fluctuating parts of the vertical velocity component can be used to determine the order of magnitude of the terms contributing to the instantaneous error. The maximum measured vertical velocity fluctuation was a root mean square

value of approximately 3 m/s at the fundamental frequency. The maximum mean vertical velocity was 1 m/s. The maximum instantaneous value of $\rho_o \bar{u}_2 u_2'$ is thus 5.0 N/m^2. The maximum instantaneous value of $\frac{1}{2}\rho_o (u_2'^2 - \overline{u_2'^2})$ is 5.4 N/m^2.

However, if the microphone probe output is filtered such that only pressure fluctuations at the fundamental frequency are measured, only the term $\rho_o \bar{u}_2 u_2'$ will make a substantial contribution to the instantaneous error. The term $\frac{1}{2}\rho_o (u_2'^2 - \overline{u_2'^2})$ will only contribute at higher harmonic frequencies, since terms arising from multiples of the fundamental frequency of the fluctuating velocity with its higher harmonics can be neglected. Thus, at the fundamental frequency the maximum rms value of the error is 3.6 N/m^2. It is worth noting that this is certainly an upper bound to the error, since at most points in the resonator neck both the mean and rms fluctuating vertical velocities are substantially less than 1 m/s and 3 m/s, respectively.

The order of magnitude of the rms pressure fluctuation at the fundamental frequency measured with the probe tube was approximately 50 N/m^2. One can thus conclude that the fluctuating static pressure can be successfully measured in the resonator neck to within an error of less than 5% at most measuring points. This is in accordance with the conclusions of others attempting similar measurements. Both Strasberg (38) and Kobashi (39) concluded that the error terms were sufficiently small when making measurements of pressure fluctuations in the wake of a cylinder. They were both concerned with the error term $\frac{1}{2}\rho_o (u_2'^2 - \overline{u_2'^2})$ and neglected $\rho_o \bar{u}_2 u_2'$. It is clearly an advantage to be able to filter out the former leaving only the latter term, which can become negligibly small with decreasing values of $\bar{u}_2$.

5.2 Experimental Procedure

In order to minimise the insertion loss of the 0.5 mm diameter B & K probe tube, the length of the tube was cut to 20 mm from the open end of the tube to the tip of the conical microphone coupling piece (Figure 37). This was the shortest length of tube that could be used without bringing the body of the microphone too close to the neck of the resonator when making measurements.

The probe tube was calibrated using the procedure outlined in Section 3.1. The probe tube was used with a B & K 12.5 mm condenser microphone, type 4133. The microphone output was amplified using a B & K A.F. spectrometer, type 2111, and filtered using the 1/3 octave filter centered on 630 Hz. The reference microphone used in the

calibration was also used to monitor the cavity pressure fluctuation when the pressure in the resonator neck was measured. The reference microphone was a B & K 12.5 mm condenser microphone, type 4133, and its output was amplified and 1/3 octave filtered at 630 Hz using a B & K frequency analyser, type 2107. The instrumentation used for the probe calibration was also used in the experimental work with identical filtering.

The calibration procedure showed that the probe tube had an insertion loss of 39.7 dB at a frequency of 605 Hz. The phase shift measured between the filtered signals of the reference and probe microphones showed that the probe microphone signal lagged the reference microphone signal by 85^{o} at 605 Hz. Neither the insertion loss nor the phase shift were found to vary over the range 600 to 610 Hz.

In view of the high insertion loss of the probe tube, precautions were taken to minimise any transmission of sound through the microphone casing, which would by-pass the probe tube. The microphone was thus encased in a brass covering to ensure that flanking transmission would be minimised. The covering was designed to avoid any interference to the flow in the resonator neck. The orientation of the probe microphone and its casing when making measurements is shown in Figure 37. Although the presence of the microphone must clearly influence the boundary layer flow above the resonator, it is most unlikely that the microphone influences the strongly correlated flow in the resonator neck. Certainly, no influence of the presence of the microphone on the cavity pressure fluctuations could be detected when the tip of the probe tube was located at the measurement point furthest inside the cavity.

When making the pressure measurements, the measuring probe was fixed and the resonator was traversed relative to the fixed probe position with the traversing mechanism used when making the velocity measurements. The probe was first positioned with its tip in contact with the top of the upstream lip of the resonator neck at the mid point of the span of the neck. This located the reference position from which any distance traversed was monitored using the travelling microscope, as before. The initial location of the reference position was performed with the flow turned on to account for any deflection of the probe by the flow. No noticeable deflection or vibration of the probe was produced by the flow.

The amplitude and relative phase of the fluctuating pressure measured by the probe in the resonator neck was recorded at a series of

positions of the probe tip over a 0.5 mm grid in the resonator neck. The nominal position of each measurement point was assumed to be the centre of circular end of the probe tip. The amplitude was measured by monitoring the rms output voltage of the filtered probe microphone signal. The known sensitivity of the microphone used was corrected for the insertion loss of the probe tube and the gain in the microphone cathode follower circuit to give the conversion factor between measured voltage and the pressure in N/m^2 at the tip of the probe. The phase of the probe microphone signal relative to the cavity pressure fluctuation was measured using the Hewlett Packard analogue correlator type 3721A. The position of the zero crossing of the correlellogram produced by cross correlation of the probe and cavity microphone signals was monitored. The phase difference measured between the two signals was then corrected for the phase shift between the two channels to give the phase of the pressure fluctuation in the neck relative to the cavity pressure fluctuation.

All the pressure amplitude and phase measurements were recorded with the resonator at peak aerodynamic excitation. This was again controlled by maintaining the frequency of the cavity pressure fluctuation between 602 and 608 Hz. Two additional experimental checks were also made to confirm the validity of the pressure measurements made using the probe tube. Firstly, the degree of flanking transmission reaching the microphone diaphragm was checked by blocking the end of the probe and measuring the decrease in signal level when the probe was held in a specific position in the flow. A loss of signal of 30 dB was recorded showing that the microphone diaphragm was responding to the pressure fluctuations transmitted by the probe tube only. As an additional check, the end of the probe tube was held at a position 10 mm below the level of the resonator neck. The amplitude and phase of the pressure thus measured inside the cavity were in exact agreement with the amplitude and phase of the pressure measured by the cavity microphone. This confirmed the validity of the amplitude and phase calibration of the probe tube.

The measurements of the amplitude and phase of the fluctuating pressure in the resonator neck at the fundamental frequency of the oscillation are tabulated in Figures 38 and 39. It was found that these results were remarkably repeatable. The amplitude at any given position could be measured to within ± 1 N/m^2 and the phase could be measured to within $\pm 5^{o}$. Measured values were a little more uncertain

in one particular region of the flow near the downstream edge of the slot. In this region, the pressure amplitude measured was relatively low and the phase changed very rapidly with position. This made the pressure results in this region sensitive to the accuracy of positional location of the probe tip. Nevertheless, the amplitude and phase could still be measured repeatably to within ± 2 N/m^2 and $\pm 15^o$, respectively.

5.3 Discussion of Results

Contour plots of the amplitude and phase of the fluctuating pressure measured in the neck of the resonator are shown in Figures 40 and 41. The plots were produced using the I.S.V.R. PDP 11/45 computer in the same way as the contour plots of the velocity measurements were produced. The plots shown illustrate some striking features of the pressure measurements.

Firstly, consider the amplitude of the pressure fluctuations illustrated in Figure 40. The maximum pressure amplitude measured occurs in a region near the upstream lip of the neck and approaches an rms value of 70 N/m^2. The velocity measurements and flow visualisation indicate that the discrete vortices shed are formed in this region. It thus seems likely that this maximum pressure fluctuation is associated with the periodic formation of vortices having a static pressure defect associated with the vortex cores. However, towards the downstream edge, the amplitude of the pressure fluctuations falls to a minimum value of approximately 15 N/m^2. The region of this minimum pressure fluctuation also lies on the path taken by the vortex cores.

The relative phase of the pressure fluctuations illustrated in Figure 41 shows a very rapid change in the region of minimum pressure amplitude. The relative phase changes through approximately 140^o within a distance of 1 mm traversed by the measuring point in the streamwise direction. This rapid phase change was easily detected when undertaking the measurements. The 1 mm movement of the probe tube relative to the resonator neck was accompanied by a very rapid shift of the corellelogram on the screen of the analogue correlator. The precise value of the relative phase in this region was thus difficult to determine. However, this region of uncertainty was confined to an area measuring 1.5 mm in the streamwise direction and 2.0 mm in the vertical direction centered on the point having co-ordinates $x_1 = 7$ mm, $x_2 = -0.5$ mm.

The reason for this unusual behaviour of the measured amplitude and phase in this area is not easy to determine at first sight. It

certainly appears to be related to the passage of vortices through the region. It is possible that the pressure fluctuations produced by the periodic convection of the pressure field associated with the vortices interferes with pressure fluctuations related to the reciprocating neck flow driven by the cavity pressure fluctuations. More detailed consideration of the fluid dynamics involved is required before any firm conclusions can be reached as to the cause of this interference pattern. This will be undertaken in the next Chapter.

Finally, however, it is worth emphasising that the pressure measurements made provide a very good estimate of the true fluctuating static pressure in the resonator neck. Even in the region of lowest pressure amplitude, the measured rms fluctuation of 15 N/m^2 was well above the fluctuating stagnation pressure $\rho_o \overline{u_2 u_2}'$. The velocity measurements show that the rms value of the stagnation pressure in this region is only 2.5 N/m^2. It is thus impossible that the measured interference pattern is a result of the measurement of anything other than static pressure fluctuations.

6. CONCLUSIONS

A series of careful experiments has been undertaken in order to gain an understanding of the fluid dynamics of the interaction between unsteady fluid motion and an acoustic resonance. The flow excited resonance chosen for study was a Helmholtz resonator excited by a grazing boundary layer flow. The flow produced is such that detailed measurements can relatively easily be made of the mean and fluctuating parts of the velocity field and the fluctuating pressure field in the resonator neck.

The resonator used in the study had a natural frequency of 605 Hz. At low levels of excitation the resistive part of the acoustic impedance of the resonator was dominated by radiation resistance. When excited with the grazing flow, the resonator reached its peak amplitude of excitation at 605 Hz. At this frequency, the sound pressure level in the cavity reached 134 dB and 6 mW of acoustic power was radiated to the far field.

A flow visualisation study indicated that the flow in the resonator neck consisted of a series of periodically shed vortices. These vortices were formed during the first half cycle of the motion as the pressure in the cavity changed from its peak negative to its peak positive value. Discrete vortices appear to reach the mid point of the resonator neck in the streamwise direction when the pressure in the

cavity reaches its peak positive value. By the end of the cycle, when the cavity pressure returns to its peak negative value, the vortices appear to straddle the downstream lip of the resonator neck. The flow visualisation also indicated that the mean convection speed of the vortices was 6 m/s when the vortices traversed the width of the neck. This convection speed appeared to increase to 12 m/s once the vortices had been ejected from the resonator neck at the downstream lip. Another important feature of the results was that the shear layer leaving the upstream lip always appeared tangential to the upper surface of the resonator.

Measurements of the mean flow velocity in the resonator neck showed a shear layer growth which was approximately linear in the downstream direction. The mean flow speed at the upper edge of the shear layer was 12 m/s. The velocity changed across the layer to a flow speed near 1 m/s, which was associated with a large scale recirculating mean flow inside the cavity.

The behaviour of the shed vortices can be deduced from the measurements of the fluctuating streamwise velocity component. The presence of discrete vortices is confirmed by the 180° change in the phase of the streamwise component between the upper and lower halves of the shear layer. The position of this phase change enables the location of the path taken by the vortex cores. The core path can be defined to within 1 mm and confirms that the vortices travel at a mean convection speed of 6 m/s across most of the neck width. The path taken by the vortices in the region of the downstream lip is difficult to establish from the measured results. The measurements of the streamwise velocity fluctuations are consistent with the passage of vortices having a solid body rotation in their core. This is also confirmed by the recorded time histories of the velocity fluctuations. The amplitude of the streamwise velocity fluctuations is highest towards the upstream edge of the slot and decays in the downstream direction. This implies that the growth of the unstable shear layer into discrete vortices takes place rapidly at the start of the cycle and is followed by a spreading of the vortices as they are convected downstream. This spreading of influence of the vortices is roughly in accordance with the growth of the mean shear layer.

The measurements of the fluctuating vertical velocity component contain contributions from the velocity field induced by the shed vortices and the reciprocating flow driven through the resonator neck by the cavity pressure fluctuations. Both these contributions to the

net vertical velocity fluctuations are of the same order of magnitude and appear to constructively interfere to produce the maximum amplitude in the region of the centre of the neck.

Measurements of the phase difference between the vertical and streamwise velocity components show well defined regions of negative and positive Reynolds shear stress in the upper and lower halves of the shear layer, respectively. These stresses are concentrated at the upstream end of the shear layer whilst the stress distribution becomes less well defined towards the downstream end of the layer.

The fluctuating static pressure in the resonator neck has been successfully measured using a small microphone probe tube. Filtering of the microphone probe output signal enabled the minimisation of the errors introduced by sensing stagnation pressures at the tip of the probe. The results produced show a complicated interference pattern. This pattern appears to be related to the pressure fluctuations created by the periodic formation and convection of vortices. It is possible that these pressure fluctuations interfere with pressure fluctuations associated with the reciprocating flow in the resonator neck.

The experiments undertaken have thus produced a comprehensive and detailed knowledge of the behaviour of the flow in the resonator neck at peak self-excitation. However, many features of the experimental results are not easy to explain at first sight. Certainly, there is some form of interaction between the vortically induced flow field and the reciprocating flow driven by the cavity pressure fluctuations. Before any further conclusions can be reached as to the nature of this interaction, careful consideration is required of the precise definition of these interacting flows. The next Chapter will be devoted to a thorough analysis of the experimental results in an attempt to establish more precise quantitative details of the vortex shedding process. These details will then be used in the final Chapter which will examine the momentum and energy balances in the shear layer. Particular attention will be paid to achieving an understanding of how 6 mW of far field acoustic power is extracted from the mean flow of energy impinging on the resonator neck.

REFERENCES

(1) R. PARKER 1967 Journal of Sound and Vibration 6, 302-309. Resonance effects in wake shedding from compressor blading.

(2) Y.N. CHEN 1968 Transactions of ASME, Journal of Engineering for Industry, Series B90 1, 134-146. Flow induced vibration and

noise in tubebank heat exchangers due to Von Karman streets.

(3) M.O. VARNER 1975 AIAA Journal 13, 1417-1418. Noise generation in transonic tunnels.

(4) C.Y. TSUI and G.A. FLANDRO 1977 Journal of Sound and Vibration 50, 315-331. Self-induced sound generation by flow over perforated duct liners.

(5) L. CREMER and H. ISING 1967 Acustica 19, 143-153. The self-excited vibrations of organ pipes (in German).

(6) N.H. FLETCHER 1979 Annual Review of Fluid Mechanics 11, 123. Airflow and sound generation in musical wind instruments.

(7) LORD RAYLEIGH 1929 Theory of Sound, Vol. II, 2nd Edition, Chapter XXI, 8365. Vortex motion and sensitive jets.

(8) G.B. BROWN 1937 Proceedings of the Physical Society 49, 493-507. The vortex motions causing edgetones.

(9) N. CURLE 1953 Proceedings of the Royal Society, Series A 216, 412-424. The mechanics of edgetones.

(10) A. POWELL 1961 Journal of the Acoustical Society of America 33, 395-409. On the edgetone.

(11) S.A. ELDER 1973 Journal of the Acoustical Society of America 54, 1554-1563. On the mechanism of sound production in organ pipes.

(12) J.W. COLTMAN 1976 Journal of the Acoustical Society of America 60, 725-733. Jet drive mechanisms in edgetones and organ pipes.

(13) S.A. ELDER 1978 Journal of the Acoustical Society of America 64, 1721-1723. Edgetones versus pipetones (Letter to the Editor).

(14) J.E. ROSSITER 1966 Aeronautical Research Council Reports and Memoranda, R & M No. 3438. Wind-tunnel experiments on the flow over rectangular cavities at subsonic and transonic speeds.

(15) D. ROCKWELL and E. NAUDASCHER 1978 Transactions of the ASME 100, 152-163. Review - Self-sustaining oscillations of flow past cavities.

(16) A.J. BILANIN and E.E. COVERT 1973 AIAA Journal 11, 347-351. Estimation of possible excitation frequencies for shallow rectangular cavities.

(17) C.K.W. TAM and P.J.W. BLOCK 1978 Journal of Fluid Mechanics 89, 373-399. On the tones and pressure oscillations induced by flow over rectangular cavities.

(18) R. PARKER 1966 Journal of Sound and Vibration 4, 62-72. Resonance effects in wake shedding from parallel plates; some experimental observations.

(19) R. PARKER 1967 Journal of Sound and Vibration 5, 330-343. Resonance effects in wake shedding from parallel plates; calculation of natural frequencies.

(20) N.A. CUMPSTY and D.S. WHITEHEAD 1971 Journal of Sound and Vibration 18, 353-369. The excitation of acoustic resonances by vortex shedding.

(21) H.S. RIBNER 1962 University of Toronto UTIAS Report No. 86. Aerodynamic sound from fluid dilatations.

(22) F.S. ARCHIBALD 1975 Journal of Sound and Vibration 38, 81-103. Self-excitation of an acoustic resonance by vortex shedding.

(23) J.S. BOLTON 1976 M.Sc. Thesis, University of Southampton. The excitation of an acoustic resonator by pipe flow.

(24) S.A. ELDER 1978 Journal of the Acoustical Society of America 64, 877-890. Self-excited depth-mode resonance for a wall mounted cavity in turbulent flow.

(25) L.E. KINSLER and A.R. FREY 1962 Fundamentals of Acoustics (John Wiley), Second Edition, p. 186.

(26) P.M. MORSE and K.U. INGARD 1968 Theoretical Acoustics (McGraw-Hill), p. 483.

(27) M.S. HOWE 1976 Journal of Sound and Vibration 45, 427-440. On the Helmholtz resonator.

(28) U. INGARD and H. ISING 1967 Journal of the Acoustical Society of America 42, 6-17. Acoustic nonlinearity of an orifice.

(29) P.M. MORSE and K.U. INGARD 1968 Theoretical Acoustics (McGraw-Hill), p. 344.

(30) P.D. DEAN 1974 Journal of Sound and Vibration 34, 97-130. An in-situ method of wall acoustic impedance measurement in flow ducts.

(31) F.R. HAMA 1962 Physics of Fluids 5, 644-650. Streaklines in a perturbed shear flow.

(32) Y. YEH and H.Z. CUMMINS 1964 Applied Physics Letters 4, 176-178. Localised flow measurements with an He-Ne laser spectrometer.

(33) F. DURST, A. MELLING and J.H. WHITELAW 1976 Principles and Practice of Laser Doppler Anemometry (Academic Press).

(34) T.H. WILMSHURST and J.E. RIZZO 1974 Journal of Physics E: Scientific Instruments 7, 924-930. An autodyne frequency tracker for laser doppler anemometry.

(35) J.E. RIZZO and N.A. HALLIWELL 1978 Review of Scientific Instruments 49, 1180-1185. Multi-component frequency shifting self-aligning laser velocimeters.

(36) P.M. MORSE and K.U. INGARD 1968 Theoretical Acoustics (McGraw-Hill), p. 701.

(37) T.E. SIDDON 1969 University of Toronto UTIAS Report No. 136. On the response of pressure measuring instrumentation in unsteady flow.

(38) M. STRASBERG 1963 AGARD Report No. 464. Measurements of fluctuating static and total head pressure in a turbulent wake.

(39) Y. KOBASHI 1957 Journal of the Physical Society of Japan 12, 533-543. Measurements of the pressure fluctuations in the wake of a cylinder.

APPENDIX 1. LIST OF SYMBOLS

c_o	ambient sound speed
C	acoustic compliance
d_μ	viscous boundary layer thickness
f_d, f_o	Doppler frequency
f_n	natural frequency
h	slit thickness (in this case, the thickness of the material forming the resonator neck)
k	acoustic wavenumber
ℓ	effective length of air mass comprising resonator inertance
L	length of resonator neck in streamwise direction
M	acoustic inertance
n	refractive index
p_t, p_m	true and measured static pressure
Q	quality factor of resonance
r	radial distance of laser scattering point from axis of scattering disc
R	acoustic resistance
R_r	radiation resistance
R_μ	viscous resistance
S	area of cross section of resonator neck
U	velocity of scattering particles
U_∞	velocity at the edge of the boundary layer
u_1, u_2	velocities in the streamwise (x_1) and vertical (x_2) component directions
$\overline{u}_{1max}$	maximum mean streamwise velocity at upper edge of shear layer
x_1, x_2, x_3	cartesian coordinates specifying streamwise vertical and spanwise directions respectively
z	acoustic impedance
ϕ	angle of azimuth of laser scattering point position on scattering disc

λ_ℓ	laser light wavelength
μ	coefficient of viscosity
ξ	acoustic volume displacement
ω	radian frequency
ω_n	natural radian frequency
ω_d	angular velocity of scattering disc
ρ_o	ambient density
θ	laser scattering angle
ψ_1, ψ_2	relative phases of fluctuating streamwise and vertical velocity signals

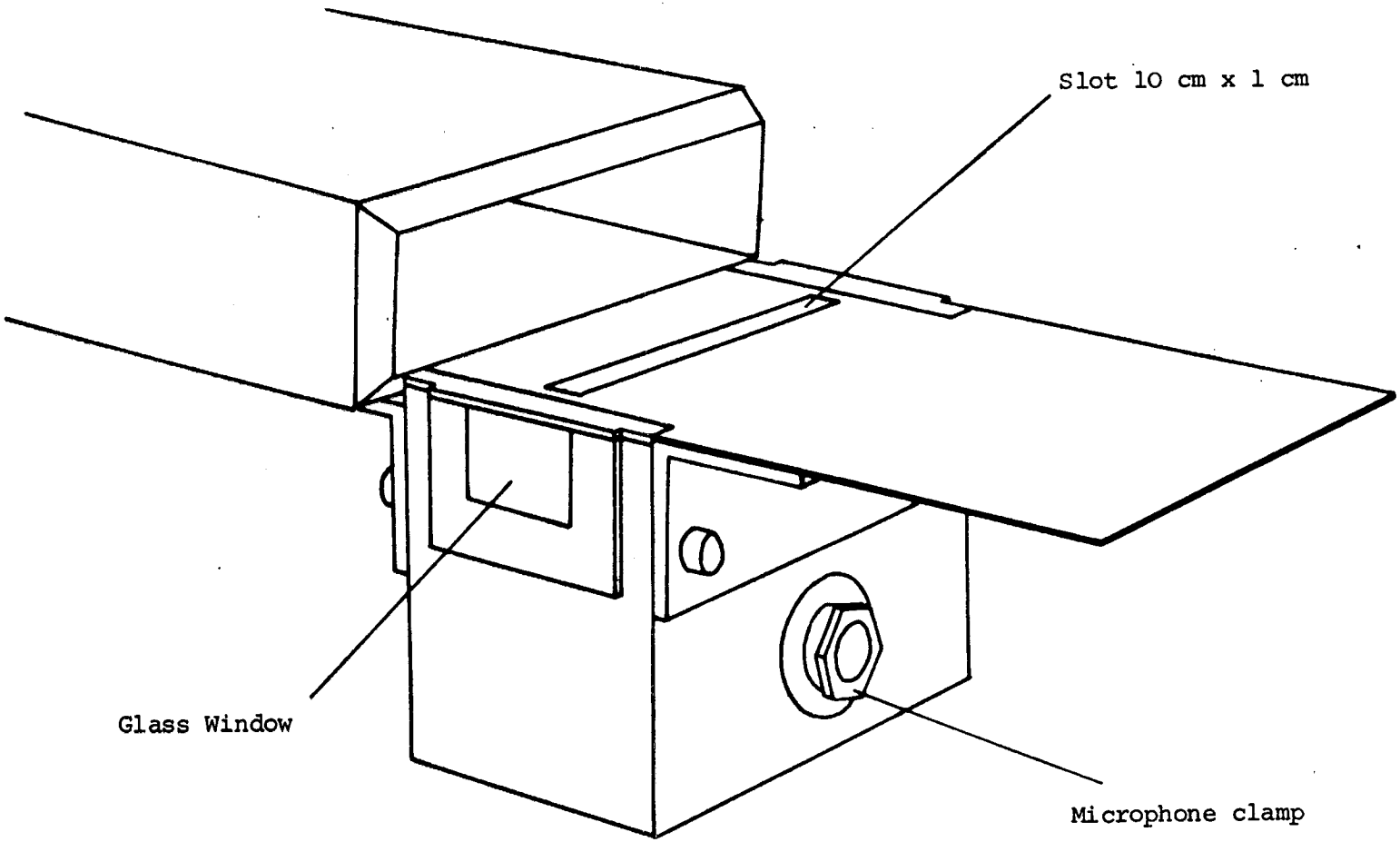

FIGURE 1 The resonator and jet nozzle.

FIGURE 2 Resonator frequency response test (the test was conducted in anechoic surroundings).

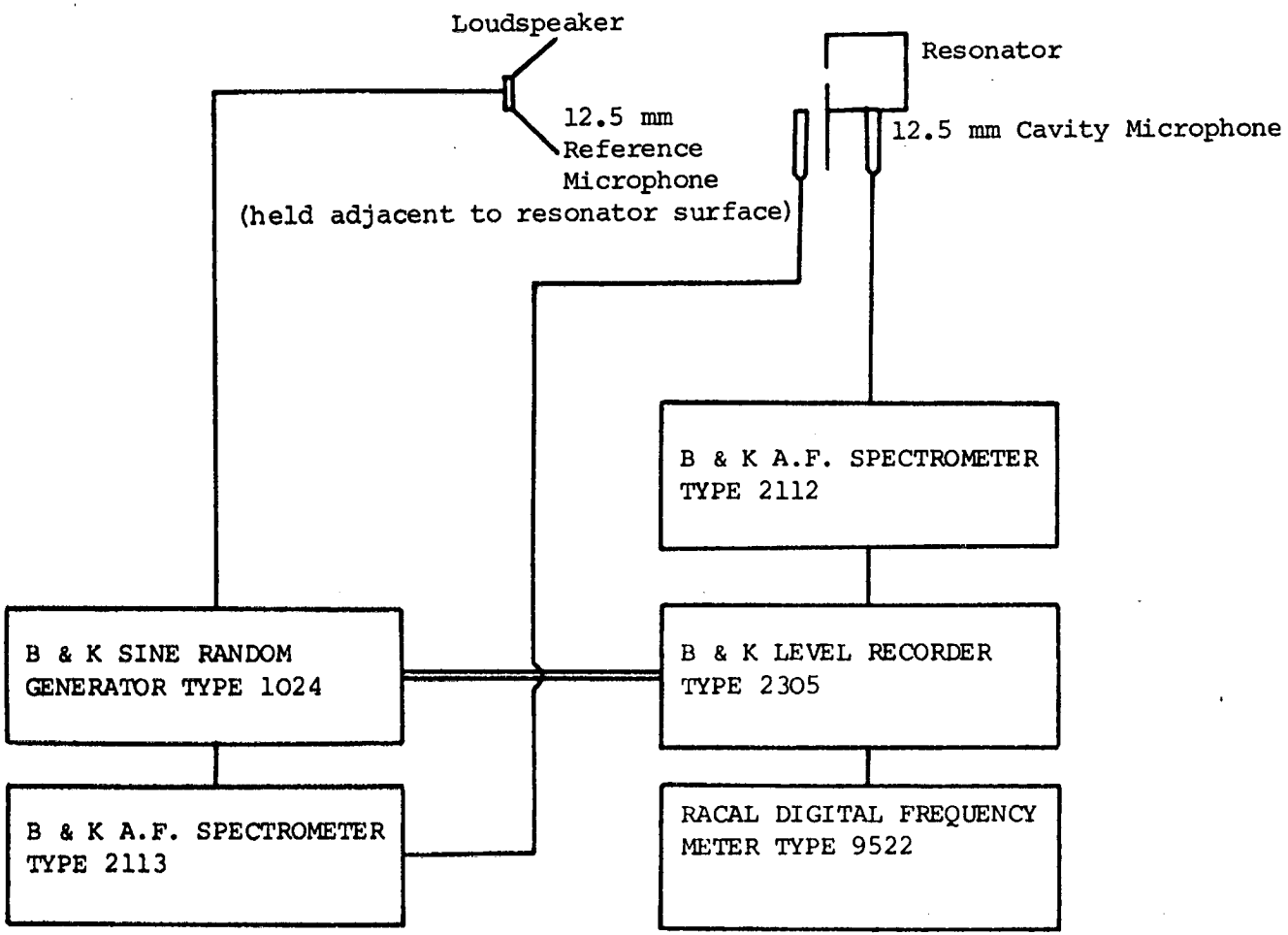

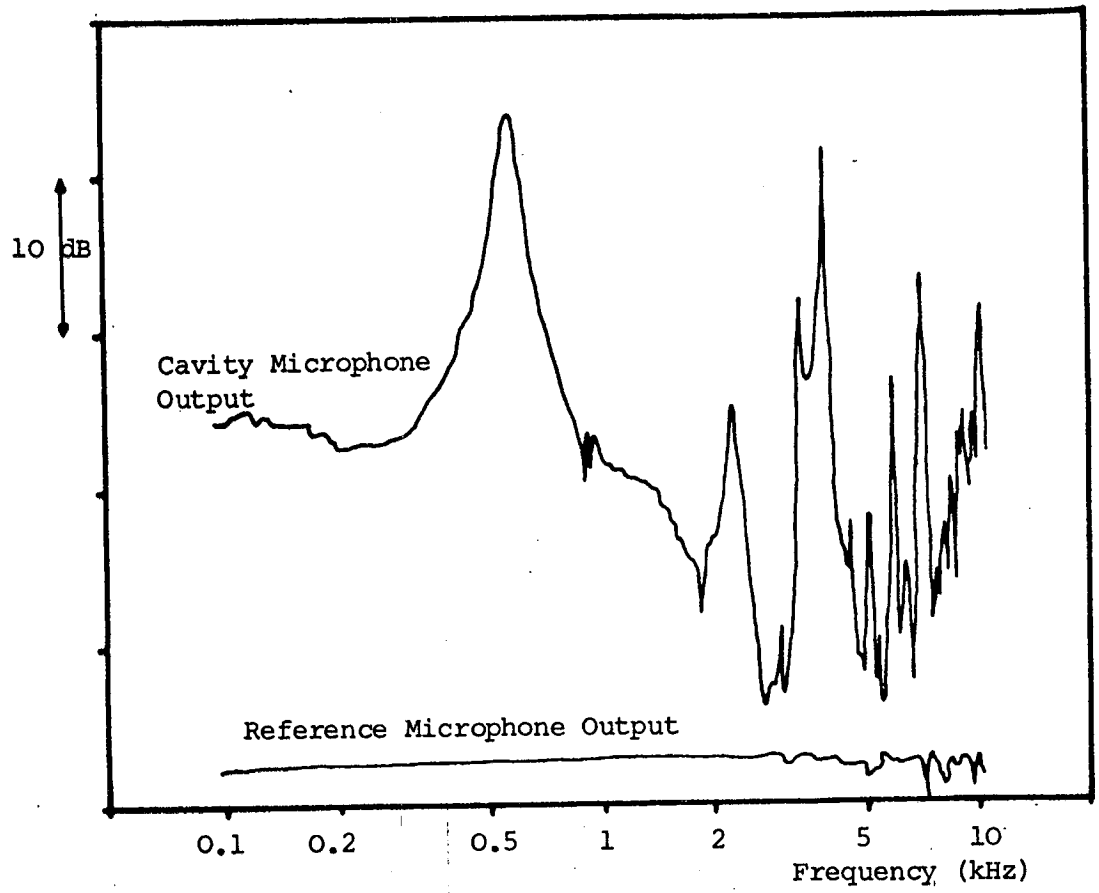

FIGURE 3 Results of resonator frequency response test.

FIGURE 4 The detailed frequency response of the resonator near the Helmholtz frequency

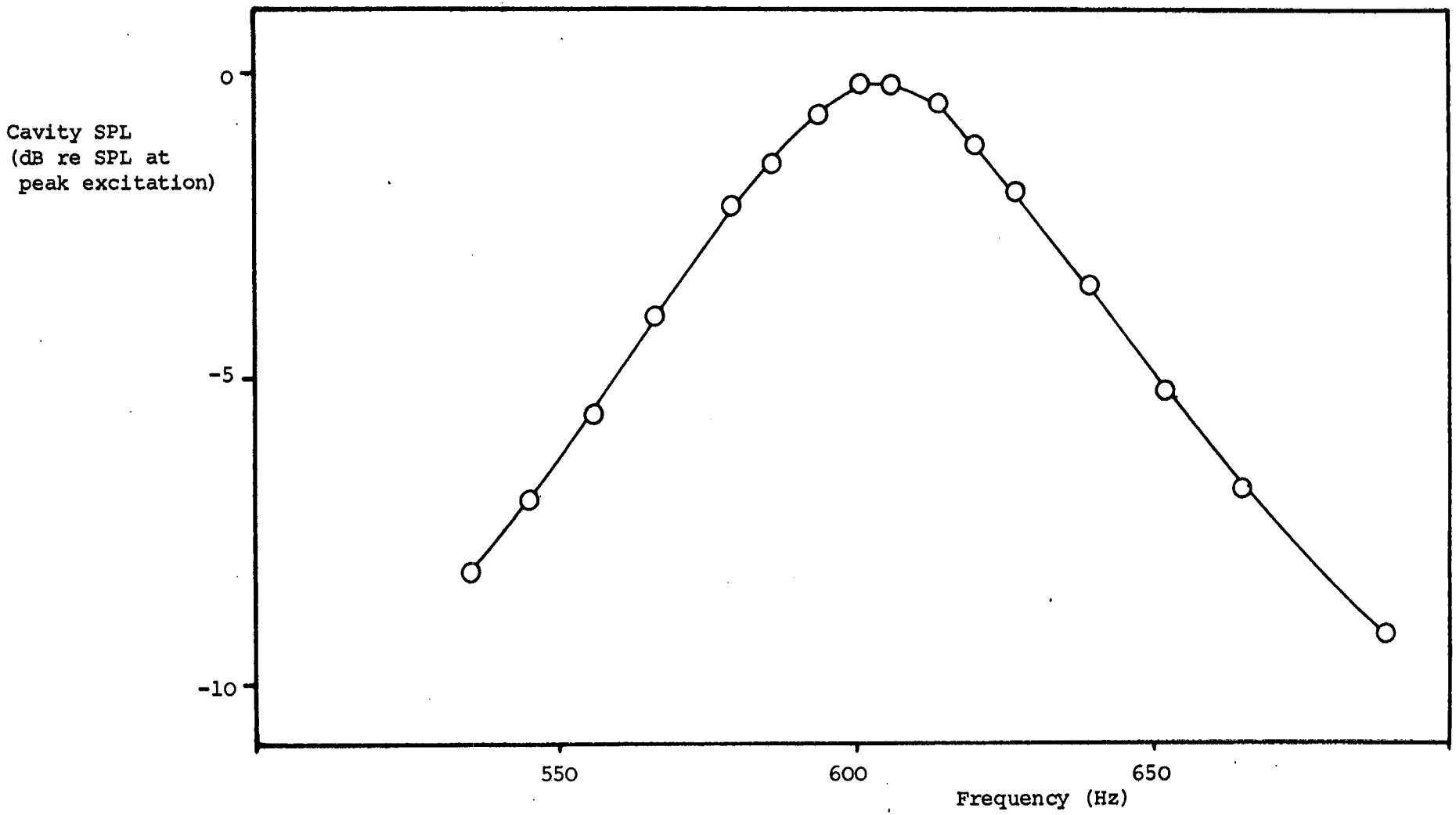

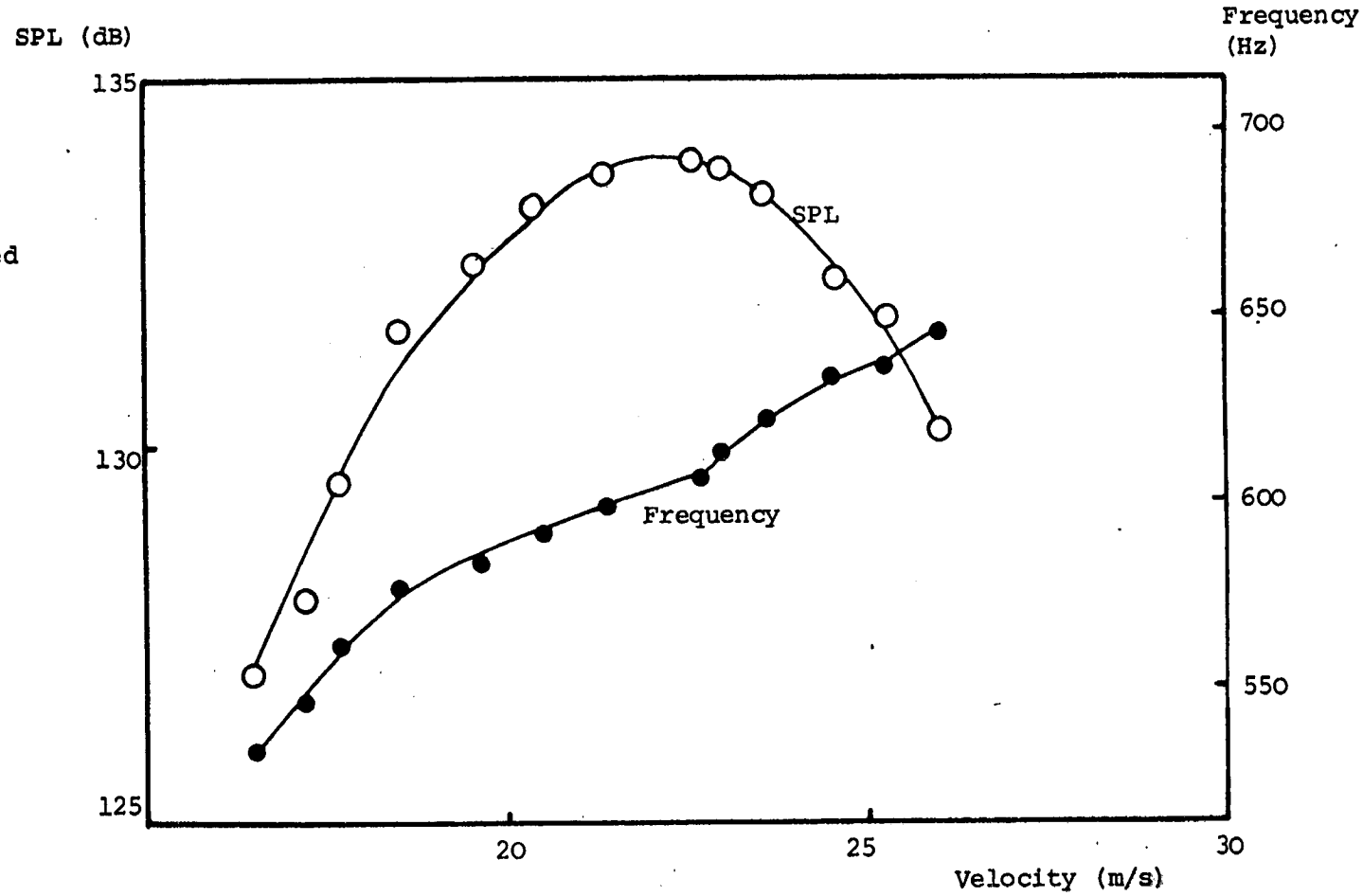

FIGURE 5 The response of the resonator when excited aerodynamically.

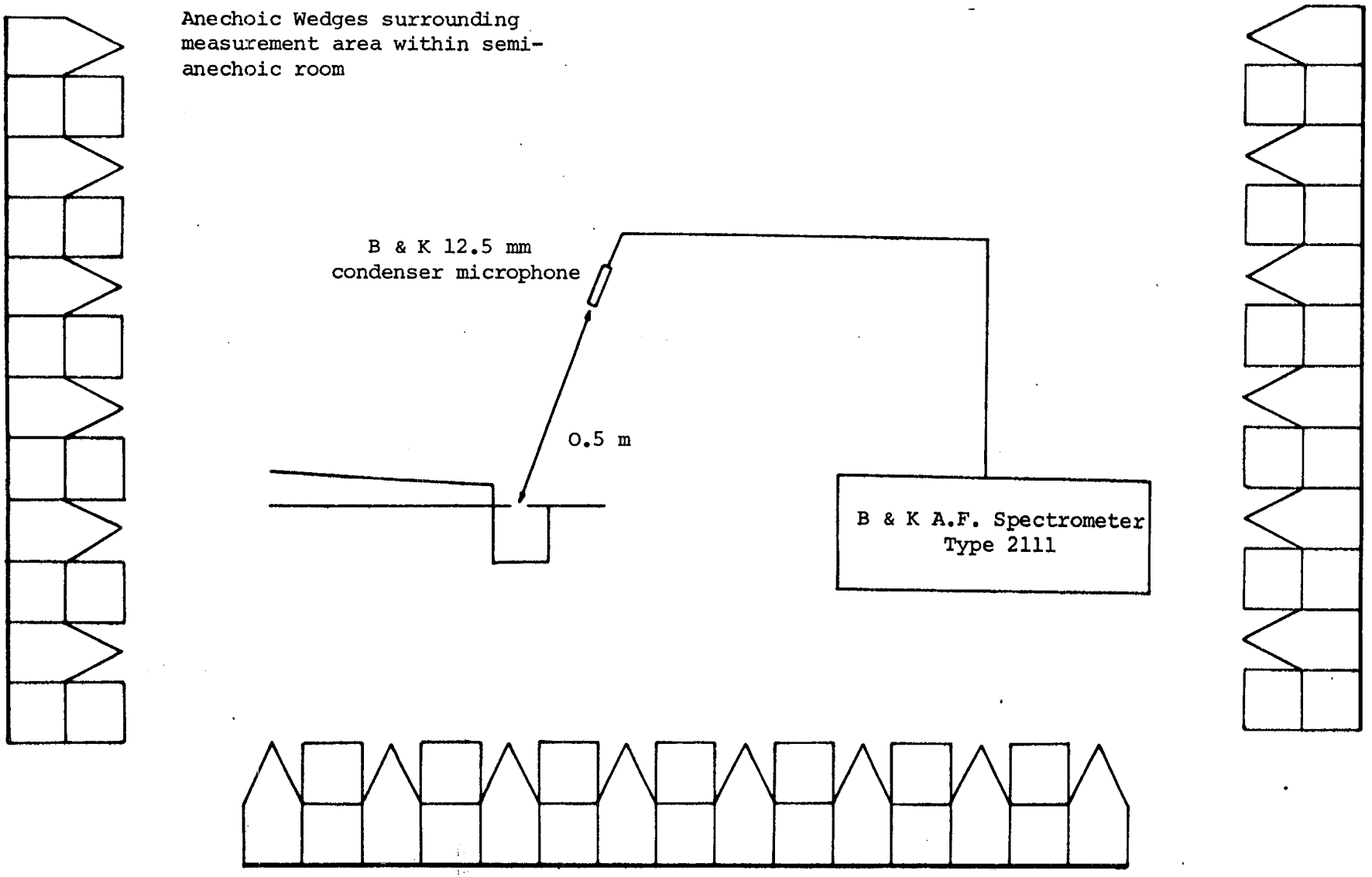

FIGURE 6 Measurement of the sound power radiated by the aerodynamically excited resonator.

FIGURE 7 The decay of sound pressure level with distance away from the resonator.

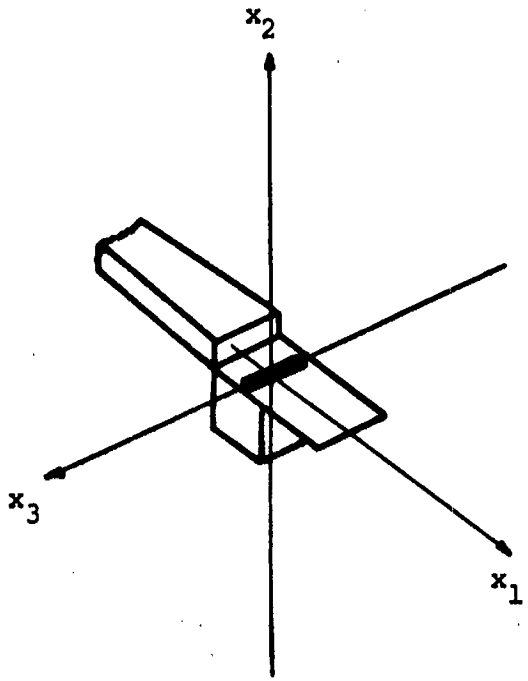

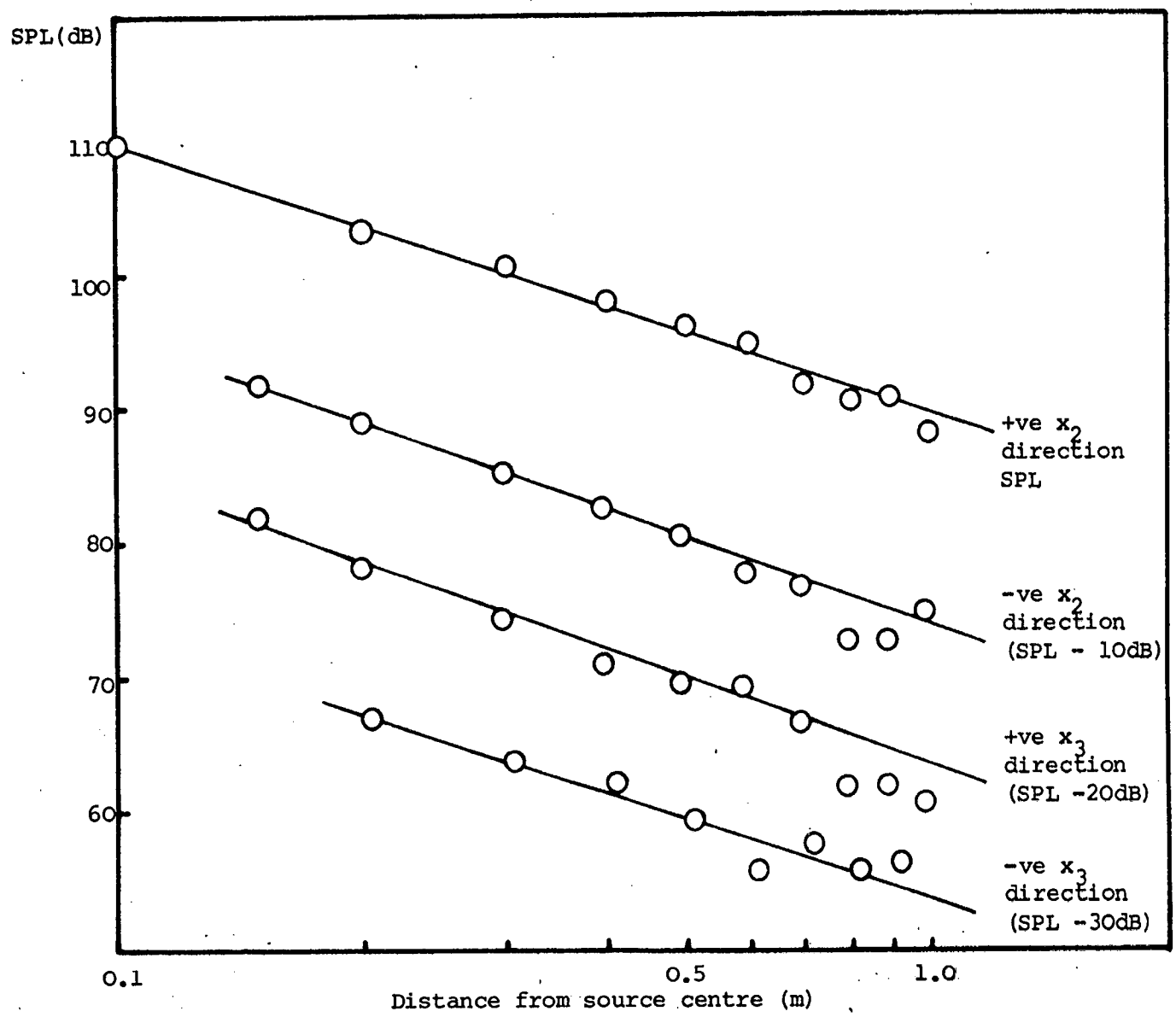

View from above the resonator

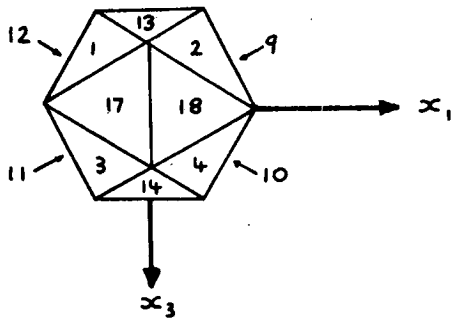

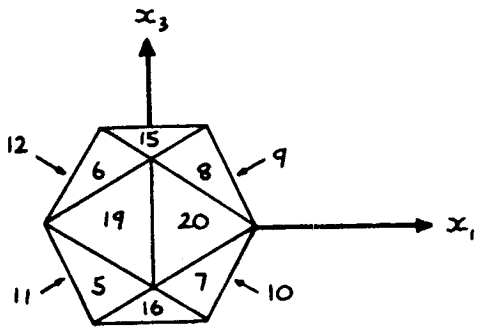

View from below the resonator

Position	Measured SPL (dB)			Position	Measured SPL (dB)		
	1	2	3		1	2	3
1	92.5	92.5	93.0	11	92.5	93.5	92.75
2	94.0	94.25	94.0	12	90.25	91.25	90.75
3	93.25	93.5	93.5	13	91.75	93.25	93.75
4	94.5	95.5	95.0	14	92.0	93.5	93.25
5	88.5	91.5	91.25	15	90.25	89.0	90.0
6	88.0	89.5	89.75	16	86.5	87.75	87.5
7	91.25	92.0	92.5	17	94.25	94.5	95.25
8	90.5	92.25	92.25	18	95.25	95.5	95.0
9	93.0	93.0	92.75	19	89.5	90.75	90.75
10	95.0	94.5	94.25	20	90.75	91.25	91.75

FIGURE 8 Results of the measurement of the SPL at 0.5 m from the resonator neck. (Measurements were taken at the centre of each face of an icosahedral surface surrounding the resonator)

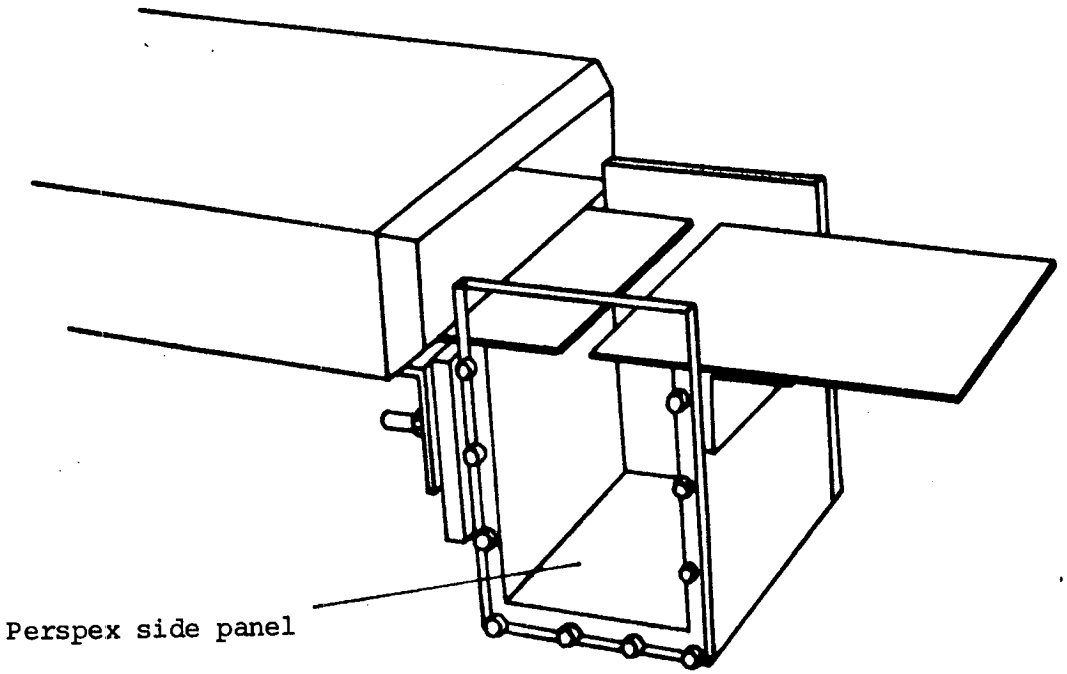

FIGURE 9 The resonator used for flow visualisation.

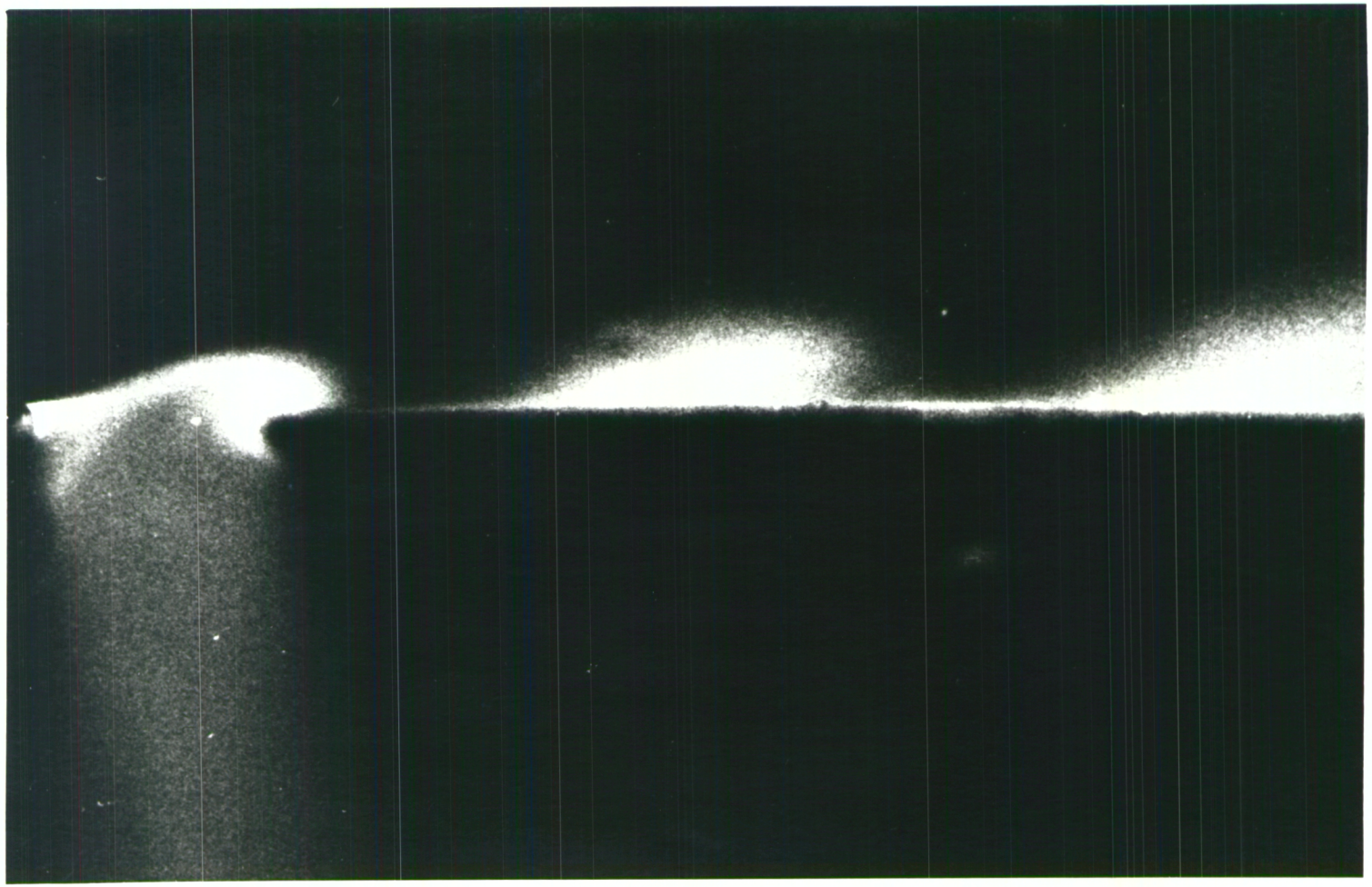

FIGURE 10. Photograph showing the flow "frozen" at a point in the vortex shedding cycle. One vortex is shown interacting with the downstream edge of the resonator neck with two previously shed vortices convecting downstream.

FIGURE 11 Instrumentation for flow visualisation experiments.

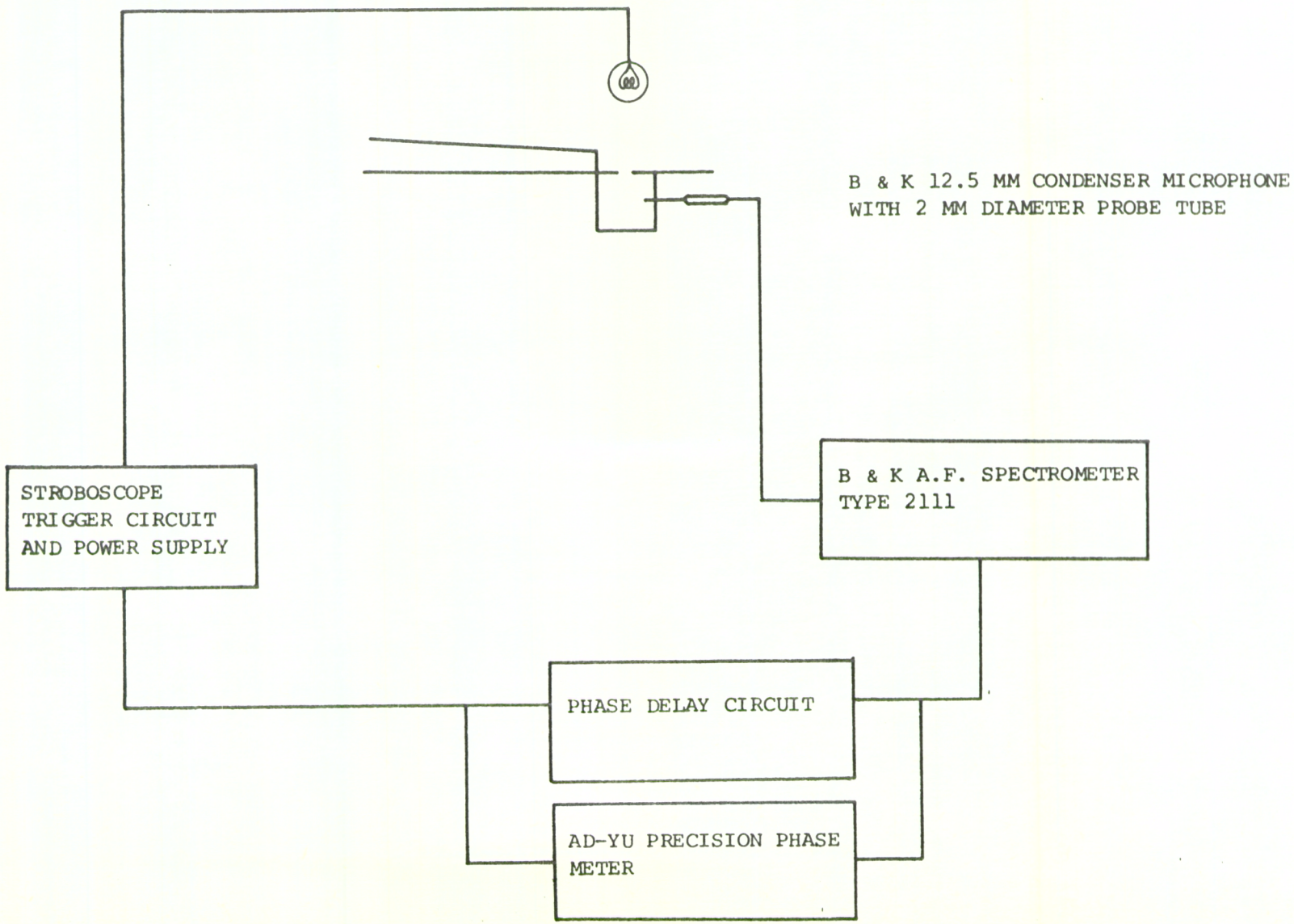

FIGURE 12. Photographs showing the flow in the resonator neck "frozen" at twelve times during the cycle. (The times shown are the times after the minimum cavity pressure occurs at the start of the first cycle; T = 1653 μs)

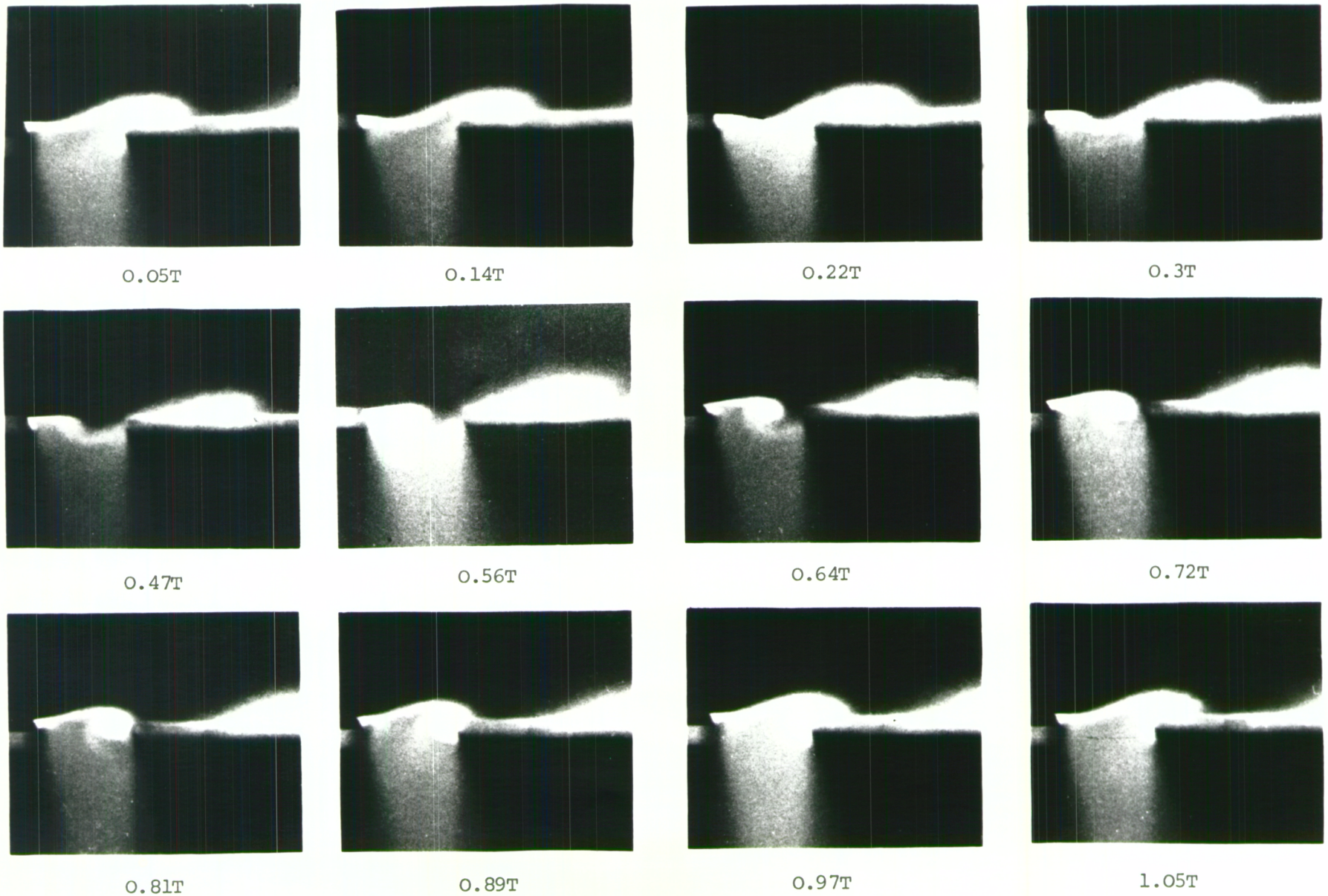

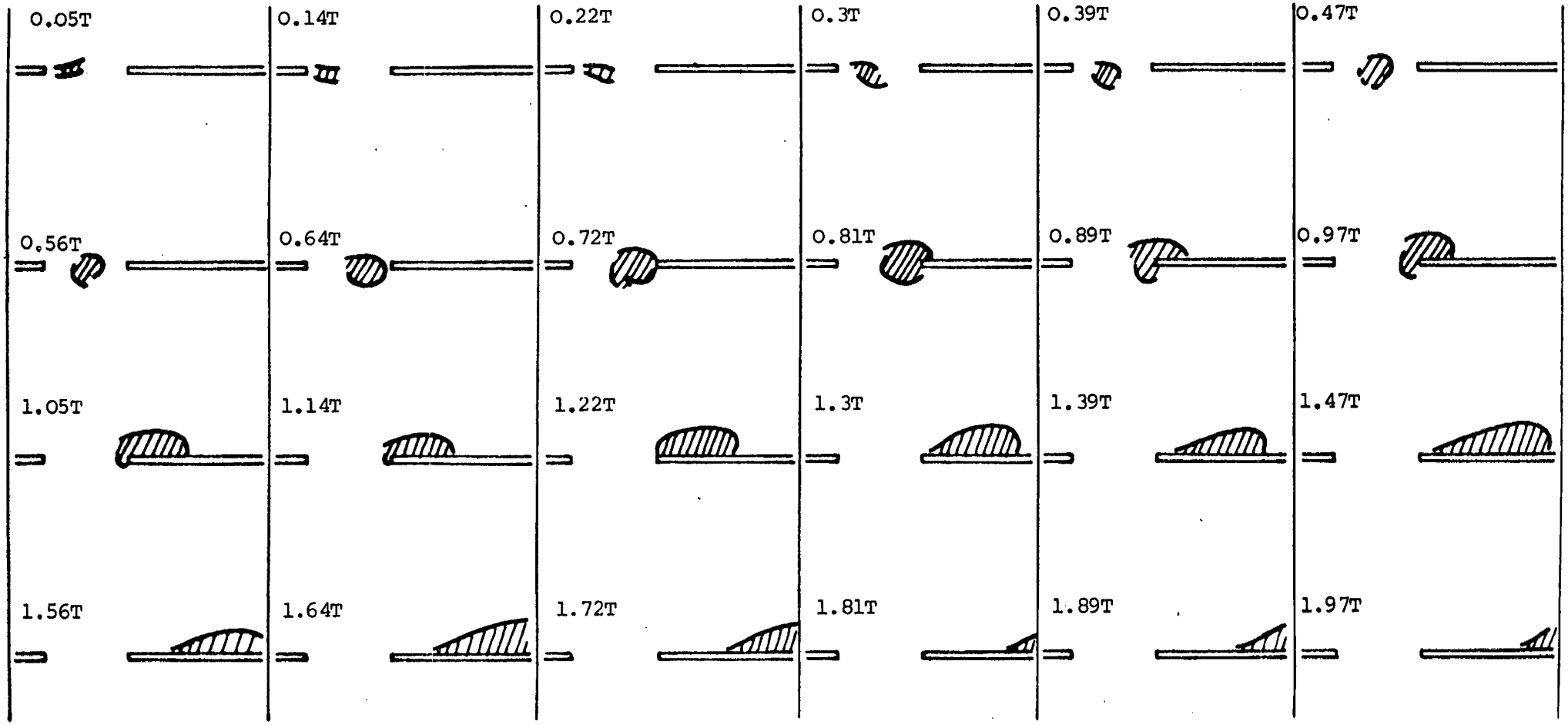

FIGURE 13 Sketches showing the approximate position of the vortex during two cycles of the motion. (The times shown are the times after the minimum cavity pressure occurs at the start of the first cycle; T = 1653 μS)

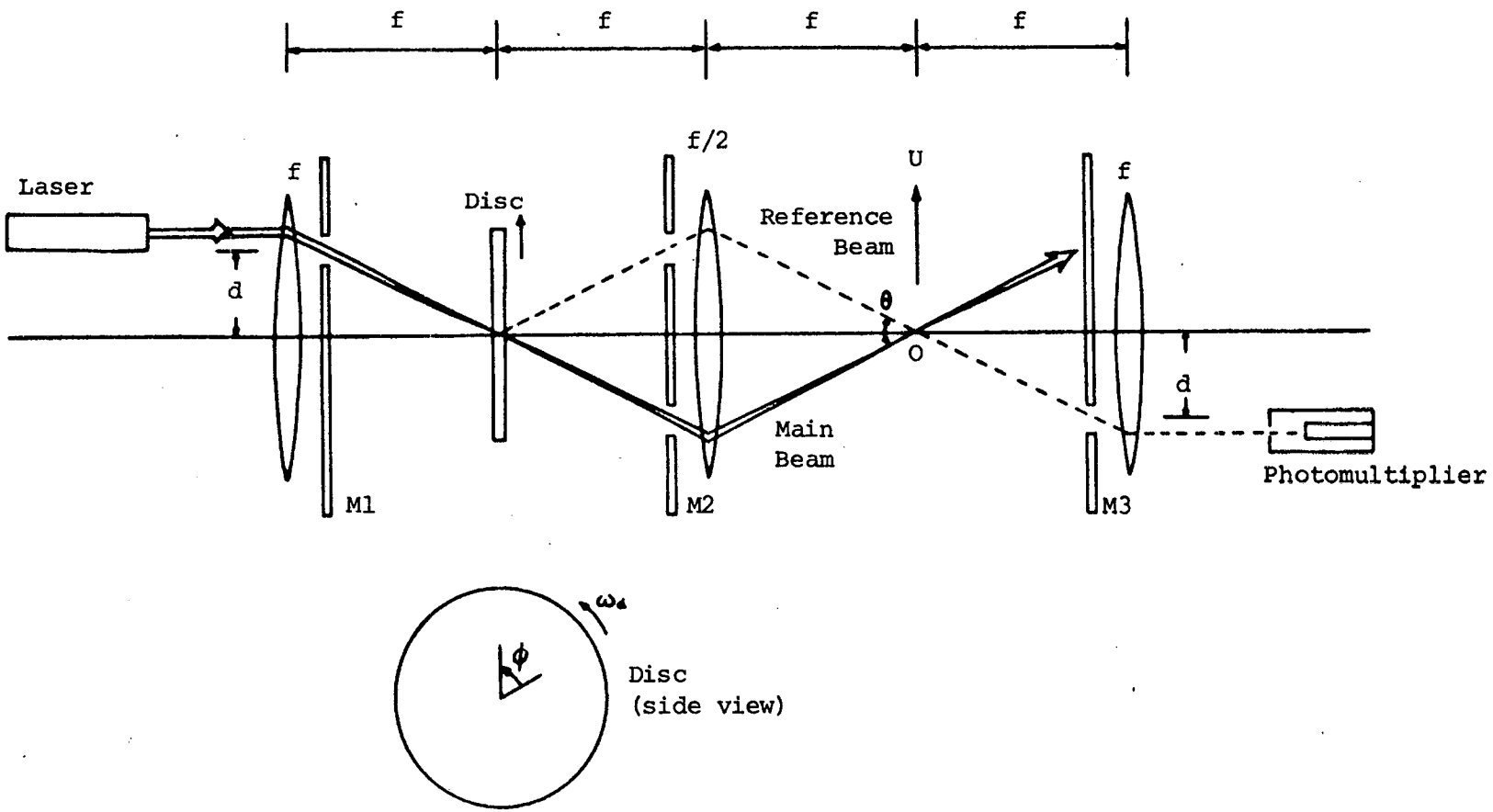

FIGURE 14 The basic optical arrangement for a one component reference beam velocimeter.

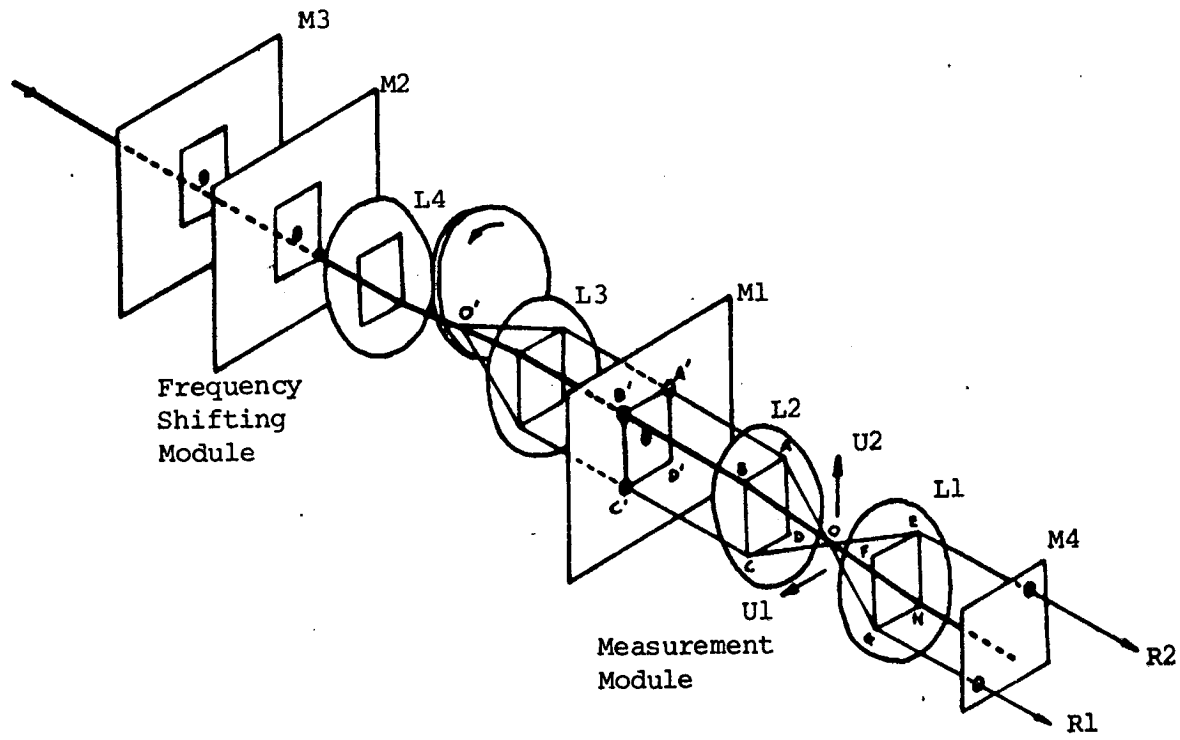

FIGURE 15 The optical arrangement for a two component velocimeter.

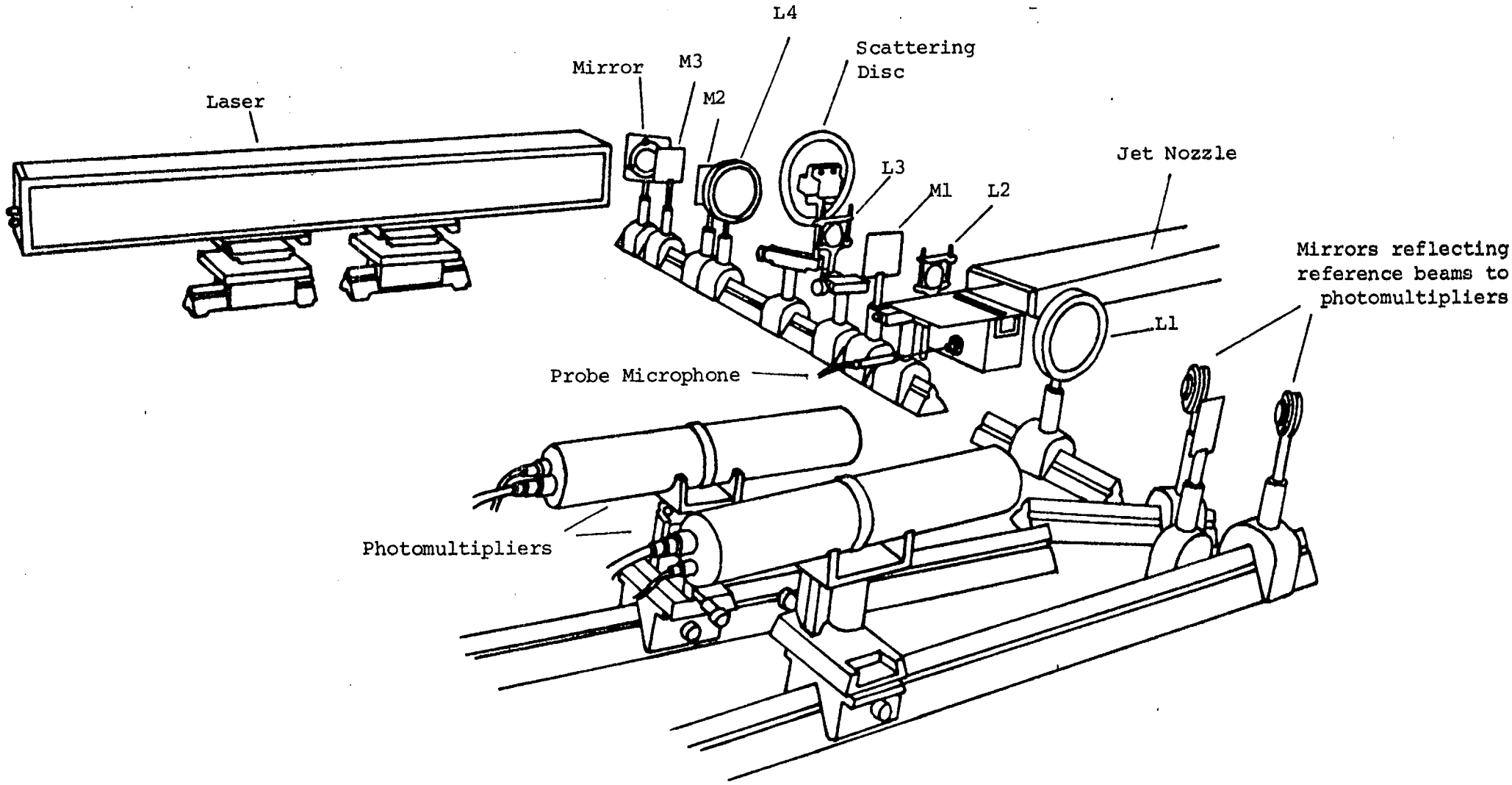

FIGURE 16 The experimental arrangement used for the velocity measurements.

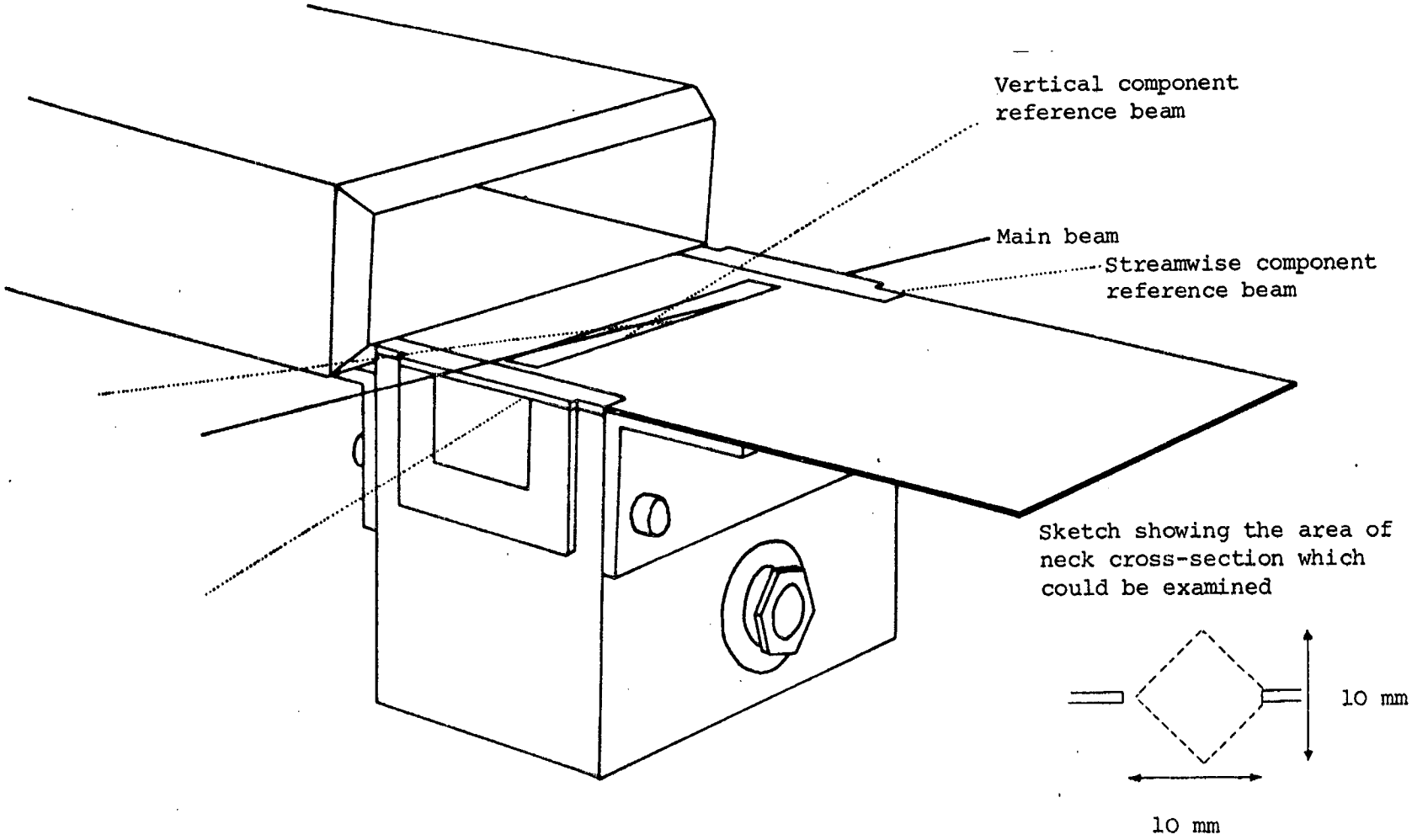

FIGURE 17 The arrangement of the main beam and reference beams in the resonator neck.

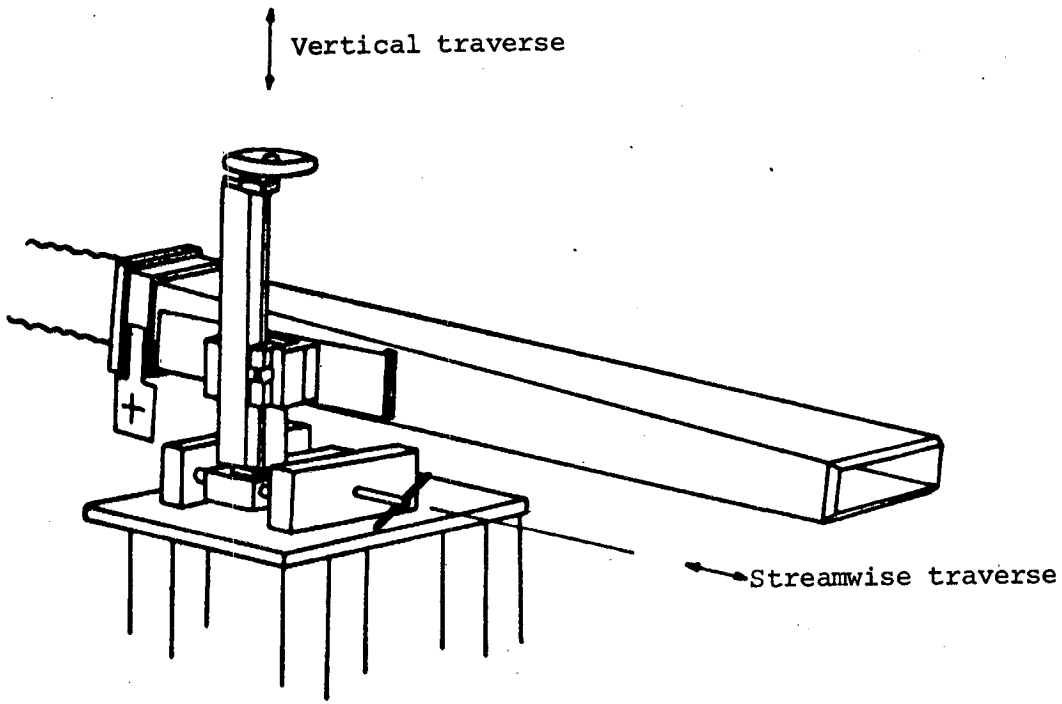

FIGURE 18 The arrangement used for traversing the jet nozzle with the resonator attached.

FIGURE 19 The instrumentation used in measuring the velocity field in the resonator neck.

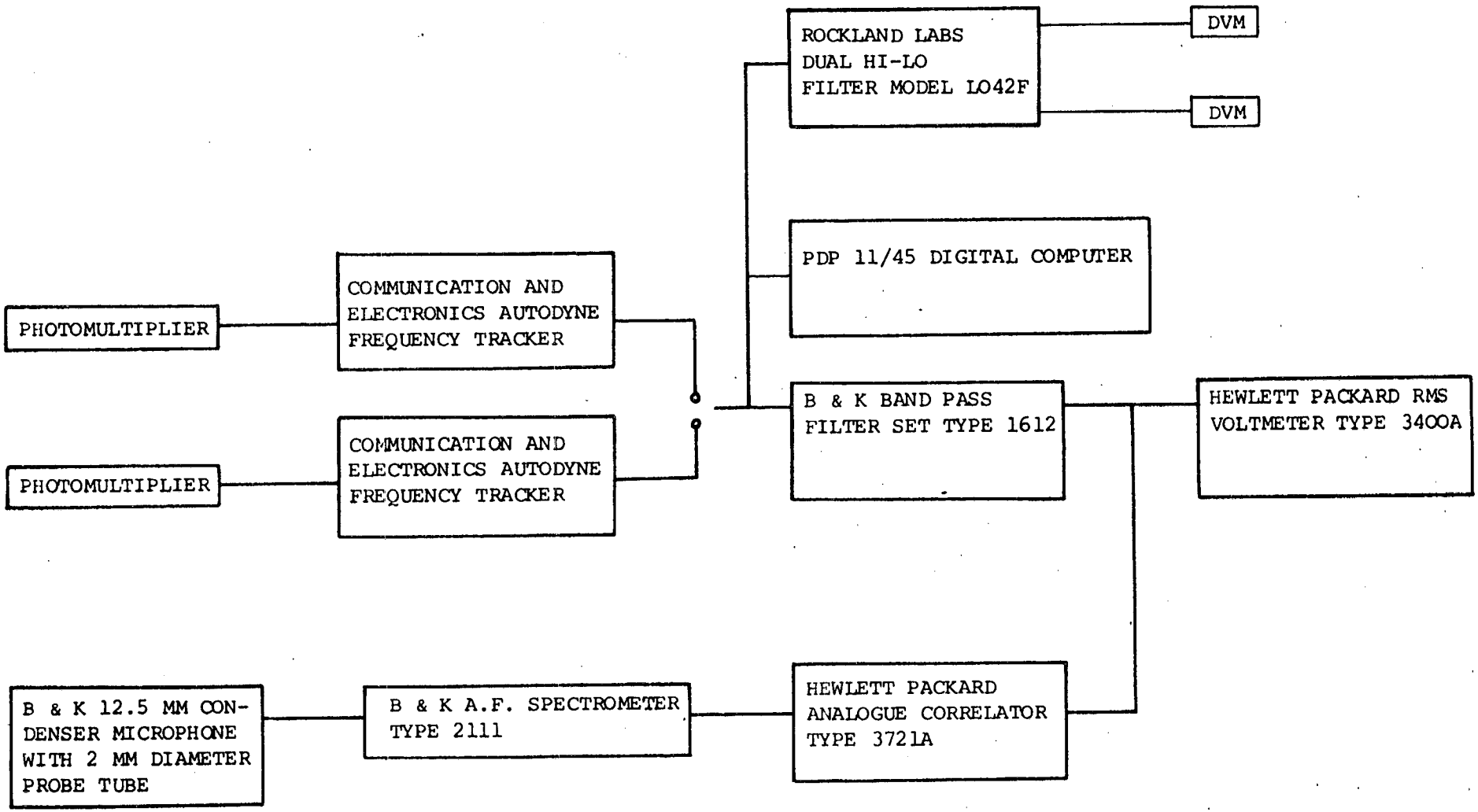

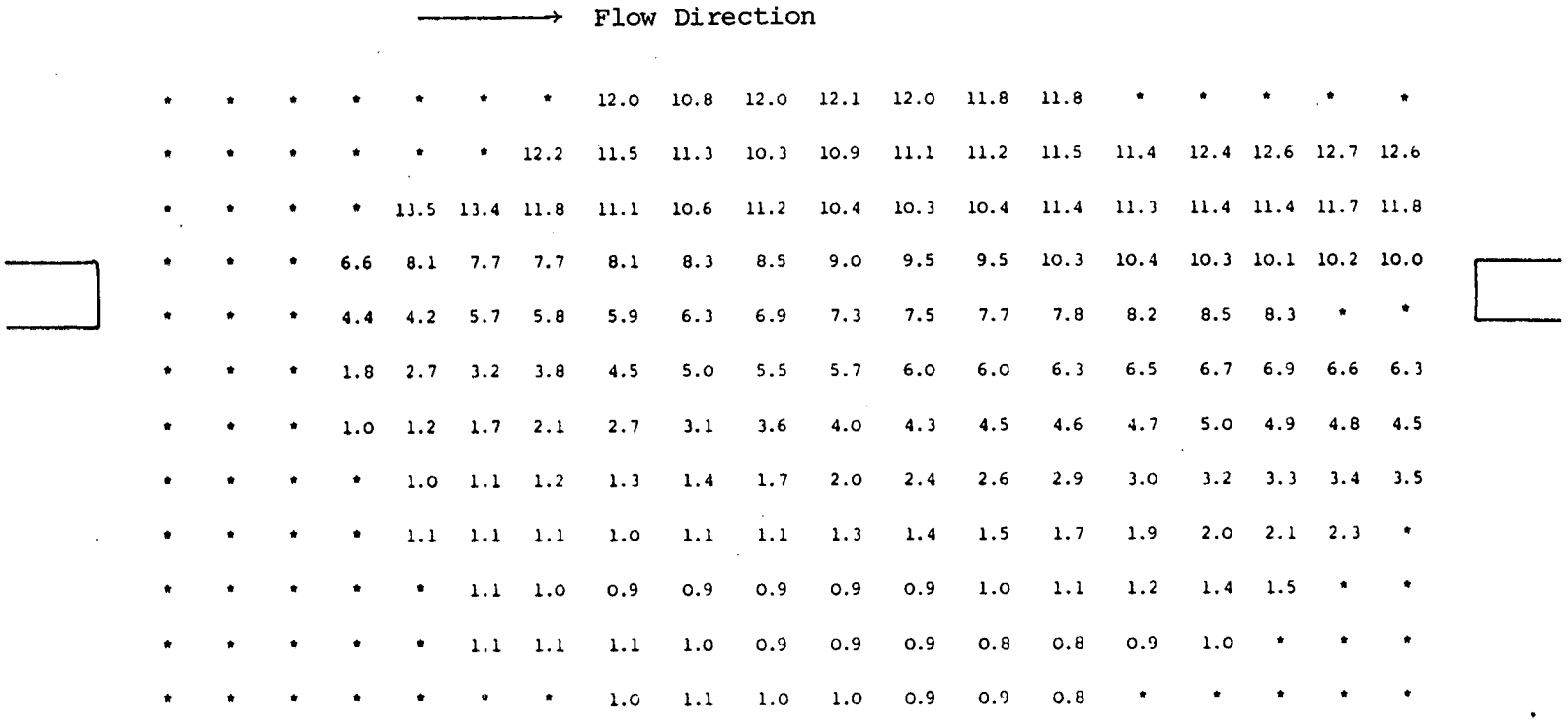

FIGURE 20 Measured values of mean velocity in the streamwise direction.
(Results in m/s ± 0.2 m/s. Measurement grid points are at 0.5 mm intervals.)

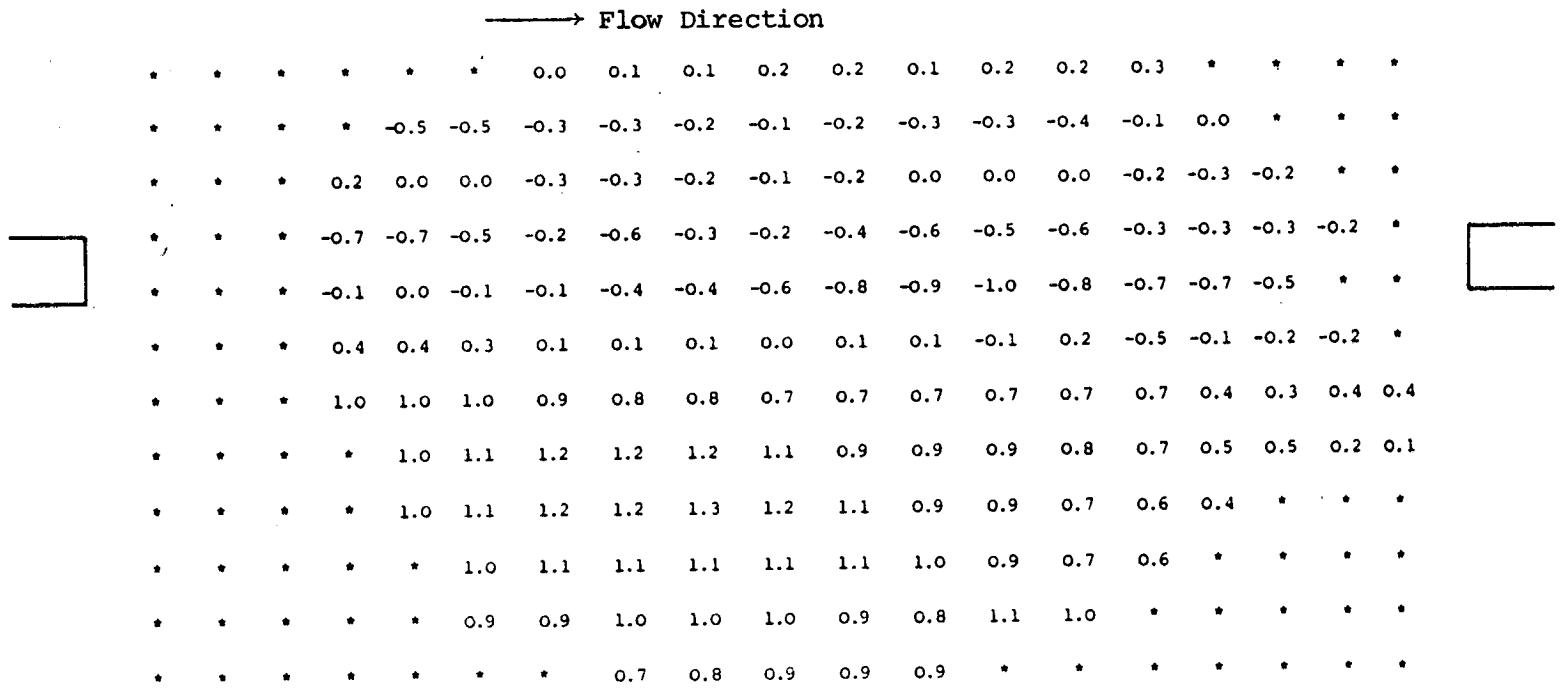

FIGURE 21 Measured values of mean velocity in the vertical direction.
(Results in m/s ± 0.2 m/s. Measurement grid points are at 0.5 mm intervals.)

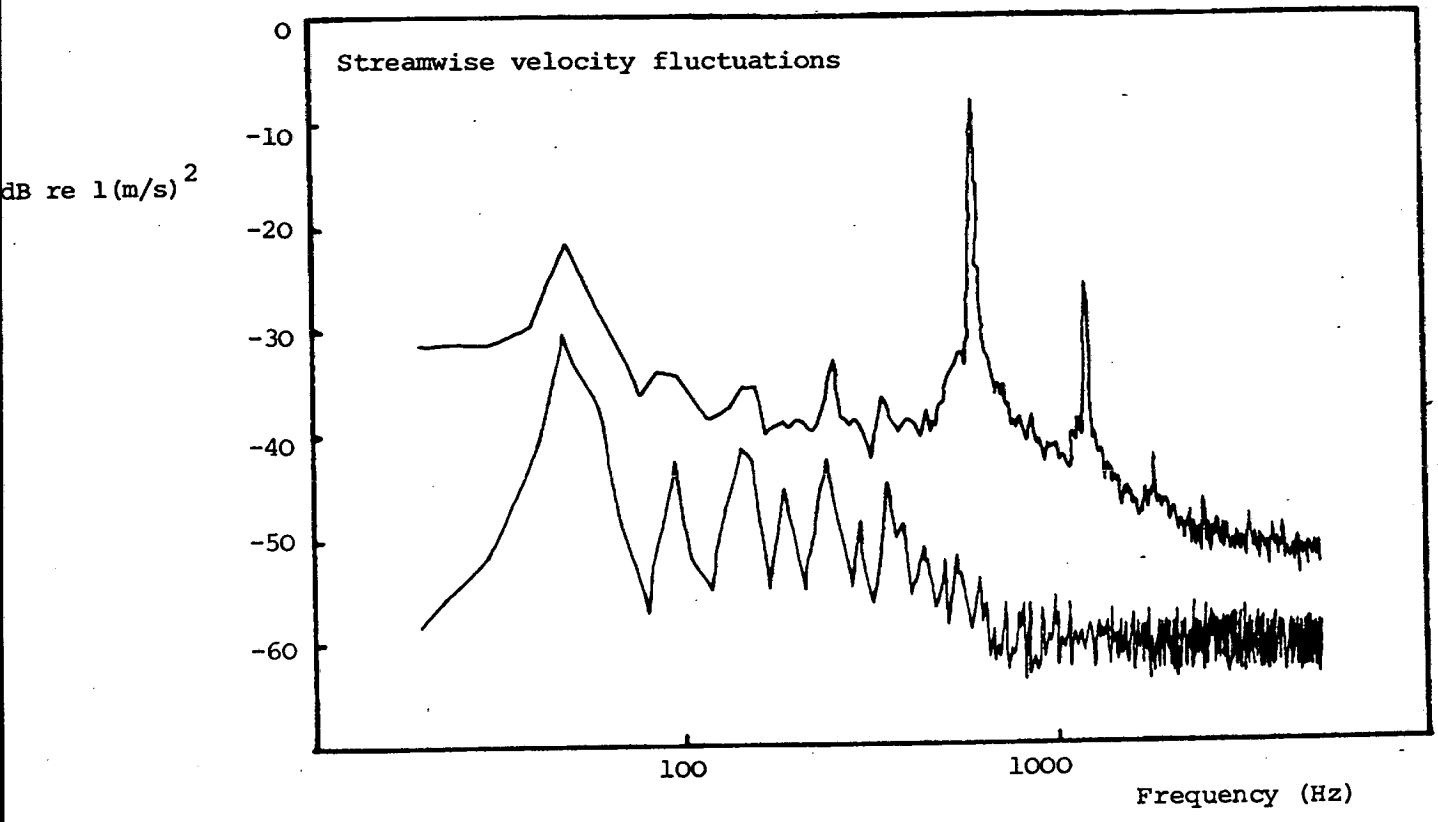

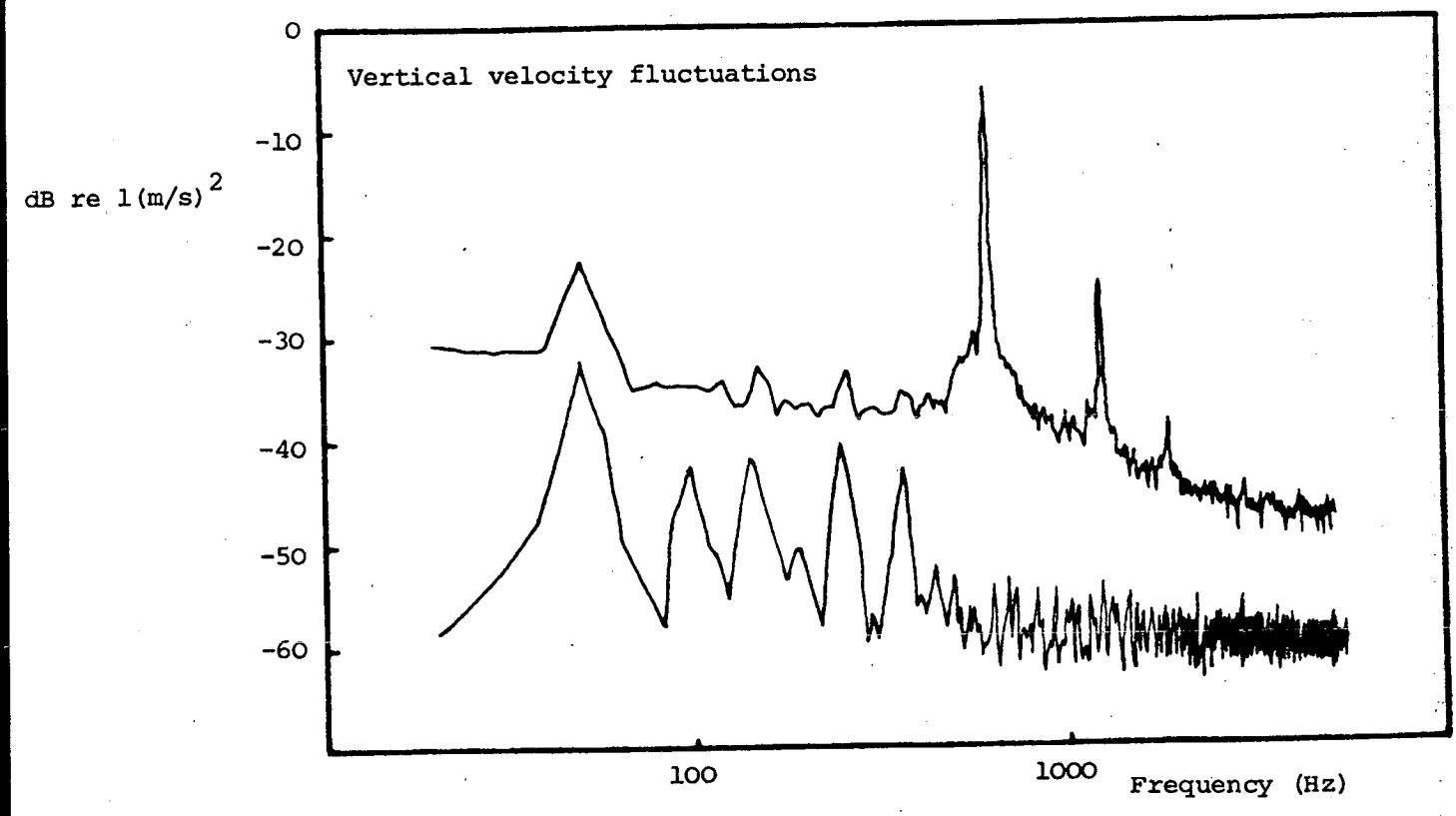

FIGURE 22 Power spectra of the measured velocity fluctuations showing the background noise due to the motion of the particles on the scattering disc.

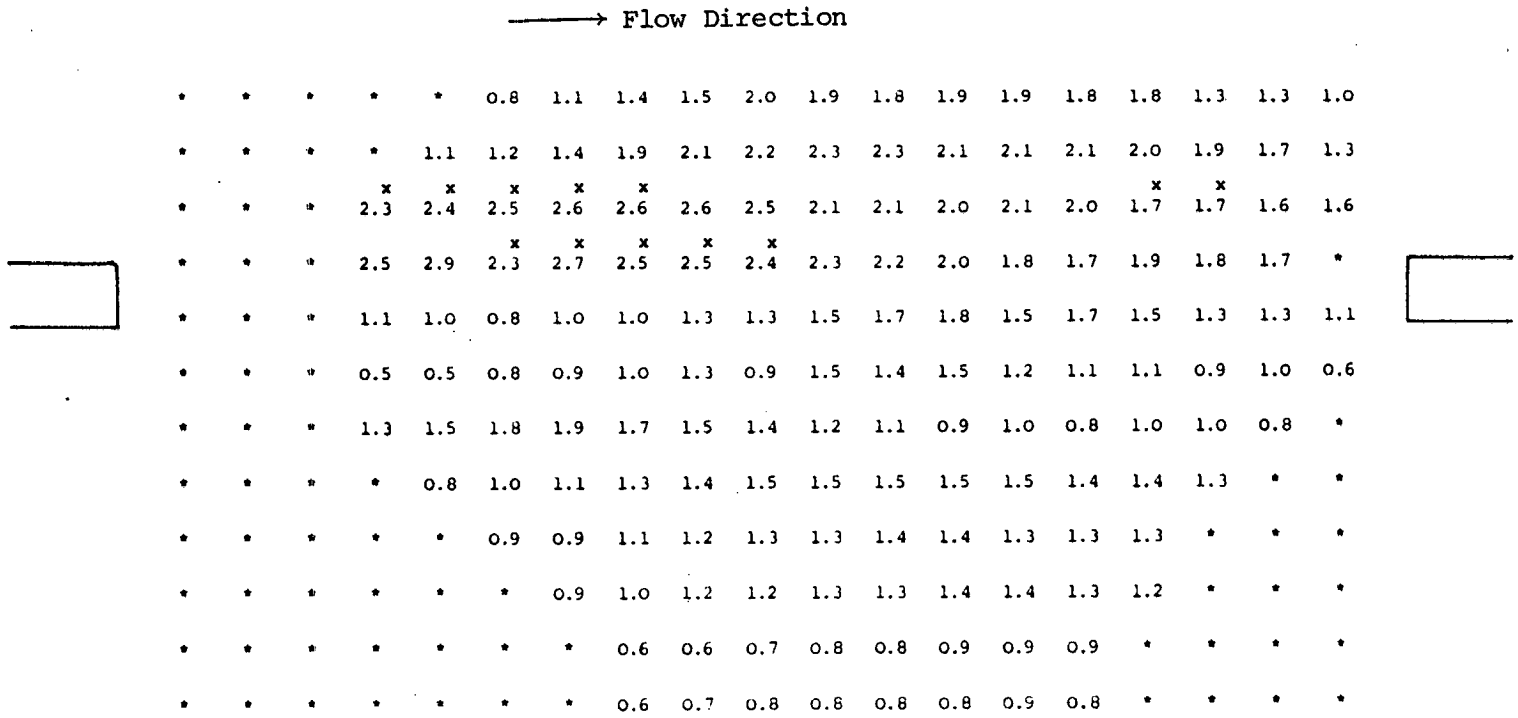

FIGURE 23 Measured r.m.s. values of the fluctuating velocity in the streamwise direction. (Results in m/s ± 0.2 m/s, except results marked x where the accuracy is ± 0.4 m/s. Measurement grid points are at 0.5 mm intervals.)

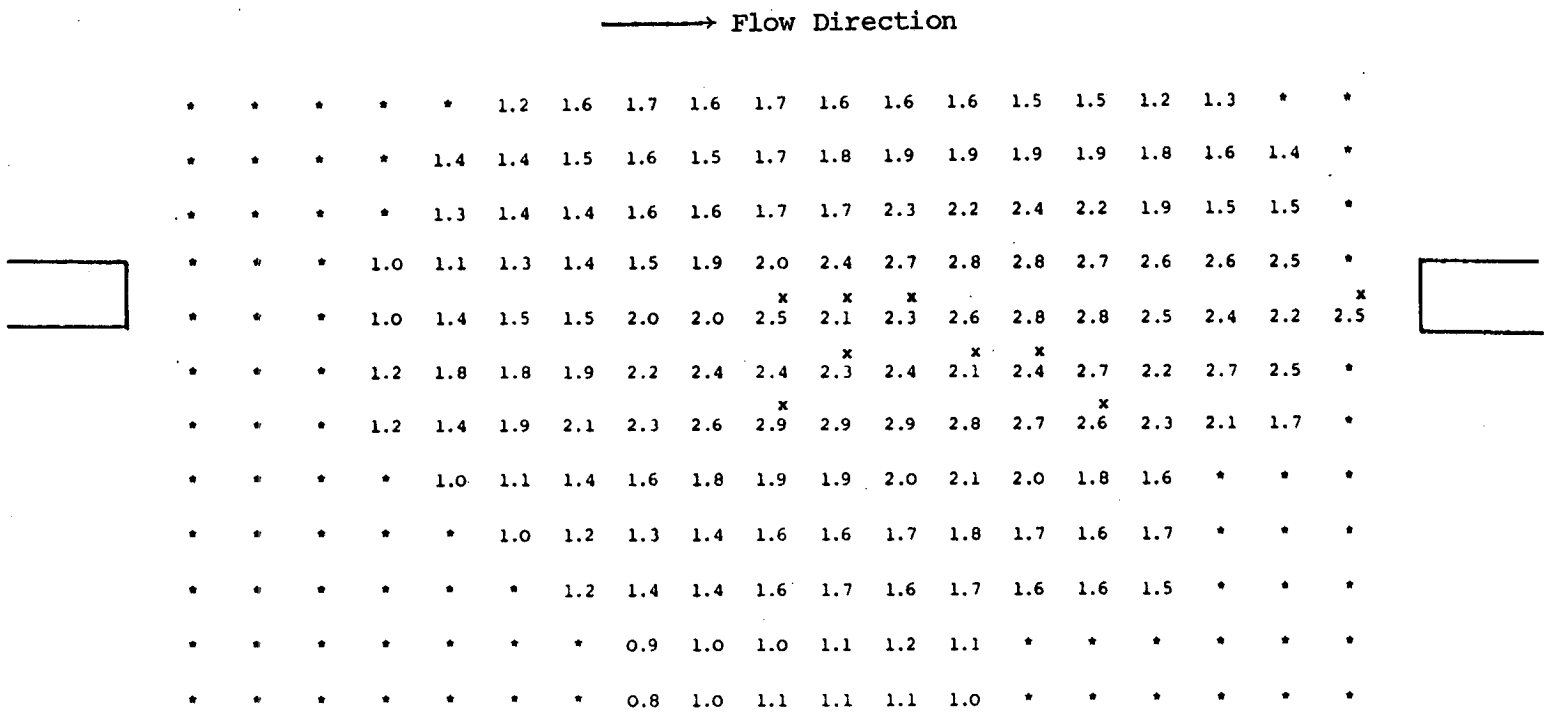

FIGURE 24 Measured r.m.s. values of the fluctuating velocity in the vertical direction. (Results in m/s ± 0.2 m/s, except results marked x where accuracy is ± 0.4 m/s. Measurement grid points are at 0.5 mm intervals.)

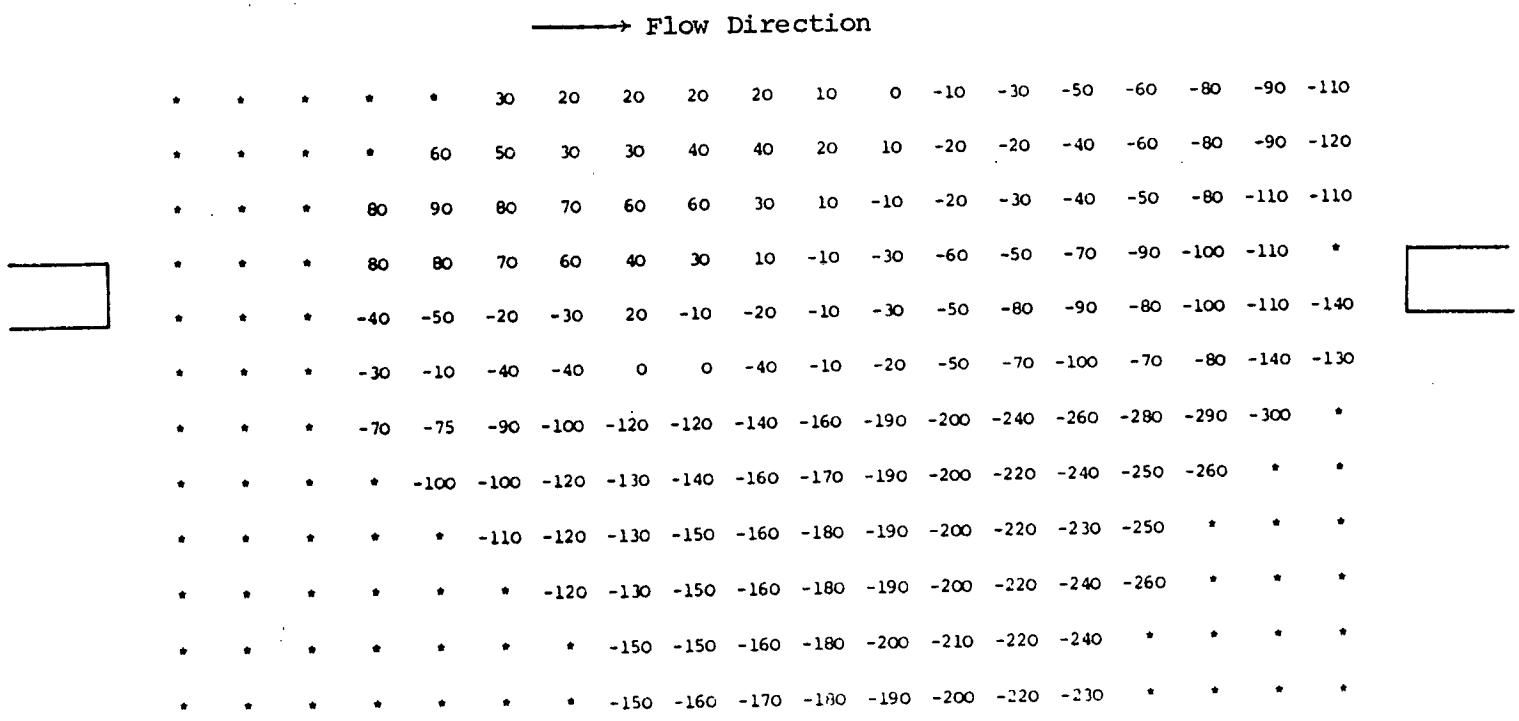

FIGURE 25 Measured values of the phase of the streamwise velocity fluctuations relative to the cavity pressure fluctuations. (Results in degrees ± 10°. Measurement grid points are at 0.5 mm intervals.)

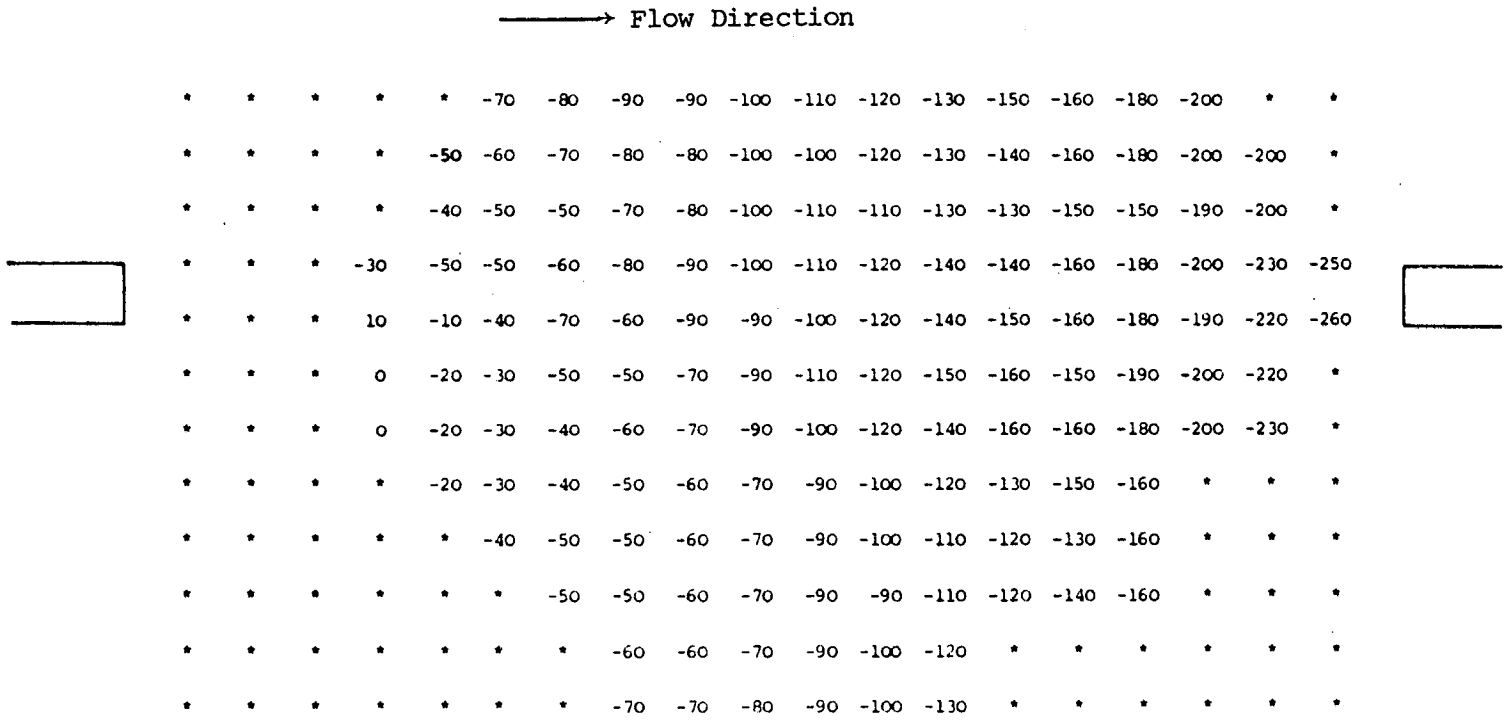

FIGURE 26 Measured values of the phase of the vertical velocity fluctuations. (Results in degrees ± 10°. Measurement grid points are at 0.5 mm intervals.)

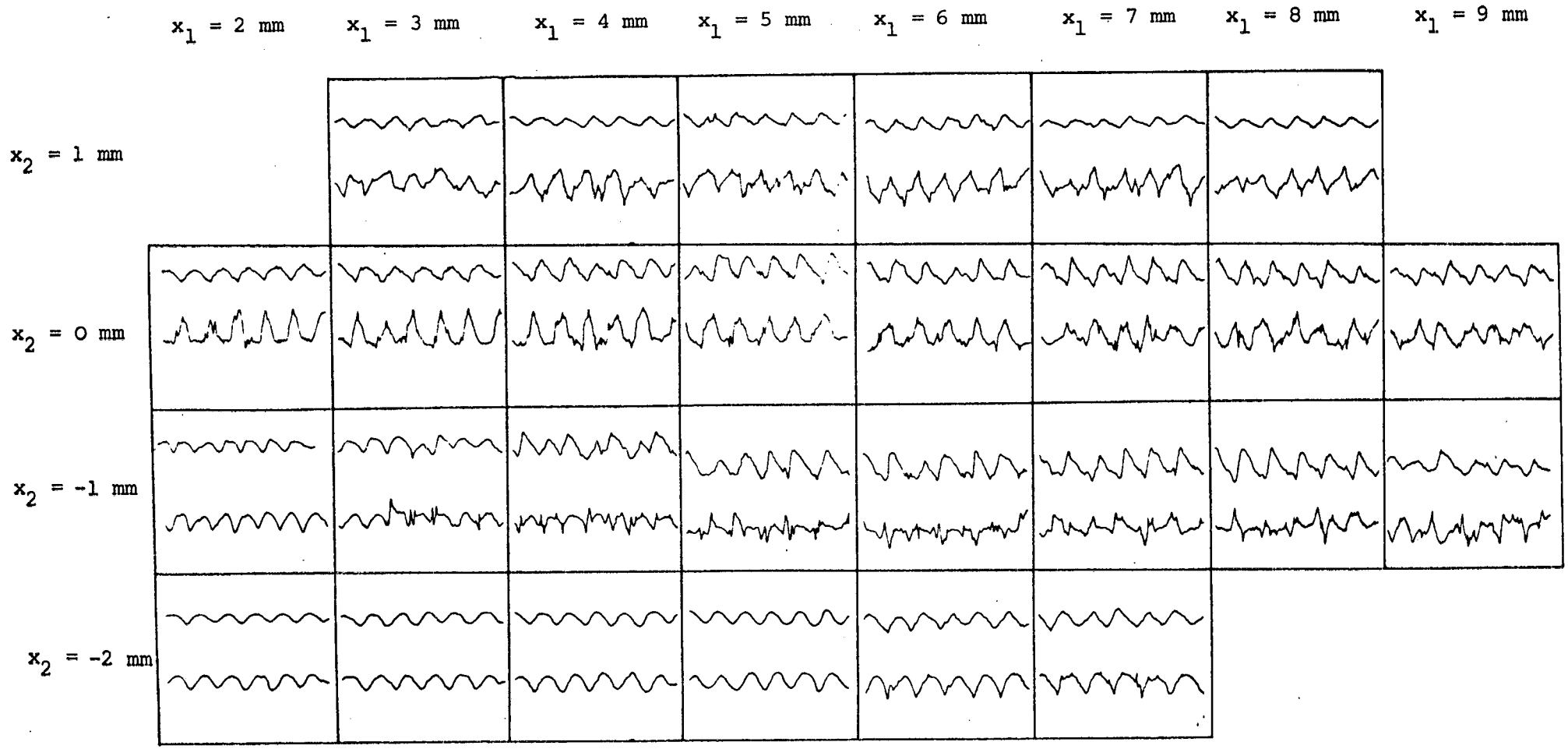

FIGURE 27 Time histories of the velocity signals at various measurement points in the resonator neck. (The upper trace shows the vertical component, the lower trace shows the streamwise component.)

FIGURE 28 A field representation of the measured mean flow vectors in the resonator neck.

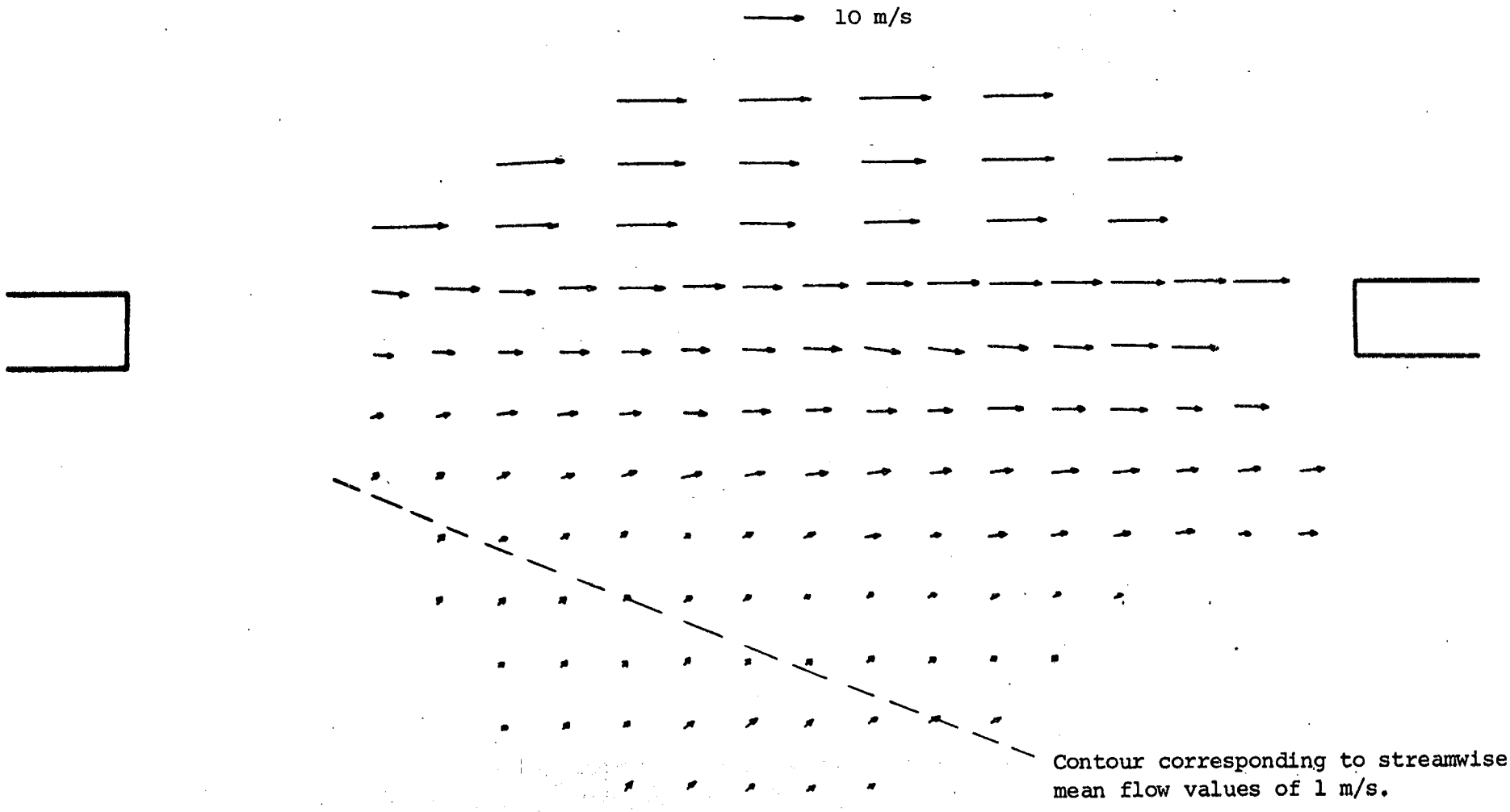

FIGURE 29 Collapse of data from measurements of the mean flow in the streamwise (x_1) direction.

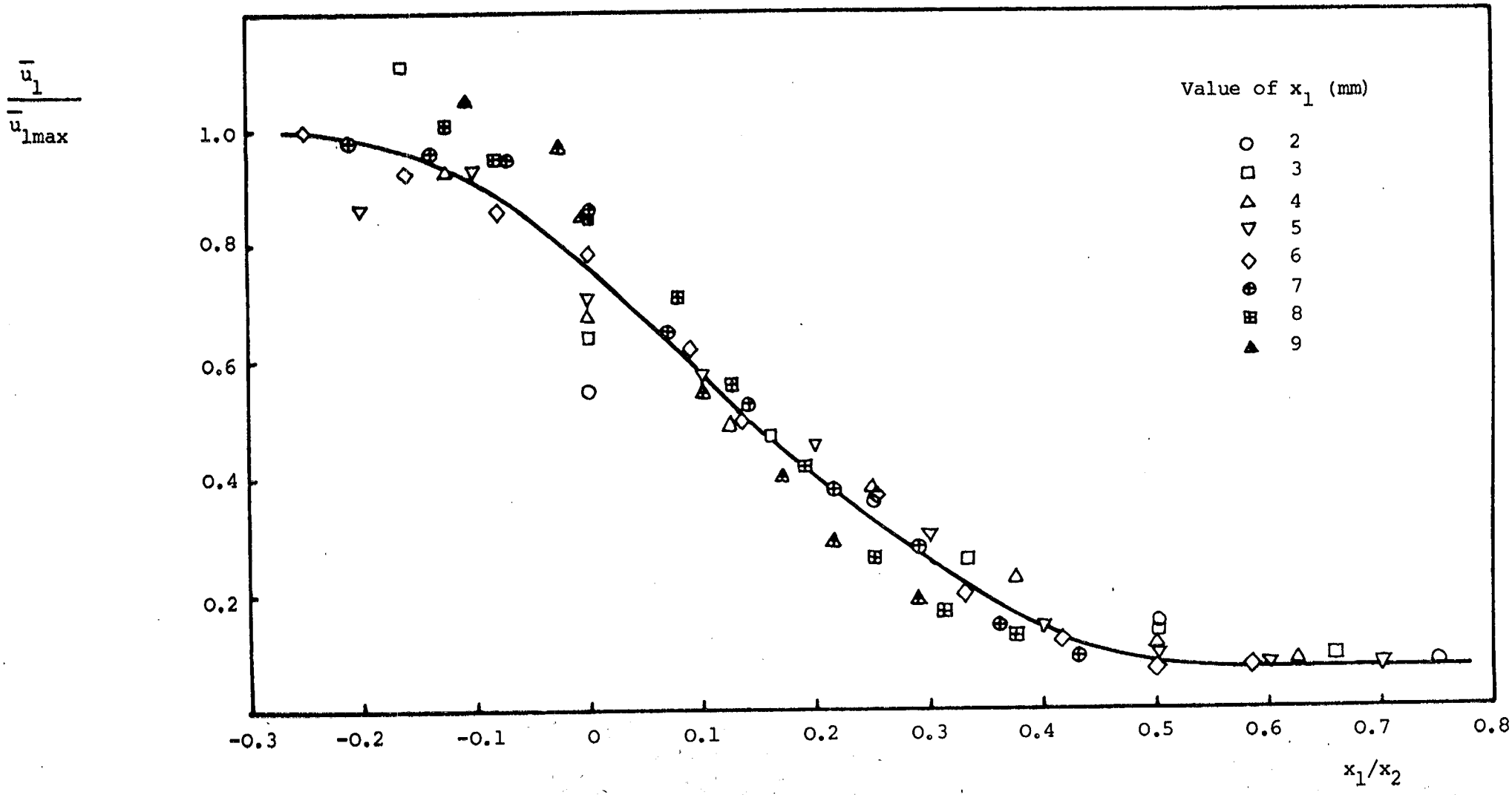

FIGURE 30 Contours of the r.m.s. values of the streamwise velocity fluctuations. (Contours are in increments of 0.1 m/s with the following contours marked: - 1.0, = 1.5, ≡ 2.0, ≣ 2.5 m/s.)

FIGURE 31 Contours of the phase of the streamwise velocity fluctuations relative to the cavity pressure fluctuations.
(Contours are in increments of 20°, with the following contours marked:
- -240°, = -180°, ≡ -120°, ≣ -60°, ≣ 0°, ≣ $+60^{\circ}$.)

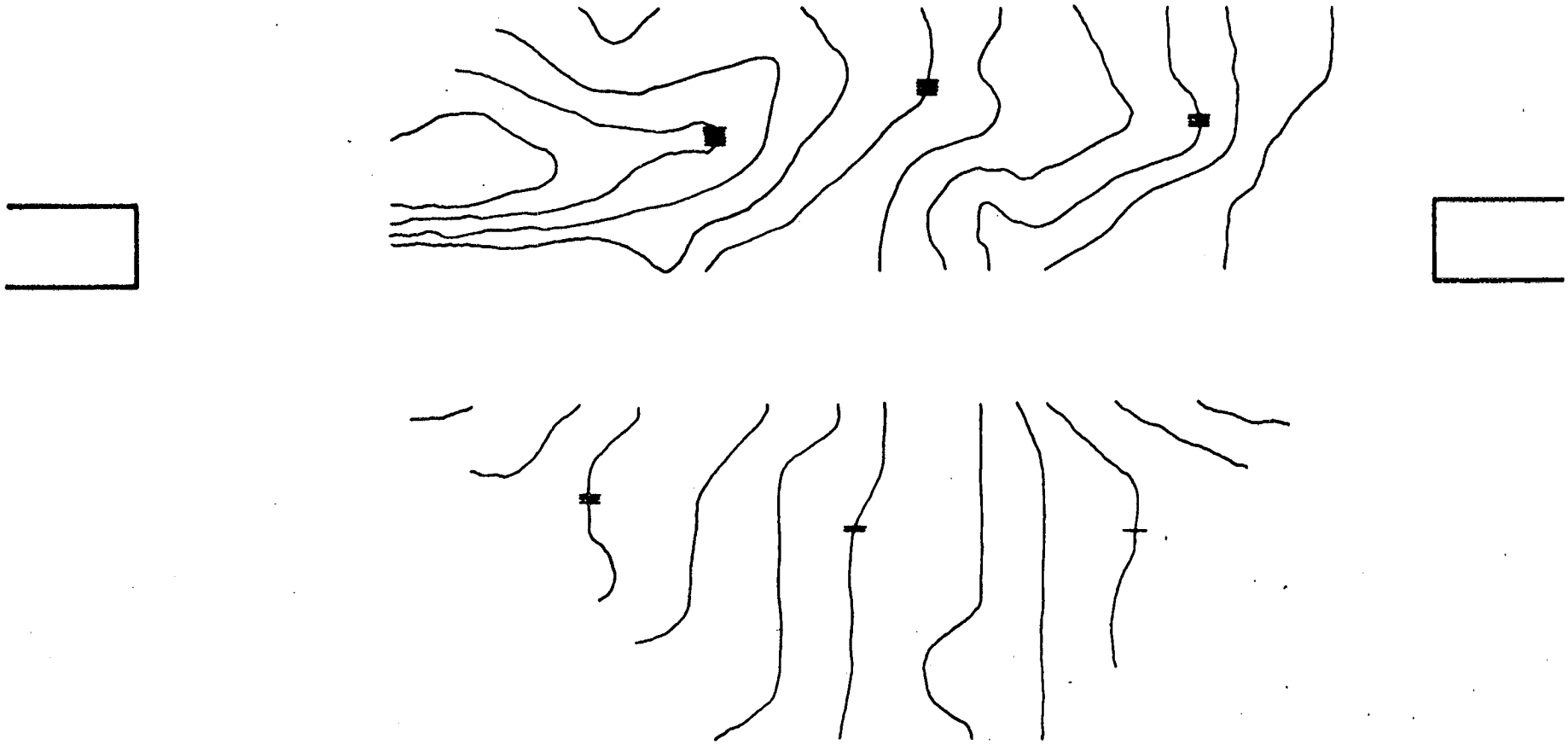

FIGURE 32 Contours of the r.m.s. values of the vertical velocity fluctuations (Contours are in increments of 0.1 m/s with the following contours marked: - 1.0, = 1.5, ≡ 2.0, ≣ 2.5 m/s.)

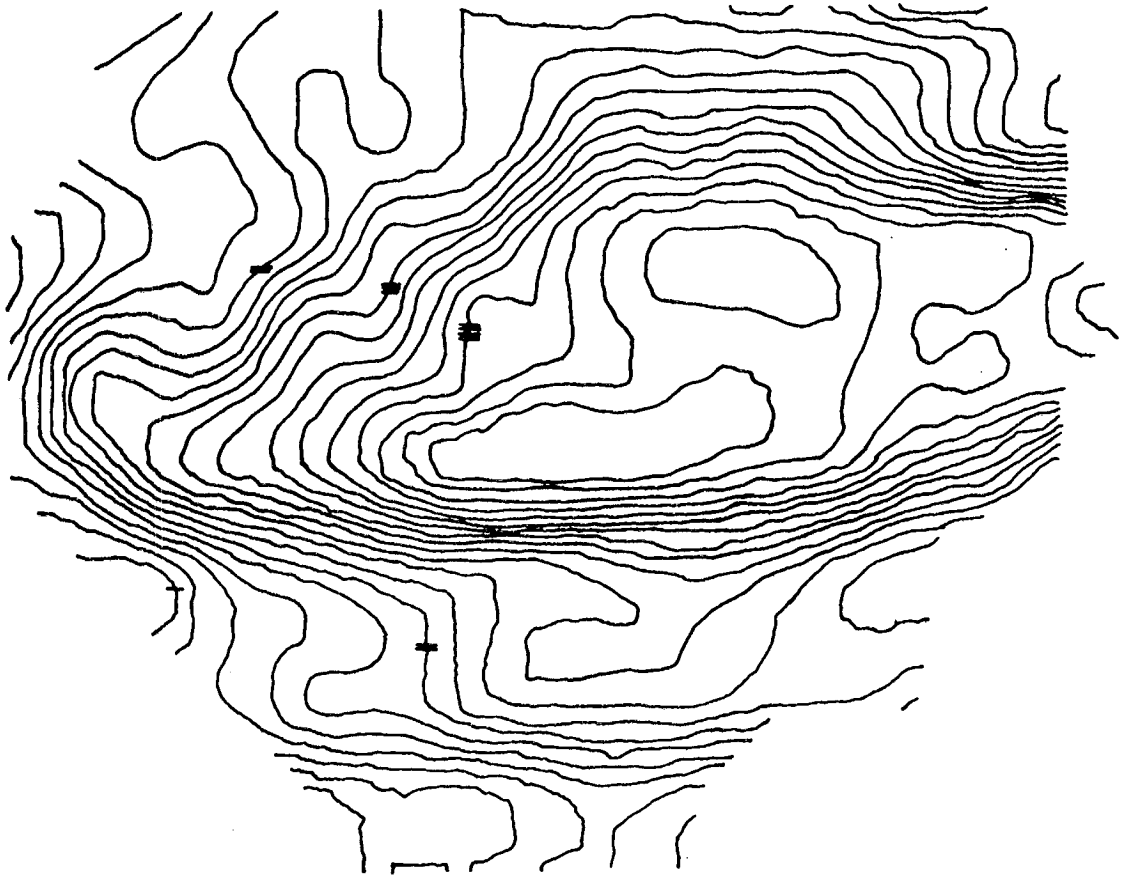

FIGURE 33 Contours of the phase of the vertical velocity fluctuations relative to the cavity pressure fluctuations.
(Contours are in increments of 20^{o} with the following contours marked:
- -240^{o}, = -180^{o}, ≡ -120^{o}, ≣ -60^{o}, ≣ 0^{o}.)

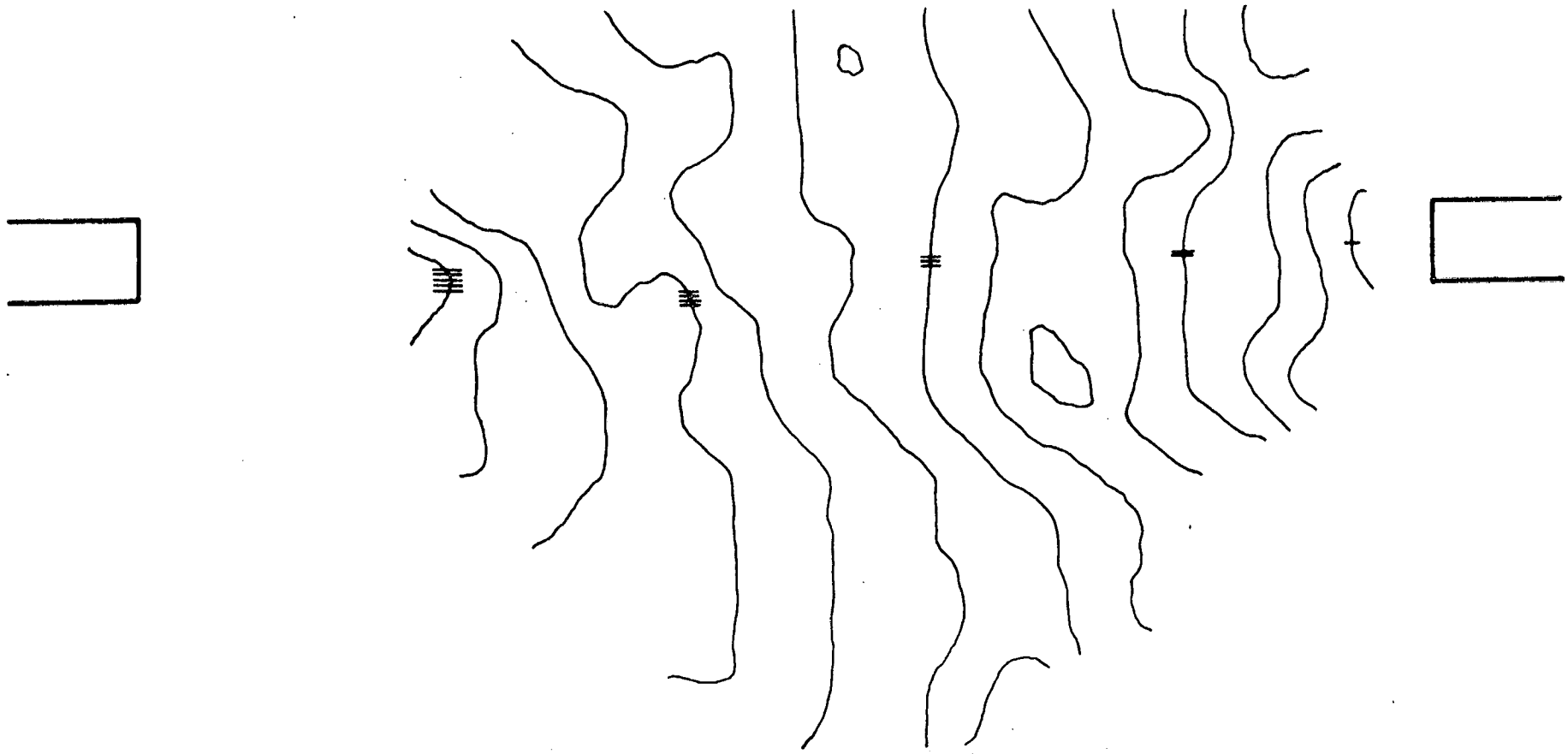

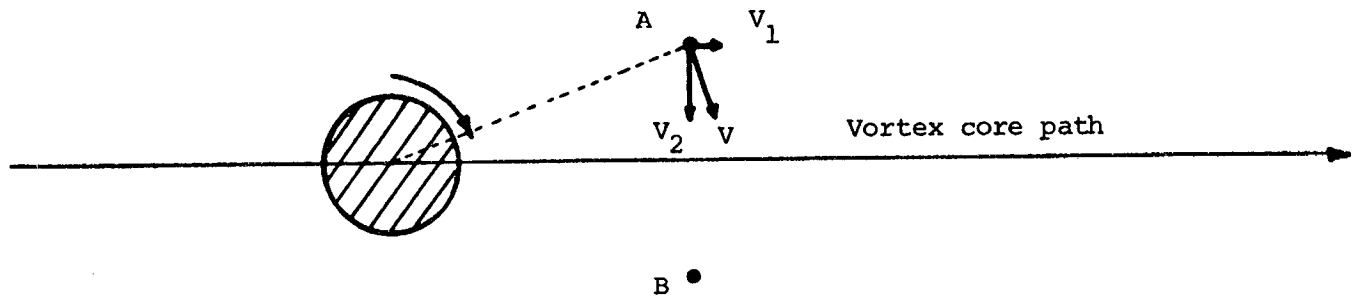

Time histories of induced velocity at point A (above the path of the vortex core)

Time histories of induced velocity at point B (below the path of the vortex core)

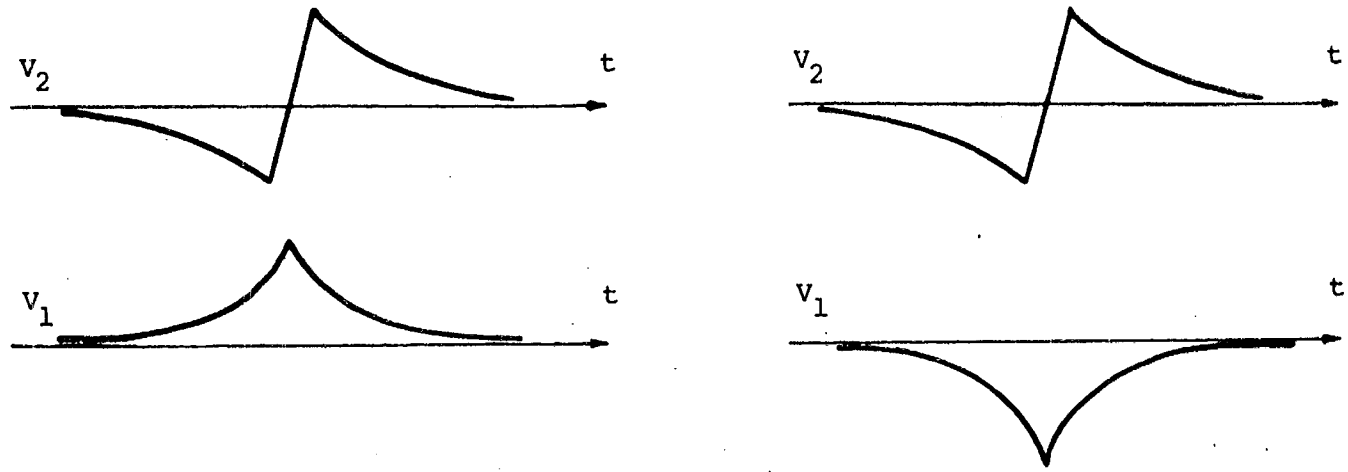

FIGURE 34 The velocity fluctuations induced by the passage of vortex convected in the streamwise direction.

FIGURE 35 Phase difference between the streamwise and vertical velocity fluctuations at the fundamental frequency.
(Values are shown at x_2 levels above and below the path taken by the vortex core.)

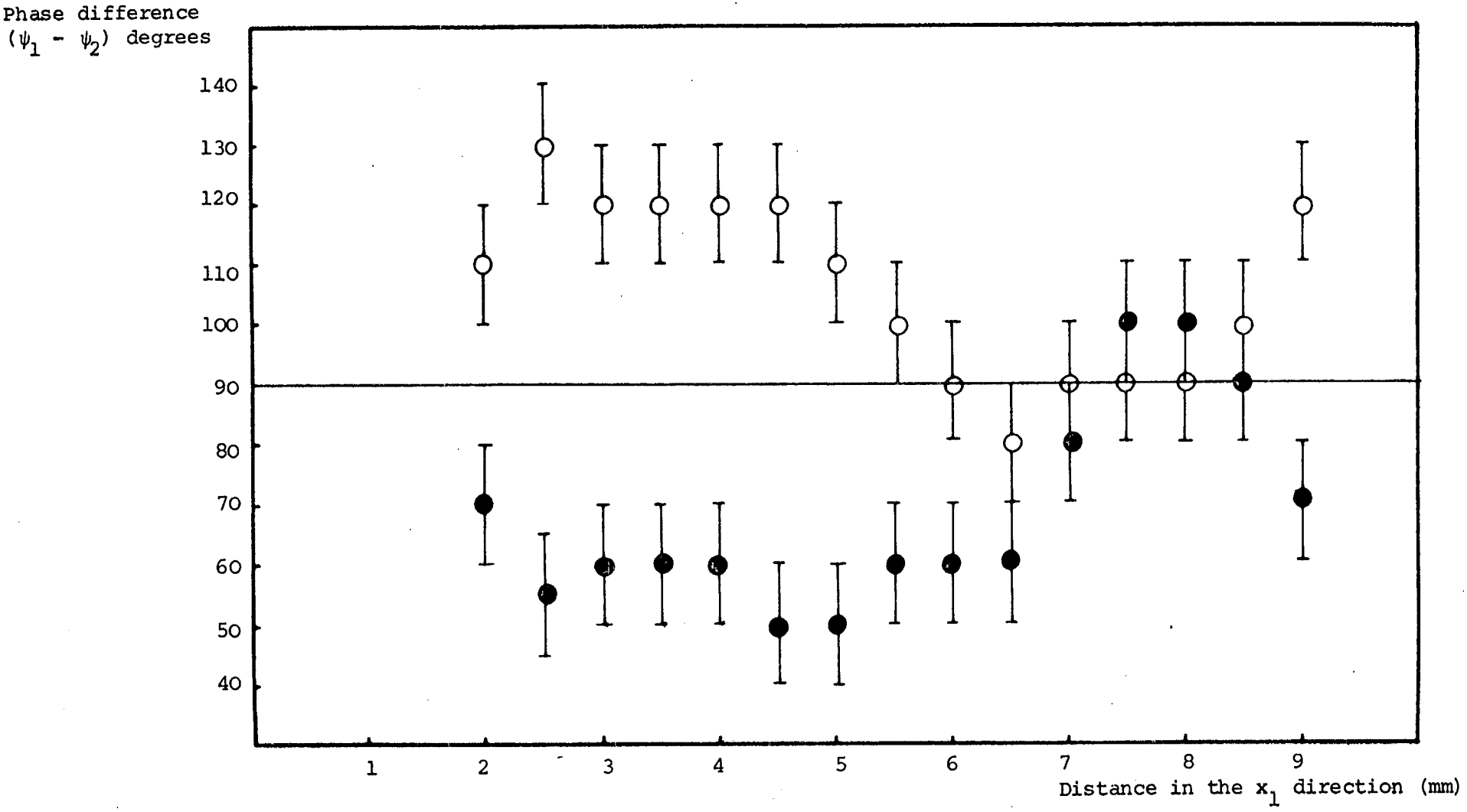

FIGURE 36 Contour plot of measured values of time averaged Reynolds shear stress. (Contours are in increments of 0.25 N/m^2 with the following contours shown: - -3.0, = -1.5, ≡ 1.5, ≝ 3.0 N/m^2.) Estimated accuracy of shear stress measurements is ±0.5 N/m^2.

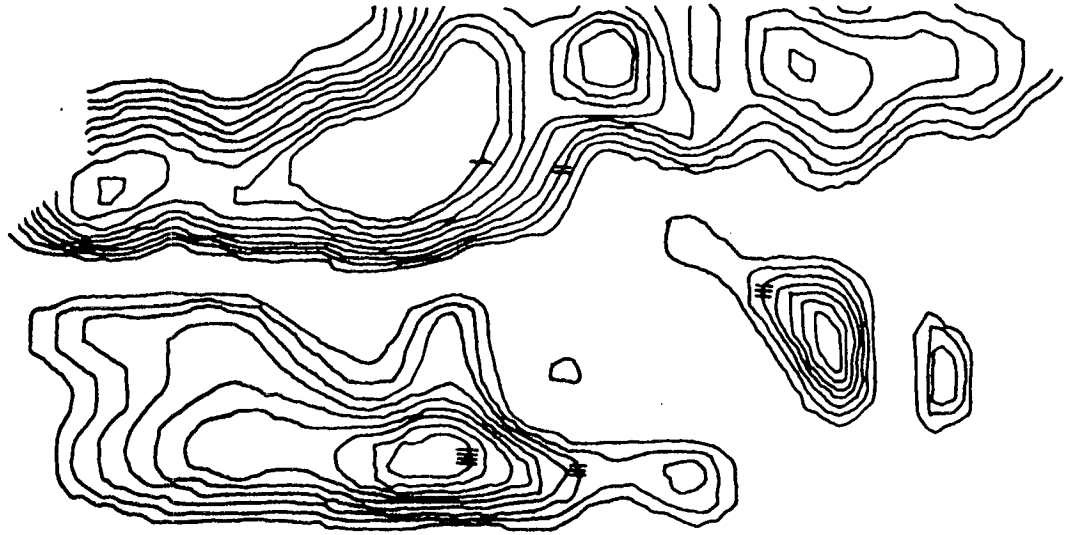

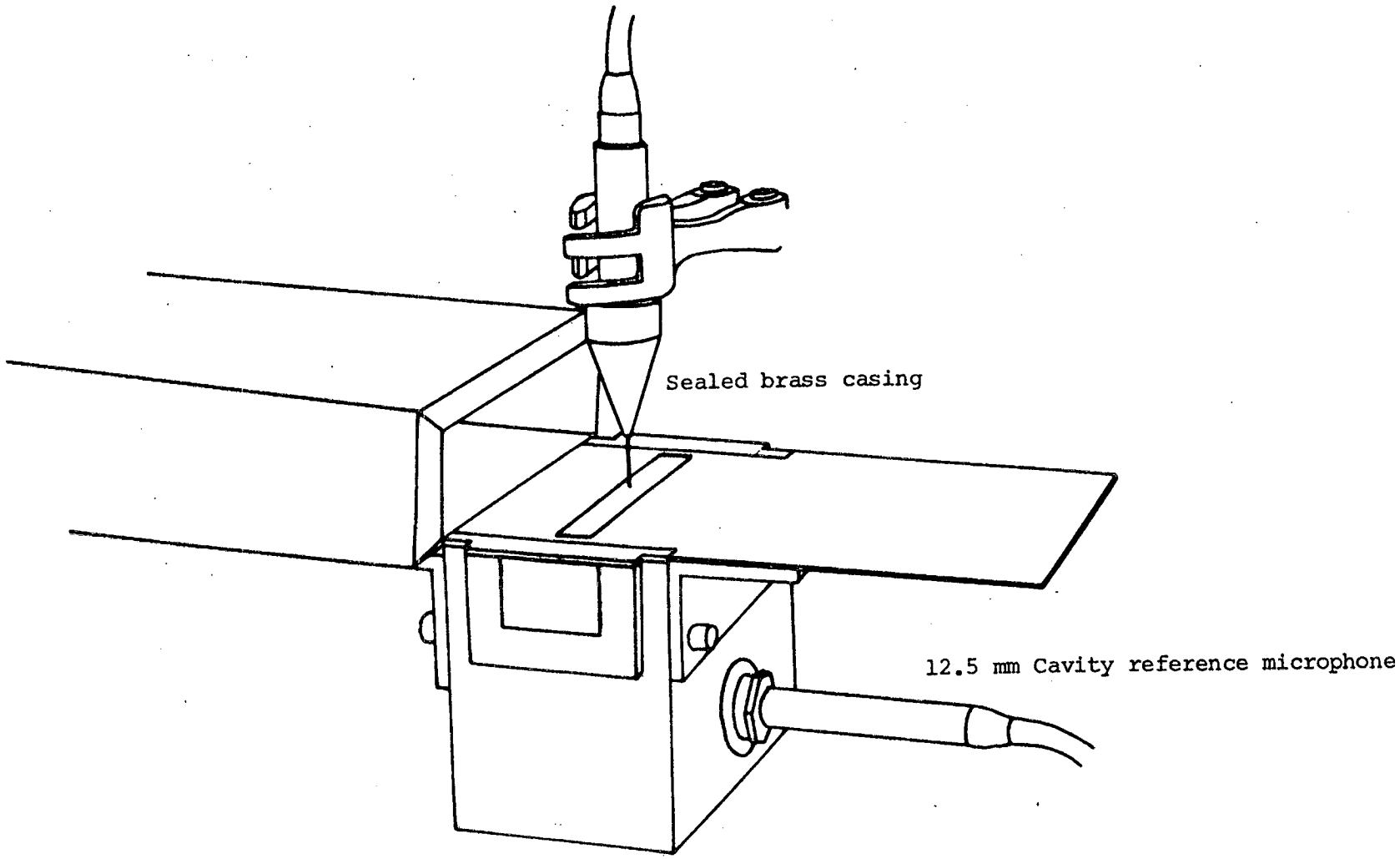

FIGURE 37 The measurement of the fluctuating pressure field using a 0.5 mm diameter probe tube.

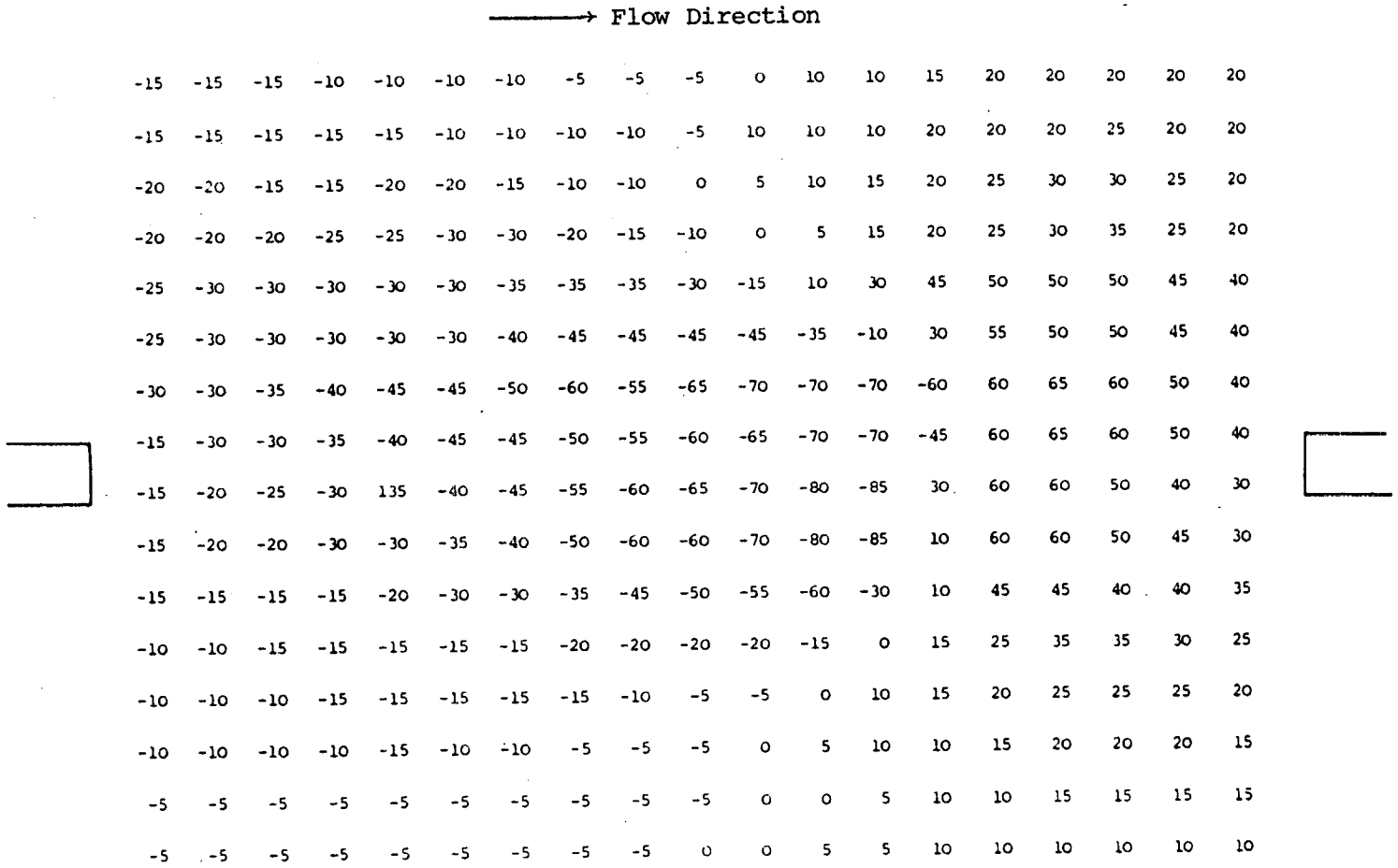

FIGURE 38 Measured values of the phase of the fluctuating static pressure relative to the cavity pressure fluctuations. . . point. ((Results in degrees ± 5°. Measurement grid points are at 0.5 mm intervals.)

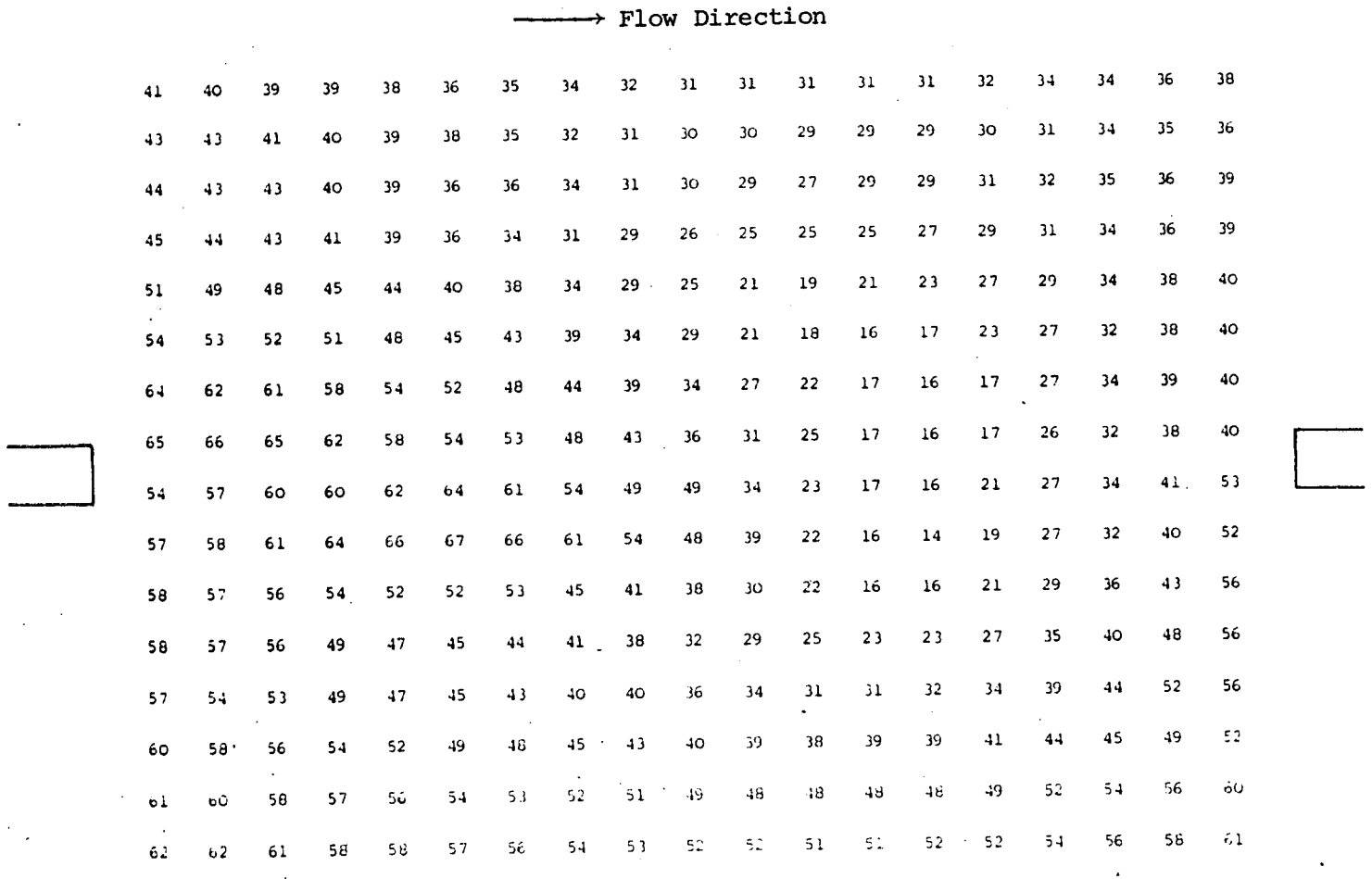

FIGURE 39 Measured values of the phase of the fluctuating static pressure relative to the cavity pressure fluctuations.
(Results in degrees ± 5°. Measurement grid points are at 0.5 mm intervals.)

FIGURE 39 Measured r.m.s. values of the fluctuating static pressure.
(Results in N/m^2 ± 1 N/m^2. Measurement grid points are at 0.5 mm intervals.)

FIGURE 40 Contours of the r.m.s. values of the static pressure fluctuations. (Contours are in increments of 2.5 N/m^2 with the following contours marked: - 20, = 30, ≡ 40, ≣ 50, ⩵ 60 N/m^2.)

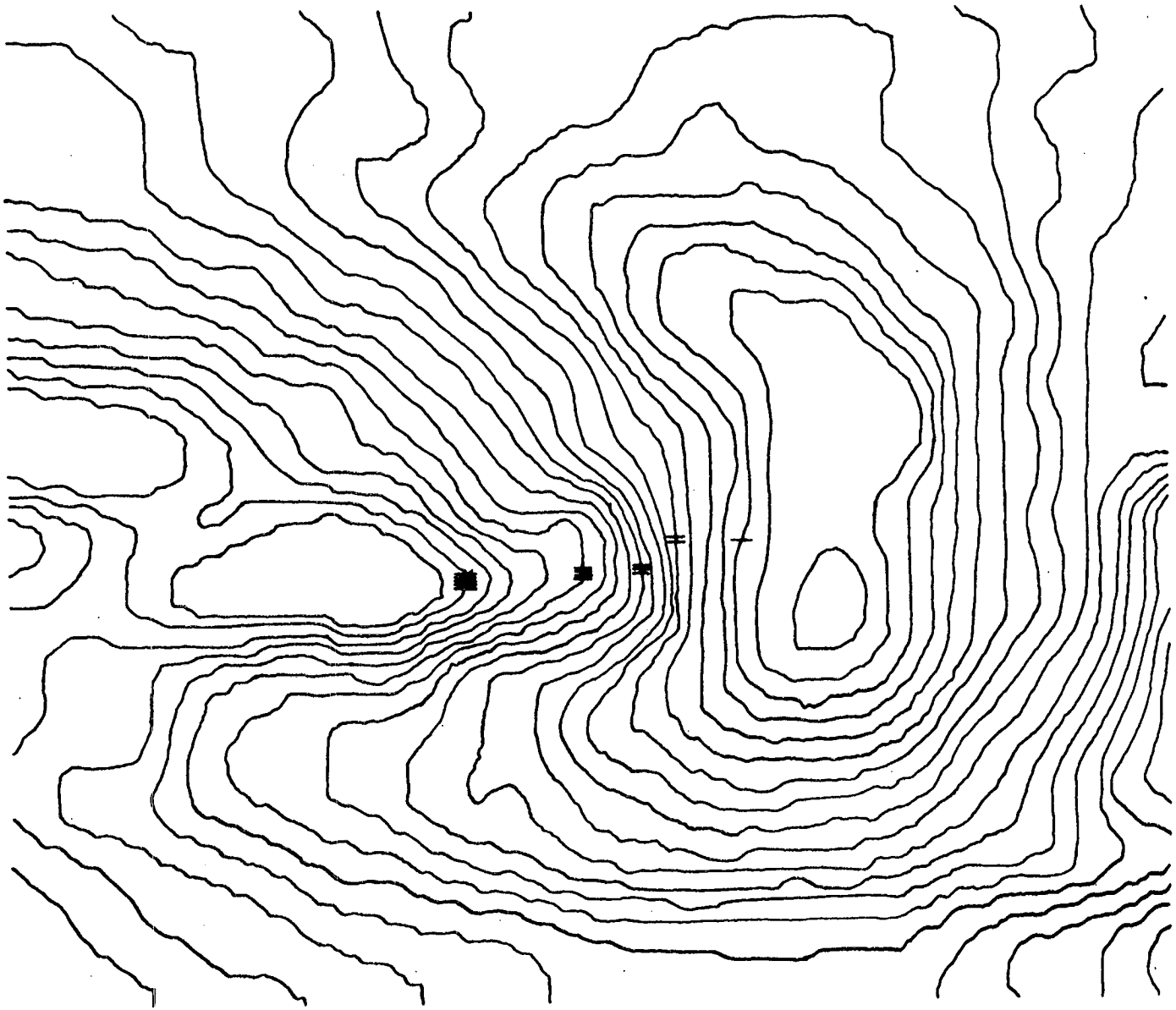

FIGURE 41 Contours of the phase of the static pressure fluctuations relative to the cavity pressure fluctuations.
(Contours are in increments of 10° with the following contours marked:
- -60°, = -30°, ≡ 0°, ≣ 30°, ⩵ 60°.)

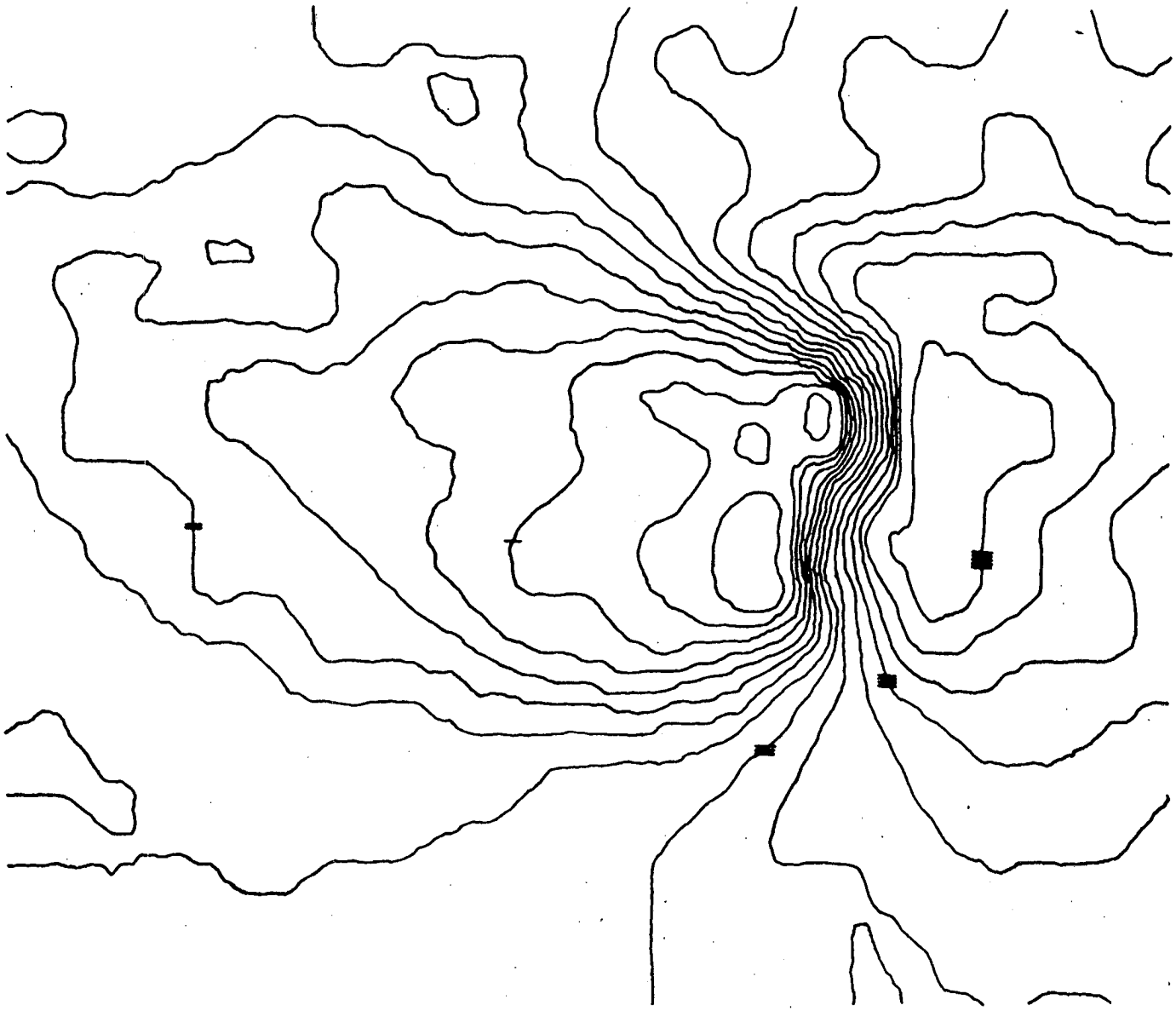

CHAPTER 5

THE FLUID DYNAMICS OF A FLOW EXCITED RESONANCE

(II) ANALYSIS AND DISCUSSION OF RESULTS

1. INTRODUCTION

The experiments described in the previous chapter have provided detailed information regarding the nature of the flow field produced in the neck of a flow excited Helmholtz resonator. Further interpretation of these measurements is required in order to provide a deeper understanding of the dynamics of the interaction of the flow with the acoustic resonance. In this Chapter it will be assumed that the total flow field can be regarded as consisting of two velocity fields; a purely vortical flow field directly associated with the shed vorticity and a potential flow, the unsteady part of which is associated with the acoustic resonance. The experimental results will be used to determine the principal features of these two flow fields and the dynamics of their interaction.

Firstly, a very simple model of periodic vortex shedding will be used to deduce further quantitative details of the behaviour of the vorticity shed at the upstream lip of the resonator neck. In particular, the model will be used to deduce the strength and approximate distribution of the vorticity in the streamwise convected vortices. The vortex shedding model used evaluates the velocity field induced by the uniform convection of vortices by a mean potential flow. The vortices used in the model have a Gaussian vorticity distribution, which is characterised by a given strength and effective core radius. It will be demonstrated that the strength of the vortices is primarily determined by the mean grazing flow across the top of the resonator neck. The strength of the periodically shed vortices observed in the experiment can thus be fairly readily established.

The core radius of the vortices shed is used as a measure of how "tightly packed" the vorticity becomes as the vortices are formed. It is shown that the approximate core radius of the vortices observed in the experiment can be deduced from the experimental results. Both the mean shear profile and the magnitude of the velocity fluctuations in the streamwise component direction give a good indication of the effective vortex core radius.

The net velocity fluctuations observed in the vertical component direction can be explained by the superposition of the velocity fluctuations induced by the passage of the vortices with the velocity fluctuation associated with a uniform reciprocating potential flow. Use of the measured phase of the velocity fluctuations in the resonator neck enables the position of the convecting vortex to be established during

the course of the cycle. The amplitude and relative phase of the reciprocating potential flow is then estimated using a simple model of the acoustic motion in the resonator neck. The model used assumes that the resonator behaves as if no flow is present and the values of the resistive and reactive parts of the acoustic impedance of the resonator neck are those determined in the previous Chapter. Combination of this reciprocating potential flow with the vertical velocity fluctuations induced by the passage of the vortices reveals a net pattern of vertical velocity fluctuations that is in good qualitative agreement with the measured results.

The net amplitude of the observed vertical velocity fluctuation tends to a small value towards the upstream edge of the resonator neck. This is confirmed by the interference of the reciprocating potential flow with the vortically induced velocity deduced using the model. This suggests that there is no net vertical displacement of the unstable shear layer leaving the upstream lip. Reference to the results of the flow visualisation study appears to confirm this and that the Kutta condition is satisfied at the upstream edge of the resonator neck.

Having established the strength and approximate core radius of the shed vortices, it becomes possible to estimate the static pressure fluctuations induced by the passage of the vortices. It will be demonstrated that, to a first approximation, the measured net fluctuating pressure field appears to consist of a simple superposition of the pressure fluctuations generated by the passage of the vortices with the "acoustic" pressure fluctuations associated with the reciprocating potential flow. This is shown by combining the pressure fluctuations estimated from the uniformly convected vortex model with those deduced using the simple acoustic model. This produces a net pattern of pressure fluctuations that is in remarkably good agreement with experimental results. This apparent superposition of the two pressure fields provides some useful insight into the mechanism of the interaction of the vortical and potential flows. The possible independent momentum balances suggested by the measured pressure interference pattern will be considered in the light of the full equation of conservation of momentum in the next Chapter.

Firstly, in Section 2 various aspects of the kinematics of the flow field will be discussed and the parameters controlling the strength of the shed vorticity will be identified. In Section 3 the simple model of vortex shedding will be introduced and the computation of the

vortically induced flow field will be described. Sections 4 and 5 will then be concerned with the simulation of the net measured pressure and velocity fields and the principal conclusions of this Chapter will be outlined in Section 6.

2. THE VORTICAL FLOW FIELD

2.1 The Specification of the Velocity Fields

During the following discussion of experimental results, the total velocity field will be considered as consisting of two distinct components. The total velocity vector $\underline{u}$ will be written

$$\underline{u} = \underline{v} - \nabla\phi. \tag{1}$$

A list of symbols is given in Appendix 1. The velocity field has been split into its rotational part $\underline{v}$ and its irrotational part $\nabla\phi$. This decomposition of the total velocity vector into its component parts follows from Helmholtz's theorem (Morse and Feshbach (1)). Further details of this procedure are also discussed by Batchelor (2). The rotational part $\underline{v}$ of the velocity vector is purely solenoidal and has the property

$$\nabla.\underline{v} = 0. \tag{2}$$

In what follows, $\underline{v}$ will be considered as that part of the velocity field which is directly induced by the presence of a given distribution of vorticity in the flow. The vorticity vector $\underline{\Omega}$ is given by

$$\underline{\Omega} = \nabla \wedge \underline{u} = \nabla \wedge \underline{v}, \tag{3}$$

since the irrotational part of the velocity field has zero curl. The velocity vector $\underline{v}$ is determined from the velocity distribution by the Biot-Savart Law (Lighthill (3))

$$\underline{v} = \int_V \frac{\underline{\Omega} \wedge \underline{s}}{4\pi s^3} \, dV, \tag{4}$$

where the volume integral in the fluid is over the whole vorticity field and $\underline{s}$ is the position vector relative to the volume element dV.

With a specified vorticity distribution, $\underline{v}$ is determined by (4) and the remaining velocity field must be expressible as the gradient of a scalar (Batchelor (2)). It is worth pointing out that there may also be parts of $\underline{v}$ that can be expressed as the gradient of a scalar, but

these must have zero divergence (and as a consequence, satisfy Laplace's equation). By choosing $\underline{v}$ to be defined by (4), the part of the velocity field that must be solenoidal has been isolated. Note that it is also possible for the irrotational part of the velocity field to have zero divergence. This is the case in an incompressible fluid, but in the more general case of a compressible fluid it is <u>not automatic</u> that $\nabla^2\phi = 0$ whereas $\nabla.\underline{v} = 0$ must always hold.

With the vorticity distribution specified (and thus $\underline{v}$), the remaining part of the velocity field $\nabla\phi$ is at least partly determined by the boundary conditions. In the present case, it is firstly required that there be zero net normal velocity on the solid surfaces in the fluid, that is

$$v_n - \frac{\partial\phi}{\partial n} = 0. \qquad (5)$$

where v_n and $\partial\phi/\partial n$ are the components of $\underline{v}$ and $\nabla\phi$ on the surface in the outward normal direction. It is often possible in dealing with problems of this kind to deduce $\nabla\phi$ such that the necessary boundary conditions are satisfied by considering $\nabla\phi$ to be induced by the "image" of the vorticity distribution in the solid surface. For the case of an incompressible fluid, this will determine $\nabla\phi$ uniquely (Batchelor (2)).

In the present case, where a strong sound field is present, $\nabla\phi$ must also contain the contribution to the total velocity field which arises from compressibility. In previous attempts to deal with this type of problem (Howe (4), Crighton (5)), the flow has been considered to be locally incompressible, provided the scale of the flow is small compared to the acoustic wavelength and the mean flow Mach number is small. The local flow field is then solved by specifying the vorticity distribution and its resulting image flow. The sound field is then superposed on this flow, subject to the boundary conditions of zero normal velocity on the surface ($\partial\phi/\partial n = 0$ for the acoustic part of $\nabla\phi$) and an outgoing wave condition at infinity. This acoustic field is then related to the inner locally incompressible flow by the use of a suitable matching procedure.

In the present case, a formal approach of this type has not been attempted. Rather, the experimentally observed results have been used to deduce approximate analytic forms of $\underline{v}$ and $\nabla\phi$ in the resonator neck. Both rotational and irrotational velocity contributions can be expressed as a sum of mean and fluctuating parts, the total velocity being written as

$$\underline{u} = \overline{\underline{v}} + \underline{v}' - \nabla\overline{\phi} - \nabla\phi'. \qquad (6)$$

As usual the overbar denotes the time average value of the velocity component and the prime denotes the fluctuating part of the velocity component (which has a zero time average value).

The sum of $\overline{\underline{v}} - \nabla\overline{\phi}$ is the total mean flow vector $\overline{\underline{u}}$. In the following work $\overline{\underline{v}}$ will be deduced from the time average of the velocity field induced by the shed vorticity according to (4). The term $\nabla\overline{\phi}$ will be assumed to be produced by an appropriate grazing mean potential flow which is directed across the top of the resonator neck. In the immediate region of the neck, it will be demonstrated that it is the flow responsible for the steady convection of the vorticity across the resonator mouth. It will be shown that the measured mean shear profile in the resonator neck is reproduced to a good approximation by the periodic convection of a specified distribution of vorticity by this mean potential flow in the streamwise direction.

The fluctuating velocity $\underline{v}'$ is also deduced from the convection of a specified vorticity distribution which induces the fluctuations in $\underline{v}$. However, the remaining part of the fluctuating velocity field $\nabla\phi'$ contains unsteady contributions from the image vorticity flow field and any acoustic motion present. In the analysis of the experimental results it becomes evident that in the region of the resonator neck, the net reciprocating potential flow $\nabla\phi'$ can be accounted for by the estimated acoustic motion alone. It thus seems that the unsteady image vorticity flow field is either very small compared to this acoustic motion in the region to be considered, or that it is indistinguishable from it. In either case, the results indicate that the acoustic motion only, as defined here, satisfies the required boundary conditions:

$$v_n' - \frac{\partial\phi'}{\partial n} = 0. \qquad (7)$$

Thus, it will be demonstrated that the flow in the resonator neck consists of an interaction between the convected vorticity with its directly induced velocity field and a reciprocating potential flow. Although the precise physical origin of this potential flow remains obscure, evidence suggests that it can be predicted from a knowledge of the acoustic motion inside the cavity. The remainder of this section will be concerned with deducing the details of the vortical flow from the experimental results.

2.2 The Basis for Modelling the Vortex Shedding

The separation of the flow from the upstream edge of the resonator neck results in vorticity being shed into the flow. It will be assumed that the only vorticity relevant to the mechanism of the interaction of the vortical and potential flows is that shed from the upstream lip. Any vorticity in the boundary layer flow above the upper surface of the resonator will be neglected. In addition, no account will be taken of any vorticity inside the resonator that is associated with the slowly recirculating mean flow in the cavity. The experimental results certainly suggest that it is the vorticity in the shear layer in the resonator neck that has the dominant influence on the structure of the flow field.

The vorticity shed at the edge is initially confined to a thin vortex sheet across which the streamwise velocity component varies from the value of the grazing flow just above the resonator surface to the value of the grazing flow just below the upstream lip. This vortex sheet is unstable to small disturbances. The stability of such fluid layers was first thoroughly investigated by Rayleigh (6) and has since evolved as a subject of study in its own right. (See, for example, the reviews by Lin (7), Drazin and Howard (8) and Betchov and Criminale (9)). The essence of stability theory is to examine the behaviour of small velocity perturbations on a specified mean velocity distribution by using the linearised vorticity equation. Such analyses furnish details of the likelihood that disturbances will either grow or damp out on a specified shear layer. The result of shear layer instability is a wavelike oscillation which grows exponentially until the shear layer rolls up and vortices are formed. The "gathering together" of the vorticity in the layer during this process is well illustrated, for example, in the treatment by Michalke (10).

The question arises as to whether such an analysis of the shear layer motion is applicable to the present case. Certainly, a good estimate could be made of the natural instability properties of the thin layer leaving the upstream edge when provided with a knowledge of the velocity profile of the layer. However, the presence of the relatively strong reciprocating potential flow in the resonator neck suggests that the layer is in some sense forced by the additional transverse motion. This is the interpretation given by Mungur (11) of the additional terms occurring in the linearised vorticity equation when the stability characteristics of a shear layer are considered with an

additional acoustic motion. An inhomogeneous Rayleigh equation can be formed with a source term apparently driving the shear layer instability that is given by the product of the transverse acoustic velocity and the mean transverse velocity gradient. To the author's knowledge, however, no sufficiently illuminating solutions to this problem have yet been found.

Further to this, the use of a linearised equation to describe the growth of disturbances soon becomes invalid once the velocity perturbations have grown to be a significant fraction of the mean flow. The growth of the disturbance to sufficient amplitude would eventually distort the mean flow upon which it has been superposed. In such finite amplitude circumstances, the non-linear terms previously neglected in the vorticity equation must be considered (and possibly compressibility terms, if they have been neglected). The distortion of the mean flow by the disturbance growth occurs principally through the action of the mean Reynolds stress. In certain problems, like those treated by Stuart (12) for example, a nonlinear analysis can be conducted in which the energy transfer is considered between the mean flow and the disturbance through the action of the Reynolds stresses. This type of analysis can yield results for the amplitude to which the disturbance will ultimately grow.

In the present case, the experimental results show that the region in which linear stability theory could be used to describe the behaviour of the shear layer leaving the upstream lip is probably confined to the very early stages of the growth of the shear layer oscillation. If the streamwise velocity component fluctuations are used as a measure of the amplitude of the shear layer disturbance, these show that the disturbance has grown to its maximum amplitude within about 3 mm of the upstream lip (see Figure 30 of the previous Chapter). The presence of a well-defined mean Reynolds shear stress (Figure 36 of the previous Chapter) also indicates that the disturbance growth is influencing the structure of the mean flow. It thus seems that any rigorous mathematical treatment of the shear layer behaviour in the region of the resonator neck must be capable of dealing with a hydrodynamic stability problem that is both forced and nonlinear. Such an analysis has not been attempted.

Another possible approach that could be used to describe the development of the shear layer is that involving the computation of the flow field at successive time increments as discrete vortex elements

are shed into the flow. After the initial introduction of the approach by Rosenhead (13), the use of high speed computing techniques has made such a scheme feasible and has been applied with some success to several problems such as the behaviour of the flow in axisymmetric jets (Edwards (14)) in the wake of a bluff body (Clements (15)) and over rectangular cut-outs (Hardin (16)). However, there are still problems involved in such an approach and the case of a flow with a strong sound field present that is generated by the flow itself has yet to be treated.

From this brief discussion, it is evident that there is no immediately feasible means of precisely modelling the behaviour of the vorticity that is based on a solution to the full equations of motion of the fluid. However, the experimental results reveal some important details of the behaviour of the vortical flow. A realistic model has thus been chosen with the emphasis on reproducing the observed features of the flow rather than on attempting to provide an exact modelling. The experimental results clearly show the formation of discrete vortices near to the upstream lip with their growth appearing to be completed well within the first half-cycle of the motion (as the cavity pressure is increasing from its minimum to its maximum value). These vortices are then convected across the resonator neck at an approximate convection speed of 6 m/s (about one half of the grazing flow speed over the resonator neck). These and the other experimental results imply that a good representation of the vortical flow field must be based on a model which provides, at the least, for a periodic convection of vortices of finite core size across the resonator neck. These vortices will contain a total vorticity that is distributed in some way in their core. Such a model of the vortical flow will be outlined in the next sections, and the experimental results will then be used to deduce the total vorticity shed per cycle and the distribution of this vorticity within the vortices.

2.3 The Parameters Controlling the Behaviour of the Shed Vorticity

Implicit in the following is the assumption that the flow in the resonator neck can be considered two dimensional. The co-ordinate system will be the same as that used in the previous Chapter, with a set of right-handed axes with the x_1 and x_2 co-ordinates pointing in the streamwise and vertical directions, respectively. The origin will again be assumed to be located at the corner formed between the upper surface of the resonator and the edge of the upstream lip in the resonator neck. It will be assumed that the only vorticity in the flow is that shed from

the upstream lip and that the total vorticity in the flow is conserved.

The experimental results also suggest that the vorticity is principally convected across the resonator neck in the streamwise (x_1) direction. The vorticity vector $\underline{\Omega}$ will point in the negative x_3 direction, since only negative circulation is shed according to a "right hand screw" sign convention. Thus the instantaneous rate of shedding of circulation can be found from

$$\frac{d\Gamma}{dt} = \int_{\substack{\text{shear}\\\text{layer}}} u_1 \Omega_3 dx_2 = \int_{\substack{\text{shear}\\\text{layer}}} u_1 \left(\frac{\partial u_2}{\partial x_1} - \frac{\partial u_1}{\partial x_2}\right) dx_2, \tag{8}$$

where the integral is evaluated between appropriate limits to cover the region of vorticity in the shear layer.

It will now be assumed that the Kutta condition at the upstream lip is satisfied. That is, the shear layer always leaves the upstream edge in a direction tangential to the upper surface of the resonator. The streamwise rate of change of vertical displacement of the shear layer is thus zero at the upstream edge. This in turn implies that $\partial u_2/\partial x_1$ is always zero at the upstream edge. This enables equation (8) for the rate of shedding of circulation to be written as

$$\frac{d\Gamma}{dt} = \int_{\substack{\text{shear}\\\text{layer}}} - u_1 \frac{\partial u_1}{\partial x_2} dx_2, \tag{9}$$

and the integral can be evaluated to give

$$\frac{d\Gamma}{dt} = \left[- \tfrac{1}{2} u_1^2 \right]_{\substack{\text{shear}\\\text{layer}}} . \tag{10}$$

The instantaneous rate of shedding of circulation from the upstream edge is thus determined by the instantaneous difference in the streamwise velocity component above and below the separating shear layer. The reciprocating potential flow driven through the resonator neck by the cavity pressure fluctuations clearly influences the instantaneous rate of shedding of circulation. There will be substantial differences in the streamwise velocity component immediately above and below the upstream lip of the resonator neck as the potential flow negotiates the sharp edge. A similar viewpoint is adopted by Howe (4) when dealing with the theory of the flute. In that case it is claimed that the circulation is shed as a direct result of the separation of the "acoustic" potential flow from the downstream lip of the mouth of the

flute. The Kutta condition is then applied to determine the strength of the shed vorticity from the magnitude of the potential flow. A similar procedure has been adopted by Howe in dealing with a number of other problems involving "acoustically induced" vortex shedding (17,18).

A slightly different approach will be taken here. Firstly it will be assumed that the mean streamwise velocity varies from zero below the shear layer to a value $\overline{u}_{1max}$ above the shear layer. The latter will be the value of the streamwise mean grazing flow just above the top of the resonator neck. This amounts to neglecting the effect of the slowly recirculating mean flow inside the cavity. In this case, the time average rate of shedding of circulation can be written as

$$\overline{\frac{d\Gamma}{dt}} = -\tfrac{1}{2}\,\overline{u}_{1max}^{\,2} \,. \qquad (11)$$

The minus sign is consistent with the sign convention used. A net negative circulation is shed from the upstream lip.

The average rate of shedding of circulation is thus determined solely by the mean grazing flow across the top of the resonator neck. This is a very important result. It shows that on average the reciprocating potential flow in the resonator neck cannot change the total vorticity shed. However, it is observed experimentally that the shedding of the vorticity is controlled by the reciprocating potential flow. Discrete vortices are formed periodically with the whole process clearly synchronised with the cavity pressure fluctuations. It is thus apparent that the circulation shed during a cycle of the motion depends only on the mean grazing flow over the resonator and that the vorticity is shed in discrete "packets". It is the distribution of the vorticity in these packets that is in some way controlled by the potential flow.

In modelling the vortex shedding, the fact that the mean grazing flow over the resonator neck determines the average rate of shedding of circulation will be used to determine the strength of the vorticity shed during the course of one cycle of the motion. A vortex shedding model will be used in which circulation of the necessary strength is shed once per cycle. This circulation will be assumed to be shed in a discrete vortex having a given "core radius" which will be used to characterise the distribution of the vorticity it contains. The experimental results will then be used to establish the approximate core radius of the vortices observed in the experiment. The influence of the vorticity distribution and its implications for the dynamics of the flow excited

resonance will be discussed in more detail in the next Chapter.

3. A VORTEX SHEDDING MODEL

3.1 A Model of Two Dimensional Periodic Vortex Shedding

The vortical flow in the neck of the resonator will be assumed to be the flow field directly induced by the periodic passage of vortices at a steady rate in the streamwise direction. The flow model that will be used is illustrated in Figure 1. The model essentially satisfies the same boundary conditions as the mean flow in the real case. The vortex shedding in the real flow will be assumed to result from the separation of a uniform grazing flow of velocity $\bar{u}_{1max}$ from the upstream lip of the resonator neck (Figure 1). In the model, the net flow is that produced by an infinite array of vortices embedded in a uniform steady potential flow. The strength of the vortices is chosen such that the average rate of shedding of circulation (defined by equation (11)) is identical to that in the real flow. The steady potential flow $-\nabla\bar{\phi}$ responsible for the convection of the vortex array is then chosen such that the total streamwise mean flow varies from $\bar{u}_{1max}$ above the shear layer to zero below the shear layer. This is given by a value of $-\nabla\bar{\phi} = \frac{1}{2}\,\bar{u}_{1max}$.

The vortices will pass across the region of the resonator neck at a time interval T. The vorticity can thus be thought of as an infinite line array of discrete vortices embedded in the steady potential flow such that the axes of the vortices are separated by a distance L where $-\nabla\bar{\phi} = \frac{1}{2}\,\bar{u}_{1max} = L/T$. It will also be assumed that this array of vortices is stable and that the vortices do not interact. This is partly justified by the experimental results, where the presence of the boundaries appears to allow a stable train of vortices to form which were not observed to interact within any appreciable distance of the resonator neck.

The vorticity in each of the discrete vortices will be assumed to be distributed with rotational symmetry about a core axis such that

$$\Omega_3(r) = \frac{\kappa}{\pi r_c^2}\, e^{-r^2/r_c^2}, \qquad (12)$$

where r is the radial distance from the core axis and r_c is the core radius. The value of r_c^2 is analogous to twice the variance of a Gaussian distribution of vorticity. Ignoring any contribution from

neighbouring vortices, the circulation about a particular vortex is given by

$$\Gamma(r) = \int_A \underline{\Omega}.\underline{n}\, dA, \tag{13}$$

where $\underline{n}$ is the outward normal from the area element dA. Evaluation of this integral over the vorticity distribution of a single vortex yields

$$\Gamma(r) = \kappa(1 - e^{-r^2/r_c^2}). \tag{14}$$

Thus, as $r \to \infty$, $\Gamma(r) \to \kappa$ such that κ is the strength of each vortex.

The flow in each vortex, again with contributions from neighbouring vortices ignored, has circular streamlines and a tangential velocity $v_\theta = \Gamma/2\pi r$ such that

$$v_\theta(r) = \frac{\kappa}{2\pi r}(1 - e^{-r^2/r_c^2}). \tag{15}$$

Note that for $r >> r_c$, $v_\theta(r) \to \kappa/2\pi r$ and for $r << r_c$, $v_\theta(r) \to \kappa r/2\pi r_c^2$. Thus, at large radial distances from the core axis the vortex has a velocity distribution of a "free" vortex, whilst there is a solid body rotation of a "forced" vortex in the core. The value of r_c is the core radius of the equivalent Rankine vortex, where the "free" and "forced" vortices meet. This is illustrated in Figure 2. It will later be convenient to non-dimensionalise r and v_θ in terms of r_c and v_c where $v_c = \kappa/2\pi r_c$. Writing the ratios $r/r_c = R$ and $v_\theta/v_c = V_\theta$ gives

$$V_\theta = (1 - e^{-R^2})/R. \tag{16}$$

With the form of the vorticity distribution of each vortex and its resulting induced velocity field thus specified, the vortical velocities produced by the periodic passage of the vortices through the region of interest can be deduced. Thus, the time history of the net induced velocity has to be simulated at a series of points (x_1,x_2) in the flow field. Firstly, consider the velocity field induced by the passage of the m-th vortex in the array across the region of interest. It will be assumed that the axis of the m-th vortex has co-ordinates (ξ_{m1},ξ_{m2}) which are specified as a function of time. The radial distance of the point (x_1,x_2) from the core axis of the m-th vortex is given by

$$r_m = \sqrt{[(x_1 - \xi_{m1})^2 + (x_2 - \xi_{m2})^2]}. \tag{17}$$

The net velocity induced by the vortex at (x_1,x_2) can be derived by resolving the induced tangential velocity $v_{m\theta}$ into velocity components in the x_1 (streamwise) and x_2 (vertical) directions. As illustrated in Figure 3 the two components are given by

$$v_{m1}(t) = -v_{m\theta}\cos\theta = -v_{m\theta}\frac{(x_2 - \xi_{m2})}{r_m}, \tag{18}$$

$$v_{m2}(t) = v_{m\theta}\sin\theta = v_{m\theta}\frac{(x_1 - \xi_{m1})}{r_m}. \tag{19}$$

The total velocity field induced by all the vortices in the array is given by summing the contributions from each vortex in the infinite array:

$$v_1(t) = \sum_{m=-\infty}^{\infty} v_{m1}(t), \tag{20}$$

$$v_2(t) = \sum_{m=-\infty}^{\infty} v_{m2}(t). \tag{21}$$

Thus by using the relations (18,19) and substituting for $v_{m\theta}$, the net induced velocities at (x_1,x_2) can be written in terms of the co-ordinates (ξ_{m1},ξ_{m2}) of each vortex and the parameters κ and r_c. The two velocity components can be expressed as

$$v_1(t) = \sum_{m=-\infty}^{\infty} -\frac{\kappa(x_2 - \xi_{m2})}{2\pi r_m^2}(1 - e^{-r_m^2/r_c^2}), \tag{22}$$

$$v_2(t) = \sum_{m=-\infty}^{\infty} \frac{\kappa(x_1 - \xi_{m1})}{2\pi r_m^2}(1 - e^{-r_m^2/r_c^2}). \tag{23}$$

Note that the co-ordinates (ξ_{m1},ξ_{m2}) are a function of time, which has to be specified, and this determines r_m as a function of time for a given (x_1,x_2). The variation of the vorticity as a function of time at a given point (x_1,x_2) can also be written in a similar fashion:

$$\Omega_3(t) = \sum_{m=-\infty}^{\infty} \frac{\kappa}{\pi r_c^2} e^{-r_m^2/r_c^2}. \tag{24}$$

The computation of the velocity and vorticity as a function of time for specified values of (ξ_{m1},ξ_{m2}) will be dealt with in the next section.

3.2 The Computation of the Vortically Induced Velocity Field

In order to provide a basis for comparing the model vortical flow with that measured in the real case, the model will be used to compute the mean value of the vortically induced velocity field, together with the amplitude and phase of the velocity fluctuations produced at the fundamental frequency of the oscillation. These are the quantities that have been measured in detail in both component directions in the resonator neck. Thus, for each velocity component $v_k(t)$ (where the subscript k takes the value 1 or 2) the induced velocity time histories will be approximated by the mean value of the function and the first component of the Fourier series representation of the unsteady part of the function of period T: i.e.

$$v_k(t) \simeq \bar{v}_k + v_k', \tag{25}$$

where

$$\bar{v}_k = \frac{1}{T}\int_0^T v_k(t)\,dt, \tag{26}$$

$$v_k' = a_k \cos\omega t + b_k \sin\omega t, \tag{27}$$

in which the Fourier coefficients a_k and b_k are given by

$$a_k = \frac{2}{T}\int_0^T v_k(t)\cos\omega t\,dt, \qquad b_k = \frac{2}{T}\int_0^T v_k(t)\sin\omega t\,dt. \tag{28}$$

The fundamental velocity fluctuation v_k' can also be written in terms of an amplitude $|v_k|$ and phase ψ_k such that

$$v_k' = |v_k|\cos(\omega t + \psi_k), \tag{29}$$

where

$$|v_k| = \sqrt{(a_k^2 + b_k^2)}, \qquad \psi_k = \tan^{-1}(-b_k/a_k). \tag{30}$$

Thus, by using the expressions (22,23) for $v_k(t)$ the amplitude and phase of the vortically induced velocity fluctuations can be computed. Firstly, however, the co-ordinates (ξ_{m1}, ξ_{m2}) of each of the vortices in the array have to be specified. For uniform convection parallel to the x_1 axis at a speed $-\nabla\bar{\phi}$ of the array of vortices each spaced a distance L apart, the co-ordinates of the m-th vortex can be written as

$$\xi_{m1} = \bar{\xi}_1 - \nabla\bar{\phi}t + mL, \qquad \xi_{m2} = \bar{\xi}_2. \tag{31}$$

where $(\bar{\xi}_1, \bar{\xi}_2)$ is the position of the particular vortex specified by $m = 0$ at the time $t = 0$. As L is related to the convection speed $-\nabla\bar{\phi}$ and the period T (since $-\nabla\bar{\phi} = L/T$), the co-ordinates can be expressed as

$$\xi_{m1} = \bar{\xi}_1 - \nabla\bar{\phi}(t + mT), \qquad \xi_{m2} = \bar{\xi}_2. \tag{32}$$

Thus, the co-ordinates of the m-th vortex can be expressed as a function of $(t + mT)$. This implies that the velocity field induced by the m-th vortex can also be expressed as a function of $(t + mT)$. Hence, the total velocity induced as given by equations (22,23) can be written in the form

$$v_k(t) = \sum_{m=-\infty}^{\infty} f_k(t + mT). \tag{33}$$

This enables a useful simplification in the computation of the Fourier coefficients. Firstly, consider the coefficient a_k. This will be given by

$$a_k = \frac{2}{T}\int_0^T \sum_{m=-\infty}^{\infty} f_k(t + mT)\cos\omega t \, dt. \tag{34}$$

This can be written as

$$a_k = \sum_{m=-\infty}^{\infty} \frac{2}{T}\int_0^T f_k(t + mT)\cos\omega t \, dt. \tag{35}$$

Choosing $\alpha = t + mT$ as the variable of integration yields

$$a_k = \sum_{m=-\infty}^{\infty} \frac{2}{T}\int_{mT}^{(m+1)T} f_k(\alpha)\cos\omega\alpha \, d\alpha, \tag{36}$$

where $\cos\omega(\alpha - mT) = \cos\omega\alpha$ (since $\omega mT = m(2\pi)$ and m is an integer). Thus, the coefficient a_k can be evaluated from the time history $f_k(t)$ produced by the passage of the single vortex in the array corresponding to $m = 0$:

$$a_k = \sum_{m=-\infty}^{\infty} \frac{2}{T}\int_{mT}^{(m+1)T} f_k(t)\cos\omega t \, dt. \tag{37}$$

Exactly analogous relations to this can also be easily shown to hold for the evaluation of b_k and also $\bar{v}_k$. Thus, substituting for the specified co-ordinates of the axis of the vortex corresponding to

$m = 0$ and writing the radial distance from the core axis to the point (x_1,x_2) as r_o the complete expressions for the Fourier coefficients of the velocity induced in the two component directions can be written as

$$\bar{v}_1 = \sum_{m=-\infty}^{\infty} \frac{1}{T} \int_{mT}^{(m+1)T} -\frac{\kappa(x_2 - \bar{\xi}_2)}{2\pi r_o^2} (1 - e^{-r_o^2/r_c^2}) dt, \quad (38)$$

$$a_1 = \sum_{m=-\infty}^{\infty} \frac{2}{T} \int_{mT}^{(m+1)T} -\frac{\kappa(x_2 - \bar{\xi}_2)}{2\pi r_o^2} (1 - e^{-r_o^2/r_c^2}) \cos\omega t \, dt, \quad (39)$$

$$b_1 = \sum_{m=-\infty}^{\infty} \frac{2}{T} \int_{mT}^{(m+1)T} -\frac{\kappa(x_2 - \bar{\xi}_2)}{2\pi r_o^2} (1 - e^{-r_o^2/r_c^2}) \sin\omega t \, dt, \quad (40)$$

$$\bar{v}_2 = \sum_{m=-\infty}^{\infty} \frac{1}{T} \int_{mT}^{(m+1)T} \frac{\kappa(x_1 - \bar{\xi}_1 + \nabla\bar{\phi}t)}{2\pi r_o^2} (1 - e^{-r_o^2/r_c^2}) dt, \quad (41)$$

$$a_2 = \sum_{m=-\infty}^{\infty} \frac{2}{T} \int_{mT}^{(m+1)T} \frac{\kappa(x_1 - \bar{\xi}_1 + \nabla\bar{\phi}t)}{2\pi r_o^2} (1 - e^{-r_o^2/r_c^2}) \cos\omega t \, dt, \quad (42)$$

$$b_2 = \sum_{m=-\infty}^{\infty} \frac{2}{T} \int_{mT}^{(m+1)T} \frac{\kappa(x_1 - \bar{\xi}_1 + \nabla\bar{\phi}t)}{2\pi r_o^2} (1 - e^{-r_o^2/r_c^2}) \sin\omega t \, dt, \quad (43)$$

where

$$r_o = \sqrt{\left[(x_1 - \bar{\xi}_1 + \nabla\bar{\phi}t)^2 + (x_2 - \bar{\xi}_2)^2\right]}. \quad (44)$$

Approximations to the above quantities have been evaluated by using a computer programme. A listing of the programme YVCOEM.FTP designed for use on the I.S.V.R. PDP 11/45 computer can be found in Appendix 2. The programme evaluates $\bar{v}_1$, a_1, b_1, $\bar{v}_2$, a_2, b_2 at each point (x_1,x_2) over a specified range of positions in the flow field. The input parameters that can also be specified are the strength κ and core radius r_c of the vortices and the position $(\bar{\xi}_1,\bar{\xi}_2)$ of the "m = 0" vortex at the time t = 0. The period T can be chosen and the convection speed $-\nabla\bar{\phi}$ of the array is fixed by choice of the vortex spacing L. The integration over a number of periods of length T is performed numerically by using the trapezoidal rule. The range of values of m determining the number of vortices over which the integration is performed is also a programme input parameter. Thus, the infinite summation of integrals in the above expressions is approximated by a finite number of the integrals by choice of the range of values of m.

The additional programs YOCOEM.FTP and XOTOTM.FTN (listed in Appendices 3 and 6) have been written in order to evaluate the mean and fundamental fluctuation of the vorticity as a function of time at a series of points in the flow field. The program YOCOEM.FTP has an identical structure to that used for the computation of the velocity field with the same range of input parameters. Exactly analogous arguments to those above can be used to show that the mean and fluctuating vorticity can be expressed as

$$\Omega_3(t) \simeq \overline{\Omega}_3 + \Omega_3', \tag{45}$$

where

$$\Omega_3' = a_\Omega \cos\omega t + b_\Omega \sin\omega t, \tag{46}$$

or

$$\Omega_3' = |\Omega_3| \cos(\omega t + \psi_\Omega), \tag{47}$$

with the mean value $\overline{\Omega}_3$ and the Fourier coefficients a_Ω and b_Ω given by

$$\overline{\Omega}_3 = \sum_{m=-\infty}^{\infty} \frac{1}{T} \int_{mT}^{(m+1)T} \frac{\kappa}{\pi r_c^2} e^{-r_o^2/r_c^2} dt, \tag{48}$$

$$a_\Omega = \sum_{m=-\infty}^{\infty} \frac{2}{T} \int_{mT}^{(m+1)T} \frac{\kappa}{\pi r_c^2} e^{-r_o^2/r_c^2} \cos\omega t \, dt, \tag{49}$$

$$b_\Omega = \sum_{m=-\infty}^{\infty} \frac{2}{T} \int_{mT}^{(m+1)T} \frac{\kappa}{\pi r_c^2} e^{-r_o^2/r_c^2} \sin\omega t \, dt. \tag{50}$$

Again, the infinite summation of integrals is approximated by specifying a finite range of m. This essentially accounts for the velocity and vorticity produced at a given point by only a finite number of vortices in the array.

3.3 The Deduction of the Vorticity Distribution from the Experimental Results

Although the model outlined in the previous sections is clearly a considerable idealisation of the vortically induced flow field, it will nevertheless provide a very useful aid to the interpretation of the measurements described in the previous chapter. Firstly, the model will be used to deduce the strength and approximate core radius of the vortices

shed in the real case. In the experiment, the vortices shed are clearly in a continual state of development as they are convected across the resonator neck. However, the approximate core radius of the vortices can be deduced once they have been formed and reached the downstream region of the resonator neck.

The strength of the vortices can be deduced reasonably easily. As demonstrated in section 2.3, the average rate of shedding of circulation given by equation (11) is governed by the value $\bar{u}_{1max}$ of the mean streamwise grazing flow over the top of the resonator neck. Thus, since the circulation shed is associated with discrete vortices formed once per period, equation (11) can be used to deduce the strength of each vortex. This is given by

$$\kappa = -\tfrac{1}{2}\bar{u}_{1max}^{2}\,T. \qquad (51)$$

This result can be confirmed by using an alternative argument. Assume that the vorticity is shed from the upstream lip as a thin sheet separating a uniform flow of $\bar{u}_{1max}$ from a stationary fluid. The circulation κ due to a length L of the sheet is $\kappa = -\bar{u}_{1max}L$. If the length L is shed during a period T where the vorticity is convected away from the edge at a velocity $\tfrac{1}{2}\bar{u}_{1max} = L/T$, then the circulation κ associated with the length L is again given by $\kappa = -\tfrac{1}{2}\bar{u}_{1max}^{2}T$. This again illustrates the important point that once the mean flow over the neck is specified, the strength of the total vorticity shed per period is fixed. This vorticity can be shed in a distribution ranging from a continuous vortex sheet to discrete vortices having an arbitrary core size. The experimental results show that $\bar{u}_{1max}$ is approximately 12 m/s and the period T of the shedding is approximately 1.66×10^{-3} s. Thus, the strength of each vortex shed must be approximately 0.12 m^2/s.

The core radius of the vortices can be taken as a measure of how "tightly" the vorticity is packed into the core of each vortex. The Gaussian distribution is obviously an idealisation of the true vorticity distribution, but serves as a useful and probably fairly realistic model. The computer program can be used to deduce the mean and fluctuating velocities induced by the passage of the model vortices as a function of their core radius r_c. The value of the vortex strength κ input to the program is 0.12 m^2/s, as deduced above. The value of the period T is again 1.66×10^{-3} s and the length L is 10 mm. This implies a convection speed $-\bar{V\phi}$ of 6.0 m/s. The values of L and $-\bar{V\phi}$ are thus based on well-

established experimental results.

The range of values of the parameter m was chosen to be from m = -10 to m = +10. Thus, at any instant the vortical velocity induced at a given point is the sum of the velocities induced by the nearest 10 vortices upstream and the nearest 10 vortices downstream of the point, the contributions from the vortices further away from the point being neglected.

The mean velocities and the fundamental velocity fluctuations can be computed as a function of the distance across the shear layer, which the passage of the vortices forms. With the co-ordinates of the "m = 0" vortex at t = 0 taken to be simply $\bar{\xi}_1 = 0$ and $\bar{\xi}_2 = -1$ mm, the mean and fluctuating velocities can be computed as a function of x_2 at the fixed streamwise position of $x_1 = 0$. The programme YVCOEM.FTP run with these values of κ, T, L, $\bar{\xi}_1$, $\bar{\xi}_2$, x_1 and with x_2 varied from -6 mm to +4 mm in steps of 0.5 mm yields the shear layer profiles plotted in Figures 4, 5 and 6. The value of r_c input was varied from 0.5 mm to 3.0 mm which, from the scale of the flow in the real case, covers the possible range of core radii that could conceivably be produced by the roll up of the vortices. The results presented in Figures 4, 5 and 6 are in the form of $\bar{u}_1$, v_{1rms} and v_{2rms} where the rms values v_{krms} are given by $\sqrt{[(a_k^2 + b_k^2)/2]}$. The value $\bar{u}_1$ is derived by adding the computed value $\bar{v}_1$ to the convection speed $-\nabla\bar{\phi}$ in the x_1 direction. As expected, a zero value of the vertical mean flow $\bar{v}_2$ was computed, thus giving no net mean flow in the vertical direction. The profiles shown in Figure 4 are independent of the value of x_1 chosen and only the relative phase of the velocity fluctuations will be a function of x_1. The phase of the fluctuations was not computed for present purposes.

An approximate idea of the value of the typical core radius of the vortices formed in the real case can be found by comparing the measured values of the shear layer profile with those computed from the model. Measured values of $\bar{u}_1$ and u_{1rms}, u_{2rms} are thus also shown plotted in Figures 4, 5 and 6. These are taken from the measured results as a function of x_2 at a streamwise location given by $x_1 = 7.5$ mm. At this position in the downstream region of the resonator neck, the vortex sheet in the real case appears to have been "rolled up" sufficiently to be considered as a discrete vortex. There is a good match of the experimental streamwise mean flow data to the values computed for a core radius r_c of approximately 1.5 mm. The streamwise velocity fluctuations measured at the fundamental oscillation frequency above the vortex core

path ($x_2 > -1$) also agree reasonably well with those produced by the convection of vortices with a core radius of 1.5 mm. Below the vortex core path ($x_2 < -1$), the results agree slightly better with computed values using r_c = 2.0 mm. This implies, however, that the measured streamwise velocity fluctuations are a result of the vortical flow only and contain no substantial contribution from the fluctuating potential flow $-\nabla\phi'$. The values of the computed vertical velocity fluctuations v_{2rms} associated with a value of r_c = 1.5 mm in the model are somewhat larger than those measured; better agreement in this case is found with r_c = 2.0 mm. This may possibly be explained by the fact that there is a substantial contribution to the measured results from the reciprocating potential flow. This point will be returned to in a later section.

3.4 The Influence of Viscosity on Shear Layer Development

In summary, the experimental results indicate that the vortical flow in the resonator neck consists of a periodic formation of vortices having a strength κ of 0.12 m^2/s, and an approximate core radius r_c of 1.5 mm. In the model of the flow no attempt is made to simulate the development of the vortices and no account taken of the observed spreading of the mean shear layer in the downstream direction as vortices are formed. The measured results for the streamwise velocity fluctuations imply that the core radius of the vortices may be increasing as they travel across the resonator neck. Higher streamwise velocity fluctuations are induced towards the upstream end of the neck (see Figure 30 of the previous Chapter).

This is probably because the unstable shear layer is being rolled up at the upstream end and the vorticity is still in the fairly concentrated form of a thin rolled sheet. This thin sheet can be relatively rapidly diffused, locally, by the action of viscosity. This can be understood by first recognising that the vorticity distribution chosen (as specified by equation (12)) is of the form of a solution to the diffusion equation governing the influence of viscosity on a line vortex (Batchelor (19)). The parameter r_c is equivalent to $(4\nu\tau)^{\frac{1}{2}}$ where ν is the kinematic viscosity and τ is the time measured from the starting conditions of a concentrated line vortex. The core radius r_c thus increases from zero to a value of $(4\nu\tau)^{\frac{1}{2}}$ during the time τ. An identical form of time dependence is found for the thickness of a sheet vortex diffusing under viscous action from zero thickness (Batchelor (19)). Thus, if r_{c1} is the core radius of a vortex or the thickness of a shear layer at a time τ_1 and r_{c2} is the value at a time τ_2, the difference

$(r_{c2}^2 - r_{c1}^2)$ is given by $4\nu(\tau_2 - \tau_1)$ and thus

$$r_{c2} = \sqrt{[r_{c1}^2 + 4\nu(\tau_2 - \tau_1)]}. \qquad (52)$$

With $(\tau_2 - \tau_1)$ as the value T of one period of oscillation and ν equal to 15×10^{-6} m^2/s, equation (52) enables the increase in core radius of sheet thickness during one cycle of the motion to be calculated numerically. For r_{c1} = 1.5 mm a value of r_{c2} of 1.53 mm is obtained. Thus, once the vortex has been "rolled up", viscosity produces no appreciable diffusion of vorticity, within the period of the motion, from the vortex structure. However, if one considers the diffusion of the initial sheet of vorticity which is rolled into the vortex with an initial thickness r_{c1} of, say, 0.25 mm, this will have diffused to a value of 0.4 mm during the time of one cycle.

The above calculations serve to illustrate that viscosity may have some appreciable diffusing effect on the initially concentrated vorticity in the unstable sheet shed from the upstream edge, presumably during the roll-up process only. Thus, calculations based on the overall core radius indicate that the measured thickening of the mean shear layer over the resonator neck region as a whole cannot be explained by viscous diffusion. However, the possibility cannot be ruled out that the detailed profile of the vortex core structure is affected by the local diffusion of the relatively thin rolled-up sheet from which it is formed. This may then explain some of the features of the observed vortex development and its influence on the mean shear. More definite conclusions are difficult to reach without a far more detailed analysis of the type recently presented by Guiraud and Zeytounian (20).

This completes the present discussion of the vortically induced flow field. Although all the subtleties of the vortex development have not been exhaustively discussed, some important basic parameters have been deduced from the experimental results. In the following section a model for the fluctuating potential flow will be introduced and will be used in conjunction with the vortex shedding model in an attempt to understand the total fluctuating velocity and pressure fields measured in the resonator neck.

4. THE TOTAL FLUCTUATING VELOCITY FIELD

4.1 A Model for the Reciprocating Potential Flow

The total fluctuating flow field in the resonator neck will be considered to consist of the vortical velocity fluctuations induced

directly by the passage of the streamwise convecting vortices, plus a reciprocating potential flow in the vertical (x_2) direction only. It will be demonstrated in the next section that this gives an adequate representation of the form of the measured flow field, although precise quantitative agreement is difficult to obtain due to inadequacies in the vortex shedding model. However, a remarkably good reproduction of the measured fluctuating pressure field can be achieved by using this representation of the flow field and this will be covered in subsequent sections.

As previously discussed in section 2.1, a formal solution of the potential flow in the resonator neck requires a calculation of the fluctuating contribution from the "image vorticity", this being largely determined by the strength and the path taken by the shed vortices. Any such contribution is indistinguishable from (or at least not measurably significant compared to) the reciprocating potential flow calculated from acoustical considerations with a knowledge of the cavity pressure fluctuations. The explanation for this is that the fluctuating potential flow necessary to satisfy the boundary conditions is actually indistinguishable from the "acoustically" produced potential flow, as described here. The reciprocating potential flow will thus be determined from simple acoustic parameters.

The acoustical behaviour of the resonator can be represented by the equivalent circuit illustrated in Figure 7. The acoustic response of the cavity results in a volume velocity q_n in the cavity neck. This is related to the effective inertance M and resistance R_r of the cavity neck by the impedance

$$p_c/q_n = (R_r + i\omega M), \tag{53}$$

where p_c is the cavity pressure. If p_c is given by $|p_c|\cos\omega t$ and the vertical velocity $\partial\phi'/\partial x_2$ in the resonator neck is expressed as $|\partial\phi/\partial x_2|\cos(\omega t + \psi_\phi)$, it is a straightforward matter to show that the amplitude of the fluctuating velocity in the resonator neck is given by

$$\left|\frac{\partial\phi}{\partial x_2}\right| = \frac{|p_c|}{S\sqrt{(R_r^2 + \omega^2 M^2)}}, \tag{54}$$

where S is the cross-sectional area of the resonator neck.

The phase ψ_ϕ of the reciprocating potential flow relative to the phase of the cavity pressure fluctuation is given by

$$\psi_\phi = \tan^{-1}\left(\frac{-\omega M}{R_r}\right). \qquad (55)$$

The amplitude and phase of the reciprocating potential flow can thus be easily calculated from a knowledge of the cavity pressure fluctuation with the inertance M and resistance R_r. The question then arises as to what values of M and R_r should be used. The problem of predicting the acoustic impedance of cavities and orifices with grazing flow has already received considerable attention. However, a completely satisfactory theoretical and physical description of the processes involved in the modification of the "no flow" acoustic impedance has yet to be found. The analogous problem of the acoustic impedance of orifices with a flow through the aperture has been adequately treated (see the discussion by Morse and Ingard (21)). In this case the resistive part of the impedance is increased by the presence of the flow whilst the effective attached mass is decreased. These general trends have been found to be convincingly reproduced in Ronneberger's (22) experiments with grazing flow over orifices, although in the transition region from high to low Strouhal numbers the orifice impedance curve was found to exhibit a complicated spiral form in the complex plane. The general increase in resistance and decrease in attached mass has also been observed by Dean (23) in connection with the impedance of cavity duct liners. These trends have also been predicted by Howe (17) with a surprisingly good agreement with experimental results since, as the present work reveals, Howe's model is a considerable idealisation of the nature of the flow found in the real case.

Thus, there is no real basis for predicting the flow dependence of R_r and M, the problem of the determination of the impedance being intimately related to the interaction between the vortical and potential flows being investigated. The amplitude and phase of the reciprocating potential flow can, however, be estimated from the "no flow" values of R and M determined approximately in the previous Chapter. A value of M of 22 kg/m^2 (corresponding to an effective length ℓ of 18 mm) and a value of R_r of 8.4 x 10 $kg/m^4/s$ result in a value of $|\partial\phi/\partial x_2|$ of 1.68 m/s for the measured rms cavity pressure of 100 N/m^2. The phase of the velocity fluctuation lags the cavity pressure fluctuation by 84^o.

4.2 The Resultant Vertical Velocity Fluctuation

The resultant fluctuating velocity field produced in the vertical direction can thus be modelled by superposing the "acoustical" uniform

potential flow deduced above in section 4.1 and the vertical velocity fluctuations induced by the passage of the vortices. The latter have been calculated by computation of the Fourier coefficients of the fundamental vertical velocity fluctuation produced by the passage of the vortices for a range of values x_1 and x_2. The programme YVCOEM.FTP was run with x_1 ranging from 0 to 10 mm in increments of 0.5 mm and x_2 ranging from -6 mm to +4 mm, also in increments of 0.5 mm. The values of the vortex strength κ, period T and spacing L were all chosen as before, with the value of the core radius r_c of 1.5 mm.

The values of the co-ordinates $(\bar{\xi}_1, \bar{\xi}_2)$ of the "m = 0" vortex at t = 0 also need to be established. The time t = 0 can be taken to be the time during the cycle at which the cavity pressure is a maximum. The phase ψ_k of the velocity fluctuations $|v_k|\cos(\omega t + \psi_k)$ can thus be expressed relative to the cavity pressure fluctuations. The values ψ_1 of the measured phase of the streamwise velocity fluctuations can be used to deduce the streamwise position $\bar{\xi}_1$ of the vortex shed in the resonator neck when the cavity pressure reaches its maximum value (i.e., at t = 0). Measured values of ψ_1 have been plotted against x_1 for the three values of x_2 = 0.5, 1.0 and 1.5 mm (Figure 8). In the downstream region of the resonator neck (x_1 > 5.0 mm) the results fall roughly onto a straight line, implying a uniform vortex convection speed. The slope of this straight line is consistent with a vortex convection speed of 6 m/s. Clearly at the upstream end of the resonator neck the disturbance convection speed (given by the spatial rate of change of phase) is somewhat less than 6 m/s in the region where the vortices are formed. The streamwise position of the shed vortex when the cavity pressure is a maximum is given by the position at which the streamwise velocity fluctuations induced above the core path are in phase with cavity pressure fluctuations. The intersection of the straight line in Figure 8 with the x_1 axis at ψ_1 = 0 shows that this position is given by x_1 = 6.25 mm.

The position of the vortex at t = 0 in the vertical direction is approximately x_2 = -1.0 mm. This is established from the approximate position of the 180° phase change in the phase of the streamwise velocity fluctuations as the shear layer is traversed in the vertical direction at x_1 = 6.25 mm. The values of the co-ordinates $\bar{\xi}_1$ and $\bar{\xi}_2$ can thus be taken to be 6.25 mm and -1.0 mm, respectively. In the real case, the vortex core path appears to be slightly curved as the vortex convects across the resonator neck. This is probably due to the

convection of the vortex by the reciprocating potential flow. This is neglected in the model where the vortices are simply convected parallel to the x_1 axis along the path defined by $x_2 = -1.0$ mm.

The output of the program YVCOEM.FTP run with the input parameters described above has been used to establish the vortically induced vertical velocity fluctuations. The program XVTOTM.FTN (listed in Appendix 5) has been used to combine the vortical fluctuations with the uniform potential flow having the amplitude and phase deduced from the no flow acoustic impedance of the resonator neck. This latter program calculates the net amplitude and phase of the harmonic fluctuation produced by the linear combination of the two fluctuating velocity signals. The output of the program is shown in the form of a contour plot (Figure 9) based on the values computed over the 0.5 mm grid used. The plot produced can be compared with the measured values of the rms amplitude of the net vertical velocity fluctuation shown in Figure 32 of the previous Chapter.

It can be seen that the superposition of the two forms of velocity fluctuations, "acoustical" and "vortical", implicit in the model give an amplitude pattern that is in rough agreement with the form of the measured vertical velocity field. The combination of the velocity fields shows in particular that the maximum vertical velocity fluctuation occurs in the region towards the downstream edge of the slot at a value of x_1 around 6.0 mm. The vortically induced fluctuation is in phase with the reciprocating potential flow in this region. Conversely, in the upstream region of the resonator neck the fluctuating potential and vortical flows are out of phase such that a lower net fluctuating velocity amplitude is produced. This implies that the vortical and potential flows may be related by the need to satisfy the Kutta condition at the upstream lip. The flow visualisation and the measured values of vertical velocity both imply that the vortical and potential flow velocities cancel towards the upstream lip. This is confirmed by the relative phase of the two fluctuations deduced with the aid of the model.

The quantitative agreement between the model and experiment is not entirely convincing. This may be because the amplitude of the vortical fluctuations in the vertical direction is over-estimated by the model. This is likely to be caused by the assumption that the vertical velocity is the sum of the contributions from the line array of vortices. In the real case, the vertical velocity will be induced by each vortex

during and after its process of formation and the assumption that each vortex is inducing its maximum velocity during all the cycle is obviously a considerable idealisation.

The failure to model the formation of the vortices adequately also makes the precise nature of the link between the vortical and potential flows through the Kutta condition difficult to establish firmly. The present model indicates that the vortically induced velocity at the upstream edge in the vertical direction is very dependent on how "tightly wound" the shed vorticity becomes, this being characterised by the core radius of the shed vortices. This suggests that a high value of the fluctuating potential flow results in the vortices becoming tightly wound in order to induce sufficiently large vertical velocity fluctuations at the upstream edge to ensure no net vertical displacement of the separating shear layer. The extent to which this applies in the real case depends on how close to the edge the vortices are formed. If the vortices are formed at a distance much greater than one core radius away from the edge, one would not expect the velocity induced at the edge to be sensitive to the degree of concentration of the vorticity in the core (since at large distances from the core, the induced velocity is insensitive to core radius). The results of the flow visualisation indicate that the formation of the vortex begins to occur at a distance of the order of the core radius away from the edge. It can thus be only tentatively concluded that the amplitude of the reciprocating potential flow influences the concentration of vorticity wound into the vortex core, the vortex being wound sufficiently tightly to satisfy the Kutta condition at the upstream edge.

5. THE FLUCTUATING PRESSURE FIELD

5.1 The Pressure Fluctuations associated with the Passage of the Vortices

The measurements of the fluctuating static pressure field in the resonator neck presented in the previous Chapter revealed an interesting form of interference pattern shown in the measured values of the amplitude and phase of the pressure fluctuations. It will be demonstrated that this interference pattern can be satisfactorily explained by a simple superposition of the pressure fluctuations generated by the passage of the vortices with the pressure fluctuations associated with the reciprocating potential flow. Rigorously speaking, the net pressure field can be deduced from a knowledge of the total velocity field by

taking the divergence of the momentum conservation equation and solving the resulting Poisson equation for the pressure. This type of approach has not been taken. Rather, the pressure fluctuations associated with each part of the velocity field have been deduced. This is based on the assumption that independent momentum balances exist between the accelerations associated with each component of the velocity field and the gradient of a distinct part of the pressure field. The success of these independent momentum balances in explaining the measured results has some interesting implications for the nature of the interaction between the vortical and potential flows. This will be discussed in the next Chapter with reference to the full momentum equation.

Firstly, the static pressure fluctuations caused by the passage of the vortices will be estimated by deducing the static pressure defect produced in the core of an isolated vortex. This can be found by integration of the momentum equation expressing the balance between the radial pressure gradient in the vortex core and the centripetal acceleration of the fluid rotating about the vortex axis. This will be performed for a single stationary vortex in free space. Writing the pressure as p, the momentum equation for steady two dimensional flow with circular streamlines reduces to

$$\frac{1}{\rho_o}\frac{\partial p}{\partial r} = \frac{v_\theta^2}{r} . \qquad (56)$$

The density ρ_o is assumed constant for the purposes of estimating the pressure p. In terms of the variables V_θ and R defined in equation (16) for the model vorticity distribution chosen, the above equation can be written as

$$\frac{1}{\rho_o v_c^2}\frac{\partial p}{\partial R} = \frac{V_\theta^2}{R} \qquad (57)$$

and substitution of $V_\theta = (1 - e^{-R^2})/R$ yields

$$\frac{1}{\rho_o v_c^2}\frac{\partial p}{\partial R} = \frac{1}{R^3}(1 - 2e^{-R^2} + e^{-2R^2}) . \qquad (58)$$

An equation identical to this has been treated by Newman (24) in connection with the flow in a viscous trailing vortex. Integration of the equation from R to ∞ yields the value of $(p_\infty - p)$ where p_∞ is the ambient static pressure;

$$\frac{p_\infty - p}{\frac{1}{2}\rho_o v_c^2} = \frac{1}{R^2} - 2\left[\frac{e^{-R^2}}{R^2} + Ei(-R^2)\right] + \left[\frac{e^{-2R^2}}{R^2} + 2\,Ei(-2R^2)\right]. \qquad (59)$$

Here $Ei(-R^2)$ is the exponential integral $-\int_2^\infty (e^{-s}/s)\,ds$. Writing the right-hand side of equation (59) as $F(r^2/r_c^2)$ and putting the value of the static pressure defect $p_\infty - p$ as $-p_v$ yields

$$p_v = -\frac{\rho_o \kappa^2}{8\pi^2 r_c^2} F(r^2/r_c^2). \qquad (60)$$

This then establishes the form of the static pressure defect as a function of radial distance r from the core axis and the parameters κ and r_c.

In order to estimate the static pressure fluctuations produced by the passage of the vortices, it will be assumed that each vortex in the model array has an associated radial static pressure distribution differing from the ambient pressure in accordance with equation (60). This is equivalent to assuming that there is a negligible contribution from the velocity fields of the neighbouring vortices to the radial momentum balance of each vortex in the array. This is a reasonable assumption, since the vortex spacing in the array is considerably larger than the typical value of core radius considered. The radial pressure fields associated with each vortex will thus be assumed to superpose. The static pressure fluctuations generated by the passage of this spatial distribution of static pressure can thus be estimated. The dependence of the magnitude of these fluctuations on the parameters of vortex strength and core radius can also be deduced.

By use of an exactly analogous argument to that used in finding the mean and fluctuating velocity field induced by the passage of the vortex array, the pressure as a function of time produced by the uniform convection of the array can be expressed as

$$p_v(t) \simeq \overline{p_v} + p_v', \qquad (61)$$

$$\overline{p_v} = \sum_{m=-\infty}^{\infty} \frac{1}{T} \int_{mT}^{(m+1)T} -\frac{\rho_o \kappa^2}{8\pi^2 r_c^2} F(r_o^2/r_c^2)\,dt, \qquad (62)$$

where

$$p_v' = a_{pv}\cos\omega t + b_{pv}\sin\omega t, \qquad (63)$$

$$a_{pv} = \sum_{m=-\infty}^{\infty} \frac{2}{T} \int_{mT}^{(m+1)T} -\frac{\rho_o \kappa^2}{8\pi^2 r_c^2} F(r_o^2/r_c^2) \cos\omega t \, dt, \qquad (64)$$

$$b_{pv} = \sum_{m=-\infty}^{\infty} \frac{2}{T} \int_{mT}^{(m+1)T} -\frac{\rho_o \kappa^2}{8\pi r_c^2} F(r_o^2/r_c^2) \sin\omega t \, dt. \qquad (65)$$

The program YPCOEM.FTP (listed in Appendix 4) has been written to compute these quantities. Use has been made of the fact that $F(r_o^2/r_c^2) \rightarrow 2\ell n2 = 1.386$ as $(r_o^2/r_c^2) \rightarrow 0$ and the exponential integrals comprising $F(r_o^2/r_c^2)$ were approximated by (Abbramowitz and Stegun (25));

$$Ei(-R^2) = \gamma + \ell n(-R^2) + \sum_{n=1}^{\infty} \frac{(-R^2)^n}{nn!}, \qquad (66)$$

where γ is Euler's constant (0.5772) and only the first six terms of the series were needed to give an adequate representation of the function.

The program YPCOEM.FTP was run with the values of κ, T and L established above with a fixed value of $x_1 = 0$ and with x_2 varied from -6 mm to +4 mm in increments of 0.5 mm. The resulting values of $p_{v\ rms}$ given by $\sqrt{[(a_{pv}^2 + b_{pv}^2)/2]}$ are plotted in Figure 10 as a function of the distance across the shear layer (x_2) and core radius r_c. It can be seen that for a core radius of 1.5 mm the amplitudes of the pressure fluctuations produced are of the order of those measured in the resonator neck (see Figure 40 of the previous Chapter). This implies that the model is giving a reasonable estimate of the fluctuating pressures that could be expected to be associated with the passage of the vortices of the strength and core size of those observed in the experiment.

5.2 The Pressure Fluctuations associated with the Reciprocating Potential Flow

Having established the order of magnitude of the pressure fluctuations generated by the passage of the vortices based on the assumption that the vortical flow only is present, the pressure fluctuations associated with the reciprocating potential flow will now be estimated on the assumption that only the potential flow is present. The model of the potential flow in the neck will again be based on the assumption that identical acoustical conditions exist in the resonator as in the case without any flow. Thus the "no flow" values of the inertance and resistance associated with the resonator neck will be assumed to determine the structure of an "acoustic" pressure field.

In order to estimate the pressure fluctuations in the region of the neck, the model represented by the equivalent circuit shown in Figure 7 will be used. The variation of pressure across the resonator neck will be calculated by assuming that the neck characteristics can be represented by a continuous distribution of inertance, i.e. the amplitude and phase of the pressure fluctuations in the neck will vary in the x_2 direction as if the effective mass of the neck varies linearly across the whole "effective length" ℓ attributable to the reciprocating plug flow in the resonator neck. At a particular value of x_2 in the neck region, the inertance of the fluid comprising the plug flow in the area above the position considered will be assumed to be M_1. The inertance of the fluid below this position will be $(M - M_1)$, M being the total inertance due to the neck flow. If at $x_2 = 0$, $M_1 = M'$, say, and M' can be expressed in terms of the effective length $\ell' = M'S/\rho_o$ of the fluid in the region $x_2 > 0$, the variation of M_1 across the neck can be written (see Figure 7)

$$M_1 = (\ell' - x_2)(\rho_o/S) \quad \text{for} \quad (\ell - \ell') < x_2 < \ell', \tag{67}$$

$$\text{with } M_1 = \ell(\rho_o/S) \quad \text{for} \quad x_2 < (\ell - \ell') \tag{68}$$

$$\text{and} \quad M_1 = 0 \quad \text{for } x_2 > \ell'. \tag{69}$$

The value of the complex pressure p_ϕ at a given value of x_2 can be expressed in terms of the cavity pressure p_c by noting that the volume velocity q_n is related to p_ϕ and p_c by

$$q_n = \frac{p_c}{R_r + i\omega M} = \frac{p_\phi}{R_r + i\omega M_1} \tag{70}$$

such that

$$p_\phi = p_c \left[\frac{R_r + i\omega M_1}{R_r + i\omega M}\right] . \tag{71}$$

It is a straightforward matter to show that the amplitude $|p_\phi|$ and phase $\psi_{p\phi}$ of the pressure fluctuation $|p_\phi|\cos(\omega t + \psi_{p\phi})$ is related to the amplitude and phase of the cavity pressure fluctuation $|p_c|\cos\omega t$ by

$$|p_\phi| = |p_c| \frac{\sqrt{\left[(\omega^2 M_1 M + R_r^2)^2 + (\omega R_r (M_1 - M))^2\right]}}{(R_r^2 + \omega^2 M^2)} \tag{72}$$

$$\psi_{p\phi} = \tan^{-1}\left[\frac{\omega R_r (M_1 - M)}{R_r^2 + \omega^2 M_1 M}\right] . \tag{73}$$

This amplitude and phase have been plotted against $[x_2 + (\ell - \ell')]$. The inductance M_1 is assumed to vary as a function of x_2 in accordance with the relations (67,68,69). The values of M and R_r used are the "no flow" values deduced in the previous Chapter and the amplitude of the cavity pressure fluctuation has again been taken from the measured rms value of 100 N/m^2. The variation of amplitude and phase of the pressure fluctuations shown in Figure 11 would thus be obtained in the resonator neck if the pressure fluctuations were driven by an acoustic source inside the cavity under no flow conditions. The location of the effective mass of the air in the neck relative to the position of the resonator mouth is characterised by the parameter ℓ' which has been left undetermined.

5.3 The Measured Pressure Fluctuation

It can now be demonstrated that the measured pressure interference pattern (Figures 40 and 41 of the previous Chapter) in the resonator neck appears to consist of a simple superposition of the pressure fluctuations generated by the passage of the vortices with the pressure field associated with the reciprocating potential flow. These two fluctuating pressure fields appear to constructively interfere towards the upstream lip of the resonator neck where the maximum net pressure fluctuations are measured. A destructive interference occurs towards the downstream edge, the minimum amplitude of the net pressure fluctuation being measured on the vortex core path at the position $x_1 \simeq 6.5$ mm. This implies that the two pressure fluctuations are 180° out of phase at this position.

The relative phase of the pressure fluctuations associated with the passage of the vortices varies linearly with x_1 for uniform streamwise convection of the vortices. For the uniform convection of the model vortex array, the phase of the pressure fluctuations produced at the fundamental frequency is 180° out of phase with the streamwise velocity fluctuations produced above the vortex core path. At the streamwise location $x_1 = 6.5$ mm the experimental results plotted in Figure 8 show that the streamwise velocity fluctuations lag the cavity pressure fluctuations by 10°. This implies the pressure fluctuations produced by the passage of the vortices lead the cavity pressure fluctuations by 170°. Thus, for destructive interference at $x_1 = 6.5$ mm the pressure fluctuations associated with the reciprocating potential flow must lag the cavity pressure fluctuations by 10°.

The minimum pressure amplitude also appears to occur along the line of the core path at a vertical location of $x_2 = -1.0$ mm. The model of the pressure fluctuations associated with the potential flow indicates that a phase of -10° relative to the cavity pressure fluctuations will occur at a vertical position corresponding to a value of $\{x_2 + (\ell - \ell')\}$ of 11.0 mm. Thus, for the assumed value of ℓ, the value of ℓ' can be deduced. This will specify the distribution of inertance in the neck of the resonator, which will result in the pressure fluctuations associated with the reciprocating potential flow being in anti-phase with the pressure fluctuations produced by the passage of the vortices at $x_2 = -1.0$ mm. For a value of ℓ of 18 mm (corresponding to the "no flow" value) and a value of $\{x_2 + (\ell - \ell')\}$ of 11.0 mm the value of ℓ' must be 6.0 mm. Thus, the effective mass appears to be distributed in the resonator neck with approximately 1/3 above the resonator mouth and 2/3 below the resonator mouth inside the cavity.

A check on this is provided by consideration of the amplitude of the pressure fluctuations associated with the reciprocating potential flow. Figure 10 shows that for a phase $\psi_{p\phi}$ of -10° relative to the cavity pressure, the amplitude of the pressure fluctuations is 40 N/m^2 (rms). This is of an almost identical value to the amplitude of the pressure fluctuations induced by the passage of vortices having a core radius of 1.5 mm. The resulting destructive interference of the two pressure fluctuations of very similar magnitude explains the relatively low net pressure amplitude measured towards the downstream edge.

An estimate has been made of the amplitude and phase of the pressure fluctuations produced by linear combination of the two model component pressure fields over the region of interest. The program YPCOEM.FTP was run in order to evaluate the Fourier coefficients of the vortex induced pressure fluctuations over a range of values of x_1 from 0 to 10 in 0.5 mm intervals, and of x_2 from -4 to +2, also in 0.5 mm intervals. The values of vortex strength and core radius used were again those deduced above as being closely representative of the values in the real case. The program XPTOTM.FTN (listed in Appendix 7) was then used to evaluate the combination of the vortex induced pressure fluctuations with those associated with the reciprocating potential flow over the same range of values of x_1 and x_2. The model for the latter was that outlined above with use, again, of the "no flow" values of inertance and resistance. A value of ℓ' of 6.0 mm was chosen with the object of reproducing the measured pressure interference pattern.

The net amplitude and phase of the pressure fluctuations evaluated over the 0.5 mm grid are presented as contour plots in Figures 11 and 12. Comparison of these with the measured values of amplitude and phase in Figures 40 and 41 of the previous Chapter shows remarkably good agreement in both qualitative and quantitative aspects between the model representation of the pressure interference pattern and the experimentally measured values. The success of the model in reproducing experimental results gives a strong indication that, at least to a first approximation, the net pressure field in the resonator neck appears to be generated by the superposition of a pressure field that is associated with the shed vorticity with pressure fluctuations "locked" into the cavity pressure fluctuation. The implications of this finding for the mechanics of the vortical/potential flow interaction will be discussed in the next Chapter.

6. CONCLUSIONS

The velocity field in the resonator neck can be considered as consisting of two parts. The first is purely vortical and is the velocity field directly induced by the vorticity shed from the upstream lip of the resonator neck. The remainder of the velocity field is irrotational and appears to consist approximately of a uniform mean potential flow in the streamwise direction and a reciprocating potential flow in the vertical direction.

The strength of the vortices shed periodically from the upstream lip depends only on the mean grazing flow across the top of the resonator neck. This is confirmed using a simple model of vortex shedding, which shows that the structure of the mean shear layer is intimately related to the strength of the shed vortices and the distribution of vorticity in their core. The effective core radius of the vortices formed can be approximately deduced from the observed thickness of the mean shear layer and the velocity fluctuations induced in the streamwise component direction. The periodically shed vortices observed in the experiment thus appear to have a strength of 0.12 m/s and an approximate core radius of 1.5 mm.

The pattern of vertical velocity fluctuations measured in the resonator neck appears to be explained by a superposition of a reciprocating uniform potential flow with the velocity fluctuations induced by the passage of the streamwise convected vortices. These two velocity fluctuations constructively interfere to produce the

observed maximum value of vertical velocity fluctuation towards the downstream edge of the resonator neck. Towards the upstream edge, the two velocity fields appear to interfere destructively and hence minimise the net vertical displacement of the fluid. This confirms the results of the flow visualisation experiment, which show that the unstable shear layer leaves the upstream edge tangentially, thus implying that the Kutta condition at the upstream edge is satisfied. It is possible that the amplitude of the reciprocating potential flow influences the effective core radius of the vortices formed, the vortices becoming more tightly wound in order to induce a sufficient velocity to cancel the reciprocating potential flow velocity.

The interesting interference pattern observed in the measurements of the fluctuating pressure field appears to be explained by a superposition of the pressure fluctuations induced by the passage of the vortices with the pressure fluctuations associated with the reciprocating potential flow. In order to estimate the pressure fluctuations associated with the reciprocating potential flow, an acoustic model is used which assumes the "no flow" values of the acoustic impedance of the resonator neck deduced in the previous Chapter. Although this procedure is of doubtful validity, the pressure interference pattern produced is in very good agreement with both the amplitude and phase of the experimentally observed values. In any event, to a first approximation, the observed interference pattern certainly consists of a superposition of a pressure disturbance convected in the streamwise direction, with a pressure fluctuation that is approximately uniform in both amplitude and phase over the region considered.

The possible independent momentum balances suggested by the observed fluctuating pressure field will be considered in the light of the full linearised momentum conservation equation in the next Chapter. An attempt will be made to identify the accelerations in the fluid that are primarily responsible for the interaction of the vortex shedding with the reciprocating potential flow. The strength and core radius of the vortices observed in the experiment will also be used to enable the evaluation of various energy production terms in an attempt to understand the energy balance occurring in the flow at the resonance condition observed.

REFERENCES

(1) P.M. MORSE and H. FESHBACH 1953 Methods of Theoretical Physics, Part 1, Ch. 1, p. 52. McGraw-Hill.

(2) G.K. BATCHELOR 1970 An Introduction to Fluid Dynamics. Cambridge University Press. See Ch. 2, pp. 84-87 and also pp. 99-100.

(3) M.J. LIGHTHILL 1963 Laminar Boundary Layers (Editor L. Rosenhead), Ch. 2, p. 56. Clarendon Press, Oxford.

(4) M.S. HOWE 1975 Journal of Fluid Mechanics 71, 625-673. Contributions to the theory of aerodynamic sound with application to excess jet noise and the theory of the flute.

(5) D.G. CRIGHTON 1972 Journal of Fluid Mechanics 51, 357-362. Radiation from vortex filament motion near a half plane.

(6) J.W.S. RAYLEIGH 1894 The Theory of Sound, Vol. 2, Ch. 21. Dover, New York (1945 reprint of 2nd edition).

(7) C.C. LIN 1955 The Theory of Hydrodynamic Stability. Cambridge University Press.

(8) P.G. DRAZIN and L.N. HOWARD 1966 Advances in Applied Mechanics 9, 1-89. Hydrodynamic stability of parallel flows of inviscid fluid.

(9) R. BETCHOV and W.O. CRIMINALE 1967 Stability of Parallel Flows. Academic Press.

(10) A. MICHALKE 1965 Journal of Fluid Mechanics 22, 371-383. Vortex formation in a free boundary layer according to stability theory.

(11) P. MUNGUR 1977 A.I.A.A. Paper 77-1369. On the sensitivity of shear layers to sound.

(12) J.T. STUART 1958 Journal of Fluid Mechanics 4, 1-21. On the non-linear mechanics of hydrodynamic stability.

(13) L. ROSENHEAD 1931 Proceedings of the Royal Society of London Series A 134, 170-192. The formation of vortices from a surface of discontinuity.

(14) A.V.J. EDWARDS 1978 Ph.D. Thesis, University of Southampton. The computer simulation of an unsteady flow.

(15) R.R. CLEMENTS 1973 Journal of Fluid Mechanics 57, 321-336. An inviscid model of two dimensional vortex shedding.

(16) J.C. HARDIN and J.P. MASON 1977 A.I.A.A. Journal 15, 632-637. Broadband noise generation by a vortex model of cavity flow.

(17) M.S. HOWE 1979 Journal of Sound and Vibration 67, 533-544. The influence of grazing flow on the acoustic impedance of a cylindrical wall cavity.

(18) M.S. HOWE 1979 Journal of Fluid Mechanics 91, 209-229. Attenuation of sound in a low Mach number nozzle flow.

(19) G.K. BATCHELOR 1970 An Introduction to Fluid Dynamics. Cambridge University Press. See p. 187 and also p. 204.

(20) J.P. GUIRAUD and R.KH. ZEYTOUNIAN 1979 Journal of Fluid Mechanics 90, 197-201. On the viscous diffusion of rolled vortex sheets.

(21) P.M. MORSE and K.U. INGARD 1968 Theoretical Acoustics, Ch. 11, p. 758. McGraw-Hill.

(22) D. RONNEBERGER 1972 Journal of Sound and Vibration 24, 133-150. The acoustical impedance of holes in the wall of flow ducts.

(23) P.D. DEAN 1974 Journal of Sound and Vibration 34, 97-130. An in-situ method of wall acoustic impedance measurement in flow ducts.

(24) B.G. NEWMAN 1959 Aeronautical Quarterly 10, 149-162. Flow in a viscous trailing vortex.

(25) M. ABRAMOWITZ and I.A. STEGUN 1965 Handbook of Mathematical Functions, p. 229. Dover.

APPENDIX 1. LIST OF SYMBOLS

a_k, b_k	Fourier coefficients of vortical velocity fluctuations at the fundamental frequency
a_Ω, b_Ω	Fourier coefficients of vorticity fluctuations at the fundamental frequency
a_{pv}, b_{pv}	Fourier coefficients of vortically induced static pressure fluctuations at the fundamental frequency
f_k	function of time expressing the velocity field induced by a given vortex in the model array
F	function expressing the dependence of the static pressure defect of an isolated vortex on core radius and radial distance from core axis
k	used as a subscript taking the values 1 or 2
ℓ, ℓ'	effective lengths of air masses forming inertance of resonator neck
L	vortex separation distance
M, M_1, M'	values of acoustic inertance in resonator neck
$\underline{n}$	vector normal to surface, or denoting the surface outward normal direction when used as a subscript n
p	static pressure
p_v	static pressure defect associated with an isolated vortex
p_c	acoustic cavity pressure
p_ϕ	acoustic pressure in resonator neck
p_∞	free stream static pressure
q_n	acoustic volume velocity in resonator neck
r	radial distance from vortex core axis
r_m	radial distance from core axis of m-th vortex in the model array
r_o	radial distance from core axis of m = 0 vortex in the model array
r_c	vortex core radius
R	ratio of radial distance from vortex core axis to vortex core radius (r/r_c)

R_r	acoustic radiation resistance
$\underline{s}$	position vector
S	area of cross section of resonator neck
t	time
T	period of one cycle of motion
$\underline{u}$	total velocity vector
$\overline{u}_{1max}$	value of total streamwise velocity at upper edge of shear layer
$\underline{v}$	vortical velocity vector
$v_{m\theta}, v_{m1}, v_{m2}$	vortical velocity induced by the m-th vortex in the model array in the tangential, streamwise and vertical component directions
v_θ	vortical velocity induced by an isolated vortex in the tangential component direction
v_c	tangential velocity induced at edge of core of equivalent Rankine vortex
V_θ	non-dimensional tangential velocity (v_θ/v_c)
x_1, x_2, x_3	cartesian coordinates
α	used as a variable of integration
Γ	circulation
θ	used as a subscript to denote tangential direction
κ	vortex strength
ν	coefficient of kinematic viscosity
ξ_{m1}, ξ_{m2}	position coordinates of m-th vortex in the model array
$\overline{\xi}_1, \overline{\xi}_2$	position coordinates of the m = 0 vortex at t = 0
ρ_o	ambient air density
τ	time during which viscous diffusion takes place
ϕ	velocity potential
ψ_k	relative phase of vortically induced velocity fluctuations at fundamental frequency

ψ_Ω	relative phase of vorticity fluctuations at fundamental frequency
ψ_ϕ	relative phase of reciprocating potential flow
$\psi_{p\phi}$	relative phase of pressure fluctuations associated with reciprocating potential flow
ω	radian frequency

APPENDIX 2. LISTING OF PROGRAM YVCOEM.FTP

For the calculation of Fourier coefficients of "streamwise" and "vertical" velocity fluctuations induced by the passage of the model vortex array

```
      DIMENSION B(300),C(300),D(300),CB(128)
      EQUIVALENCE (CB(33),ICB)
      CALL TYPE ('&YVCOEM')
      CALL ASKN (B,'&COEFS V1A,V1B=')
      CALL ASKN (C,'&COEFS V2A,V2B=')
      CALL ASKN (D,'&MEAN VALUES V1M,V2M=')
      CALL ASKI (IT,'&MIN TIME=')
      CALL ASKI (ITM,'&MAXTIME=')
      CALL ASKI (ITT,'&PERIOD=')
      CALL ASKI (M,'&NO OF PERIODS <IT1=')
      CALL ASKI (N,'&NO OF PERIODS >IT1=')
      CALL ASKR (G,'&VORTEX STRENGTH=')
      CALL ASKR (RO,'&CORE RADIUS=')
      CALL ASKR (SL,'&SHEDDING LENGTH=')
      CALL ASKR (X1,'&FIRST X1 VALUE=')
      CALL ASKR (XMAX,'&LAST X1 VALUE=')
      CALL ASKR (XINC,'&X1 INC=')
      CALL ASKR (Y1,'&FIRST X2 VALUE=')
      CALL ASKR (YMAX,'&LAST X2 VALUE=')
      CALL ASKR (YINC,'&X2 INC=')
      CALL ASKR (XO,'&X1 POSITION AT T=0 =')
      CALL ASKR (YO,'&X2 POSITION AT T=0 =')
      CALL OUTPUT(B)
      CALL OUTPUT(C)
      CALL OUTPUT(D)
      TP1=6.284
      G=-G
      W=TP1/ITT
      UC=SL/ITT
      Y=Y1
11    X=X1
10    SXA=0.0
      SXB=0.0
      SYA=0.0
      SYB=0.0
      VXM=0.0
      VYM=0.0
      ITR=X/UC
30    DO 1 I=IT,ITM
      VX=0.0
      VY=0.0
      T=I
      XC=X-(UC*T)-XO
      YC=Y-YO
50    RP=SQRT((XC*XC)+(YC*YC))
      RP2=RP*RP
      RO2=RO*RO
3     E=-(RP2/RO2)
      IF (E.GT.-80.0) GO TO 5
4     EE=0
      GO TO 6
5     EE=EXP(E)
6     IF (RP2.NE.0.0) GO TO 7
      VX1=0
      VY1=0
      GO TO 2
7     VX1=((-G)*YC*(1-EE))/(TP1*RP2)
      VY1=(G*XC*(1-EE))/(TPI*RP2)
      VX=VX+VX1
      VY=VY+VY1
2     IT1=ITR
      IT2=IT1-(M*ITT)+1
      IT3=IT1+(N*ITT)
      TS=T-IT1
      IF (I.LT.IT2) GO TO 1
      IF (I.GT.IT3) GO TO 1
      PXA=VX*COS(W*TS)
      PXB=VX*SIN(W*TS)
      PYA=VY*COS(W*TS)
      PYB=VY*SIN(W*TS)
      SXA=SXA+PXA
      SXB=SXB+PXB
      SYA=SYA+PYA
      SYB=SYB+PYB
      VXM=VXM+VX
      VYM=VYM+VY
      IF (I.NE.IT3) GO TO 1
      F=2.0/ITT
      SXA=SXA*F
      SXB=SXB*F
      SYA=SYA*F
      SYB=SYB*F
      VXM=VXM*(F/2.0)
      VYM=VYM*(F/2.0)
      CALL OUT (B,SXA)
      CALL OUT (B,SXB)
      CALL OUT (C,SYA)
      CALL OUT (C,SYB)
      CALL OUT (D,VXM)
      CALL OUT (D,VYM)
1     CONTINUE
      X=X+XINC
      IF(X.LE.XMAX) GO TO 10
      Y=Y+YINC
      IF(Y.LE.YMAX) GO TO 11
      ICB=3
      CB(2)=1000.0
      CB(3)=0.0
      CB(4)=1.0
      CALL OUTEND (B,CB)
      CALL OUTEND (C,CB)
      CALL OUTEND (D,CB)
      END
```

APPENDIX 3. LISTING OF PROGRAM YOCOEM.FTP

For the calculation of Fourier coefficients of vorticity fluctuations induced by the passage of the model vortex array

```
      DIMENSION A(300),B(300),CB(128)
      EQUIVALENCE (CB(33),ICB)
      CALL TYPE ('&YOCOEM')
      CALL ASKN (A,'&COEFS SOA,SOB=')
      CALL ASKN (B,'&MEAN VALUE,SOM=')
      CALL ASKI (IT,'&MIN TIME=')
      CALL ASKI (ITM,'&MAX TIME=')
      CALL ASKI (ITT,'&PERIOD=')
      CALL ASKI (M,'&NO OF PERIODS <IT1=')
      CALL ASKI (N,'&NO OF PERIODS >IT1=')
      CALL ASKR (G,'&VORTEX STRENGTH=')
      CALL ASKR (RO,'&CORE RADIUS=')
      CALL ASKR (SL,'&SHEDDING LENGTH=')
      CALL ASKR (X1,'&FIRST X1 VALUE=')
      CALL ASKR (XMAX,'&LAST X1 VALUE=')
      CALL ASKR (X1NC,'&X1 INC=')
      CALL ASKR (Y1,'&FIRST X2 VALUE=')
      CALL ASKR (YMAX,'&LAST X2 VALUE=')
      CALL ASKR (Y1NC,'&X2 INC=')
      CALL ASKR (XO,'&X1 POSITION AT T=0 =')
      CALL ASKR (YO,'&X2 POSITION AT T=0 =')
      CALL OUTPUT (A)
      CALL OUTPUT (B)
      TP1=6.284
      G=-G
      W=TPI/ITT
      UC=SL/ITT
      Y=Y1
11    X=X1
10    SOA=0.0
      SOB=0.0
      SOM=0.0
      ITR=X/UC
30    DO 1 I=IT,ITM
      OM=0.0
      T=I
      XC=X-(UC*T)-XO
      YC=Y-YO
50    RP=SQRT((XC*XC)+(YC*YC))
      RP2=RP*RP
      RO2=RO*RO
      DD=G/(3.142*RO2)
      EE=RP2/RO2
      IF(-EE.GT.-80.0) GO TO 20
      EEE=0.0
      GO TO 21
20    EEE=EXP(-EE)
21    OM1=DD*EEE
12    OM=OM+OM1
      IT1=ITR
      IT2=IT1-(M*ITT)+1
      IT3=IT1+(N*ITT)
      TS=T-IT1
      IF(I.LT.IT2) GO TO 1
      IF(I.GT.IT3) GO TO 1
      OA=OM*COS(W*TS)
      OB=OM*SIN(W*TS)
      SOA=SOA+OA
      SOB=SOB+OB
      SOM=SOM+OM
      IF(I.NE.IT3) GO TO 1
      F=2.0/ITT
      SOA=SOA*F
      SOB=SOB*F
      SOM=SOM*(F/2.0)
      CALL OUT (A,SOA)
      CALL OUT (A,SOB)
      CALL OUT (B,SOM)
      CALL OUT (B,0.0)
1     CONTINUE
      X=X+X1NC
      IF(X.LE.XMAX) GO TO 10
      Y=Y+Y1NC
      IF(Y.LE.YMAX) GO TO 11
      ICB=3
      CB(2)=1000.0
      CB(3)=0.0
      CB(4)=1.0
      CALL OUTEND (A,CB)
      CALL OUTEND (B,CB)
      END
```

APPENDIX 4. LISTING OF PROGRAM YPCOEM.FTP

For the calculation of Fourier coefficients of static pressure fluctuations induced by the passage of the model vortex array

```
      DIMENSION A(300),B(300),CB(128)
      EQUIVALENCE (CB(33),ICB)
      CALL TYPE ('&YPCOEM')
      CALL ASKN (A,'&COEFS SPA,SPB=')
      CALL ASKN (B,'&MEAN VALUE,SPM=')
      CALL ASKI (IT,'&MIN TIME=')
      CALL ASKI (ITM,'&MAX TIME=')
      CALL ASKI (ITT,'&PERIOD=')
      CALL ASKI (M,'&NO OF PERIODS <IT1=')
      CALL ASKI (N,'&NO OF PERIODS >IT1=')
      CALL ASKR (G,'&VORTEX STRENGTH=')
      CALL ASKR (RO,'&CORE RADIUS=')
      CALL ASKR (SL,'&SHEDDING LENGTH=')
      CALL ASKR (X1,'&FIRST X1 VALUE=')
      CALL ASKR (XMAX,'&LAST X1 VALUE=')
      CALL ASKR (XINC,'&X1 INC=')
      CALL ASKR (Y1,'&FIRST X2 VALUE=')
      CALL ASKR (YMAX,'&LAST X2 VALUE=')
      CALL ASKR (YINC,'&X2 INC=')
      CALL ASKR (XO,'&X1 POSITION AT T=0 =')
      CALL ASKR (YO,'&X2 POSITION AT T=0 =')
      CALL OUTPUT (A)
      CALL OUTPUT (B)
      TPI=6.284
      RHO=1.2E-9
      G=-G
      W=TPI/ITT
      UC=SL/ITT
      Y=Y1
11    X=X1
10    SPA=0.0
      SPB=0.0
      SPM=0.0
      ITR=X/UC
30    DO 1 I=IT,ITM
      P=0.0
      T=1
      XC=X-(UC*T)-XO
      YC=Y-YO
50    RP=SQRT((XC*XC)+(YC*YC))
      RP2=RP*RP
      RO2=RO*RO
14    IF(ABS(RP2).GT.0.0001) GO TO 8
      PP=1.3863
      GO TO 9
8     R=RP/RO
      R2=R*R
      C=1.0/R2
      IF(-R2.GT.-80.0) GO TO 3
      DD=0.0
      GO TO 4
3     DD=EXP(-R2)
4     IF(-(2.0*R2).GT.-80.0) GO TO 5
      EE=0.0
      GO TO 6
5     EE=EXP(-(2.0*R2))
6     DDD=EXP1(-R2)
      EEE=EXP1(-(2.0*R2))
      PP=C-(2.0*((DD/R2)+DDD))+((EE/R2)+(2.0*EEE))
      V1=G/(TPI*RO)
      V12=V1*V1
      P1=(PP*RHO*V12)/2.0
      P=P+P1
      P=-P
      IT1=ITR
      IT2=IT1-(M*ITT)+1
      IT3=IT1+(N*ITT)
      TS=T-IT1
      IF(I.LT.IT2) GO TO 1
      IF(I.GT.IT3) GO TO 1
      PA=P*COS(W*TS)
      PB=P*SIN(W*TS)
      SPA=SPA+PA
      SPB=SPB+PB
      SPM=SPM+P
      IF(I.NE.ITR) GO TO 1
      F=2.0/ITT
      SPA=SPA*F
      SPB=SPB*F
      SPM=SPM*(F/2.0)
      CALL OUT (A,SPA)
      CALL OUT (A,SPB)
      CALL OUT (B,SPM)
      CALL OUT (B,0.0)
1     CONTINUE
      X=X+XINC
      IF(X.LE.XMAX) GO TO 10
      Y=Y+YINC
      IF(Y.LE.YMAX) GO TO 11
      ICB=3
      CB(2)=1000.0
      CB(3)=0.0
      CB(4)=1.0
      CALL OUTEND (A,CB)
      CALL OUTEND (B,CB)
      END
      FUNCTION EXP1(X)
      X=-X
      IF(X.LE.2.0) GO TO 100
      EXP1=0.0
      GO TO 200
100   GAM=0.57721
      S=0.0
      SN=0.0
      SN1=0.0
      DO 1 N=1,5
      NF=1
      DO 2 J=0,(N-1)
      NF=NF*(J+1)
2     CONTINUE
      SN=(X**N)/(N*NF)
      SN1=SN*((-1)**N)
      S=S+SN1
1     CONTINUE
      EXP1=GAM+ALOG(X)+S
200   RETURN
      END
```

APPENDIX 5. LISTING OF PROGRAM XVTOTM.FTN

For the calculation of the amplitude and phase of the "streamwise" and "vertical" velocity fluctuations induced by the passage of the model vortex array; also calculates the amplitude and phase of the total vertical velocity fluctuation produced by a superposition of a uniform fluctuating vertical velocity with the vortex induced vertical velocity

```
      DIMENSION A(300),B(300)
      DIMENSION C(300),D(300),E(300),CB(128)
      CALL TYPE ('%XVTOTM')
      CALL ASKN (A,'%COEFS V1A,V1B=')
      CALL ASKN (B,'%COEFS V2A,V2B=')
      CALL ASKN (C,'%V1 COMPONENT=')
      CALL ASKN (D,'%V2 COMPONENT=')
      CALL ASKN (E,'%V2 COMPONENT WITH ACOUSTIC MOTION=')
      CALL ASKI (ITT,'%PERIOD=')
      CALL ASKR (SL,'%SHEDDING LENGTH=')
      CALL ASKR (X1,'%FIRST X1 VALUE=')
      CALL ASKR (XMAX,'%LAST X1 VALUE=')
      CALL ASKR (X1NC,'%X1 INC=')
      CALL ASKR (Y1,'%FIRST X2 VALUE=')
      CALL ASKR (YMAX,'%LAST X2 VALUE=')
      CALL ASKR (Y1NC,'%X2 INC=')
      CALL ASKR (VA,'%AMPLITUDE OF ACOUSTIC VELOCITY=')
      CALL ASKR (VP,'%PHASE OF ACOUSTIC VELOCITY (RAD)=')
      CALL INPUT (A,CB,M)
      CALL INPUT (B,CB,M)
      ASSIGN 100 TO M
      CALL INS (A,0,0)
      CALL INS (B,0,0)
      CALL OUTPUT (C)
      CALL OUTPUT (D)
      CALL OUTPUT (E)
      TP1=6.284
      W=TP1/ITT
      UC=SL/ITT
      Y=Y1
11    X=X1
10    CALL IN (A,SXA)
      CALL IN (A,SXB)
      CALL IN (B,SYA)
      CALL IN (B,SYB)
      ITR=X/UC
      IT1=ITR
      TORX=(ATAN2((SXA),(SXB)))-(W*IT1)-1.571
      TORY=-(ATAN2((SYB),(SYA)))-(W*IT1)
      SXA2=SXA*SXA
      SXB2=SXB*SXB
      SYA2=SYA*SYA
      SYB2=SYB*SYB
      VA2=VA*VA
      AMX=SQRT(SXA2+SXB2)
      AMPX=0.707*AMX
      AMY=SQRT(SYA2+SYB2)
      AMPY=0.707*AMY
      AMPA=0.707*SQRT((SYA2+SYB2+VA2)+(2*AMY*VA*COS(TORY-VP)))
      CO=COS(TORY)
      SI=SIN(TORY)
      CY=COS(VP)
      SY=SIN(VP)
      AA=(AMY*SI)+(VA*SY)
      BB=(AMY*CO)+(VA*CY)
      TORA=ATAN2(AA,BB)
      CALL OUT (C,AMPX)
      CALL OUT (C,TORX)
      CALL OUT (D,AMPY)
      CALL OUT (D,TORY)
      CALL OUT (E,AMPA)
      CALL OUT (E,TORA)
      X=X+X1NC
      IF(X.LE.XMAX) GO TO 10
      Y=Y+Y1NC
      IF(Y.LE.YMAX) GO TO 11
100   CALL INEND (A)
      CALL INEND (B)
      CALL OUTEND (C,CB)
      CALL OUTEND (D,CB)
      CALL OUTEND (E,CB)
      END
```

APPENDIX 6. LISTING OF PROGRAM XOTOTM.FTN

For the calculation of the amplitude and phase of the vorticity fluctuations produced by the passage of the model vortex array

```
      DIMENSION A(300),B(300),CB(128)
      CALL TYPE ('&XOTOTM')
      CALL ASKN (A,'&COEFS SOA,SOB=')
      CALL ASKN (B,'&FLUCTUATING VORTICITY=')
      CALL ASK1 (ITT,'&PERIOD=')
      CALL ASKR (SL,'&SHEDDING LENGTH=')
      CALL ASKR (X1,'&FIRST X1 VALUE=')
      CALL ASKR (XMAX,'&LAST X1 VALUE=')
      CALL ASKR (X1NC,'&X1 INC=')
      CALL ASKR (Y1,'&FIRST X2 VALUE=')
      CALL ASKR (YMAX,'&LAST X2 VALUE=')
      CALL ASKR (Y1NC,'&X2 INC=')
      CALL INPUT (A,CB,M)
      ASSIGN 100 TO M
      CALL INS (A,0,0)
      CALL OUTPUT (B)
      TPI=6.284
      W=TPI/ITT
      UC=SL/ITT
      Y=Y1
11    X=X1
10    CALL IN (A,SOA)
      CALL IN (A,SOB)
      ITR=X/UC
      IT1=ITR
      TORX=(ATAN2((SOA),(SOB)))-(W*IT1)-1.571
C     TORX=TORX+3.142
      SOA2=SOA*SOA
      SOB2=SOB*SOB
      AM=SQRT(SOA2+SOB2)
      AMPX=0.707*AM
      CALL OUT (B,AMPX)
      CALL OUT (B,TORX)
      X=X+XINC
      IF(X.LE.XMAX) GO TO 10
      Y=Y+YINC
      IF(Y.LE.YMAX) GO TO 11
100   CALL INEND (A)
      CALL OUTEND (B,CB)
      END
```

APPENDIX 7. LISTING OF PROGRAM XPTOTM.FTN

For the calculation of the amplitude and phase of the static pressure fluctuations produced by the passage of the model vortex array; also calculates the amplitude and phase of the "acoustic" pressure fluctuation in the resonator neck, and the amplitude and phase of the net pressure fluctuations produced by the superposition of "acoustic" and vortex induced pressure fluctuations

```
      DIMENSION A(300),B(300),C(300),D(300),CB(128)
      CALL TYPE ('%XPTOTM')
      CALL ASKN (A,'%COEFS SPA,SPB=')
      CALL ASKN (B,'%VORTICAL PRESSURE=')
      CALL ASKN (C,'%TOTAL PRESSURE=')
      CALL ASKN (D,'%ACOUSTIC PRESSURE=')
      CALL ASK1 (ITT,'%PERIOD=')
      CALL ASKR (SL,'%SHEDDING LENGTH=')
      CALL ASKR (X1,'%FIRST X1 VALUE=')
      CALL ASKR (XMAX,'%LAST X1 VALUE=')
      CALL ASKR (XINC,'%X1 INC=')
      CALL ASKR (Y1,'%FIRST X2 VALUE=')
      CALL ASKR (YMAX,'%LAST X2 VALUE=')
      CALL ASKR (YINC,'%X2 INC=')
      CALL ASKR (CP,'%AMPLITUDE OF CAVITY PRESSURE=')
      CALL ASKR (PP,'%PHASE OF CAVITY PRESSURE=')
      CALL ASKR (RR,'%RADIATION RESISTANCE=')
      CALL ASKR (EL,'%TOTAL NECK EFFECTIVE LENGTH=')
      CALL ASKR (EL2,'%EFFECTIVE LENGTH LZ=')
      CALL INPUT (A,CB,M)
      ASSIGN 100 TO M
      CALL INS (A,0,0)
      CALL OUTPUT (B)
      CALL OUTPUT (C)
      CALL OUTPUT (D)
      TP1=A 284
      RHO=1 2E-9
      SS=1000
      CC=3. 1E13
      W=TP1/ITT
      UC=SL/ITT
      Y=Y1
11    X=X1
10    CALL IN (A,SPA)
      CALL IN (A,SPB)
      TTR=X/UC
      IT1=ITR
      TORX=ATAN2((SPA),(SPB))-(W*IT1)-1.571+6.284
      CO=COS(TORX)
      S1=SIN(TORX)
      SPA2=SPA*SPA
      SPB2=SPB*SPB
      AM=SQRT(SPA2+SPB2)
      AMPX=0.707*AM
      EM=EL*(RHO/SS)
      EL1=EL2-EL
70    EM2=(EL2-Y)*(RHO/SS)
      IF(Y LT EL1) EM2=EM
      IF(Y GT EL2) EM2=0.0
      F1=(W*W*EM*EM2)+(RR*RR)
      F2=(W*RR*(EM2-EM))
      F3=(W*W*EM*EM)+(RR*RR)
      F1=F1*(1.0E30)
      F2=F2*(1.0E30)
      F3=F3*(1.0E30)
      AM1=SQRT((F1*F1)+(F2*F2))
      AM2=AM1/F3
      AMA=AM2*CP
      AMAX=0.707*AMA
      TORA=PP+ATAN2(F2,F1)
      CA=COS(TORA)
      SA=SIN(TORA)
      AA=(AM*CO)+(AMA*CA)
      BB=(AM*S1)+(AMA*SA)
      AMT=SQRT((AA*AA)+(BB*BB))
      AMTX=0.707*AMT
      TORT=ATAN2(BB,AA)
90    CALL OUT (B,AMPX)
      CALL OUT (B,TORX)
      CALL OUT (C,AMTX)
      CALL OUT (C,TORT)
      CALL OUT (D,AMAX)
      CALL OUT (D,TORA)
      X=X+XINC
      IF(X.LE.XMAX) GO TO 10
      Y=Y+YINC
      IF(Y.LE.YMAX) GO TO 11
100   CALL INEND (A)
      CALL OUTEND (B,CB)
      CALL OUTEND (C,CB)
      CALL OUTEND (D,CB)
      END
```

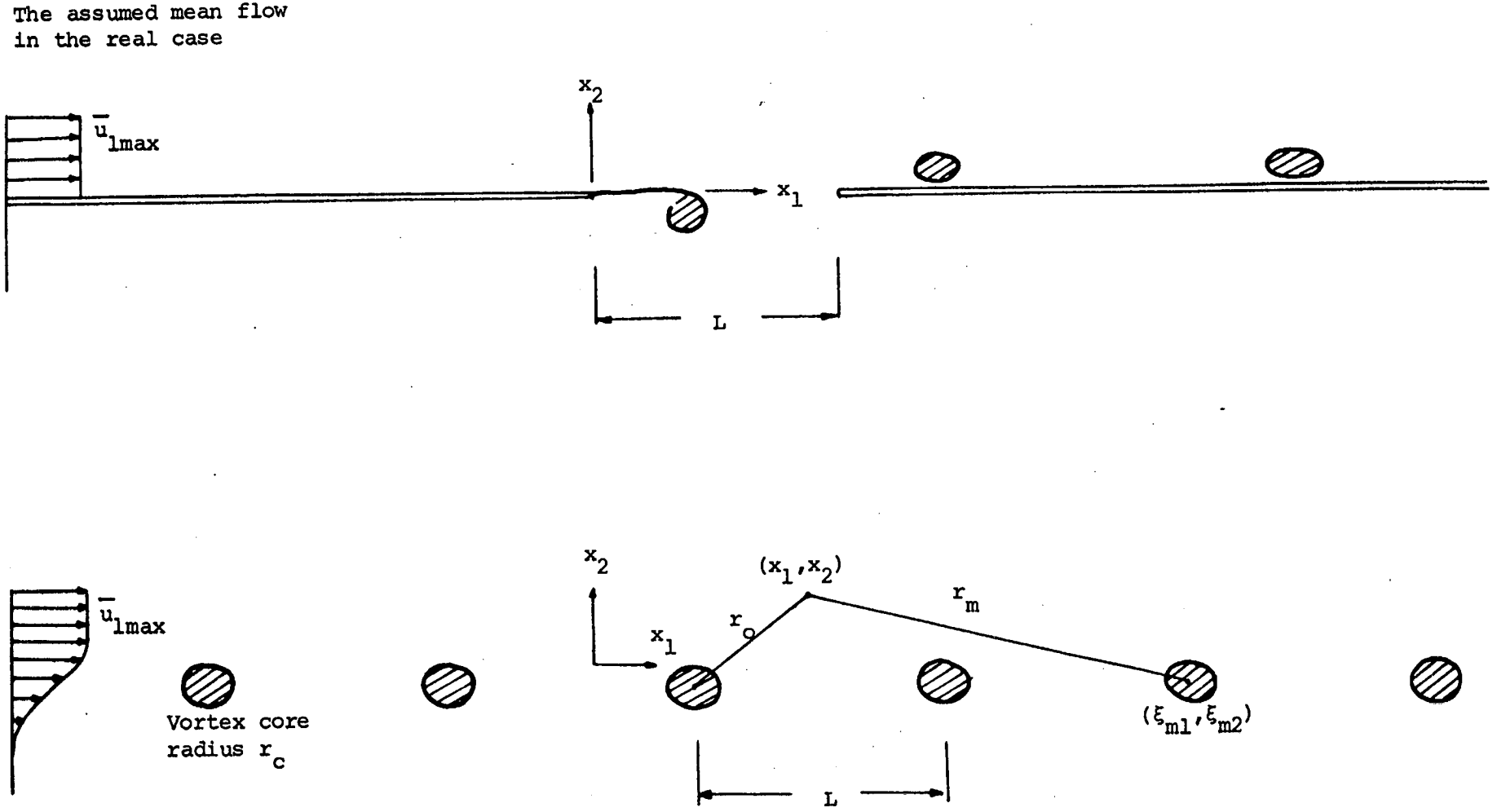

FIGURE 1 The vortex shedding model; the model vortex array is convected by a uniform mean potential flow $\frac{1}{2}\bar{u}_{1max}$ in the streamwise (x_1) direction.

Vorticity Distribution

$\Omega_3(r)$ $\left\{ \frac{\pi r_c^2}{\kappa} \right\}$

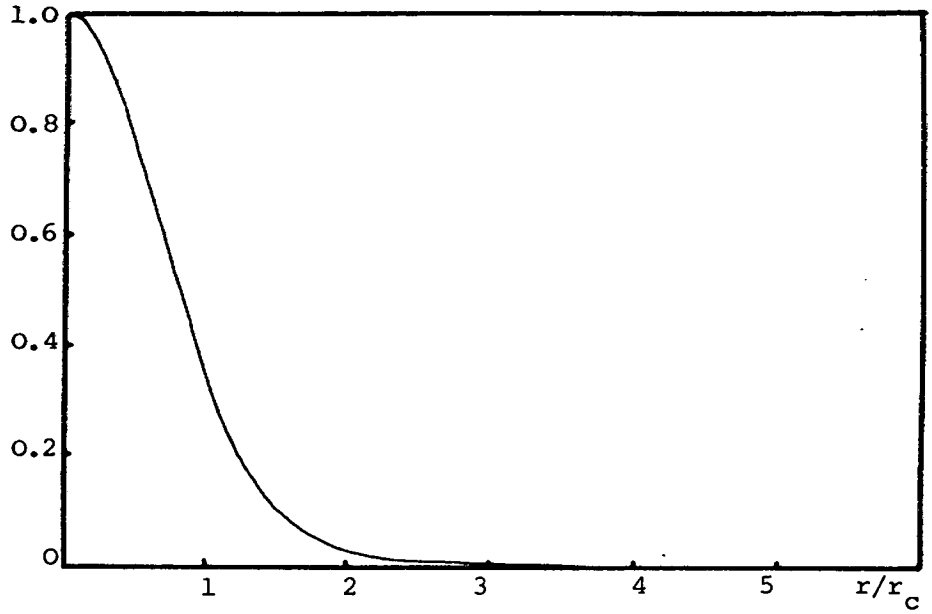

Tangential Velocity Distribution

$V_\theta(r)$ $\left\{ \frac{2\pi}{\kappa} \right\}$

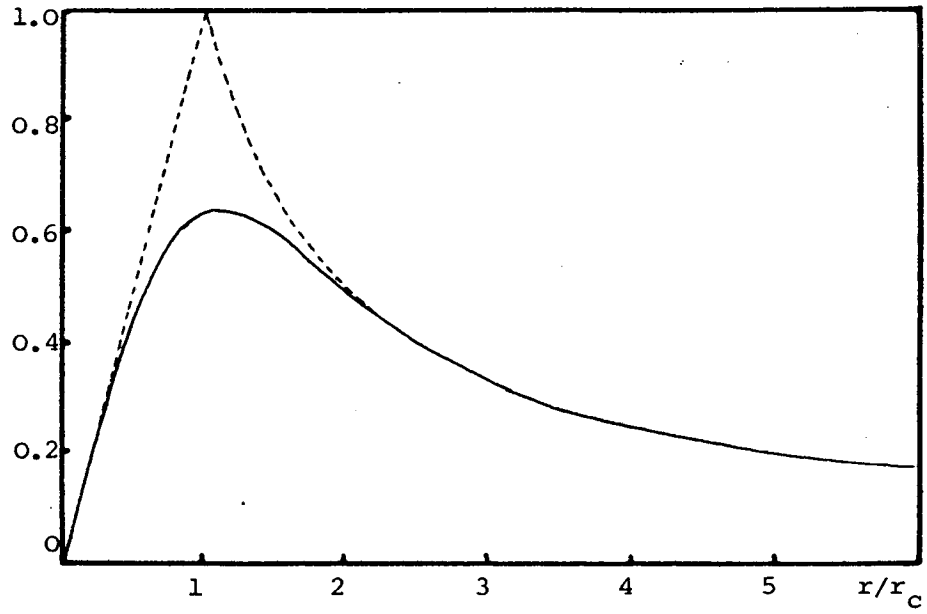

Static Pressure Distribution

$p_v(r)$ $\left\{ \frac{8\pi^2 r_c^2}{\rho_o \kappa^2} \right\}$

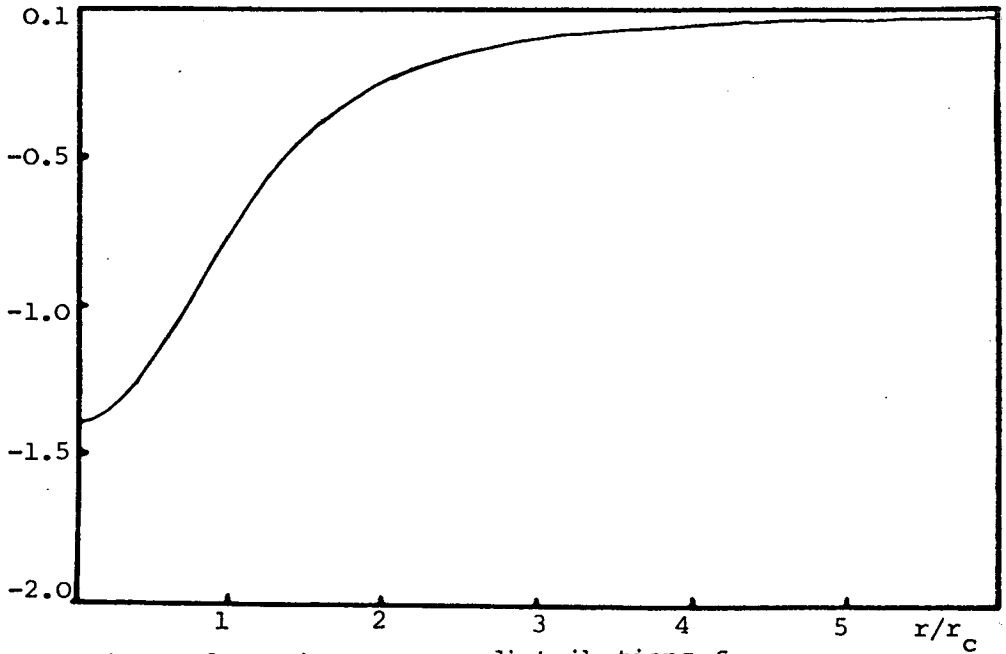

FIGURE 2 Vorticity, velocity and static pressure distributions for the model vortex.

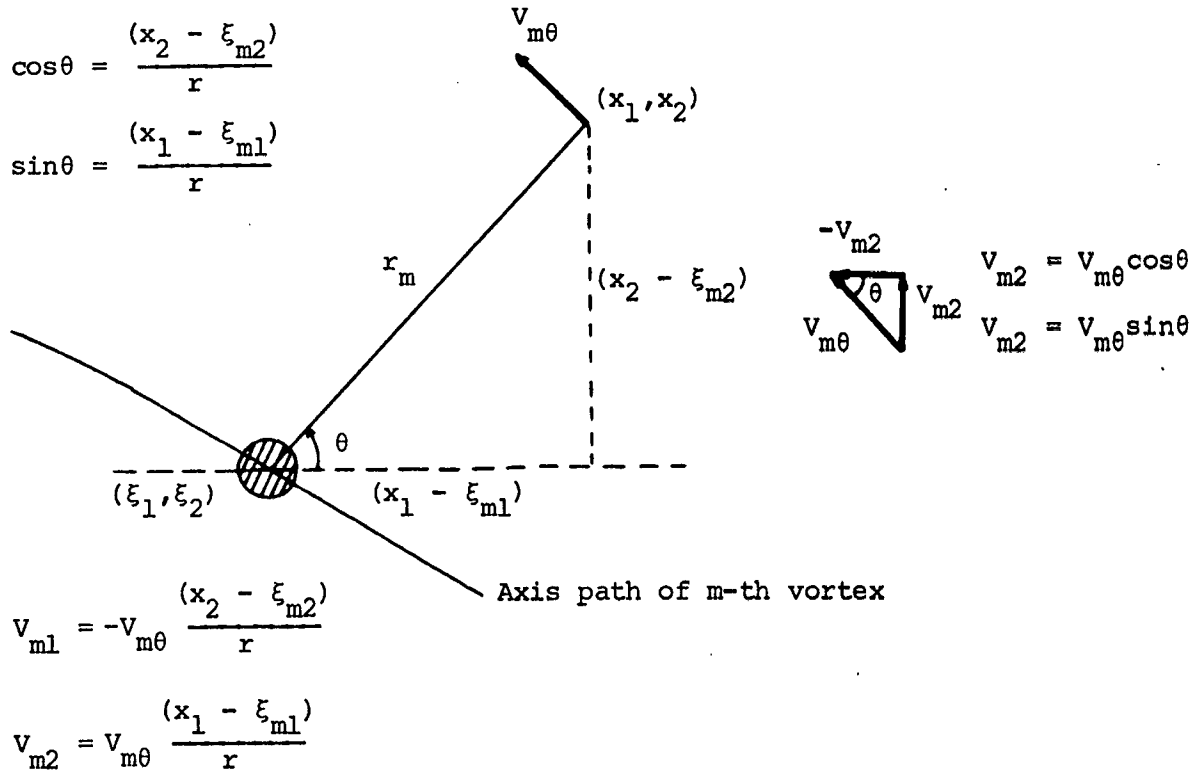

FIGURE 3 Resolution of vortically induced tangential velocity into "vertical" and "streamwise" components.

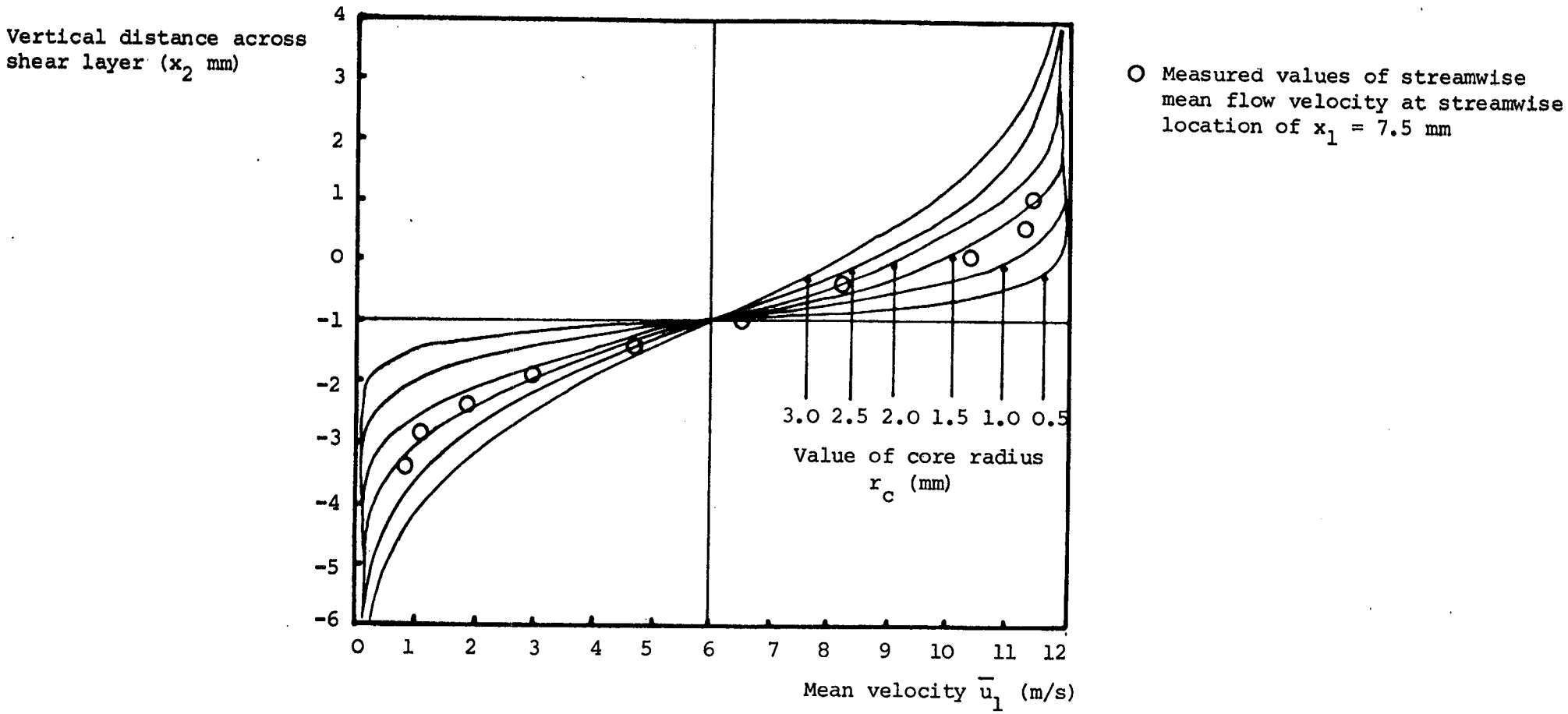

FIGURE 4 Comparison of measured streamwise mean flow values with values computed using the vortex shedding model with variation in vortex core radius.

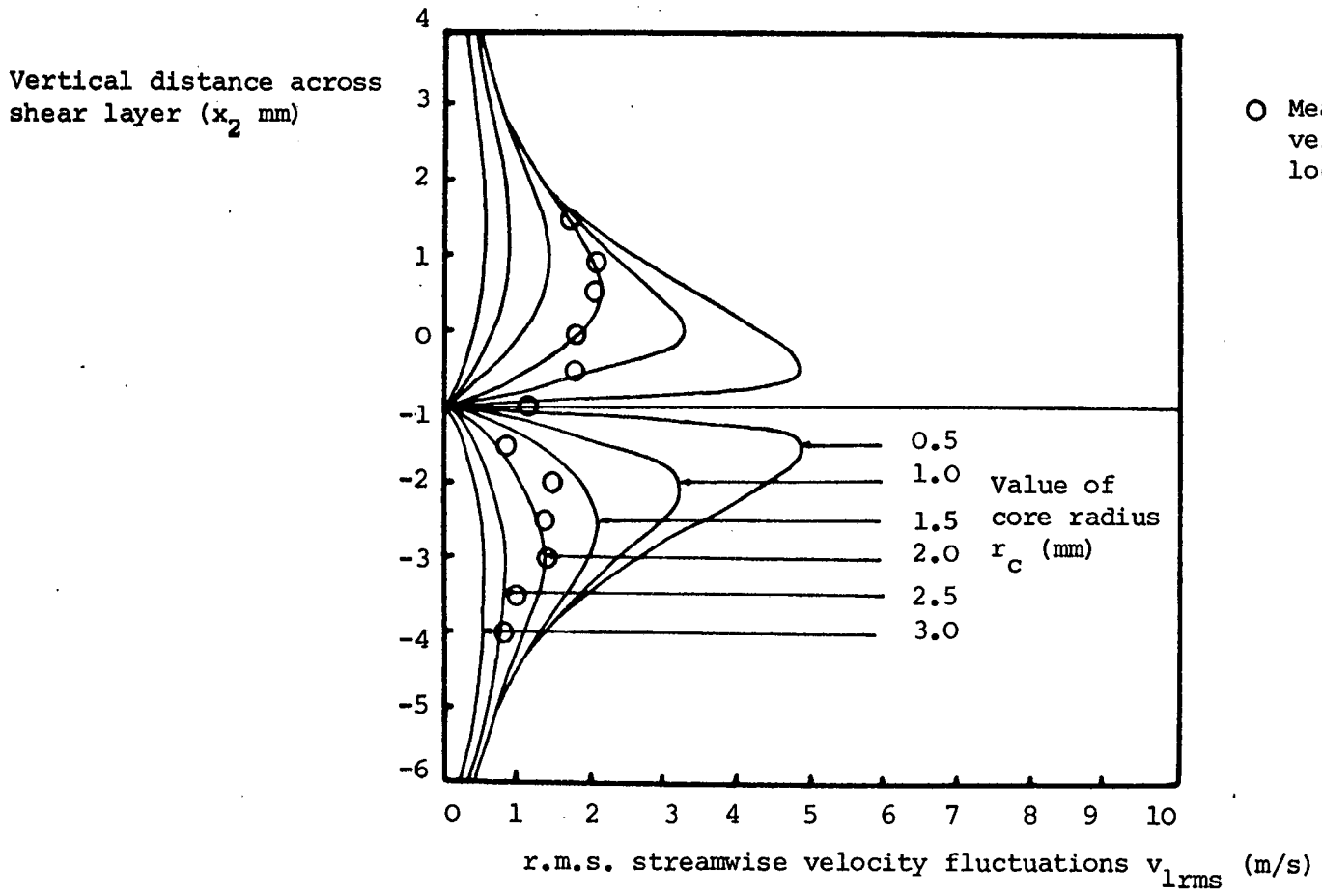

FIGURE 5 Comparison of measured streamwise velocity fluctuations with values computed using the vortex shedding model with variation in core radius.

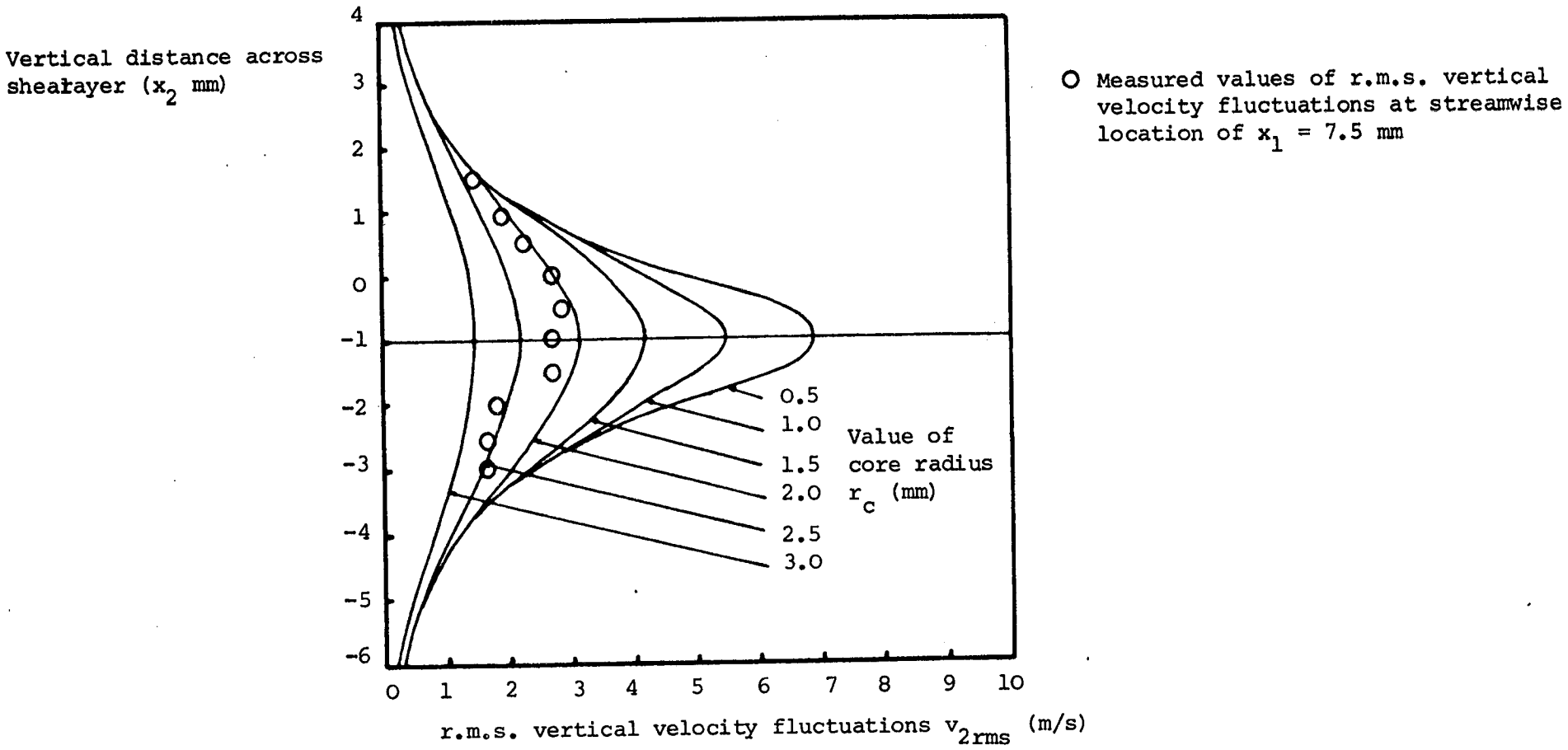

FIGURE 6 Comparison of measured vertical velocity fluctuations with values computed using the vortex shedding model with variation in core radius.

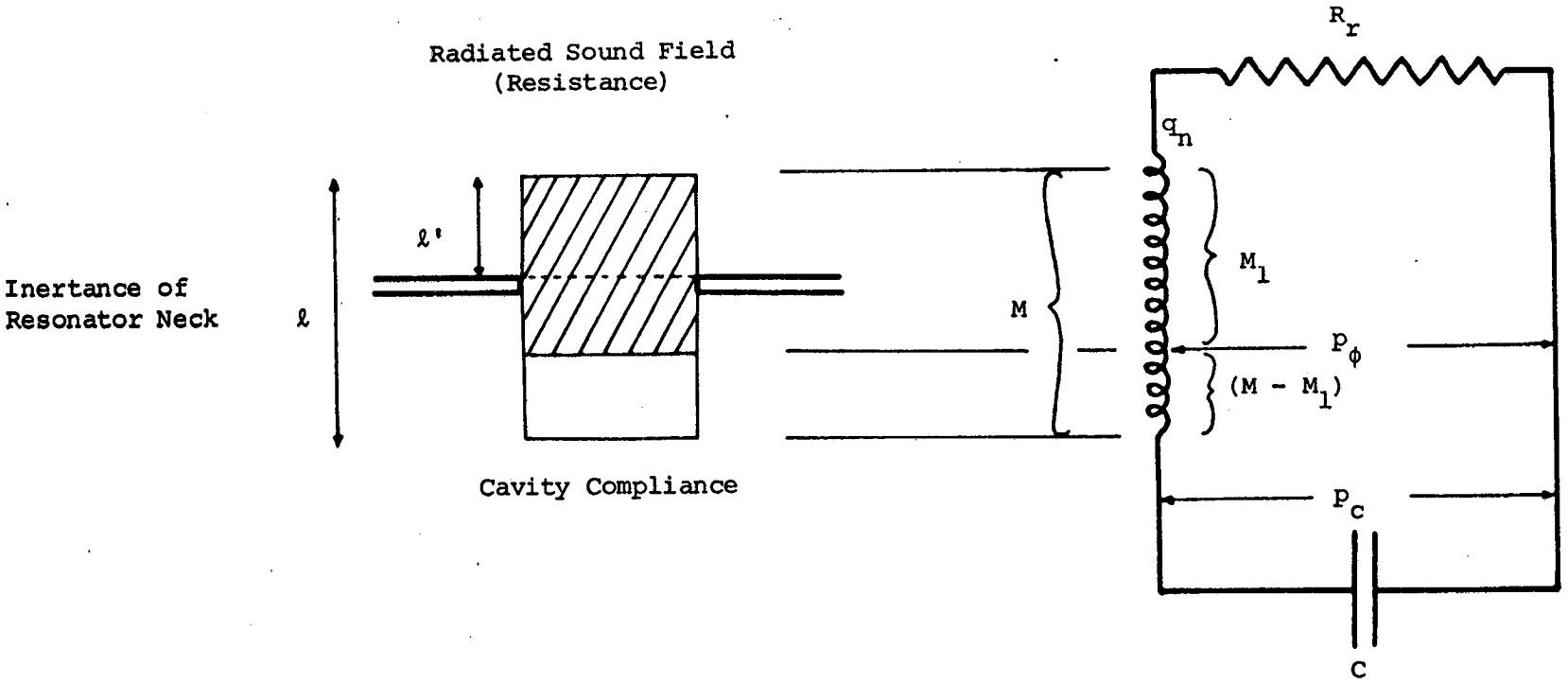

FIGURE 7 Equivalent circuit representation of the acoustical characteristics of the resonator neck flow.
(Pressure is shown analogous to voltage and volume velocity analogous to current.)

FIGURE 8 Variation of phase of measured streamwise velocity fluctuations with distance in streamwise direction.

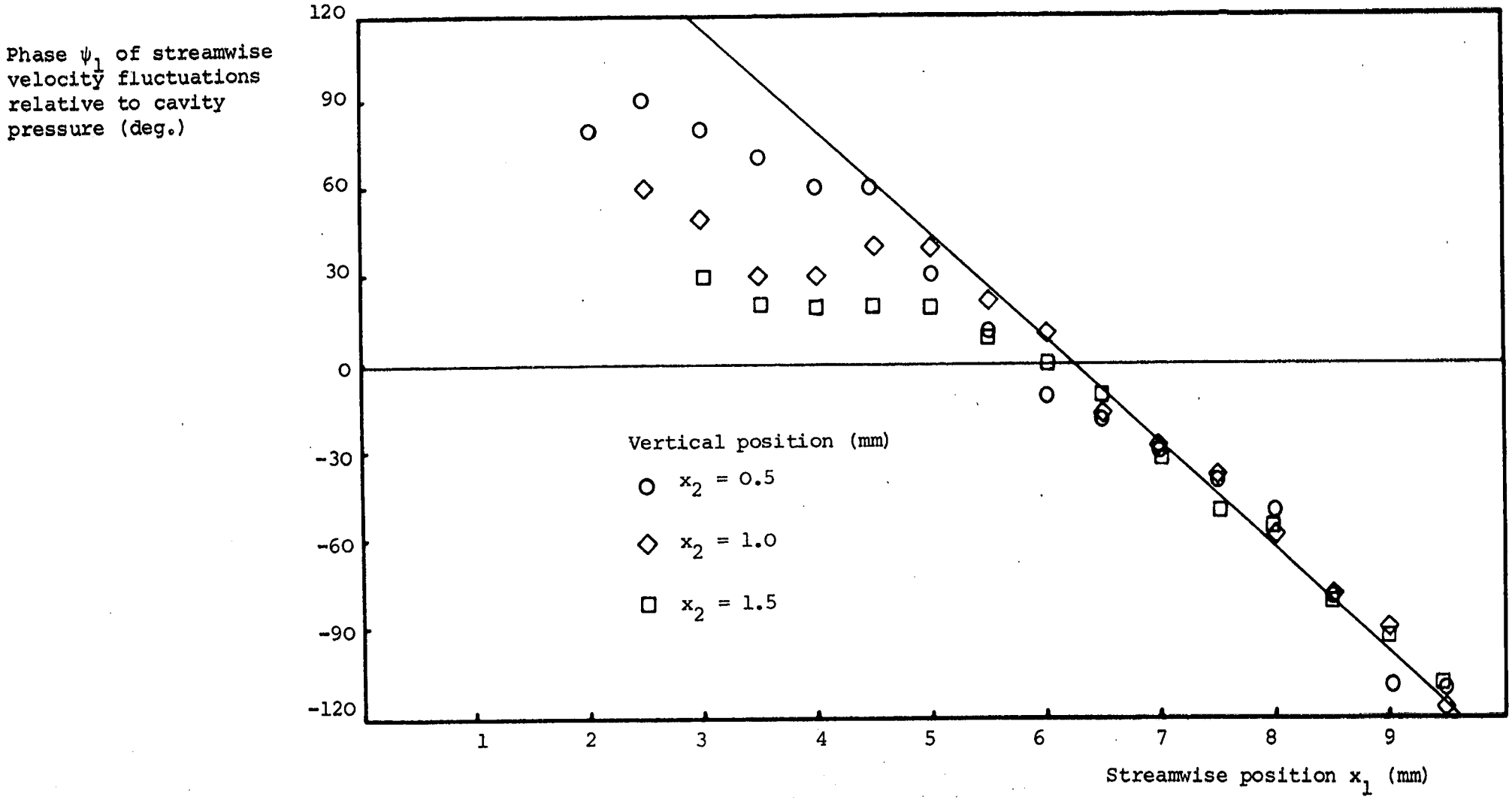

FIGURE 9 Contours of r.m.s. values of vertical velocity fluctuation computed by combining the uniform potential flow with the vortically induced vertical velocity fluctuation. (Contours are in increments of 0.2 m/s with the following contours marked: - 2.0, = 3.0, ≡ 4.0, ≣ 5.0 m/s.)

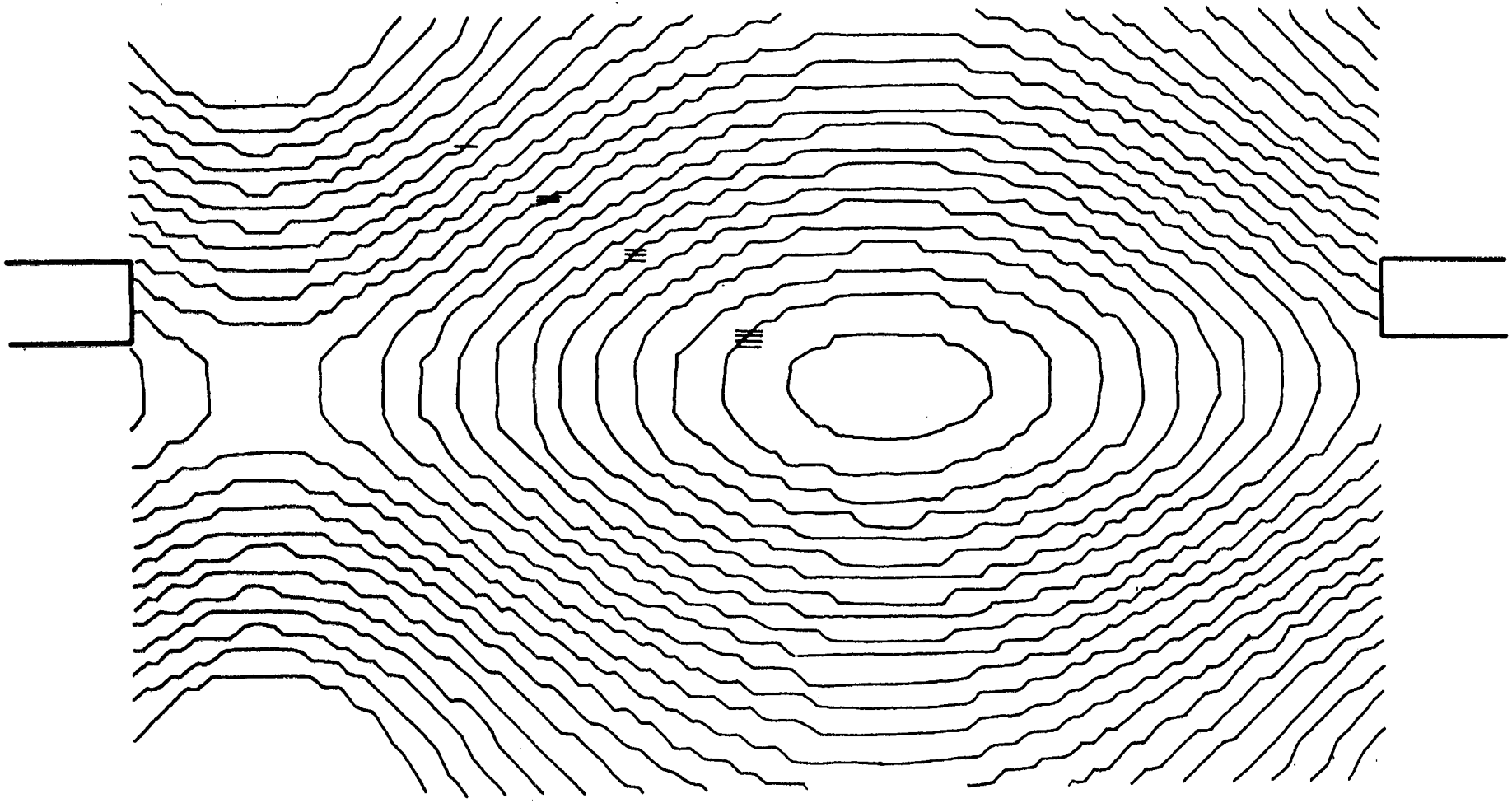

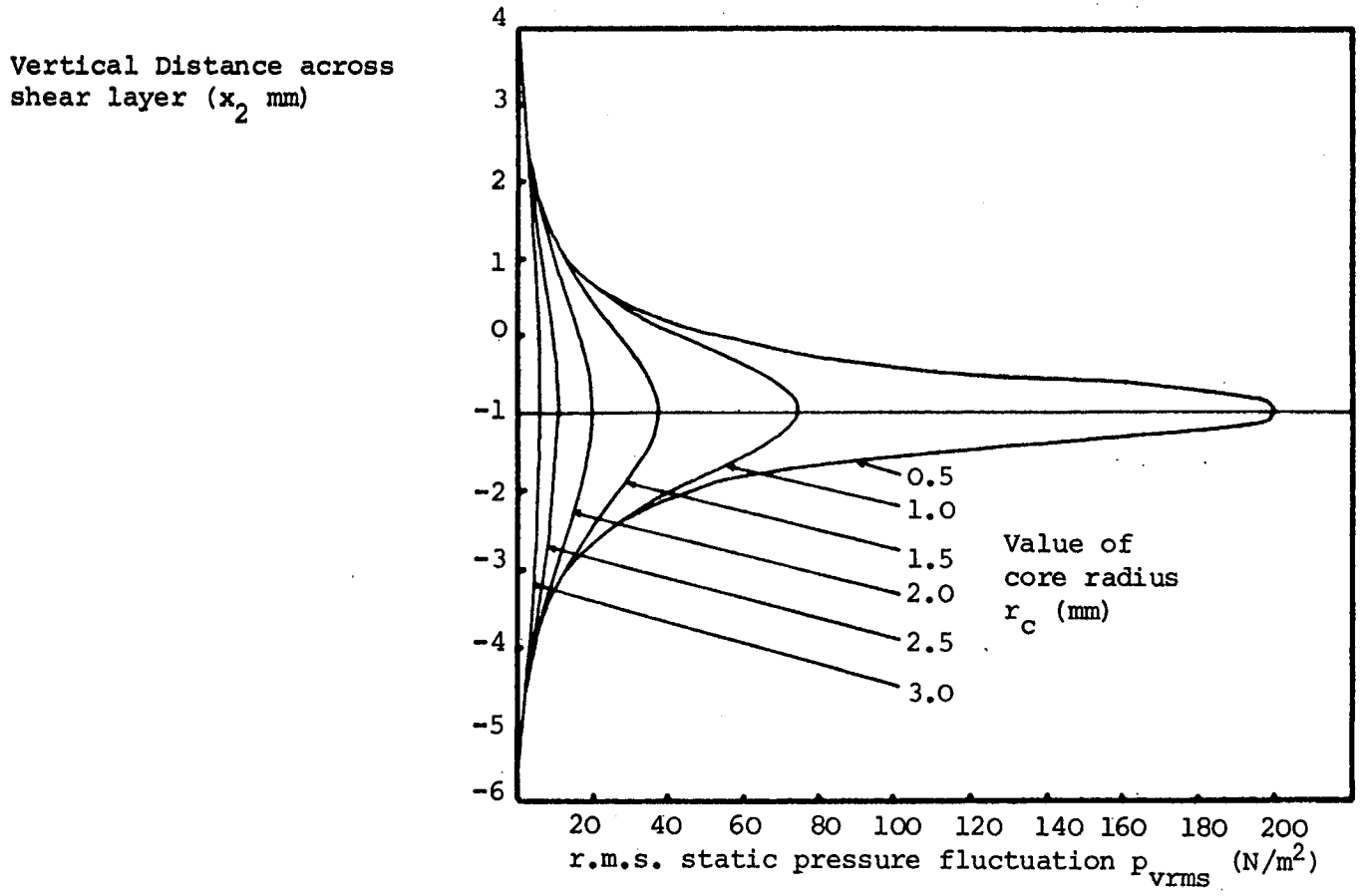

FIGURE 10 Values of static pressure fluctuations produced by the passage of the vortices computed from the vortex shedding model with variation in core radius.

FIGURE 11 Variation in amplitude and phase of the "acoustic" pressure fluctuations in the resonator neck.

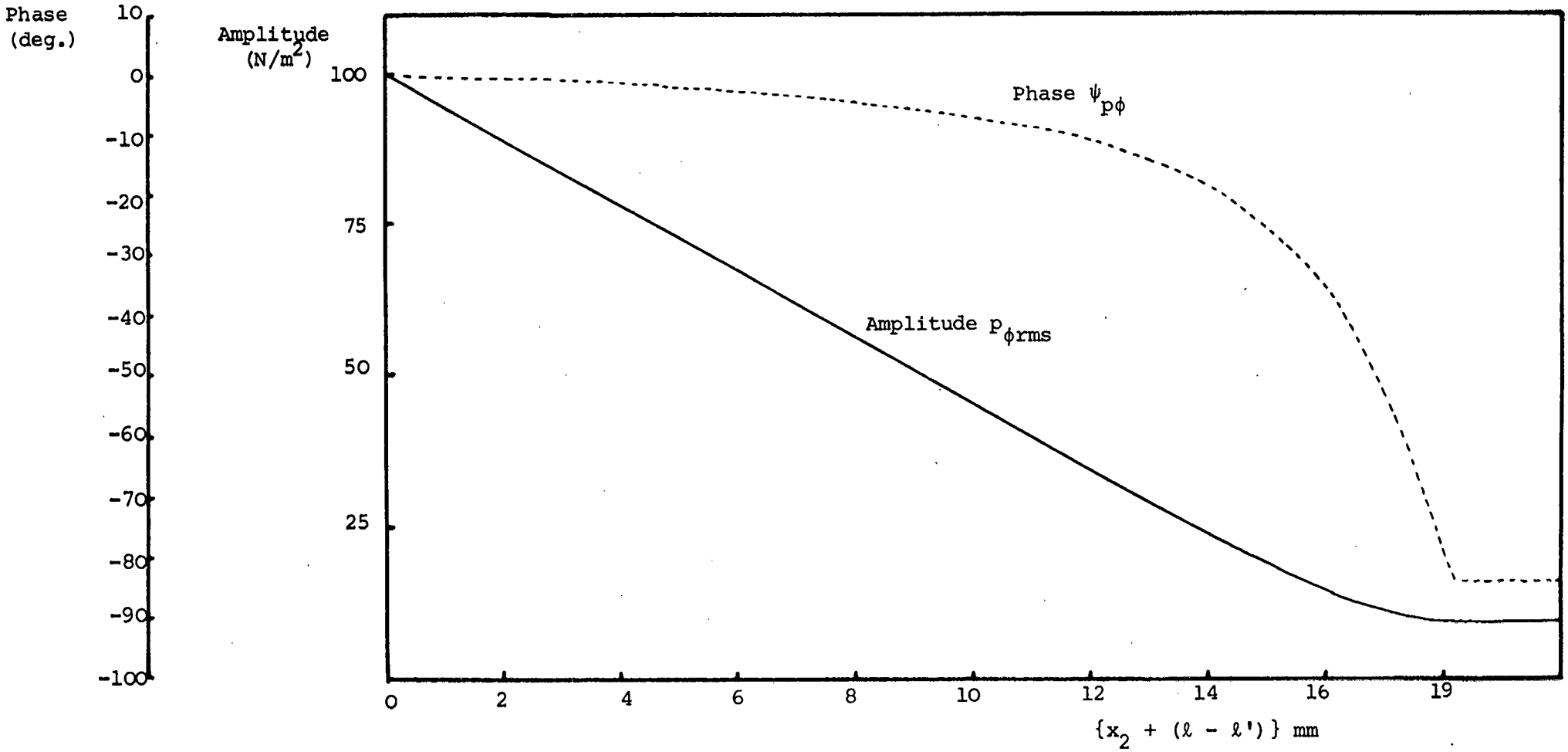

FIGURE 12 Contours of r.m.s. values of static pressure fluctuations computed by combining the "acoustic" pressure fluctuations with those produced by the passage of the vortices.
(Contours are in increments of 2.5 N/m^2 with the following contours marked: - 20, = 30, ≡ 40, ≡ 50, ≡ 60, ≡ 70 N/m .)

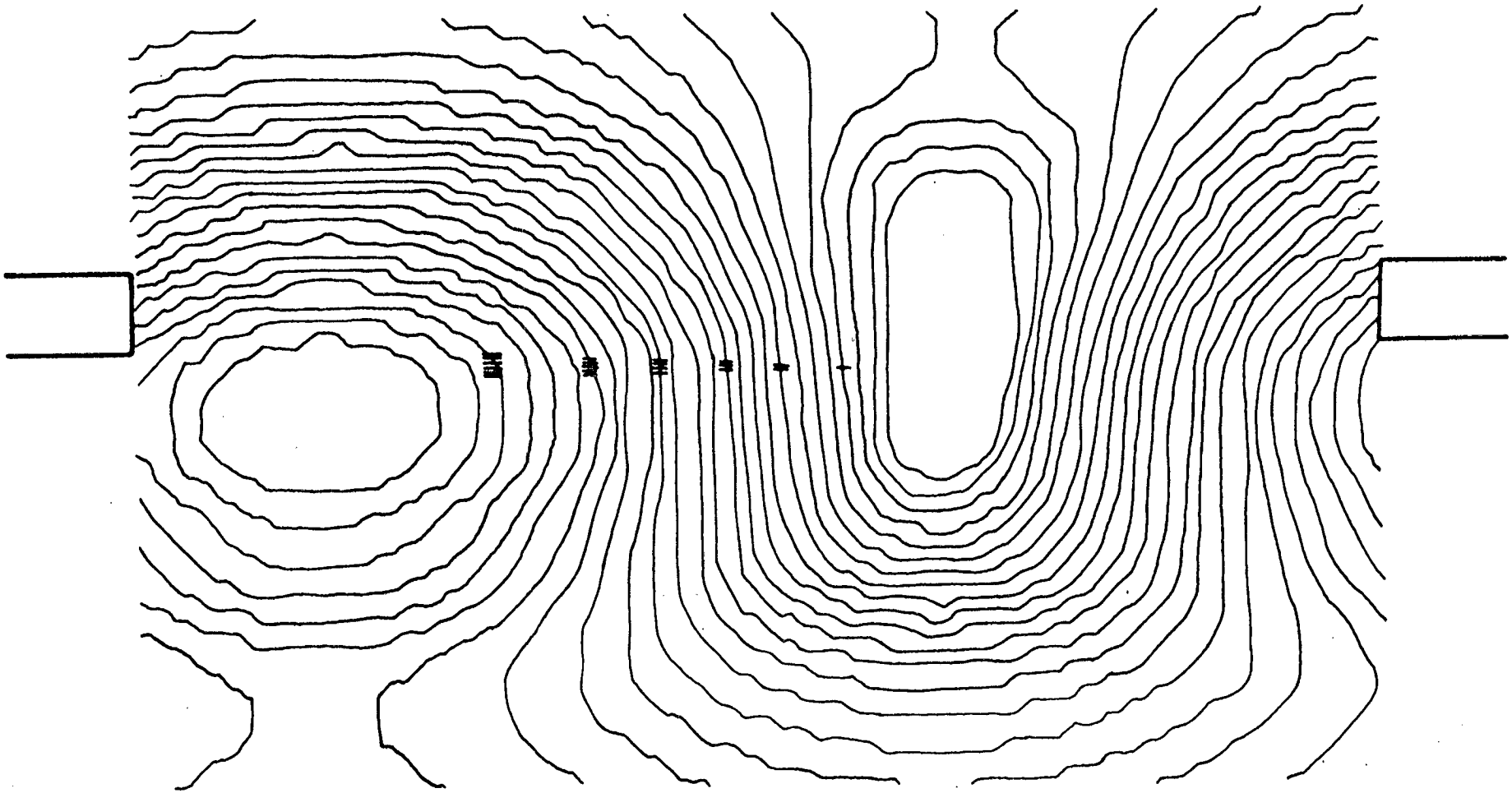

FIGURE 13 Contours of the relative phase of the static pressure fluctuations computed by combining the "acoustic" pressure fluctuations with those produced by the passage of the vortices.
(Contours are in increments of 10° with the following contours marked: - -60°, = -30°, ≡ 0°, ≣ 30°, ≣ 60°.)

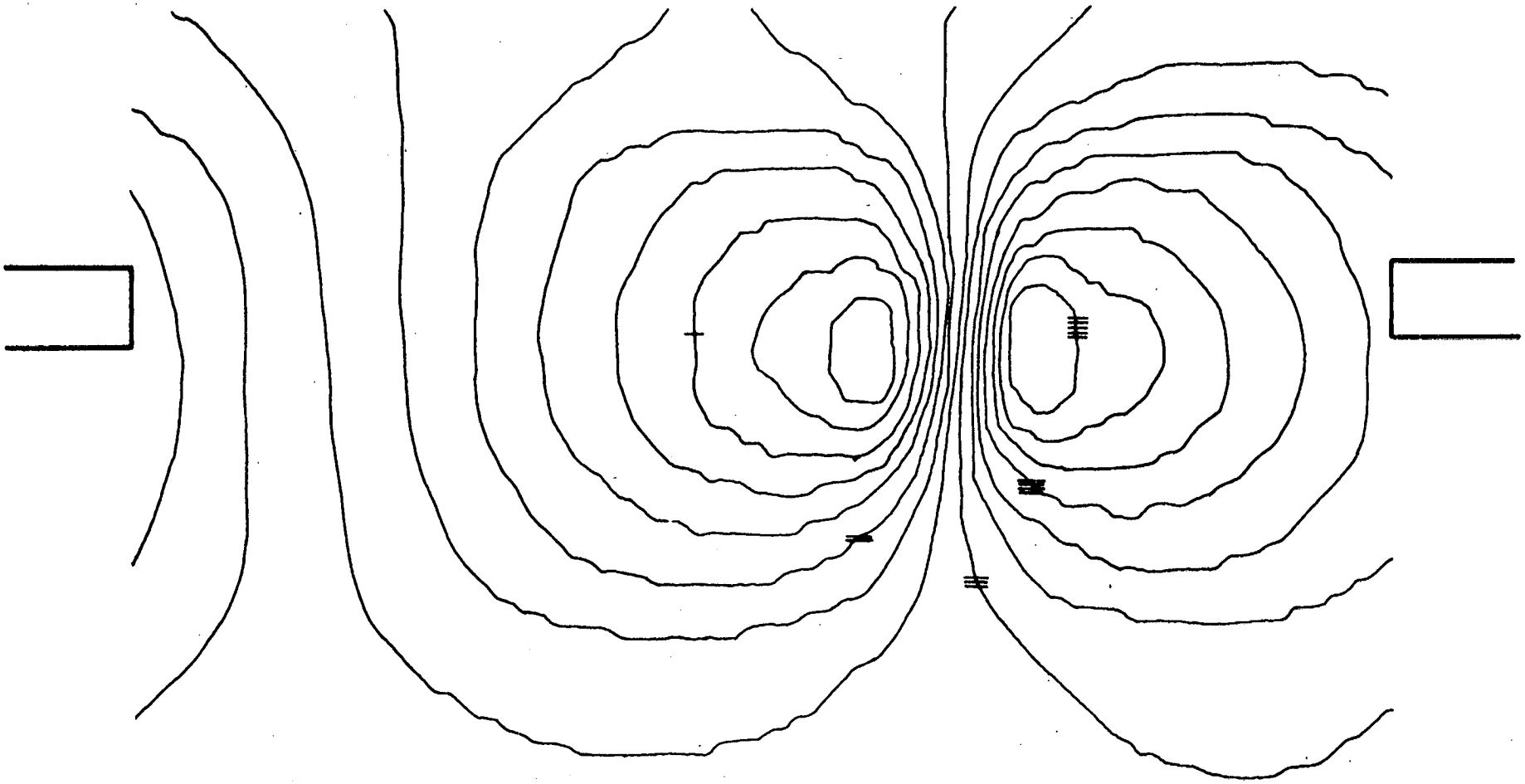

CHAPTER 6

THE FLUID DYNAMICS OF A FLOW EXCITED RESONANCE

(III) MOMENTUM AND ENERGY BALANCES

1. INTRODUCTION

The work described in the previous Chapter has succeeded in establishing the approximate strength and distribution of the vorticity shed in the neck of the flow excited resonator. It has also been demonstrated that an adequate representation of the flow is provided by the interference of streamwise convected vortices with a reciprocating potential flow. Further, it has been demonstrated that the observed pressure interference pattern can be explained by the superposition of the pressure fluctuations generated by the passage of the vortices with the pressure fluctuations apparently associated with the reciprocating potential flow. These principal observations will be used in this Chapter in an attempt to further understand the momentum balances and energy interchanges occurring in the resonator neck.

Firstly, the local momentum balance in the resonator neck will be considered. The apparent superposition of the two separately identifiable pressure fields provides a useful starting point for the analysis of the accelerations occurring in the flow. A re-arrangement of the full linearised momentum conservation equation is put forward, which allows definitions of the pressure fluctuations associated with the potential flow and those associated with the vortical flow. The former are essentially those produced in providing the pressure gradient necessary to balance the acceleration of the reciprocating potential flow. The definition chosen also includes the convective effects of the mean flow on the unsteady potential flow, although these effects are negligible in the case considered. The "vortical" pressure fluctuations are those associated with the usual convection of the vorticity distribution, but with the inclusion of an additional term which suggests the mechanism responsible for the effect of the unsteady potential flow on the vortical flow. This additional term is the fluctuating Coriolis acceleration produced by the action of the reciprocating potential flow on the mean vorticity.

The hypothesis is then advanced that the Coriolis acceleration is largely responsible for the control of the vortex shedding by the potential flow. It is suggested that the Coriolis acceleration is instrumental in the control of the vortex formation. Vorticity shed from the upstream lip of the resonator neck is likely to be "rolled up" by the deflecting Coriolis force. At the end of the cycle, when the vortex reaches the downstream lip, the Coriolis force will tend to

accelerate the vortices in the streamwise direction. This view is further reinforced by the increase in convection speed at the downstream lip of the vortices observed in the experiment. An estimate of this increased convection speed produced by the action of the reciprocating potential flow on the vortices of the strength observed is in good agreement with the observed acceleration.

An analysis of the energy balance in the flow is then undertaken. Doak's (1) theory is used to examine the interchange between the mean energy flux associated with the mean momentum and the mean energy flux associated with the fluctuating momentum. It is found that the fluctuating Coriolis acceleration is responsible for extracting mean energy associated with the fluctuating motion from the energy of the mean flow. The model representation of the flow, consisting of streamwise convected vortices with a superposed transverse potential flow, is then used to estimate the rate of energy extraction from the mean flow. The model indicates that the maximum power extraction occurs near the downstream edge of the resonator neck. A localised "source" of mean energy flux associated with fluctuating momentum is thus identified. It is also found that there is a localised "sink" of mean energy flux associated with momentum fluctuations towards the upstream edge of the resonator neck. In this region, the model infers that the fluctuating Coriolis acceleration is responsible for increasing the mean flow of energy associated with the mean momentum. The model is also used to estimate the order of magnitude of the power extracted from the mean flow by the energy source. The total power emitted by the source region is of the order of magnitude of the acoustic power radiated to the far field.

The mean flow of energy associated with momentum fluctuations in the region of the resonator neck is deduced from the experimental results. A recirculating flow of energy is clearly shown. There is a mean flow of energy from the region of the downstream edge to the region of the upstream edge along the lower half of the mean shear layer. This flow shows the "feedback" of energy from the "source" region to the "sink" region. This basic pattern of energy flow is also reproduced by the model of the fluctuating pressure and velocity fields.

The mean energy balance of the fluid in the volume enclosed in the resonator neck is considered. There is a net production of mean energy associated with momentum fluctuations. Some of this energy is radiated to the acoustic far field and some is carried away by the vortices

ejected from the downstream lip of the resonator neck. It is suggested that this net energy production results from an imbalance between the power produced by the energy "source" and that absorbed by the energy "sink". The model representation of the flow is then used to estimate both the net power flowing from the volume enclosed in the resonator neck and the power produced by the energy source. The dependence of these quantities on the core radius of the model vortices is deduced.

Following the success of the work of Howe (2,3) in predicting the absorption of "acoustic energy" by flow, the Kutta condition is used to determine the dependence of the vortically induced velocity fluctuations on the amplitude of the reciprocating potential flow. In the context of the flow model used here, the Kutta condition is used to determine the relationship between the reciprocating potential flow and the core radius of the shed vortices. The implication is that the greater the potential flow amplitude, the greater the concentration of vorticity into the vortices shed at the upstream edge. It is then demonstrated that once the vortex shedding becomes "phase locked" to the acoustic motion, the concentration of vorticity will increase until the net rate of energy extraction from the mean flow can no longer balance the power radiated to the far field and that carried off by the vortices. An equilibrium of this kind may well dictate the maximum amplitude to which the system oscillations will grow.

Finally, the interpretation of the source of energy associated with momentum fluctuations as the source of far field acoustic energy will be discussed. "Acoustic intensity" as such eludes definition in the region of the flow responsible for its production. As pointed out by Morfey (4), a possible approach is to find a vector intensity which satisfies a continuity property over a wide range of conditions and reduces to the classical definition of acoustic intensity in an ideal fluid at rest. The mean energy flux associated with fluctuating momentum defined by Doak (1) constitutes such a vector intensity. The order of magnitude of the energy source and the energy carried by vortices indicates that it may be useful to view the process of acoustic energy generation in terms of the production of mean energy flux associated with fluctuating momentum. This does not, of course, preclude the adoption of an alternative definition of some generalised "acoustic" intensity, which may satisfy the continuity property over an even wider range of flow conditions. Such an intensity may not

necessarily have "source" regions coinciding with those of the "momentum" mean intensity used here.

The momentum balance is first considered in section 2, and the production of energy from the mean flow is considered in section 3. The possible form of the mean energy balance is outlined in section 4, and the principal conclusions are presented in section 5.

2. THE MOMENTUM BALANCE IN THE RESONATOR NECK

2.1 The Equation of Conservation of Momentum

As pointed out in the discussion of the previous Chapter, the contribution of viscosity to the diffusion of the vorticity distribution is not clearly established, although the indication is that the process of diffusion is too slow to have any appreciable influence on the behaviour of the vorticity distribution during the time taken for a vortex to traverse the resonator neck. It will thus be assumed that it plays no central part in the interaction between the vortical and potential flows.

It is also important to clarify the influence of the compressibility of the fluid on the nature of the interaction. The effects of compressibility will have little direct influence on the local acceleration of the fluid in the resonator neck. The mean flow Mach number is very much less than unity and, more importantly, both the streamwise and transverse dimensions of the shear layer in the neighbourhood of the neck are very much less than the wavelength of the radiated sound, the latter restriction being a more stringent requirement for incompressible behaviour in the case of unsteady flow.

However, the compressibility of the fluid inside the cavity is clearly vital to the functioning of the mechanism, and it is the compressibility of the medium above the cavity that enables acoustic energy to escape. An estimate of the amplitude and phase of the reciprocating potential flow made by using the simple "acoustic" model described in the previous section produced results in reasonable agreement with experimental values. The compressibility of the fluid thus plays a significant role in determining the unsteady potential flow, although only in the sense that the potential flow forms part of an extensive acoustic field, which, in turn, must satisfy the necessary boundary conditions.

Using the identity $(\underline{a}.\nabla)\underline{b} = \nabla(\underline{a}.\underline{b}) - (\underline{b}.\nabla)\underline{a} - \underline{b} \wedge \nabla \wedge \underline{a} - \underline{a} \wedge \nabla \wedge \underline{b}$ and since $\nabla \wedge \overline{\underline{u}} = \overline{\underline{\Omega}}$ and $\nabla \wedge \nabla\phi' = 0$, the term $\overline{\underline{u}}.\nabla(-\nabla\phi')$ can be expanded as follows;

$$\overline{\underline{u}}.\nabla(-\nabla\phi') = \nabla(\overline{\underline{u}}.(-\nabla\phi')) + \nabla\phi'.\nabla\overline{\underline{u}} + \nabla\phi' \wedge \overline{\underline{\Omega}}. \qquad (4)$$

The linearised equation can now be written as

$$\frac{\partial \underline{v}'}{\partial t} + \overline{\underline{u}}.\nabla\underline{v}' + \underline{v}'.\nabla\overline{\underline{u}} - \overline{\underline{\Omega}} \wedge \nabla\phi' - \nabla\left(\frac{\partial\phi'}{\partial t} + \overline{\underline{u}}.\nabla\phi'\right) + \frac{1}{\rho_o}\nabla p' \simeq 0. \qquad (5)$$

This re-arrangement of the linearised momentum equation helps make explicit the nature of the interaction between the vortical and potential flows. The influence of the mean flow on the reciprocating potential flow is principally contained in the convection term $-\nabla(\overline{\underline{u}}.\nabla\phi')$ whilst the influence of the reciprocating potential flow on the structure of the fluctuating vortical flow is entirely contained in the Coriolis acceleration $-\overline{\underline{\Omega}} \wedge \nabla\phi'$. The equation will be used in the next section in order to understand the independent momentum balances possible and to illustrate the dominant features of the interaction.

2.2 The Vortical/Potential Flow Interaction

The above re-arrangement of the linearised momentum equation can now be used in an attempt to outline the possible independent balancing of terms suggested by the decomposition of the net measured fluctuation into two separately identifiable parts. Firstly, the pressure field associated with the unsteady potential flow will be arbitrarily defined by

$$p_\phi' = \rho_o\left(\frac{\partial\phi'}{\partial t} + \overline{\underline{u}}.\nabla\phi'\right). \qquad (6)$$

This definition of the "acoustic" pressure fluctuation includes the influence of the net mean flow (consisting of both vortical and irrotational components) on the pressure field produced due to the convection of the disturbance represented by the term $\overline{\underline{u}}.\nabla\phi'$. In the present case of a low Mach number mean flow predominantly in the x_1 direction, and an unsteady potential having an appreciable gradient only in the x_2 direction, the distortion of the pressure field by the convective effects of the mean flow is negligible. Thus, one can take

$$p_\phi' \simeq \rho_o \frac{\partial\phi'}{\partial t}. \qquad (7)$$

Thus, as far as the local balance of momentum of the fluid in the resonator neck is concerned, the flow can be considered as both inviscid and incompressible. The full equation of conservation of momentum in the absence of body forces can thus be written simply as

$$\frac{D\underline{u}}{Dt} + \frac{1}{\rho_o} \nabla p = 0, \qquad (1)$$

where $(D/Dt) \equiv (\partial/\partial t + \underline{u}.\nabla)$, the material derivative.

The success of the model of the net fluctuating pressure field in predicting the experimental results suggests that some form of independent momentum balance exists whereby a particular part of the total pressure gradient can be identified with the acceleration of the fluid due to the vortical flow only, and another part can be identified with acceleration associated with the reciprocating potential flow.

The momentum equation will now be considered in the light of these possible momentum balances. Since the structure of the fluctuating pressure field at the fundamental frequency is presently of concern, only the linear terms involved in the fluctuating part of the momentum equation will be considered. This is consistent with the evidence (see Chapter 4) that fluctuations at the second harmonic frequency are always some 5-15 dB less than those at the fundamental, but it should be made clear that this does not necessarily mean that non-linear terms are completely negligible in the complete momentum balance. The linear analysis is conducted in order to assist in identification of the principal influences involved in the vortical/potential flow interaction. Thus, the linearised momentum equation can be written as follows, where the dash used as a superscript refers to the fluctuating part of the velocity or pressure field at the fundamental frequency;

$$\frac{\partial \underline{u}'}{\partial t} + \overline{\underline{u}}.\nabla\underline{u}' + \underline{u}'.\nabla\overline{\underline{u}} + \frac{1}{\rho_o} \nabla p' \simeq 0. \qquad (2)$$

This equation can now be written in terms of the vortical flow and potential flow fluctuations by separating $\underline{u}'$ into $\underline{v}' - \nabla\phi'$. The total mean flow $\overline{\underline{u}}$ will not be separated into vortical and potential flow components. The equation can thus be written as

$$\frac{\partial \underline{v}'}{\partial t} - \nabla \frac{\partial \phi'}{\partial t} + \overline{\underline{u}}.\nabla\underline{v}' + \overline{\underline{u}}.\nabla(-\nabla\phi') + \underline{v}'.\nabla\overline{\underline{u}} - \nabla\phi'.\nabla\overline{\underline{u}} + \frac{1}{\rho_o} \nabla p' \simeq 0. \qquad (3)$$

This is the essential form used for p_ϕ' when deduced from the simple acoustic model that appeared so successful in predicting the pressure fluctuations associated with the reciprocating potential flow. It will now be assumed that the independent balance involving the gradient of the pressure fluctuation p_ϕ' can be extracted from the full linearised equation to leave the terms involved in balancing the gradient of the remaining "vortically induced" pressure fluctuations p_v'. (Here p_v' is not necessarily the same as in the previous Chapter.) Thus, defining $p' = p_\phi' + p_v'$ and using the relationship $\nabla(p_\phi' - \rho_o(\partial\phi'/\partial t + \underline{\bar{u}}.\nabla\phi')) = 0$, the remainder of the momentum equation can be written as

$$\frac{\partial \underline{v}'}{\partial t} + \underline{\bar{u}}.\nabla\underline{v}' + \underline{v}'.\nabla\underline{\bar{u}} - \underline{\bar{\Omega}} \wedge \nabla\phi' + \frac{1}{\rho_o}\nabla p_v' \simeq 0. \qquad (8)$$

Now consider the pressure fluctuations that would be produced by the convection of the model array of vortices by the mean potential flow $-\nabla\bar{\phi}$ in the absence of any transverse unsteady flow $-\nabla\phi'$ (as considered in the previous Chapter). The only velocity components produced are thus $\underline{\bar{u}} = (\underline{\bar{v}} - \nabla\bar{\phi})$ and $\underline{v}'$. As the array is convected, the local pressure fluctuations generated will satisfy a momentum equation that, to a linear approximation, is of the form

$$\frac{\partial \underline{v}'}{\partial t} + \underline{\bar{u}}.\nabla\underline{v}' + \underline{v}'.\nabla\underline{\bar{u}} + \frac{1}{\rho_o}\nabla p_v' \simeq 0. \qquad (9)$$

This is exactly equation (8) but with the omission of the Coriolis acceleration $-\underline{\bar{\Omega}} \wedge \nabla\phi'$. This term is the essential term involved in the control of the vortical flow by the unsteady potential flow; it is the principal influence in determining the nature of the vortical/potential flow interaction. The part taken by the Coriolis acceleration can be further illuminated by observing that its omission from the momentum balance in the previous calculations of the generation of vortically associated pressure fluctuations (see section 3.3) did not appear to seriously influence the prediction of those pressure fluctuations, i.e., the simple convection of the vortex array gave reasonable predictions of the pressure fluctuations produced by the passage of the vortices.

This important observation can be understood by considering the physical part played by the action of the reciprocating potential flow on a vortex convecting across the resonator neck. It is well-known that a two-dimensional body (or any material region) with circulation in steady translational motion is acted on by a lift force perpendicular to the

direction of translation of the body. The magnitude of this lift force is given by the Kutta-Joukowsky formula as the product of the fluid density with the translational velocity and the circulation around the body. The Coriolis acceleration produced by the action of the reciprocating potential flow on the vortex behaves in an analogous manner. An element of vorticity shed from the upstream lip of the resonator neck will be acted on by a deflecting acceleration $-\underline{\Omega} \wedge \nabla\phi'$. For the vector $\underline{\Omega}$ in the x_3 direction only and $\nabla\phi'$ in the x_2 direction only, the Coriolis acceleration will be in the x_1 direction and given by $(\Omega_3 \partial\phi'/\partial x_2)\underline{i}$.

During the first half cycle, $\partial\phi'/\partial x_2$ will be positive (corresponding to a negative vertical velocity) and Ω_3 is negative. Thus, the elements of vorticity will be deflected in the negative x_1 direction by the action of the potential flow sweeping down into the cavity. The streamwise progress of the vorticity will thus be retarded by the action of the Coriolis acceleration.

During the second half cycle, as the potential flow sweeps up out of the cavity, $\partial\phi'/\partial x_2$ will be negative and thus the Coriolis acceleration will act in the positive x_1 direction. The elements of vorticity will be accelerated in the streamwise direction. The magnitude of the change of the streamwise velocity of a typical vortex element can be estimated by integrating the acceleration acting over the time of the upwards motion of the potential flow. Thus, the change in streamwise velocity ΔV between times t_1 and t_2 of a vortex element having vorticity Ω_3 is given by

$$\Delta V \simeq \int_{t_1}^{t_2} \Omega_3 \partial\phi'/\partial x_2 \, dt. \tag{10}$$

Since $\partial\phi'/\partial x_2$ has a time variation of the form $|\partial\phi/\partial x_2| \cos(\omega t + \psi_\phi)$, evaluation of this integral yields

$$\Delta V \simeq \left[(\Omega_3/\omega)\,|\partial\phi/\partial x_2| \sin(\omega t + \psi_\phi)\right]_{t_1}^{t_2}. \tag{11}$$

Thus, if the velocity change considered is that produced during the time of the quarter cycle during which the vertical velocity changes from zero to its maximum value, the expression can be written as

$$\Delta V \simeq (\Omega_3/\omega)\,|\partial\phi/\partial x_2|. \tag{12}$$

Now consider an element of vorticity at the very centre of the vortex core. The model vorticity distribution used, where $\Omega_3(r)$ is given by $(\kappa/\pi r_c^2)e^{-r^2/r_c^2}$, shows that at $r = 0$, $\Omega_3 = \kappa/\pi r_c^2$. Thus, the change in streamwise velocity produced by the Coriolis acceleration acting on this element will be approximately given by

$$\Delta V \simeq \frac{\kappa\left|\partial\phi/\partial x_2\right|}{\omega\pi r_c^2} . \qquad (13)$$

The values of κ and r_c of the vortices shed in the resonator neck have been established as 0.12 m^2/s and 1.5 x 10^{-3} m, respectively. The amplitude of the reciprocating potential flow $\left|\partial\phi/\partial x_2\right|$ has been estimated to be 1.68 m/s. Substitution of these values into the above expression yields a value of ΔV of 7.5 m/s. This value of the increase in streamwise velocity produced as a result of the Coriolis acceleration is in good agreement with the observed acceleration of the vortices as they reach the downstream lip of the resonator neck. An increase in convection speed of the vortex structure was observed as a result of the flow visualisation experiment. The approximate convection speed of the vortices was observed to change from 6 m/s to 12 m/s; an increase in ΔV of 6 m/s. In addition, the vortex structure at the downstream edge appears to be stretched into a "comet like" form as it traverses the edge region. The explanation for this may also lie in the action of the Coriolis acceleration. Elements of higher vorticity will be accelerated more; This would result in the vorticity concentrated at the core of a vortex being "pulled out" to the leading edge of the vortex whilst the surrounding regions of lower vorticity trail behind to form the tail of the comet-like structure.

These considerations imply that the principal action of the Coriolis acceleration is to modify and control the form of the vorticity distribution - the vorticity being pushed back along its path at the upstream edge as it is shed and being stretched out as it traverses the downstream edge. The Coriolis acceleration thus will modify the pressure fluctuations p_v' principally by modifying the convection speed of the vortices, and thus correspondingly affecting the vortically associated pressure fluctuations as previously calculated. The local static pressure defect associated with the vorticity, and thus convected with the vortex, will consequently be modified as the vorticity distribution is modified. This may be the explanation for the success of the model of the vortically associated pressure fluctuations, in which the Coriolis acceleration was neglected. The convection speed of 6 m/s chosen for

the vortex array represents the average convection speed of the vortices traversing the resonator neck. This convection speed is valid during the half cycle of the motion during which the reciprocating potential flow velocity is near zero and changing from its maximum negative to its maximum positive value. During this period the vortex traverses a large part of the neck area examined.

3. THE ENERGY BALANCE IN THE RESONATOR NECK

3.1 The Mean Energy Balance

In the previous section, an explanation has been given for the interaction between the vortical and the unsteady potential flow in the resonator neck. It has been established that, in terms of the momentum balance involved, the vortical flow appears to influence the potential flow only weakly whilst the unsteady potential flow appears to control the vortex shedding, principally through the action of the Coriolis acceleration. This acceleration emerges as the only obvious term in the momentum balance equation that does not appear to be directly balanced by pressure fluctuations. Further insight into the part played by the fluctuating Coriolis acceleration can be gained by considering the energy balance equations developed by Doak (1). The work done by the fluctuating Coriolis acceleration is responsible for the transfer of energy from the "mean flow" to the "fluctuating flow" in an inviscid, non-heat conducting fluid in the absence of external heat addition or externally applied body forces.

The energy transport equation for such a fluid (to which the case considered closely approximates) can be written as follows:

$$\frac{\partial}{\partial t}(\rho E + \tfrac{1}{2}\rho\,\underline{u}^2) + \nabla.(H\rho\underline{u}) = 0, \qquad (14)$$

where E is the internal energy per unit mass and H is the stagnation enthalpy per unit mass given by

$$H = E + p/\rho + \tfrac{1}{2}\underline{u}^2. \qquad (15)$$

For a time stationary total energy density $(E + \frac{1}{2}\underline{u}^2)$, the time average of the energy balance equation (14) reduces to

$$\nabla.\overline{(H\rho\underline{u})} = 0, \qquad (16)$$

which can be written as

$$\nabla.(\overline{H}(\overline{\rho\underline{u}})) + \nabla.(\overline{H'(\rho\underline{u})'}) = 0. \qquad (17)$$

The vector intensity $\overline{H}(\overline{\rho\underline{u}})$ represents the mean energy flux associated with the mean momentum, which is a convenient definition of the total energy associated with the "mean flow". The vector $\overline{H'(\rho\underline{u})'}$ represents the mean energy flux associated with the fluctuating momentum. The principal usefulness of this definition is that it reduces to the expression for the usual mean acoustic intensity $\overline{p'\underline{u}'}$ in an acoustic medium at rest having uniform density and sound speed. As such, $\overline{H'(\rho\underline{u})'}$ represents a convenient generalisation of the mean energy flux associated with the "fluctuating flow", although in the presence of momentum fluctuations associated with the vortical flow, it will clearly contain both "acoustic" and "vortical" components. The conservation equation (17) clearly shows that in the confines of an inviscid non-heat conducting fluid with no external heat addition or externally applied forces, a local generation of energy associated with the fluctuating flow must be accompanied by an equal local loss of energy associated with the mean flow.

The mechanism of transfer of mean energy from the mean flow to the fluctuating flow has been shown by Doak to be dependent on the work done by the fluctuating Coriolis acceleration. This can be illustrated by considering the momentum equation for an inviscid non-heat conducting fluid. This can be written in terms of the stagnation enthalpy per unit mass as

$$\frac{\partial\underline{u}}{\partial t} + \underline{\Omega} \wedge \underline{u} + \nabla H = 0. \qquad (18)$$

The time average of this equation is

$$\nabla\overline{H} + \overline{(\underline{\Omega}/\rho \wedge \rho\underline{u})} = 0, \qquad (19)$$

and taking the scalar product of $\overline{\rho\underline{u}}$ with this gives

$$\overline{\rho\underline{u}}.\nabla\overline{H} + \overline{\rho\underline{u}}.\left[\overline{(\underline{\Omega}/\rho)} \wedge \overline{(\rho\underline{u})}\right] + \overline{\rho\underline{u}}.\left[\overline{(\underline{\Omega}/\rho)' \wedge (\rho\underline{u})'}\right] = 0. \qquad (20)$$

Since $\nabla.\overline{\rho\underline{u}} = 0$ (as a consequence of time averaging the mass conservation equation), and since the first of the two triple scalar products is zero, this reduces to

$$\nabla.\overline{H}\,\overline{\rho\underline{u}} = -\overline{\rho\underline{u}}.\left[\overline{(\underline{\Omega}/\rho)' \wedge (\rho\underline{u})'}\right]. \qquad (21)$$

As a direct consequence of this relationship, it follows that a separate conservation equation can be written for the mean flow of energy associated with the fluctuating momentum. Combining equations (17) and (21) shows that

$$\nabla.\overline{\underline{H}'(\rho\underline{u})'} = \overline{\rho\underline{u}}.\left[\overline{(\underline{\Omega}/\rho)'\wedge(\rho\underline{u})'}\right]. \qquad (22)$$

Thus, the only mechanism of production of mean flow energy associated with momentum fluctuations (of which far field acoustic energy constitutes a part) is by the action of the fluctuating Coriolis acceleration working on the mean flow. It is worth pointing out at this stage that the case under consideration constitutes an ideal situation for the production of the vector $\overline{\underline{H}'(\rho\underline{u})'}$. With the vorticity vector in the x_3 direction and a strong transverse flow in the x_2 direction, it has already been pointed out that a large Coriolis acceleration $\underline{\Omega}'\wedge\underline{u}'$ will be produced in the x_1 direction. If this product has a finite time average, then a finite scalar product of $\left[\overline{(\underline{\Omega}/\rho)'\wedge(\rho\underline{u})'}\right]$ with the mean momentum $\overline{\rho\underline{u}}$ will be produced, since the mean flow vector $\overline{\underline{u}}$ is also predominantly in the x_1 direction.

The order of magnitude of energy production involved in the flow considered will be estimated by evaluating this production term in the next section. The form taken by the flow of the vector intensity $\overline{\underline{H}'(\rho\underline{u})'}$ in the resonator neck will also be deduced.

3.2 The Production of Energy associated with Momentum Fluctuations

The finite value of the divergence of the vector intensity $\overline{\underline{H}'(\rho\underline{u})'}$ likely to be produced in the resonator neck implies the existence of a source of energy within a region of the fluid where this "fluctuating flow" energy is converted from "mean flow" energy. The total rate of production of this fluctuating flow energy within a given volume of fluid can be found by integration of the divergence of the vector over that volume of fluid. The total power outflow W_v from a volume V within the fluid bounded by a surface S also lying in the fluid, is given by integration of the vector intensity over the surface S such that

$$W_v = \int_S \overline{\underline{H}'(\rho\underline{u})'}.\underline{dS}. \qquad (23)$$

The straightforward use of the divergence theorem shows that this can also be expressed as

$$W_v = \int_V \nabla.\overline{H'(\rho\underline{u})'}\, dV. \tag{24}$$

A further discussion of the formalities of the solution to the energy balance equation (22) can be found in Reference (1). Since the divergence of the vector intensity $\overline{H'(\rho\underline{u})'}$ has been shown above to be given by the production term associated with the fluctuating Coriolis acceleration, the net power output from the volume V can be written

$$W_v = \int_V \overline{\rho\underline{u}}.\left[\overline{(\Omega/\rho)' \wedge (\rho\underline{u})'}\right] dV. \tag{25}$$

The model of the flow consisting of periodically shed streamwise convected vortices with a transverse potential flow can be used to estimate the local magnitude of the production term occurring in the resonator neck. The value of $\overline{\rho\underline{u}}.\left[\overline{(\underline{\Omega}/\rho)' \wedge (\rho\underline{u})'}\right]$ has been found at each point over a 0.5 mm grid using the computer programs described in the previous Chapter that were developed for the evaluation of the mean and fluctuating quantities involved. Firstly, it has been assumed that the flow is locally incompressible and that the density ρ can be approximated by the ambient density ρ_o. Secondly, only the linear contributions (i.e., those occurring at the fundamental frequency) of the fluctuating vorticity and velocity have been considered. Also, upon assuming that the net mean flow is in the x_1 direction only, the energy production term can be approximated by

$$\overline{\rho\underline{u}}.\left[\overline{(\underline{\Omega}/\rho)' \wedge (\rho\underline{u})'}\right] \simeq -\rho_o \bar{u}_1 \overline{\Omega_3' u_2'}. \tag{26}$$

Note that the time averaged product $\overline{\Omega_3' u_2'}$ can be written as $(\overline{\Omega_3' v_2' - \Omega_3' (\partial\phi/\partial x_2)'})$ by splitting u_2' into its vortical and irrotational components.

The time averaging operation for harmonic variations in vorticity and velocity of the form $|\Omega_3|\cos(\omega t + \psi_\Omega)$, $|v_2|\cos(\omega t + \psi_2)$ and $|\partial\phi/\partial x_2|\cos(\omega t + \psi_\phi)$ yields

$$\overline{\Omega_3' u_2'} = \frac{|\Omega_3||v_2|}{2}\cos(\psi_\Omega - \psi_2) - \frac{|\Omega_3||\partial\phi/\partial x_2|}{2}\cos(\psi_\Omega - \psi_\phi). \tag{27}$$

The phase difference $(\psi_\Omega - \psi_2)$ is always 90° for the uniformly convected vortex model. This was confirmed by evaluating ψ_Ω and ψ_2 using the relevant computer programs. There is thus no time averaged contribution from the cross product of the vorticity fluctuations with the vertical

velocity fluctuations directly induced by the vorticity. The energy production term can thus be written, to a linear approximation, as

$$\overline{\rho \underline{u}.\left[\overline{(\Omega/\rho)' \wedge (\rho \underline{u})'}\right]} \simeq \rho_o \bar{u}_1 \frac{|\Omega_3||\partial\phi/\partial x_2|}{2} \cos(\psi_\Omega - \psi_\phi). \qquad (28)$$

The values of $\bar{u}_1$, $|\Omega_3|$, ψ_Ω, $|\partial\phi/\partial x_2|$ have been computed by running the programs YVCOEM.FTP, XVTOTM.FTN, YOCOEM.FTP and XOTOTM.FTN. The values of vortex strength κ and core radius r_c were again taken to be 0.12 m/s and 1.5×10^{-3} m, respectively, and the relevant Fourier coefficients were evaluated over the 0.5 mm grid using the range of values of x_1 from 0 to 10 mm and x_2 from -6 to +4 mm. The uniform potential flow was again assumed to have an amplitude of 1.68 m/s and a phase lag of 84^o behind the cavity pressure fluctuation. The position of the vortex at t = 0 was again taken to be x_1 = 6.25 mm and x_2 = -1.0 mm.

The approximation to the energy production term given by the expression (28) above has been evaluated from the necessary computed values and is presented as a contour plot in Figure 1. It can be seen that there are large positive values of the energy production term near the downstream edge of the resonator neck. These combine to give a net source of energy associated with the fluctuating flow such that there will be a corresponding power outflow from the region in which the positive values are found. Conversely, there is a series of large negative values towards the upstream end of the resonator neck. There is thus a net sink of this energy in this region, implying that there is a power inflow where fluctuating flow energy is converted back into mean flow energy. It is important to note that the source and sink of energy deduced from the model exactly cancel such that the total volume integral (25) over the region of the source and sink will produce a zero net result. Thus, as far as the model is concerned, there is no net production of energy associated with the fluctuating flow.

3.3 Evaluation of the Total Power Produced by the Energy Source

It is interesting to estimate the total power W_{vs} produced by the source region alone by evaluating the volume integral (25) over the region of the fluid where there is a positive divergence of the vector $\overline{H'(\rho \underline{u})'}$. Firstly, note that for a two-dimensional flow the integral (25) can be written in terms of the lateral dimension ℓ_s of the resonator neck such that

$$W_{vs} \simeq \ell_s \int_{x_1} \int_{x_2} \frac{1}{2} \rho_o \bar{u}_1 |\Omega_3| \left|\partial\phi/\partial x_2\right| \cos(\psi_\Omega - \psi_\phi)\, dx_2 dx_1. \tag{29}$$

The limits of integration with respect to the x_1 and x_2 co-ordinates will be defined such that the entire source region is included. Now note that $\bar{u}_1$ and $|\Omega_3|$ are a function of x_2 only and the phase ψ_Ω is a function of x_1 only such that the integral can be written

$$W_{vs} \simeq \ell_s \frac{1}{2} \rho_o \left|\partial\phi/\partial x_2\right| \; I_1 \int_{x_2} \bar{u}_1 |\Omega_3| dx_2, \tag{30}$$

where

$$I_1 = \int_{x_1} \cos(\psi_\Omega - \psi_\phi)\, dx_1. \tag{31}$$

For the uniformly convected vortex model, the phase ψ_Ω is a linear function of x_1. This variation of phase corresponds to the straight line fit to the measured results shown in Figure 7 of the previous Chapter. The vorticity fluctuations at the fundamental frequency are in phase with the vortically induced streamwise velocity fluctuations above the core path for the uniformly convected vortex model. The phase ψ_Ω can be written as $\psi_\Omega = (2\pi/L)(\bar{\xi}_1 - x_1)$ where $\bar{\xi}_1$ is the streamwise position of the vortex asix at $t = 0$ and L is the vortex spacing in the convected array. The phase ψ_Ω thus changes through 2π for every distance L moved in the x_1 direction. The integral I_1 can thus be evaluated between the limits x_1' and x_1'' such that

$$I_1 = \int_{x_1'}^{x_1''} \cos\left[(2\pi/L)(\bar{\xi}_1 - x_1) - \psi_\phi\right] dx_1$$

$$= \left[-(L/2\pi)\sin((2\pi/L)(\bar{\xi}_1 - x_1) - \psi_\phi\right]_{x_1'}^{x_1''}. \tag{32}$$

The maximum positive value of I_1 will be produced when the limits of integration chosen are such that $\sin((2\pi/L)(\bar{\xi}_1 - x_1) - \psi_\phi)$ takes the values +1 at $x_1 = x_1'$ and -1 at $x_1 = x_1''$. In this case, the value of I_1 is simply L/π. It is a straightforward matter to show that the limits of integration necessary to produce this result are $x_1' = 6.08$ mm and $x_1'' = 11.08$ mm. These values have been calculated assuming $\bar{\xi}_1 = 6.25$ mm with $\psi_\phi = -84^o$ and L = 10 mm. The streamwise extent of the source region is thus defined to lie between limits $x_1 = 6.08$ mm and $x_1 = 11.09$ mm.

This corresponds to the region in which a positive value of the energy production term (26) will be found. Taking the value of I_1 as L/π this gives

$$W_{vs} \simeq \frac{\ell_s L \rho_o |\partial\phi/\partial x_2|}{2\pi} \int_{x_2} \bar{u}_1 |\Omega_3| dx_2. \qquad (33)$$

The integral with respect to x_2 has been evaluated using the values of $\bar{u}_1$ and $|\Omega_3|$ computed as a function of x_2 at 0.5 mm intervals across the shear layer as described in section 3 of the previous Chapter. Since the values of $|\Omega_3|$ decay rapidly above and below the vortex core path in the x_2 direction, the integral converges for a range of x_2 values corresponding roughly to the thickness of the mean shear layer. Thus the integral has been evaluated simply by multiplication of the computed values of $\bar{u}_1$ and $|\Omega_3|$ and addition of the resulting values at each 0.5 mm increment, i.e.

$$\int_{x_2} \bar{u}_1 |\Omega_3| dx_2 \simeq \Delta x_2 \sum_{x_2} \left[\bar{u}_1 |\Omega_3|\right]_{x_2} . \qquad (34)$$

This integral has been evaluated for the value of vortex core radius of 1.5 mm. The value of $|\partial\phi/\partial x_2|$ has again been assumed to be 1.68 m/s with ρ_o equal to 1.2 kg/m^3 with L = 10 mm and ℓ_s = 100 mm. This estimation of the power produced by the source region shows that approximately 36 mW of power is generated. This constitutes a reasonable estimate of the power extracted from the mean flow in the real case. The accuracy of this estimate relies on the essential features of the real flow field being reproduced by the model. That is, streamwise convected vorticity of a known strength and distribution interferes with the transverse potential flow of known amplitude. The estimate of 36 mW is thus certainly accurate to within 50%. The important deduction from this estimate is that it is comparable in order of magnitude to the acoustic power radiated to the far field. This was measured as described in Chapter 4 and found to be 6 mW.

Further aspects of the relationship between the source power and that radiated to the far field will be discussed in a subsequent section, but it is important to note the rough correspondence between the orders of magnitude deduced. The essential conclusion is that the acoustic power radiated does not constitute a very small "leakage" resulting from a slight imbalance between actual source and sink regions that are both comparatively large.

3.4 Energy Flow in the Resonator Neck

Having established the existence of a source and sink of mean energy associated with the fluctuating flow, it is interesting to evaluate the flow of energy in the resonator neck between the source and sink. An approximation to the vector $\overline{H'(\rho\underline{u})'}$ has thus been evaluated at each measurement position in the resonator neck from both the experimental results and for the model of the flow. The local fluctuating stagnation enthalpy per unit mass H' can be written

$$H' = h' + (\tfrac{1}{2}\underline{u}^2)'. \tag{35}$$

Again, assuming an incompressible, inviscid, non-heat conducting fluid, the fluctuating enthalpy h' can be written p'/ρ_o. This follows from the thermodynamic relation $dh = TdS + dp/\rho$ for the fluid considered in which there will be no entropy changes dS. Also, the term $(\tfrac{1}{2}\underline{u}^2)'$ can be written

$$(\tfrac{1}{2}\underline{u}^2)' = \tfrac{1}{2}(\overline{\underline{u}}^2 + \underline{u}'^2 + 2\overline{\underline{u}}.\underline{u}')'. \tag{36}$$

Thus, to first order accuracy, this term can be approximated by $\overline{\underline{u}}.\underline{u}'$. The local fluctuating stagnation enthalpy per unit mass can be written to first order accuracy for the fluid considered as simply

$$H' \simeq p'/\rho_o + \overline{\underline{u}}.\underline{u}'. \tag{37}$$

Under these conditions, the vector $\overline{H'(\rho\underline{u})'}$ can thus be approximated by

$$\overline{H'(\rho\underline{u})'} \simeq \overline{p'\underline{u}'} + \rho_o\overline{(\overline{\underline{u}}.\underline{u}')\underline{u}'}. \tag{38}$$

This is in agreement with the expression derived by Morfey (4) for the same vector to second order accuracy provided an incompressible fluid is assumed (with an effectively infinite sound speed).

This vector has been evaluated directly from the experimental results for the mean and fluctuating velocity field and the fluctuating pressure field in the resonator neck. In the x_1 direction the vector becomes

$$\overline{H'(\rho u_1)'} \simeq \frac{|p||u_1|}{2}\cos(\psi_p - \psi_{u_1}) + \rho_o\overline{u}_1\frac{|u_1|^2}{2}, \tag{39}$$

and in the x_2 direction

$$\overline{H'(\rho u_2)'} \simeq \frac{|p||u_2|}{2}\cos(\psi_p - \psi_{u_2}) + \rho_o\overline{u}_1|u_1||u_2|\cos(\psi_{u_1} - \psi_{u_2}). \tag{40}$$

It has been assumed that the mean flow $\bar{u}_2$ can be neglected and, again, only the contributions of the fluctuating quantities at the fundamental frequency of the oscillation have been considered. The result of evaluating these components from the measured results is shown as a vector field in Figure 2.

The basic pattern of energy flow is clearly shown as a re-circulating flow around the region of the resonator neck. Energy emerging from the region near the downstream edge (which the model implies is a source) flows down into the cavity and back upstream towards the region of the energy sink. This basic flow pattern is clearly established by the experimental results, although the results are not sufficiently accurate or extensive to enable clear identification of the source and sink regions - these have to be inferred from the model representation of the flow.

It is interesting to compare these measurements of the energy flow with the flow derived from the model. Since the pressure field has not been rigorously deduced from the representation of the velocity field, and the resulting dynamic balance is, strictly speaking, incomplete, it must be made clear that deducing the energy flow from the model should be regarded as an approximate fit to the energy flow occurring in the real case. The validity of the procedure is based on the fact that the model reproduces the basic patterns of fluctuating pressure and velocity observed in the real case.

The relevant programmes to reproduce the net mean and fluctuating velocity field were again run using the previously deduced values of the necessary input parameters and the total vertical velocity fluctuation was again simulated by addition of the reciprocating potential flow deduced from the acoustic model. Likewise, the net fluctuating pressure field was reproduced by addition of the "vortically induced" pressure fluctuations with the "acoustic" pressure fluctuations. The resulting evaluation of the vector components (39,40) above gives the energy flow illustrated by the vector field shown in Figure 3. The pattern illustrated is substantially the same as that measured in the real case, and the source and sink of energy flow can be more clearly identified from the behaviour of the vectors, these appearing to have positive divergence towards the downstream edge and a negative divergence towards the upstream edge.

The energy flow measured and the energy flow inferred from the model both clearly show the "feedback" of mean energy associated with fluctuating momentum in the upstream direction along the lower half of the mean shear layer. Although clear identification of the net source and sink of this energy is not possible from the experimental measurements, the model clearly shows their existence near the downstream and upstream edges of the resonator neck. The finite value of the energy production term (26) relies on the interference of streamwise convected vorticity with a transverse unsteady flow. The model used certainly reproduces these principal features that are clearly observed in the experiment. There is no reason, therefore, to doubt the existence of some form of source and sink of energy in the real case in the regions shown and of the order of magnitude indicated.

4. A CONCLUDING DISCUSSION OF THE MECHANICS OF THE FLOW EXCITED RESONANCE

4.1 The Mechanism of Self Excitation

Through the use of a simple flow modelling to aid the interpretation of the experimental results, certain conclusions have been reached regarding the mechanics of the interaction between the vortical and potential flows in the resonator neck. It has been demonstrated that the vortex shedding is controlled by the reciprocating potential flow primarily through the action of the Coriolis acceleration. When the potential flow sweeps down into the cavity, the streamwise progress of the vorticity shed from the upstream edge is retarded. This leads to a concentration of the shed vorticity into the discrete vortices formed. This process is accompanied by an increase in the energy associated with the mean flow; there is a net "sink" of energy associated with the fluctuating flow in the region of vortex formation. During the second half cycle, the vorticity reaching the downstream edge of the resonator neck is accelerated in the streamwise direction by the Coriolis acceleration. This process leads to an extraction of energy from the mean flow; there is a source of energy associated with the fluctuating flow.

The mechanism of excitation of the acoustic resonance thus depends on the control of the vortical flow by the potential flow. The influence of fluctuating potential flow on vortex shedding has been considered by Howe (2,3) in dealing with the absorption of "acoustic energy" by flow. Howe (2) has used the Kutta condition to determine the strength of the fluctuating circulation shed at a nozzle edge as a

result of the pulsatile jet flow produced by an upstream acoustic disturbance. A similar procedure has been used by Howe (3) in modelling the interaction of sound with a grazing aperture flow and in dealing with the theory of the flute (5). The relative success of these models in predicting experimental observations suggests that there is an inherent relationship between the amplitude of the reciprocating potential flow and some measure of the strength of fluctuations in circulation shed from the upstream edge.

It has already been clearly demonstrated in the previous Chapter that the strength of the vorticity shed per cycle depends only on the grazing mean flow across the top of the resonator neck. One is thus led to the conclusion that the reciprocating potential flow can only influence the concentration of the vorticity shed per cycle. This is consistent with the notion that the Coriolis acceleration deflects vorticity upstream during the process of vortex formation. The action of the potential flow leads to an increase in the quantity of vorticity deflected upstream into the discrete vortices formed. The concentration of vorticity produced induces a velocity at the upstream edge which exactly cancels the potential flow. The Kutta condition is thus satisfied.

It is thus reasonable to assert that the Kutta condition provides the essential link between the amplitude of the reciprocating potential flow and the extent to which vorticity is wound into the vortices formed. This can also be illustrated using the simple vortex shedding model. As shown in the analysis of the measured vertical velocity fluctuations presented in the previous Chapter, there is a tendency for the vortically induced velocity to be cancelled by the fluctuating potential flow at the upstream edge. A decrease in core radius of the model vortices results in an increase in the maximum vortically induced velocity fluctuations in the vertical direction. This is shown in Figure 9 of the previous Chapter. Thus, although the model fails to adequately describe the process of vortex formation, it nevertheless illustrates that the concentration of vorticity (as measured by vortex core radius) is related to the amplitude of the reciprocating potential flow.

In summary, the excitation of the resonance is initiated by the interaction of the vorticity with the downstream edge. The potential flow which, in the first instance, can be thought of locally as the result of "image vorticity", sweeps out of the cavity accelerating the

vorticity in the streamwise direction and dilating the fluid in the resonant cavity. A similar process has been illustrated by Crighton (6) in predicting the radiation of acoustic energy as vorticity accelerates in the region of an edge. The subsequent compression of the fluid in the cavity results in the concentration of vorticity near the upstream edge as the potential flow sweeps down into the cavity. The concentration of vorticity produced is related to the potential flow fluctuation by the need to satisfy the Kutta condition. Once this feedback process has begun, with the shedding locked to the acoustic motion at the appropriate mean flow speed, the amplitude of oscillation will increase with increasing concentration of vorticity until an appropriate limit is reached. The limit to the growth of the amplitude of oscillation will be discussed in terms of the energy balance outlined in the next section.

4.2 A Discussion of the Likely Form of the Energy Balance

Having described the basic mechanics of the interaction between the potential flow and the shed vorticity, and in particular the part played by the Kutta condition in determining the degree of vorticity concentration, the energy balance will now be discussed in more detail. The main factor that has to be considered is the net generation of power by the flow in the resonator neck. Power associated with the fluctuating flow leaves the volume surrounding the region of the resonator neck both in the form of far field radiated acoustic energy and in the form of vortices swept away downstream of the resonator mouth. This net power must be produced by an imbalance between the downstream source and the upstream sink.

The failure of the model used to illustrate a difference in the strengths of the source and sink is due to the failure to adequately model the process of vortex formation at the upstream edge. In this region, the local vorticity fluctuations grow from zero as the vortex sheet instability amplifies. The smaller amplitude of vorticity fluctuations at the upstream edge lead to smaller local negative values of the energy production term (28). The net effect is that the integrated value of the energy production term will show a sink absorbing less power than is produced by the source.

It is interesting, for the purposes of illustration, to estimate the magnitude of the energy sink relative to the strength of the source and the power leaving the resonator neck. The acoustic power radiated was measured as 6 mW. The acoustic model used implies a net power radiation given by

$$W_a = \tfrac{1}{2} R_r \ell_s L \left| \partial\phi/\partial x_2 \right|^2. \qquad (41)$$

A value of 1.68 m/s for the amplitude of the reciprocating potential flow and the "no flow" value of the radiation resistance R_r gives a value of W_a of approximately 12 mW. This discrepancy could be due to error in estimation of either R_r or $|\partial\phi/\partial x_2|$.

An estimate of the power carried away by the vortices can be made by evaluation of the integrated value of the vector intensity crossing a surface surrounding the resonator neck. The model of the vortical flow can be used to derive this estimate. The net power carried downstream by the vortices can be evaluated by the integration of the vector $\overline{H'(\rho v_1)'}$ over the surface formed by the spanwise length ℓ_s of the resonator neck and the width of the mean shear layer in the x_2 direction. Defining W_{vv} as the power carried along the shear layer by the vortices gives

$$W_{vv} \simeq \ell_s \int_{x_2} \frac{|p_v||v_1|}{2} \cos(\psi_{pv} - \psi_1) + \rho_o \bar{U}_1 \frac{|v_1|^2}{2} dx_2. \qquad (42)$$

This, of course, assumes that no other flow is present that can contribute to the total pressure or velocity fluctuation; the only flow considered is that produced by the convection of the vortices by the mean potential flow. Since $(\psi_{pv} - \psi_1)$ is 180^o above the path taken by the axis of the vortex and is 0^o below the axis path, then the first term in the expression (42) above makes zero net contribution to the integral. Thus the expression can be written as

$$W_{vv} \simeq \tfrac{1}{2} \rho_o \ell_s \int_{x_2} \bar{u}_1 |v_1|^2 dx_2. \qquad (43)$$

This integral has been evaluated by the values of $\bar{u}_1$ and $|v_1|^2$ deduced at 0.5 mm intervals across the shear layer cross section as described in the previous Chapter. The limits to integration chosen were 5 mm below to 5 mm above the core axis path. For a value of vortex core radius in the model of 1.5 mm, a value of W_{vv} of approximately 14 mW was estimated.

In terms of the model representation of the flow, for a vortex core radius of 1.5 mm, the energy source produces 36 mW of which 12 mW is radiated as acoustic power and 14 mW is carried downstream by the vortices. This implies that approximately 10 mW of power is absorbed by the energy sink in the region of vortex formation. No great significance can be attached to the precise values of these quantities since they are

obviously based only on crude estimates of the parameters involved. Nevertheless, the important fact has been illustrated that the radiated acoustic power, the power carried by the vortices, the power produced by the source and that absorbed by the sink are all of a very similar order of magnitude. Roughly speaking, the power generated by the source is more or less equally partitioned between the acoustic field, the unsteady vortical flow and the energy sink necessary to aid in the formation of new vortices.

4.3 The Source of Far Field Acoustic Energy

The question arises as to whether the source of energy associated with momentum fluctuations at the downstream edge can be considered as the source of radiated far field acoustic energy. There are no generally accepted definitions of "acoustic intensity" inside the region of the resonator neck. It is thus necessary to adopt a definition of a "generalised acoustic intensity" in the region of the flow, which, in turn, reduced to the usual definition of acoustic intensity in the acoustic far field. The mean intensity vector $\overline{H'(\rho\ \underline{u})'}$ associated with fluctuating momentum considered has the property of reducing to the usual definition of the mean acoustic intensity vector in a medium at rest. Thus, in that the acoustic intensity vector constitutes a part of the generalised intensity vector used, it is legitimate to assert that "acoustic energy" is produced near the downstream edge of the resonator neck. This assertion has, of course, to be qualified by what "acoustic energy" is considered to consist of in the region of the flow.

Since the strength and location of such a source of acoustic intensity is clearly dependent on the definition of generalised acoustic intensity adopted, it is impossible to assert that the region near the downstream edge of the resonator neck represents an acoustic energy source in any unique sense. It is thus necessary to choose a generalised acoustic intensity which, besides satisfying a continuity property over the widest possible range of conditions, can also be judged in some sense to be a "useful" definition.

The generalised intensity $\overline{H'(\rho\ \underline{u})'}$ defined by Doak, thus appears to be very convenient in that there is a close correspondence between the order of magnitude of the power apparently extracted from the mean flow and the power radiated to the far field. For example, the radiated acoustic energy is not seen as a relatively small by-product of the imbalance between a relatively large "almost self-cancelling" source-sink combination. Also, the location of the energy source near the down-

stream edge has a certain intuitive appeal. Many of the models quoted in the introduction to Chapter 4 of this type of flow excited resonance have considered the "downstream edge" to be the "source of sound" in some sense or another. Additionally, the net flow of energy upstream from the source to the sink reinforces the view that the operation of the mechanism is by some form of feedback process.

Finally, however, the definition of generalised acoustic intensity adopted has the drawback that the production of energy is not intimately related to the compressibility of the medium. The net production of energy associated with momentum fluctuations does not, in principle, rely on the medium being compressible. Thus, for example, vortices can carry a mean flow of energy associated with momentum fluctuations away from the volume in which they were formed without the medium considered being compressible. Ideally, it should be possible to choose a generalised acoustic intensity such that there can be no net production of energy from a given fluid volume in an incompressible fluid, i.e., a fluid in which no far field acoustic energy can be generated. It is likely that only such a choice of generalised acoustic intensity will enable any further insight to be gained into the mechanism of acoustic energy production from fluctuating fluid motion.

4.4 The Energy Balance as a Limit to the Amplitude of Oscillation

It will now be demonstrated that the form of the energy balance may well determine the maximum amplitude to which the oscillations in the resonator neck will grow. Once the feedback process has been initiated, a growing amplitude of reciprocating potential flow will be produced with a consequent increase in the concentration of vorticity as vortices are formed. The dependence of the various contributions to the energy balance on the degree of concentration of vorticity can be estimated. The core radius of the vortices in the flow model will be used as a measure of this degree of concentration.

Firstly it will be assumed that the amplitude $|\partial\phi/\partial x_2|$ of the reciprocating potential flow is in direct proportion to the maximum vertical velocity fluctuations produced by the passage of the model vortices. Thus, assuming $|\partial\phi/\partial x_2|$ is 1.68 m/s at a core radius of 1.5 mm, the values of $|\partial\phi/\partial x_2|$ at other core radii can be deduced. These can be derived from the maximum values of $|V_2|$ shown in Figure 5 of the previous Chapter. This procedure essentially attempts to quantify the relationship between the potential flow amplitude and the vorticity

concentration such that the Kutta condition is satisfied.

Using this assumption, the dependence on vortex core radius can be established of the acoustic power radiated W_a, the power carried by the vortices W_{vv} and the net power produced by the source region W_{vs}. The vortex shedding model has thus been used to evaluate each of these quantities from the expressions (41), (43) and (33). The range of core radii used was from 0.5 mm to 2.5 mm in 0.5 mm intervals. The results of this evaluation have been plotted in Figure 4. Note that the acoustic power W_a and the power carried by the vortices W_{vv} increase rapidly with decreasing core radius. The total power $(W_a + W_{vv})$ released from the resonator neck exceeds the total power W_{vs} that can be produced by the source at low core radii.

At the value of core radius observed in the experiment, the source provides sufficient power to account for the energy sink and the power $(W_a + W_{vv})$ leaving the resonator neck. This suggests that the vorticity concentration into the shed vortices increases until this energy balance is reached. This is illustrated in Figure 5, which shows the dependence on core radius of an estimation of the net power ΔW_{vs} produced by the source-sink combination. It has been assumed that the power absorbed by the energy sink is a constant fraction of the power produced by the source. This fraction has been determined by the proportion of power absorbed by the sink at a core radius of 1.5 mm. This assumption relies on the mechanism of energy production and absorption in the shear layer showing the same dependence on vorticity concentration. The model certainly suggests that this is the case.

The following picture of the energy balance thus emerges. Vorticity concentrated into vortices at the upstream edge interacts with the potential flow at the downstream edge and extracts energy from the mean flow. The greater the concentration of vorticity produced, the greater is the power that can be extracted by the vortices to feed back upstream to assist in the formation of new vortices. However, some of the energy extracted from the mean flow must ultimately be carried away by the vortices or radiated to the acoustic far field. An upper limit to the concentration of the vorticity into vortices will be reached, this being determined by the point at which the energy source can no longer supply sufficient power to meet the demands of the energy sink and the "losses" from the volume of the resonator neck. Strictly speaking, additional losses of energy associated with the fluctuating flow will also be

produced by viscous and thermal effects. As shown in Chapters 4 and 5, these are likely to be of a smaller order of magnitude than the power losses considered here.

4.5 The Physical Interpretation of the Vortex Shedding Model

The various contributions to the energy balance presented in the previous section have been derived from a simple but self consistent flow model. The only major assumption used was the nature of the relationship between vortex core radius and the potential flow amplitude in order to satisfy the Kutta condition. The underlying dependence of the rate of energy production and dissipation on vortex core radius has been clearly established. The core radius of the model vortices has been used as a measure of the degree of concentration of shed vorticity into "bundles" of known strength which constitute the discrete vortices formed. However, one must be careful to interpret the "vorticity concentration" in terms of the behaviour of the real flow.

The vortices are formed in the real flow by the unstable vortex sheet winding into a spiral. This process has been reviewed by Saffmann and Baker (7) and in more detail by Kuchemann and Weber (8). Batchelor (9) also presents an interesting discussion in which it is maintained that the size of the vortex (as determined by the radius of the outer turn of the spiral) will be determined by the original dispersion of the vorticity in the unstable vortex sheet. This argument is based on Lamb's (10) observation of the invariance of the dispersion (second integral moment) of the vorticity distribution.

This suggests that the maximum vorticity concentration in the vortices may well be determined also by other considerations in addition to those suggested in the energy balance outlined above. There could be, for example, a minimum vortex size into which vorticity of a given strength could be packed. Such a maximum vorticity concentration could be the factor determining the maximum power that could be extracted by the straining of the vortex that occurs at the downstream edge.

Another interpretation of the behaviour suggested by the model is that the core radius essentially represents the degree of accumulation of vorticity into the vortex structure by the time it reaches the downstream edge, rather than a measure of the size of the vortex structure. It is likely that the rate of formation of the vortices will be increased by the action of the reciprocating potential flow. Vorticity will be entrained into the vortices at a greater rate than would otherwise occur

in the growth of the natural instability of the vortex sheet. An increased accumulation of vorticity will be produced by the time the vortex reaches the downstream edge. This explanation is more consistent with experimental observations. The "spreading of influence" of the vortices as they travel across the resonator neck revealed in the experimental results from the vortex formation process. This occurs as the initial vortex sheet winds into a spiral and is also accompanied by an observed spreading of the mean shear layer in the downstream direction. The mean shear layer will thus thicken at a greater rate as a result of the action of the reciprocating potential flow.

Thus, although a coherent picture has evolved of the mechanics of the interaction of the vorticity with the unsteady potential flow, there is still a need for further experimental studies of the influence of acoustic fields on shear layer development. In particular, an attempt should be made to establish the influence of externally applied sound fields on the accumulation of vorticity in the unsteady development of the shear layer. Further, there is a considerable need for the development of suitable analytical techniques for adequate quantification of these observations on shear layer development. It seems unlikely that linear stability theory by itself could provide an adequate mathematical framework for dealing with problems of this kind.

5. CONCLUSIONS

Certain tentative conclusions have been reached regarding the principal mechanism of the control of the vortex shedding in the resonator neck by the reciprocating potential flow. A form of the linearised momentum balance has been suggested which identifies the fluctuating Coriolis acceleration as the principal acceleration that is not directly balanced by a fluctuating pressure gradient. The view has been advanced that it is the Coriolis acceleration which is primarily responsible for providing the deflecting force resulting in the control of the vortex shedding by the reciprocating potential flow. The agreement between the calculated acceleration of the vortices at the downstream edge of the resonator neck and the observed increase in vortex convection speed provides some evidence to support this view.

Some firm conclusions can also be drawn from considerations of the mean energy balance in the resonator neck. These can be listed as follows:

(1) There is a mean rate of conversion of energy associated with mean momentum to energy associated with fluctuating momentum in the region near the downstream edge of the resonator neck. This conversion of energy occurs as a direct result of the presence of a fluctuating Coriolis acceleration caused by the interference of streamwise convected vorticity with a uniform transverse potential flow. The net "source" of energy emits a power that is a few times greater than the acoustic power radiated to the far field.

(2) There is also a "sink" of energy associated with fluctuating momentum in a region towards the upstream edge of the resonator neck. This absorbs a power that is of a similar magnitude to that emitted by the source.

(3) The mean flow of energy associated with fluctuating momentum in the resonator neck consists of a recirculating pattern in which there is a mean flow of energy upstream along the lower half of the mean shear layer.

Besides these firm conclusions, it has also been suggested that the Kutta condition determines the relationship between the amplitude of the reciprocating potential flow and the degree of concentration of vorticity in the unsteady development of the unstable vortex sheet. A possible form of the mean energy balance of the fluid in the volume surrounding the resonator neck has also been suggested. It has been proposed that an imbalance between the source and sink of energy must be responsible for a net production of energy associated with momentum fluctuations carried out of the volume both by the vortices and in the form of radiated acoustic power. It appears from consideration of the linear terms involved, that both the rate of extraction of energy from the mean flow and the power losses from the volume depend on the extent to which vorticity accumulates into the vortices reaching the downstream edge of the resonator neck. This leads to the suggestion that once the vortex shedding and the reciprocating potential flow become "phase locked" at a certain mean flow speed, the amplitude of oscillation will increase with an increased rate of accumulation of vorticity into the shed vortices until an equilibrium is reached. At this point, the net energy production in the volume exactly balances the energy released from the volume in the form of radiated acoustic energy and in the form of energy associated with the vortices.

REFERENCES

1. P.E. DOAK 1974 Proceedings of the Eighth International Congress on Acoustics. Contributed Papers, Volume II, p. 532. Acoustic, thermal and turbulent energy density and linear momentum density relationships and fluxes in fluctuating fluid flows. (A complete report on this work is being prepared for publication.)

2. M.S. HOWE 1979 Journal of Fluid Mechanics 91, 209-229. Attenuation of sound in a low Mach number nozzle flow.

3. M.S. HOWE 1980 Journal of Sound and Vibration 67, 533-544. The influence of grazing flow on the acoustic impedance of a cylindrical wall cavity.

4. C.L. MORFEY 1971 Journal of Sound and Vibration 14, 159-170. Acoustic energy in non-uniform flows.

5. M.S. HOWE 1975 Journal of Fluid Mechanics 71, 625-673. Contributions to the theory of aerodynamic sound with application to excess jet noise and the theory of the flute.

6. D.G. CRIGHTON 1972 Journal of Fluid Mechanics 51, 357-362. Radiation from vortex filament motion near a half plane.

7. P.G. SAFFMANN and G.R. BAKER 1979 Annual Review of Fluid Mechanics 11, 95-122. Vortex interactions.

8. D. KUCHEMANN and J. WEBER 1965 Z. Angew Math. Mech. 45, 457-474. Vortex motions.

9. G.K. BATCHELOR 1964 Journal of Fluid Mechanics 20, 645-658. Axial flow in trailing vortices.

10. H. LAMB 1932 Hydrodynamics. 6th Edition, Section 157. Cambridge University Press.

APPENDIX 1. LIST OF SYMBOLS

$\underline{a},\underline{b}$	arbitrary vector quantities
E	internal energy per unit mass
h	enthalpy per unit mass
H	stagnation enthalpy per unit mass
ℓ_s	spanwise length (in x_3 direction) of resonator neck
L	streamwise length (in x_1 direction) of resonator neck
p	pressure
r	radial distance from vortex core axis
r_c	vortex core radius
R_r	radiation resistance
S	surface area enclosing the volume V
t	time
$\underline{u}$	total velocity
$\underline{v}$	vortical velocity
V	volume of fluid
W_v	total power outflow from the volume V
W_{vs}	total power produced by energy source
W_{vv}	total power associated with the vortices
W_a	total radiated acoustic power
x_1,x_2,x_3	cartesian coordinates
x_1',x_1''	limits of integration
ΔV	velocity change
κ	vortex strength
$\bar{\xi}_1,\bar{\xi}_2$	coordinates of vortex core axis at t = 0
ρ_o	ambient density
ϕ	velocity potential

ψ	phase relative to cavity pressure fluctuations (used with appropriate subscripts)
ω	radian frequency
$\underline{\Omega}$	vorticity vector

FIGURE 1 Contours of the approximation to the local energy production $\nabla.\overline{H'(\rho \underline{u})'}$ computed in the region of the resonator neck.
(Contours are in increments of 5 x $10^3 kgm^{-1}s^{-3}$ with the following contours shown: - -50, = -25, ≡ +25, ≣ +50 x 10^3 $kgm^{-1}s^{-3}$.)

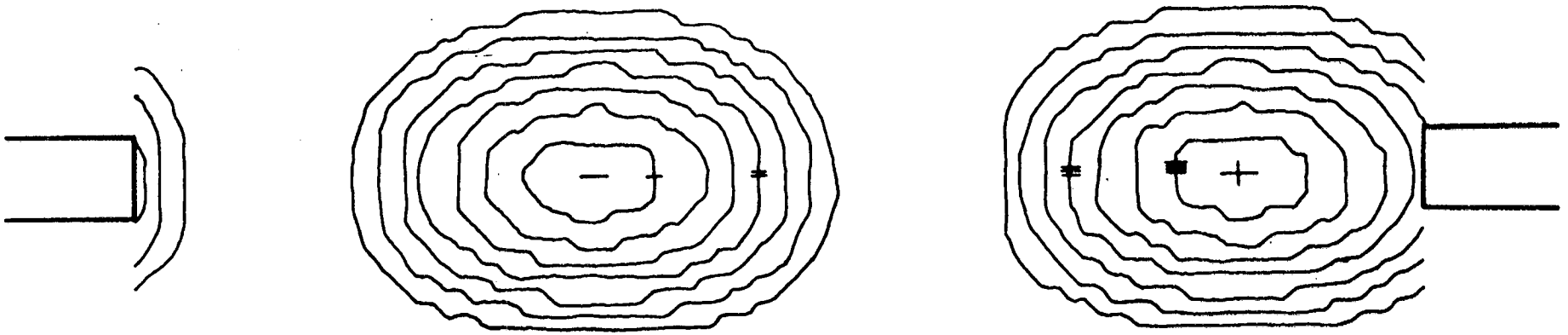

FIGURE 2 A field representation of an approximation to the vector intensity $\overline{H'(\rho \underline{u})'}$ derived from the experimental results.

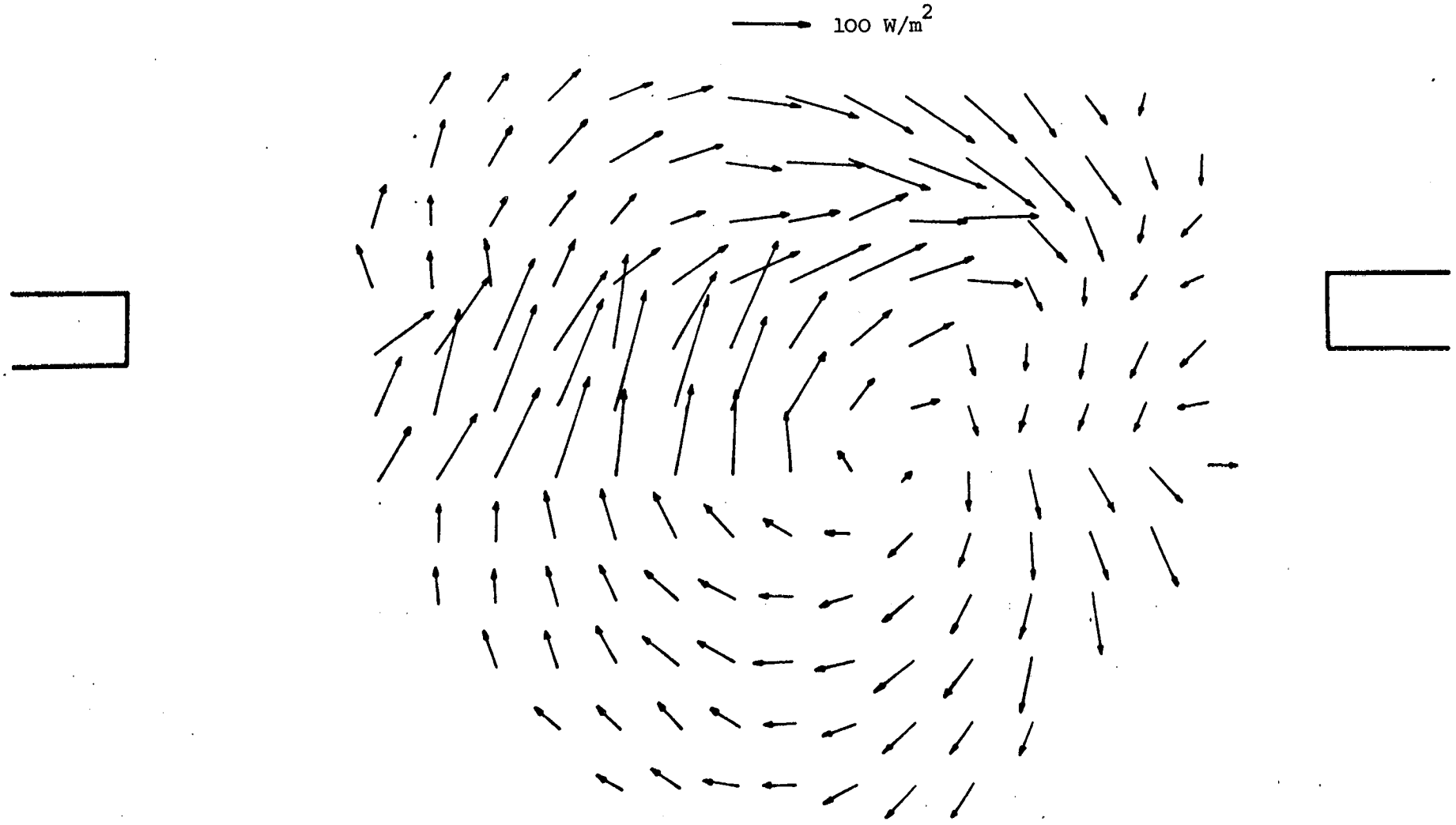

FIGURE 3 A field representation of an approximation to the vector intensity $\overline{H'(\rho \underline{u})'}$ computed from the model representation of the velocity and pressure fields.

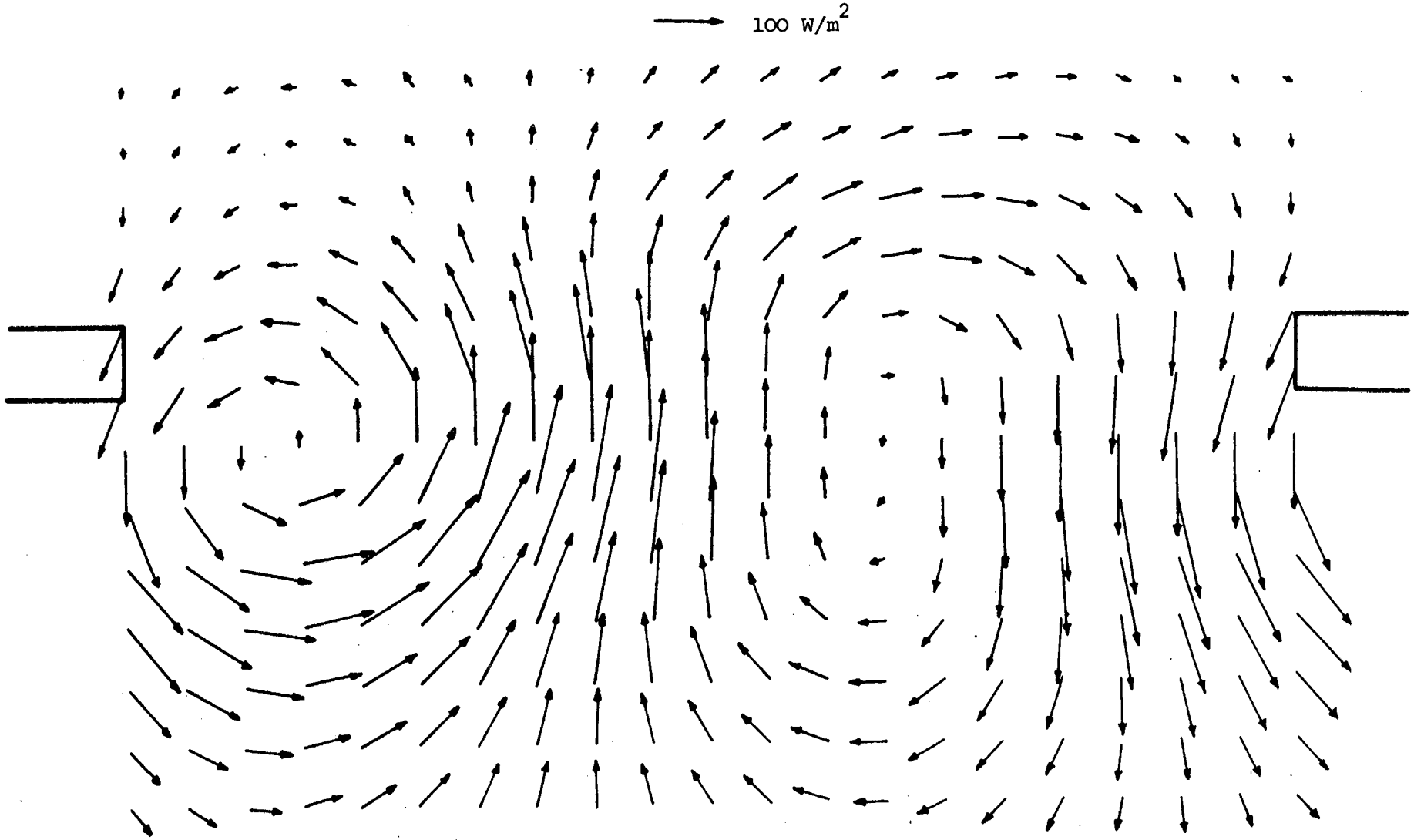

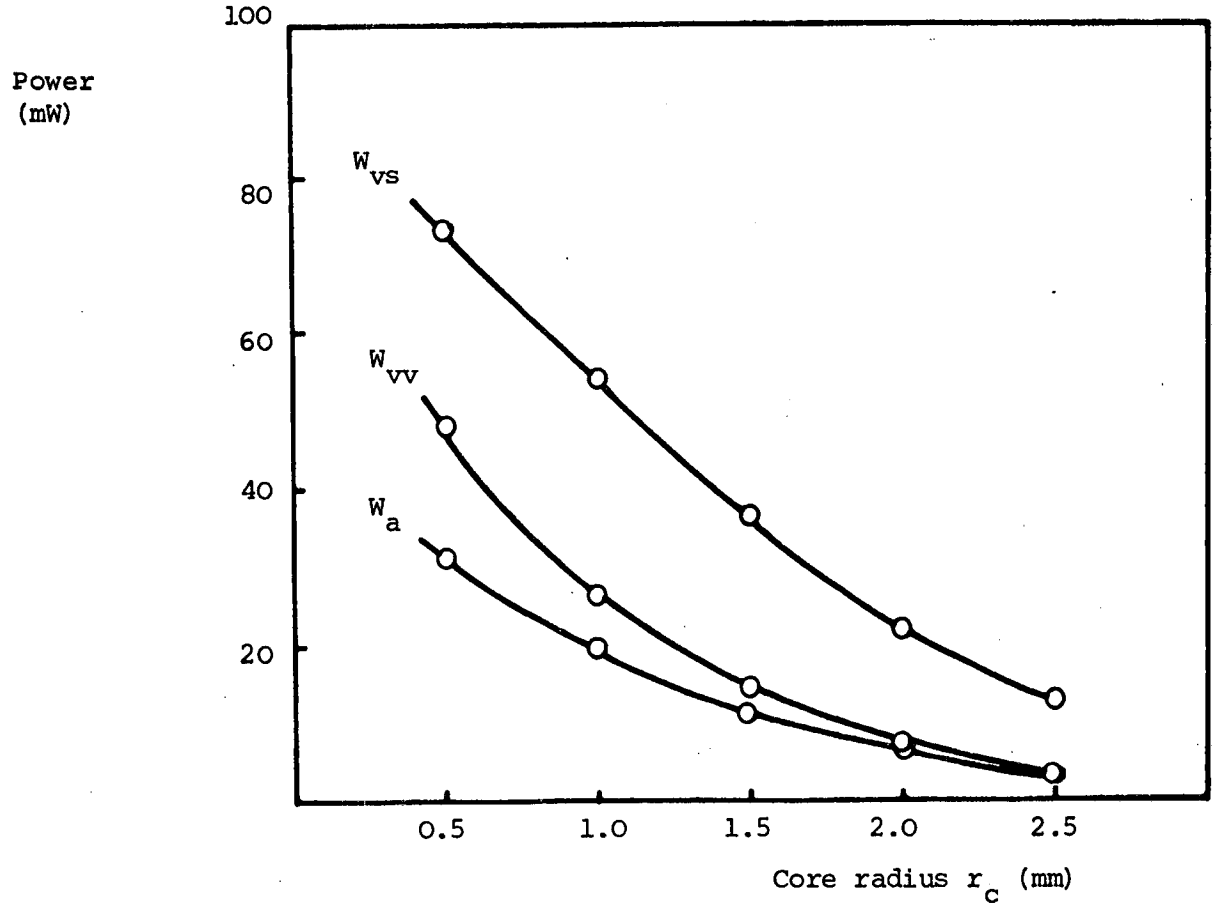

FIGURE 4 The dependence on vortex core radius of total source power W_{vs}, radiated acoustic power W_a and power carried by the vortices W_{vv} deduced from the vortex shedding model.

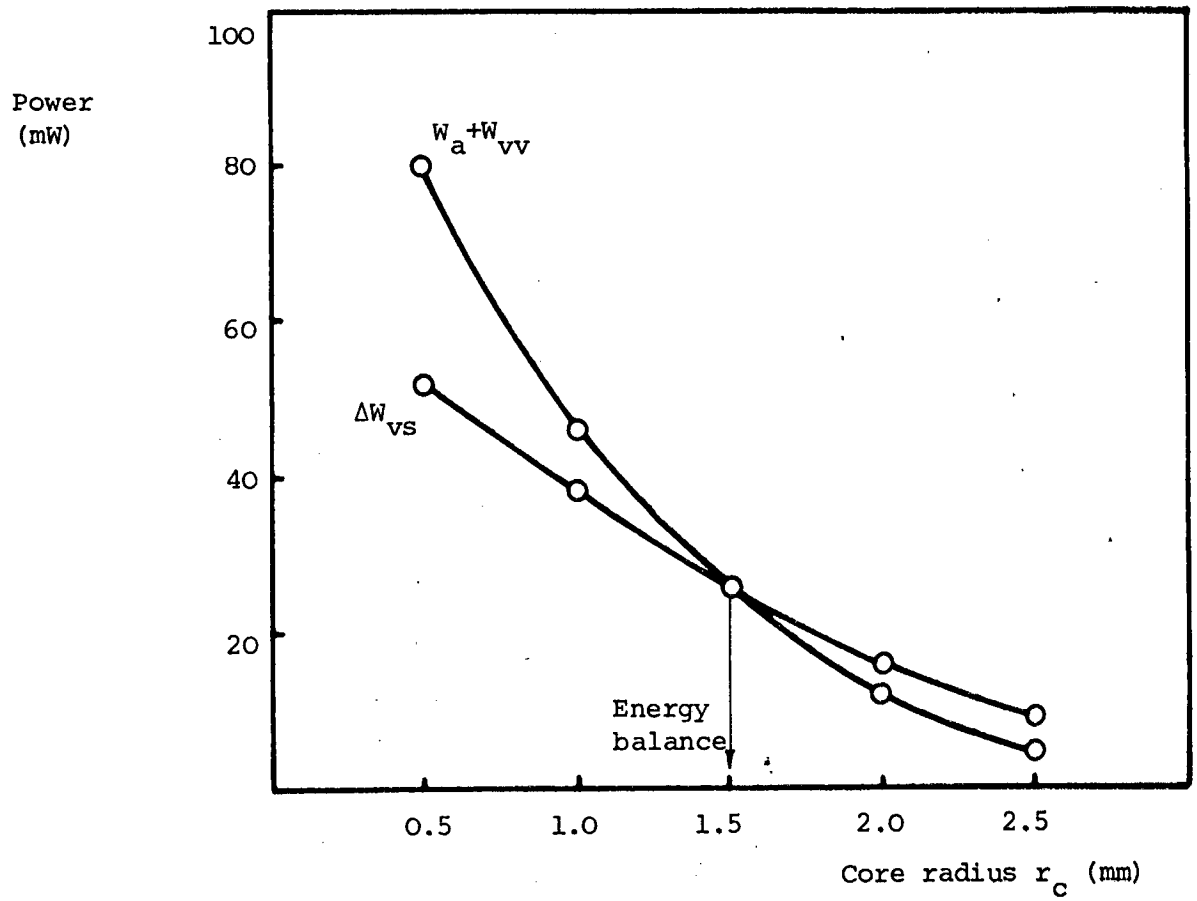

FIGURE 5 The dependence on vortex core radius of the net power ΔW_{vs} produced by the source-sink combination and the net losses (W_a+W_{vv}) from the volume surrounding the resonator neck. Values have been deduced from the vortex shedding model.

CHAPTER 7

CONCLUSIONS

CONCLUSIONS

Two engineering problems involving the generation of aerodynamic sound have been examined. The theoretical foundation for both problems has been provided by an equivalent source representation of the sound generation process.

The first problem that has been considered is the prediction of the level and spectral distribution of the additional sound power radiated when a given obstruction, or flow spoiler, is placed in a low Mach number ducted flow. A theory has been developed which models the source of sound as a distribution of dipole type sources immersed in an infinite hard walled duct. The strength of these sources is directly related to the fluctuating force exerted by the flow on the duct obstruction.

The case has been treated of a thin flat plate placed perpendicular to the flow direction. Certain statistical assumptions regarding the nature of the force fluctuations on the plate have enabled the sound power radiated to be related to the total fluctuating drag force acting. Expressions have been produced which are valid for plane wave propagation and for multi-modal propagation in the duct. A series of careful experiments have confirmed the validity of the assumptions made in the development of the theory.

The further assumption that the fluctuating drag force acting on the flow spoiler is in direct proportion to the steady state drag force acting produces a remarkably good collapse of experimental results. This leads to the possibility of an accurate engineering prediction scheme which will enable the sound power radiated to be deduced with a knowledge of relatively simple geometric and flow parameters. It remains to be seen if the sound produced by other flow duct obstructions, changes of cross section or other discontinuities can be reliably predicted from a knowledge of the steady state force acting. This may well be a profitable area of further research.

The second engineering problem dealt with is the prediction of the sound generated when turbulence interacts with the perforated surface of an acoustically absorbent duct liner. The equivalent source representation used in this instance was that of a combination of monopole type sources situated at the location of each perforation in the surface. One monopole is situated immediately above each perforation and a monopole of equal and opposite strength is situated immediately below the perforation.

The strength of the monopole sources is determined by the fluctuations in mass flow driven through the perforation by the hydrodynamic field. For acoustically transparent screens, the monopoles combine to give a net dipole radiated field. This equivalent source representation was found to produce a remarkably good description of the sound field radiated when a series of perforated screens were exposed to turbulent flow. The experiments undertaken provide a good confirmation of the validity of the theoretical model. This enables reliable predictions to be made of the level and spectral distribution of the sound radiated by practical perforated liner surfaces.

Both theory and experiment have shown that the most efficient radiation of sound occurs when eddies are shed that are of the order of the size of the liner perforations. The solution of the problem of continuous generation and absorption of acoustic energy along a duct length has enabled prediction of the net sound generated by flow over the perforated surface of a dissipative duct liner. The predictions made are in encouraging agreement with the measurements of the noise generated in practice.

Besides the examination of these two particular engineering problems, a third more fundamental study has been undertaken in an attempt to provide a deeper understanding of the physical processes involved in the extraction of acoustic energy from unsteady flow.

The first part of this third study was a detailed experimental investigation of the flow in the neck of a Helmholtz resonator excited by a mean grazing flow. Firstly, stroboscopic visualisation of the flow revealed the periodic formation of discrete vortices from the unstable shear layer leaving the upstream lip of the resonator neck. These vortices were also observed to undergo a rapid increase in convection speed when they reached the downstream edge of the resonator neck.

Further quantitative details of this vortex shedding process were established by measuring the mean and fluctuating parts of the velocity field in two orthogonal component directions. This was successfully accomplished by using a Laser Doppler Velocimeter. The measurements of both "streamwise" and "vertical" velocity components revealed many interesting features of the velocity field which may well have remained concealed had only single component measurements been made. In particular, the rapidity with which the unstable shear layer forms into discrete vortices was clearly illustrated.

Measurements of the fluctuating static pressure field in the resonator neck were also successfully accomplished by using a small diameter microphone probe tube. This showed a pressure pattern exhibiting a region of relatively small pressure amplitude near the downstream lip of the resonator neck. A very rapid spatial rate of change of the relative phase of the pressure fluctuations was also detected in this region.

In order to aid the understanding of the principal features of both the fluctuating velocity and pressure fields, a simple model of periodic vortex shedding was developed. The vortical flow field was represented by the velocity induced by the periodic passage of a series of discrete vortices each containing a specified distribution of vorticity. The strength and core radius of these vortices was determined from the experimental results. It was then demonstrated that the dominant characteristics of the measured velocity field could be explained by the interference of a uniform reciprocating transverse potential flow with the velocity field induced directly by the passage of the vortices. The measured pattern of static pressure fluctuations could also be explained by the interference of the static pressure fluctuations generated by the passage of the vortices with the pressure fluctuations associated with the reciprocating potential flow.

The implications of this apparent superposition of two separately identifiable pressure fields have been examined in terms of the local momentum balances occurring in the flow. An analysis of the linearised equation of conservation of momentum indicates that, for this particular flow model, the Coriolis acceleration due to the fluctuating potential flow is the only term in the momentum equation whose balancing is not completed by a fluctuating pressure gradient. This leads to the suggestion that the vortex shedding process is controlled by the reciprocating potential flow which deflects the shed vorticity primarily through the action of this Coriolis acceleration. This view has been reinforced by the observed streamwise acceleration of the vortices when reaching the downstream edge. This acceleration is in good agreement with the velocity increase expected as a result of the Coriolis acceleration.

The interference of streamwise convected vorticity with a transverse reciprocating potential flow also leads to an interchange between the mean energy flow associated with mean momentum and the mean energy flow

associated with fluctuating momentum. This interchange occurs as a direct result of the work done by the fluctuating Coriolis acceleration. There is a mean rate of conversion of energy associated with mean momentum to energy associated with fluctuating momentum in a region towards the downstream edge of the resonator neck. There is thus a net "source" of energy associated with fluctuating momentum. There is also a "sink" of energy associated with fluctuating momentum in the region of vortex formation towards the upstream edge of the resonator neck.

The order of magnitude of both the source and sink has been reliably established by using the simple vortex shedding model. The orders of magnitude of the power emitted by the source and that absorbed by the sink are similar to that of the acoustic power radiated to the far field. The mean flow of energy associated with fluctuating momentum in the resonator neck is also clearly established by the experimental results. There is a recirculating pattern of energy flow in which there is an upstream mean flow of energy along the lower half of the mean shear layer.

Having firmly established these details of the energy interchanges occurring in the resonator neck, a concluding discussion has been presented in which an attempt is made to interpret these observations in terms of the complete energy balance occurring in the flow. It has been suggested that there is a net production (from mean flow energy) of energy associated with fluctuating momentum from the region of the resonator neck. This results from an imbalance between the power produced by the energy source and that absorbed by the energy sink. The energy leaves the resonator neck in the form of acoustic energy radiated to the far field and in the form of vortices carried downstream of the resonator mouth. Realistic estimates of the quantities involved indicate that the total power produced by the source is divided roughly equally between the acoustic power radiated, the power carried away by the vortices and the power fed back to the "sink" to aid in the formation of new vortices.

It has thus been demonstrated that the mean energy flux associated with fluctuating momentum can be considered as a useful definition of "generalised acoustic intensity". As such, the acoustic energy radiated to the far field can be considered as having its origin in the region of the downstream edge of the resonator neck. This energy is extracted from the mean flow as a direct consequence of the work

done by the fluctuating Coriolis acceleration. This acceleration is also apparently responsible for the increase in convection speed of the vortices as they traverse the downstream edge of the resonator neck.

Finally, the relevance of the Kutta condition has also been discussed in the context of the relationship between the amplitude of the reciprocating potential flow and the rate of accumulation of vorticity into the discrete vortices formed. It has been suggested that the Kutta condition provides the essential link between reciprocating potential flow amplitude and the rate at which the initially unstable vortex sheet is wound into discrete vortices. It has also been suggested that, once the self excitation of the resonator is initiated, the amplitude of oscillation of the system will grow with increasing accumulation of vorticity into discrete vortices until an energy balance is reached. At this point, the net rate of energy extraction from the mean flow will exactly balance the power lost from the resonator neck in the form of energy associated with momentum fluctuations. These final tentative suggestions await further investigation.